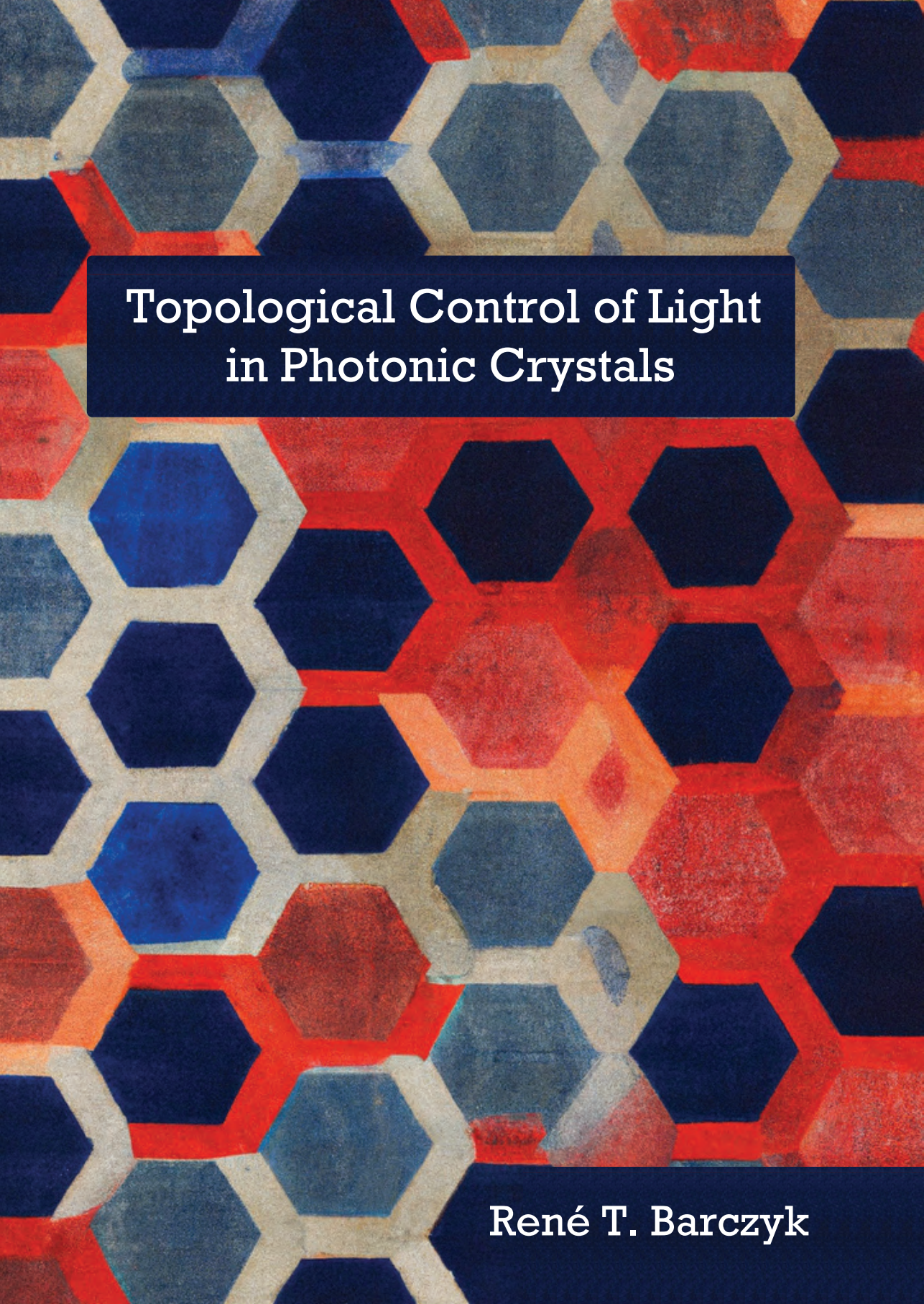
Topological Control of Light
in Photonic Crystals
René T. Barczyk

Topological Control of Light in Photonic Crystals

René Tobias Barczyk

Cover design: Derived from AI-generated image (https://openai.com/dall-e-2) using variations of the results obtained with the prompt “Oil painting of a seamless honeycomb lattice of regular hexagons, half blue half red, decorative Japanese print”. Reuse, copyright, and ownership of the generated image is regulated by the terms of use of OpenAI (https://openai.com/policies/terms-of-use).

Ph. D. Thesis, Eindhoven University of Technology, November 2023
Topological Control of Light in Photonic Crystals
René Tobias Barczyk
ISBN: 978-94-92323-71-2

The work described in this thesis was performed at:
AMOLF, Science Park 104, 1098 XG Amsterdam, The Netherlands.

This work is part of the research programme of the Netherlands Organisation for Scientific Research (NWO). The author acknowledges support from the European Research Council (ERC) Advanced Investigator grant no. 340438-CONSTANS and ERC starting grant no. 759644-TOPP.

More information about the *Photonic Forces* group at AMOLF can be found at `https://www.optomechanics.nl`.

A digital version of this thesis is freely available at:
`https://ir.amolf.nl/` and `https://research.tue.nl/`.

TOPOLOGICAL CONTROL OF LIGHT IN PHOTONIC CRYSTALS

PROEFSCHRIFT

ter verkrijging van de graad van doctor aan de
Technische Universiteit Eindhoven, op gezag van de
rector magnificus prof. dr. S.K. Lenaerts, voor een
commissie aangewezen door het
College voor Promoties, in het openbaar te verdedigen
op vrijdag 10 november 2023, om 11:00 uur

door

René Tobias Barczyk

geboren te Neurenberg, Duitsland

Dit proefschrift is goedgekeurd door de promotoren en de samenstelling van de promotiecommissie is als volgt:

Voorzitter:	prof. dr. C. Storm
1e promotor:	prof. dr. E. Verhagen
2e promotor:	prof. dr. L. Kuipers (Technische Universiteit Delft)
leden:	prof. dr. A. Szameit (Universität Rostock)
	prof. dr. D. Vanmaekelbergh (Universiteit Utrecht)
	prof. dr. L. Andreani (Università di Pavia)
	dr. ir. K.J. Tielrooij
	dr. Y. Jiao

Het onderzoek dat in dit proefschrift wordt beschreven is uitgevoerd in overeenstemming met de TU/e Gedragscode Wetenschapsbeoefening.

Not what we have, but what we enjoy, constitutes our abundance.

Jean Antoine Petit-Senn (1792 - 1870)

CONTENTS

1

INTRODUCTION

1

1.1. SHAPING THE FUTURE WITH LIGHT

As a testament to our evolutionary timeline, mankind's progression through history has been indelibly punctuated by the invention of novel materials and groundbreaking technological tools. From the Stone Age, delineated by our ancestors' deftness in knapping flint, to the Iron Age, characterized by metallurgical mastery, the discovery and ingenious utilization of materials have always driven societal metamorphosis and advancement. Each epoch is emblematic of humanity's unyielding ingenuity, as we moved from basic tools to steam-powered machines, setting the stage for the modern era.

It is within this modern era that the last century, in particular, heralds a revolution that has dramatically reshaped our society: the advent of information technology. Propelled by an explosive surge of novel digital systems, algorithms, and vast interconnected networks, this revolution has transformed almost every facet of human life, from healthcare and commerce to communication and education. Indeed, the advent of the internet, a behemoth technological marvel spanning continents and oceans, has underpinned the global dissemination of knowledge and fostered unprecedented levels of interconnectedness.

At the very heart of this colossal network lies light — an element that, while largely invisible to the end-user, is indispensable in transmitting vast quantities of information across tremendous distances at unparalleled speed. However, paradoxically, while light is key to the transport of information, the processing and computational elements of these systems primarily rely on electronics. As such, the interplay between photonic and electronic components in modern systems is both a crucial enabler of functionality and a limiting factor for efficiency and speed [1–4]. Given the powerful properties of light for communication, it is very important to (1) learn how to control light propagation at small scales, on and off chip, and (2) learn how to control the interaction of light with matter, i.e. the conversion of information from photons to other degrees of freedom.

In this regard, recent decades have seen a proliferation of research delving into the field of metamaterials [5–11]. These materials are constituted of "meta-atoms" — periodic or non-periodic assemblies of micro or nanostructured building blocks, much larger than atoms found in conventional crystalline materials. These building blocks can be made from conventional materials such as metals or dielectrics, but when arranged in specific patterns and scales, they give rise to collective behaviors and interactions that are unique to metamaterials. As such, metamaterials may be viewed as effective or artificial (photonic, plasmonic, phononic, microwave, etc.) materials within a certain energy or frequency regime. The comparatively large size of its components allows for the meticulous engineering of a metamaterial's characteristics and the precise adjustment of its inherent interactions by strategically designing the constituent units and their connections. Photonic crystals (PhCs) serve as a notable instance of metamaterials: by merging actual materials with different refractive indices in a systematic pattern, an integrated effective medium is formed, presenting an optical "crystal potential" that leads to a photonic band structure [12, 13]. Photonic crystals, with their ability to manipulate and control the propagation of light in unprecedented ways, hold large potential in furthering

the development of optical technologies, improving efficiencies, and potentially introducing new functionalities [14–17].

Venturing further into the frontiers of technological innovation, an intriguing development is the application of topological concepts to the design of photonic devices. Topology is a branch of mathematics concerned with global properties that are invariant under continuous transformations, the so-called topological invariants. It has ushered in a new paradigm in condensed matter physics, leading to the discovery and understanding of novel phases of matter that are characterized by such invariant properties, the so-called topological invariants. Topological phases of matter underpin the seminal concept of topological insulators (TIs) [18, 19] — materials that are insulating in the bulk but possess conducting surface states, a phenomenon protected by topological invariants and inherently robust to a broad range of perturbations. The introduction of topology into the physics of condensed matter and exploration of topological superconductors has not only enriched the theoretical landscape but has also spurred experimental pursuits to harness these unique properties for technological advancements [20–22].

Motivated by these advancements, topological concepts have also emerged as a promising design principle for photonics. Topological effects are being studied in a diverse set of photonic systems, such as microwave metamaterials [23], bianisotropic metamaterials [24], coupled optical waveguide arrays [25], arrays of coupled resonators [26, 27], and microcavity polaritons [28].

PhCs are especially appealing as they can bring topological photonics to small scales and on-chip applications [29–32]. The inherent immunity to scattering losses and capacity for unidirectional, backscattering-immune light transport in topological PhCs has the potential to propel the permeation of PhCs in a plethora of applications and incite a new generation of integrated photonic devices. Apart from optical communication technology, topological design principles could aid PhCs in permeating into other technological sectors such as biomedical sensing, chemical sensing, and consumer electronics [33–41]. Leveraging topological protection for enhanced light-matter interactions via slow-light and robust transport of photonic information (i.e., optical interconnects) also evokes significant interest in other areas such as the study of quantum electrodynamics, development of quantum technologies, and neuromorphic computing [42–51].

This thesis aims to explore ways to introduce topological phenomena in PhCs, study the properties of topological photonic states that emerge, and investigate their impact on the flow and confinement of light in photonic devices. We will review some basic concepts behind photonic crystals and topological physics in this introduction, starting with the general Bloch band theory of crystals.

1.2. BLOCH BAND THEORY

Bloch's theorem, named after Swiss physicist Felix Bloch, characterizes the solutions of the Schrödinger equation for an electron in a crystal lattice [52–54]. These solutions, known as Bloch states or Bloch functions, are of paramount importance for understanding the behavior of electrons in solids, thus playing a critical role in electronics, semiconductors, etc. Crucially, Bloch's theorem applies not only to

electrons in a crystal but to any wave-like phenomenon in a periodic potential. This includes, for example, the propagation of sound waves in a phononic crystal or, central for this thesis, the propagation of light in a PhC, as we will elaborate later on.

A crystal is a solid material whose atoms are arranged in a highly ordered, spatially repeating pattern, i.e., a lattice. The smallest repeating unit in this structure is called a unit cell. As an illustration, in the following we will restrict the problem to a single spatial dimension x along which the crystal's unit cell repeats with periodicity a. The overall potential $V(x)$ that an electron in this crystal experiences is also periodic, i.e., $V(x) = V(x + l \cdot a)$ ($l \in \mathbb{Z}$). Bloch's theorem emerges from the symmetries of this lattice. If an electron is bound within a crystal, the probability density of finding it should have the same periodicity as the lattice itself. This is a consequence of the translational symmetry of the Hamiltonian $\mathcal{H}$ in the time-independent Schrödinger equation [54]

$$\mathcal{H}\psi(x) = \left(-\frac{\hbar^2}{2m}\nabla^2 + V(x)\right)\psi(x) = E\psi(x), \tag{1.1}$$

where m denotes the electron's mass, $\psi(x)$ is its wavefunction, and E represents an energy eigenvalue of the Hamiltonian. The solutions to Equation (1.1) according to Bloch's theorem (for a derivation see e.g. [53]) are of the form

$$\psi_k(x) = \sum_g c_{k-g} e^{i(k-g)x} = e^{ikx} u_k(x), \tag{1.2}$$

with the lattice-periodic function $u_k(x) = u_k(x + g)$ given by

$$u_k(x) = \sum_g c_{k-g} e^{-igx}, \tag{1.3}$$

where

$$g = l \cdot \frac{2\pi}{a} \equiv l \cdot \tilde{g}, \qquad l \in \mathbb{Z} \tag{1.4}$$

denotes an arbitrary reciprocal lattice vector, and we defined the primitive reciprocal lattice vector $\tilde{g} = \frac{2\pi}{a}$. This result implies that the solutions to the eigenvalue problem in Equation (1.1) are simply given by the product of a plane wave, e^{ikx}, which is modulated by a function $u_k(x)$ that exhibits the same periodicity as the lattice. The interval $k \in [-\frac{\tilde{g}}{2}, \frac{\tilde{g}}{2}]$ is known as the first (or fundamental) Brillouin zone (BZ), and the coefficients c_{k-g} are called the weights of the respective Bloch harmonics $e^{i(k-g)x}$.

The spectrum of energy eigenvalues E_k corresponding to the eigenmodes ψ_k is called an energy band (or simply band) of the crystal. The relationship between the energy E of a particle and its momentum k is generically referred to as the dispersion relation, often also stated in terms of the angular frequency dispersion $\omega(k)$ with the Planck-Einstein relation $E = \hbar\omega$ under the de Broglie hypothesis of particle-wave duality [55, 56]. For a given lattice potential, there are in general several (potentially degenerate) eigenmodes $\psi_{n,k}$ ($n \in \mathbb{N}_0$) and respective eigenvalues $E_{n,k}$, emerging from the interaction of the various orbitals (discrete energy levels) that electrons occupy in the atoms constituting the lattice. The set of functions $E_{n,k}$ is known

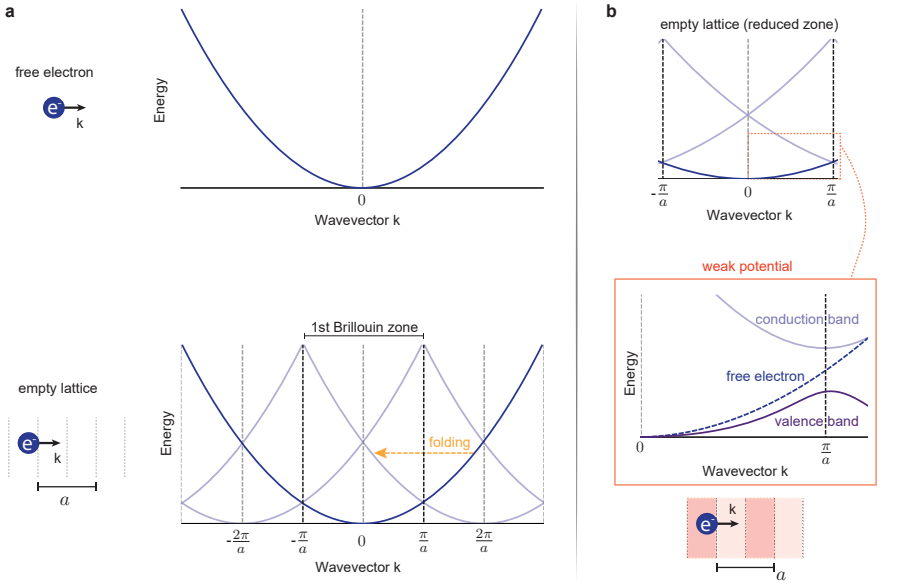

Figure 1.1: Schemes band diagrams for free electrons and electrons in a periodic potential. a, Free electron dispersion before (top) and after (bottom) imposing an artificial periodicity a in the empty lattice approximation. The free electron bands are repeated with a period of $\frac{2\pi}{a}$ after imposing the periodicity, which can be viewed as band-folding into the fundamental Brillouin zone in the reduced zone scheme (next panel). **b,** Free electron dispersion in the reduced zone scheme showing only the fundamental Brillouin zone after band folding in the empty lattice approximation (top). When introducing a weak periodic modulation, a bandgap opens at the zone boundary (bottom).

as the (energy) band structure of the material. The gaps between these bands, or bandgaps, correspond to energy ranges where no electron states can exist. They play a paramount role in solid-state physics as they give rise to distinct behaviors in different materials, explaining why some materials are conductors, some are insulators, and others are semiconductors.

Band structures are typically displayed as plots of energy versus wavevector within the first BZ. Wavevectors beyond this region are folded back into the first zone by subtracting a suitable reciprocal lattice vector, which can always be found. This operation is known as band folding and represents a helpful tool for the visualization of a crystal's energy landscape. To illustrate this with a simple example, let us consider the case of free electron propagation onto which we impose an artificial periodicity by considering the edge case of a vanishing potential, also known as empty lattice approximation. The absence of a potential in Equation (1.1) means that we are left with only the kinetic energy term which yields the well-known energy eigenvalues

$$\epsilon_k = \frac{\hbar^2 k^2}{2m}, \tag{1.5}$$

signifying a parabolic dispersion relation (Figure 1.1a). Under an arbitrary, artificially imposed periodicity a, we can write the free electron energy bands within the

first BZ as

$$E_k = \frac{\hbar^2}{2m}(k+g)^2, \tag{1.6}$$

where g runs over all reciprocal lattice vectors corresponding to our artificially imposed periodicity a. Graphically, this corresponds to the band folding of energies E_k with $|k| > \tilde{g}$ into the first BZ ($k \to k-g$, with suitable g), as schematically depicted in Figure 1.1b. Of course, as a was selected at will, we could have chosen an arbitrarily small fundamental BZ such that the band structure could display more or less bands within the plotted frequency range, hence care has to be taken when interpreting such visualizations and their physical reality. This boils down to the fact that such diagrams of the band structure only depict the eigenvalues of the Hamiltonian governing the system, and thus do not capture the (potentially vanishing) weights of individual Bloch harmonics, which is a property of the eigenmodes. In the plotted example, since we consider free electrons, the states are just plane waves. In this case, the Bloch function is trivial, and the Fourier coefficients (i.e., the weights) for all but one term are zero. Another interesting feature of this representation is the twofold degeneracy that occurs at the band edges where two bands meet. However, in the case at hand, it's important to remember that they are artifacts of our choice of representation. Degeneracies play a pivotal role in the study of materials as they are fundamentally linked to symmetries of the system, a property that is deeply rooted in Wigner's theorem [57]. They may be broken deliberately to engineer bandgaps, an approach that is ubiquitous in the design of artificial periodic structures.

With this in mind, let us now consider an electron propagating through a weak but finite periodic potential $V(x) = V_0 \cos(\tilde{g}x)$, such that the amplitude of the periodic modulation V_0 is small as compared to the kinetic energy of a free electron at the BZ edge. First, we restate Equation (1.1) in an algebraic form that will aid the treatment of this problem. To this end, we express the periodic potential $V(x)$ as a Fourier expansion in the reciprocal lattice vectors

$$V(x) = \sum_g V_g e^{igx}. \tag{1.7}$$

Substituting Equation (1.2) and Equation (1.7) into Equation (1.1) yields [53]

$$(\epsilon_k - E)c_k + \sum_g V_g c_{k-g} = 0. \tag{1.8}$$

For our weak periodic potential, at the zone boundary ($k = \frac{\tilde{g}}{2}$) it holds that $k^2 = \left(\frac{\tilde{g}}{2}\right)^2 = (k-\tilde{g})^2$, and the kinetic energy of the Fourier components $k = \pm\frac{\tilde{g}}{2}$ is equal. Retaining only the Fourier coefficients $c_{\pm\tilde{g}/2}$ in Equation (1.8) yields a two-dimensional (2D) eigenvalue problem that has nontrivial solutions $E_{\tilde{g}}$ only if [53]

$$(\epsilon_{\tilde{g}} - E_{\tilde{g}})^2 = \left(\frac{V_0}{2}\right)^2, \tag{1.9}$$

meaning the eigenenergy can take on two possible values

$$E_{\tilde{g}} = \epsilon_{\tilde{g}} \pm \frac{V_0}{2}. \tag{1.10}$$

These eigenenergies are separated by a gap of size V_0, i.e., the periodic potential with amplitude V_0 opens up a bandgap of similar size at the BZ boundary (Figure 1.1c). The bands below and above this gap are called the valence and the conduction band, respectively. We have thus demonstrated how a periodic potential which reduces the continuous translational symmetry to a discrete translational symmetry can create a bandgap in a formerly gapless material, signifying the transition from a band structure associated with a conductor to that of an insulator (or semiconductor).

Band structures allow illustrating some other key properties of wave propagation in periodic media. The phase velocity v_p of a wave is the speed at which the phase of the wave propagates in space. It is defined as the ratio of the wave's angular frequency to its wavevector $v_p = \frac{\omega}{k}$. However, phase velocity can often be misleading, as it does not always correspond to the speed at which energy or information is transferred. For that, we turn to the group velocity v_g, i.e., the velocity with which a wave packet or "group" of waves moves through space. In terms of the dispersion relation, v_g is given by the derivative of the angular frequency with respect to the wavevector $v_g = \frac{\mathrm{d}\omega}{\mathrm{d}k}$. The second derivative of the dispersion relation (i.e., its curvature) is also significant as it relates to the so-called effective mass $\frac{1}{m^*} = \hbar\frac{\mathrm{d}^2\omega}{\mathrm{d}k^2}$. The effective mass m^* can be thought of as the mass that a particle appears to have when subject to forces (like an electron in an external electric field), dictating the acceleration of the particle in response to such forces. In the empty lattice approximation mentioned earlier, the effective mass simply corresponds to the mass of the free electron $m^* = m$ (see Equation (1.5) and Figure 1.1a). When subject to a finite potential, however, m^* can deviate significantly from a particle's rest mass. In some cases, it can even be negative, leading to phenomena such as electrons moving in the direction opposite to the applied force. As it represents a parameter derived from the energy dispersion of a particle in a specific potential landscape, an effective mass can also be associated with inherently massless particles such as photons. Vice versa, massive particles can also be rendered to effectively behave like massless particles, an intriguing edge case that underlies the physics of systems with a so-called Dirac-like dispersion. As this scenario is of particular relevance in the context of this thesis, we shall next discuss it in more detail.

1.3. DIRAC PHYSICS IN TWO-DIMENSIONAL MATERIALS

Understanding Dirac physics and its manifestations in materials science opens the door to a new world of materials with unique transport properties [58–60]. This section aims to elucidate some basic phenomena associated with Dirac physics, including the emergence of Dirac cones in 2D crystals, and profound implications for 2D materials which will also allow us to introduce the intriguing concept of TIs.

The cornerstone of Dirac physics is the Dirac equation, proposed by Paul Dirac in 1928 [61]. It provides a description of elementary spin-$\frac{1}{2}$ particles, consistent with both the principles of quantum mechanics and the theory of special relativity. The Dirac equation predicts the existence of antiparticles and accounts for the electron's spin, whereby the two spin components for particles and antiparticles, respectively, are generally subsumed in a four-component spinor Ψ. The Dirac equation can be

written as [61]

$$\left(i\hbar\gamma^{\mu}\partial_{\mu} - mc\right)\Psi = 0\,, \tag{1.11}$$

where ∂_{μ} is the four-gradient ($\mu = 1,\dots,4$) and γ^{μ} are the 4×4 Dirac gamma matrices. In the time-independent case, we can rewrite Equation (1.11) as an eigenvalue problem $\mathcal{H}_D\Psi = E\Psi$. The Dirac-Hamiltonian $\mathcal{H}_D$ is given by [62]

$$\mathcal{H}_D = -i\hbar c\,\alpha\cdot\nabla + \beta mc^2\,, \tag{1.12}$$

with the 4×4 matrices $\alpha\cdot\nabla = \sum_{i=1}^{3}\alpha_i\partial_i$, $\alpha_i = \begin{pmatrix} 0 & \sigma_i \\ \sigma_i & 0 \end{pmatrix}$, and $\beta = \begin{pmatrix} \sigma_0 & 0 \\ 0 & -\sigma_0 \end{pmatrix}$, expressed in terms of the 2×2 Pauli spin matrices σ_i ($i = 1,\dots,3$), and σ_0 denoting the 2×2 identity matrix [63]. The matrices α_i and β anticommute and satisfy $\alpha_i^2 = \beta^2 = \sigma_0$. Using the definition of the canonical momentum $\mathbf{p} = -i\hbar\nabla$ and squaring the Hamiltonian yields

$$\mathcal{H}_D^2 = E^2 = \left(pc\right)^2 + \left(mc^2\right)^2\,. \tag{1.13}$$

From Equation (1.13), we see that the particle's energy is composed of a kinetic energy term and a rest mass energy term. At non-relativistic speeds, where the rest mass energy term dominates and $E \approx mc^2$, it can be shown that Equation (1.12) reduces to the well-known Schrödinger equation (Equation (1.1)) [62]. At relativistic speeds, however, the kinetic term dominates such that $E \approx p$, and the Dirac equation yields a linear energy-momentum relation that is fundamentally different from the parabolic one in non-relativistic quantum mechanics. As this linear dispersion relation also emerges for a vanishing mass term, it is often referred to as the dispersion relation of a massless Dirac fermion [60, 64, 65].

At this point, we can establish the connection to the so-called Dirac cone. A Dirac cone is a phenomenon observed in certain crystals around specific points in the BZ. The energy-momentum relation in the vicinity of these high-symmetry points in reciprocal space (Dirac points) turns out to be well approximated by an effective Hamiltonian that closely resembles a Dirac Hamiltonian $\mathcal{H}_D$ [58]. The solutions of the Dirac equation near the Dirac points exhibit a linear energy-momentum dispersion, not unlike the dispersion relation of massless Dirac particles. Around the Dirac points, where valence and conduction bands meet, the energy surfaces exhibit a conical shape that is commonly referred to as a Dirac cone.

The appearance of Dirac cones in the dispersion relation of a crystal is linked to the presence of certain symmetries. In particular, two main types of symmetry are often associated with the existence of Dirac cones: inversion symmetry and time-reversal symmetry [18, 66]. It is important to note that not all materials with these symmetries exhibit Dirac cones. Other factors, such as the specific atomic arrangement and interactions between atoms, can significantly influence the band structure of the material. However, the presence of these symmetries is often a key ingredient for the formation of Dirac cones. The necessary symmetry conditions for the emergence of Dirac cones can be realized in certain three-dimensional (3D) crystals known as Dirac semimetals [58], and also one-dimensional (1D) systems such as carbon nanotubes [67]. The most famous example, however, is the 2D material graphene [60, 66, 68, 69].

Graphene is a planar material constituted of a monolayer of carbon atoms arranged in a honeycomb lattice (Figure 1.2a) [69–71]. Carbon has four valence electrons, of which three lead to the formation of strong in-plane bonds (σ-bonds) to the neighboring atoms in the lattice via sp^2 orbital hybridization [66]. The remaining free electron in each carbon atom's out-of-plane $2p_z$ orbital forms covalent bonds (π-bonds) that give rise to the creation of valence and conduction bands. Due to the relative weakness of the π-bonds, the electronic behavior around the Fermi energy level in graphene is adequately represented by a tight binding model, assuming a single orbital per atom. In this approximation, the electron wavefunction can be represented by the Bloch states Φ_j ($j = A, B$) of the $2p_z$ orbitals that correspond to the two distinct carbon atoms (A and B) within a primitive rhombic unit cell of the honeycomb lattice. The atoms form what is known as the A and B sublattices of the crystal, and the pseudospin in graphene refers to the degree of freedom associated with this sublattice degeneracy of the honeycomb lattice, representing a quantum number analogous to the spin of a particle. The wavefunction in the tight binding approach can be written as a sum over the sublattices [72]

$$\Phi_j(\mathbf{k}) = \sum_{\mathbf{t}} e^{i\mathbf{k}\cdot(\mathbf{r}_j+\mathbf{t})}\Phi\left(\mathbf{r}-\mathbf{r}_j-\mathbf{t}\right), \quad j = A, B, \tag{1.14}$$

where $\mathbf{t}$ runs over all (real-space) lattice vectors. The invariant symmetry operations of the 2D crystal lattice (the point group) contain both mirror symmetry and rotational symmetry which, together with the sublattice degeneracy, play a crucial role in creating the Dirac cones. Indeed, the tight-binding model evidences the formation of Dirac point degeneracies (i.e., Dirac cones) at the corners of the BZ around the K and K' high-symmetry points (see Figure 1.2b), leading to extraordinary electron mobility and thermal conductivity [66, 68, 72]. At the Dirac point, the probability of finding an electron is equal for both the A and B sublattices. This gives rise to a twofold degeneracy, often referred to as "valley degeneracy" because the Dirac point can be found at the two inequivalent K and K' valleys of the BZ, whereby "valley" refers to the conical shape of the energy dispersion at the K and K' high-symmetry points.

In two spatial dimensions, the Hamiltonian near the K and K' valleys assumes the form [66, 72]

$$\mathcal{H}_D^{2D} = v_F \boldsymbol{\sigma}\cdot\mathbf{p}, \tag{1.15}$$

where $\boldsymbol{\sigma} = (\sigma_1, \sigma_2)$, $\mathbf{p}$ now denotes the in-plane (2D) momentum, and the electron's Fermi-velocity v_F takes over the role of the speed of light c in the original 2D Dirac Hamiltonian (Equation (1.11)) [58]

$$\mathcal{H}_D^{2D} = c\boldsymbol{\sigma}\cdot\mathbf{p} + mc^2\sigma_3, \tag{1.16}$$

for a vanishing mass term $m = 0$. Therefore, despite moving approximately 300 times slower than the speed of light, the low-energy excitations in graphene can be described as relativistic massless Dirac fermions which differ significantly from the Schrödinger fermions typically seen in other semiconductors.

The peculiar band structure of graphene has profound consequences for the electronic properties in the presence of external electric and magnetic fields, which

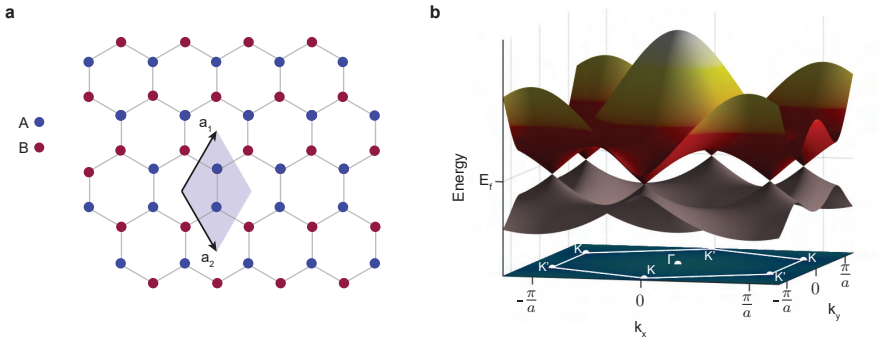

Figure 1.2: Graphene lattice and Dirac cones. a, Honeycomb lattice geometry, with the sublattices A and B as well as the primitive lattice vectors indicated. **b,** Tight binding band structure of graphene, showing the Dirac cones that emerge around the Fermi energy E_F at the K and K' high symmetry points at the edges of the Brillouin zone.

we will briefly outline here. The 2D nature of graphene alongside its linear Dirac-like dispersion renders its behavior similar to a 2D electron gas in many ways. For 2D electron gases at extremely low temperatures it is known that, under the presence of an orthogonal magnetic field with magnitude B, the formerly continuous quadratic electron dispersion splits into discrete, equidistant energy levels [29]

$$E_n = \hbar\omega_c \left(n + \frac{1}{2}\right), \tag{1.17}$$

where $\omega_c = \frac{eB}{m}$ is the cyclotron frequency and e denotes the elementary charge. These are the so-called *Landau levels* [73] Illustratively, this Landau quantization can be thought of as the transition of the linear free electron motion into quantized cyclotron orbits by means of the Lorentz force that acts on charge carriers moving through an external magnetic field, whereby the helicity of these orbits and their energy spacing is determined by the sign and the magnitude of the magnetic field, respectively.

Graphene exhibits a similar Landau level quantization when a magnetic field that breaks time-reversal symmetry is applied orthogonally to the plane of the sheet [74]. Intriguingly, the Landau level spectrum in graphene is notably different from the case of a 2D electron gas due to the Dirac-like nature of the energy dispersion. To illustrate this, we present a derivation of the energy spectrum of these levels [65, 66, 75]. Note that we employ a somewhat simplified description of graphene that does not account for certain effects like valley or spin degeneracy [76].

For a particle with charge e in a magnetic field $\mathbf{B} = B\hat{z}$, the canonical momentum $\mathbf{p}$ is replaced by $\boldsymbol{\pi} = \mathbf{p} - e\mathbf{A}$, where $\mathbf{A}$ is the magnetic vector potential satisfying $\nabla \times \mathbf{A} = \mathbf{B}$. In graphene, the low-energy electronic excitations near the K points of the BZ are described by the 2D Dirac Hamiltonian of Equation (1.15). If we only consider one of the two valleys (K or K'), the Hamiltonian in a magnetic field takes on the form

$$H = v_F \boldsymbol{\sigma} \cdot \boldsymbol{\pi}\,. \tag{1.18}$$

The generic solutions to the associated eigenvalue problem $H\psi = E\psi$ in the Landau gauge $\mathbf{A} = B(-y,0)$ are of the form $\psi(x,y) = e^{ikx}\phi(y)$, yielding

$$v_F \begin{pmatrix} 0 & \partial_y - k + eBy \\ -\partial_y - k + eBy & 0 \end{pmatrix} \phi(y) = E\phi(y)\,. \tag{1.19}$$

This can be expressed more compactly as

$$\left(O\sigma_+ + O^\dagger \sigma_-\right)\phi(\xi) = \frac{\sqrt{2}l_B E}{v_F}\phi(\xi)\,. \tag{1.20}$$

Here, $\sigma_\pm = \sigma_x \pm i\sigma_y$, $\xi = \frac{y}{\ell_B} - \ell_B k$ is a dimensionless length scale, $l_B = \sqrt{\frac{\hbar}{eB}}$ is the magnetic length, and

$$O = \frac{1}{\sqrt{2}}\left(\xi + \partial_\xi\right), \tag{1.21a}$$

$$O^\dagger = \frac{1}{\sqrt{2}}\left(\xi - \partial_\xi\right), \tag{1.21b}$$

are 1D harmonic-oscillator operators. The corresponding number operator is given by $N = O^\dagger O$. Equation (1.20) permits zero-energy solutions

$$\left(O\sigma_+ + O^\dagger\sigma_-\right)\phi_0 = 0, \tag{1.22}$$

which can be identified with a state localized on either of the sublattices A or B, e.g.,

$$\phi_0 = \psi_0(\xi) \otimes |B\rangle\,, \tag{1.23}$$

with $\psi_0(\xi)$ denoting the ground state of the 1D harmonic oscillator, i.e.,

$$O\psi_0(\xi) = 0\,. \tag{1.24}$$

All other solutions can be constructed from ψ_0 using the ladder operators (Equations (1.21)), and we obtain

$$\psi_{n,\pm}(\xi) = \psi_{n-1}(\xi)\otimes|A\rangle \pm \psi_n(\xi)\otimes|B\rangle = \begin{pmatrix}\psi_{n-1}(\xi)\\ \pm\psi_n(\xi)\end{pmatrix}, \tag{1.25}$$

where $n \in \mathbb{N}_0$. Explicitly, the wavefunctions read [66, 77]

$$\psi_n(\xi) = \frac{2^{-\frac{n}{2}}}{\sqrt{n!}} e^{-\frac{\xi^2}{2}} H_n(\xi)\,, \tag{1.26}$$

where H_n are the Hermite polynomials. The corresponding energy levels (Landau levels) for these solutions are given by

$$E_n = \mathrm{sgn}(n)\sqrt{2eB\hbar v_F^2|n|}\,, \tag{1.27}$$

where $\mathrm{sgn}(\cdot)$ denotes the sign function. This Landau level spectrum is quite unique since the energies follow a square root scaling, moreover, there is a zero-energy

Landau level (cf. Equation (1.22)). This is distinct from non-relativistic electron systems (like in conventional 2D electron gases or semiconductors) where the energy levels form a harmonic series, and there is no zero-energy level [60, 78, 79].

When the Fermi level lies in a gap between Landau levels, the bulk of the system turns into an insulator. However, in a real system with boundaries, the flat Landau levels within the bulk curve upwards or downwards near the edge of the sample. These curved levels can be thought of as Dirac cones situated at the edges (or the surface) of the insulating bulk, i.e., they provide conducting channels that allow electrons to move along the edges of the sample. For a Fermi energy in between the Landau levels, all the conducting electrons are in these so-called edge states, and each filled Landau level contributes a conductance of $\frac{e^2}{h}$ (where e is the electron charge and h is the Planck constant) to the total Hall conductance. When changing the magnetic field strength or the electron density and thereby changing the filling factor (the number of filled Landau levels), the Fermi level (the highest energy level occupied by electrons at zero temperature) moves up and down through these Landau levels. This means the Hall conductance changes in integer steps of $\frac{e^2}{h}$, revealing its quantized nature in this scenario that is known as the quantum Hall effect (QHE) [80–82]. In contrast to 2D electron gases, the existence of the zero-energy Landau level in graphene leads to the so-called anomalous QHE that displays a half-integer quantization of the Hall conductivity [64, 65, 71, 74, 83]. The related phenomena of quantum spin Hall effect (QSHE) and quantum valley Hall effect (QVHE), which involve the spin and valley degrees of freedom, respectively, also depend on lifting of the Dirac point degeneracies in graphene and can be understood using similar reasoning [84, 85]. The common theme of all these effects is the presence of an insulating bulk material that features highly conductive edge states at their boundaries which are symmetry-protected and thus extremely resilient to perturbations. Such systems are known as TIs, and we refer to Section 1.5 for a more in-depth discussion of these materials, the various QHEs, and the role topology plays in understanding the material properties.

It is worth noting that the degeneracy and the presence of Dirac cones can be affected by a plethora of symmetry-breaking mechanisms that hold the potential to open up a bandgap, such as the application of strain, or the presence of defects and impurities. In fact, it has been shown that the effects of applying strain in sheets of graphene can be mathematically described analogously to the effects of external magnetic and electric fields, i.e., as artificial gauge fields (cf. Equation (1.18)) [72, 86]. These pseudomagnetic and pseudoelectric fields provide an intriguing new pathway to control the band structure and the occurrence and properties of bandgaps without the need for any real external fields. Moreover, the magnitude of artificial gauge fields can largely exceed that of their real counterparts. As this principle can be fairly readily adopted for photonic emulations of solid state graphene (see Section 1.4 and Section 1.5.3), it constitutes an active field of research especially in the realm of PhCs, and it also underlies the work presented in Chapter 5 of this thesis.

1.4. PHOTONIC CRYSTALS

After having introduced some key concepts that govern the solid state physics of atomic materials, we now turn to their photonic counterparts where multiple analogies as well as subtle differences can be recognized. First proposed by Eli Yablonovitch and Sajeev John in 1987 [87, 88], the term "PhC" refers to a periodic arrangement of materials with different dielectric constants which can be regarded as an effective material that modulates the propagation of light waves similar to how atoms in a crystal modulate the propagation of electron waves [13, 89]. Especially in recent years, with the advent of advanced nanofabrication techniques, increasingly more elaborate and miniaturized PhCs have been realized experimentally, with periodicity on wavelength scales that pushes their operating frequencies from the microwave down to the optical regime [13–15].

Indeed, PhCs bear a striking resemblance to electronic crystals in many ways, which may not appear too surprising considering the dual particle-wave nature of both photons and electrons. Just as the periodic potential in an electronic crystal leads to the formation of electronic band structures, the periodic refractive index in a PhC leads to the formation of photonic band structures. In the Bloch band formalism (see Section 1.2) of PhC modes, Maxwell's equations take on the role of the Schrödinger equation (Equation (1.1)). The ionic crystal lattice is replaced by a periodic variation of the dielectric permittivity $\epsilon(x+a) = \epsilon(x)$, resulting in a periodic optical potential that modulates the PhC modes. The modes' electric $\mathbf{E}$ (or magnetic $\mathbf{H}$) field takes the place of the electron's wavefunction ψ. When these equations are solved within a periodic potential like a PhC, they yield solutions that are analogous to Bloch states. The solutions indicate that the light wave, like an electron wave in an atomic crystal, exhibits a periodic variation in its amplitude and phase that matches the periodicity of the crystal structure. Consider the general representation of a harmonic plane wave in terms of position $\mathbf{r}$ and time t

$$\mathbf{E}(\mathbf{r}, t) = \mathbf{E}_0 e^{-i(\omega t - \mathbf{k}\cdot\mathbf{r})}, \tag{1.28}$$

where $\mathbf{E}_0$ is the electric field vector, ω the angular frequency, and $k = |\mathbf{k}| = \frac{2\pi n}{\lambda}$ the magnitude of the wave vector $\mathbf{k}$ in a medium of refractive index n for free-space wavelength λ. A time dependence of $e^{-i\omega t}$ is adopted for the fields throughout this work. Just as in the solid state case, the effect of the periodic potential is a modulation of such plane waves by the periodic potential derived from $\epsilon(x)$, and the Bloch states are of the form

$$E_k = \sum_k c_k E_0 e^{ikx}. \tag{1.29}$$

This understanding leads to a powerful tool for the control and manipulation light. By designing PhCs with suitable lattice geometries, it is possible to create photonic bandgaps at desired frequencies. The photonic bandgap is formed due to Bragg diffraction [90]. When an electromagnetic wave propagates through a PhC, it gets scattered due to the periodic change in the dielectric constant. At specific frequencies, waves scattered from different lattice points interfere destructively, leading to the creation of a bandgap.

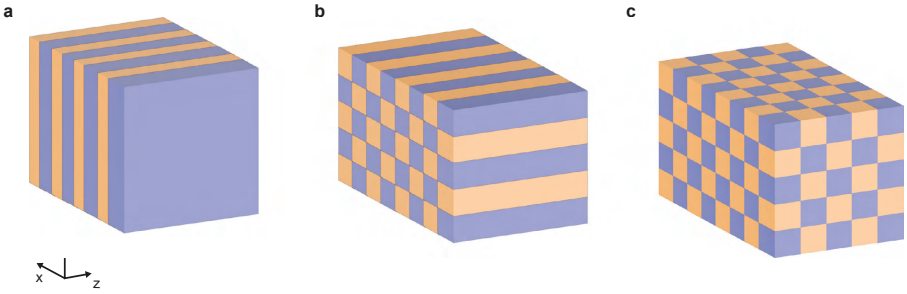

Figure 1.3: Photonic crystals in various dimensions. Schematics of PhCs with **a,** one-dimensional, **b,** two-dimensional, and **c,** three-dimensional periodicity.

Despite the plethora of analogies to electronic systems, there are also some key differences in the description of photonic (crystal) modes that should be mentioned. They largely boil down to the differences in the properties of the elementary particles constituting the modes. On the one hand we have electrons, which are (often non-relativistic) massive fermions, while on the other hand we have photons, being (relativistic) massless bosons. The massless nature of photons means that the free-space propagation of plane waves is characterized by a linear dispersion $\omega = ck$, rather than the parabolic one describing free electrons. Further, the integer spin of photons means that they obey the Bose-Einstein statistics and, unlike electrons or any other spin-$\frac{1}{2}$ particles which obey the Fermi-Dirac spin statistics, are not subject to the same Pauli exclusion principle. This has profound consequences for the realization of the photonic analogs of the QHEs in PhCs, as we will see later (Section 1.5.3). Depending on the dimensions along which the dielectric function is periodically modulated, we can construct PhCs in one, two, or three dimensions (see Figure 1.3). While 3D PhCs allow for confinement in all three dimensions and achieve complete bandgaps for light, their design and fabrication comes with various practical challenges. One-dimensional PhCs (such as Bragg reflectors), on the other hand, have the disadvantage that their bandgaps are only present for a fairly limited range of wavevectors (i.e., incident angles).

In this thesis, we study the case of 2D PhCs, which are periodic in the xy-plane and have a finite extent along the orthogonal (non-modulated) out-of-plane (z-) direction. They can perhaps more accurately be called quasi-2D PhCs, or PhC slabs, since the dielectric function is not truly homogeneous along z but rather have a narrow extent orthogonal to the PhC plane (see Figure 1.4). The slab geometry allows for confinement of light in the direction normal to the PhC plane due to the dielectric contrast of the slab (e.g., silicon) and the ambient medium (typically air), which results in index guiding via total internal reflection. The in-plane PhC modes can be classified as being either transverse electric (TE) or transverse magnetic (TM), depending on whether the magnetic or the electric field polarization points out of the PhC plane, respectively. The mode properties can then be adequately described by only considering their out-of-plane electric E_z (TM) or magnetic H_z (TE) field component. Often, only one of the two polarizations exhibits a complete bandgap

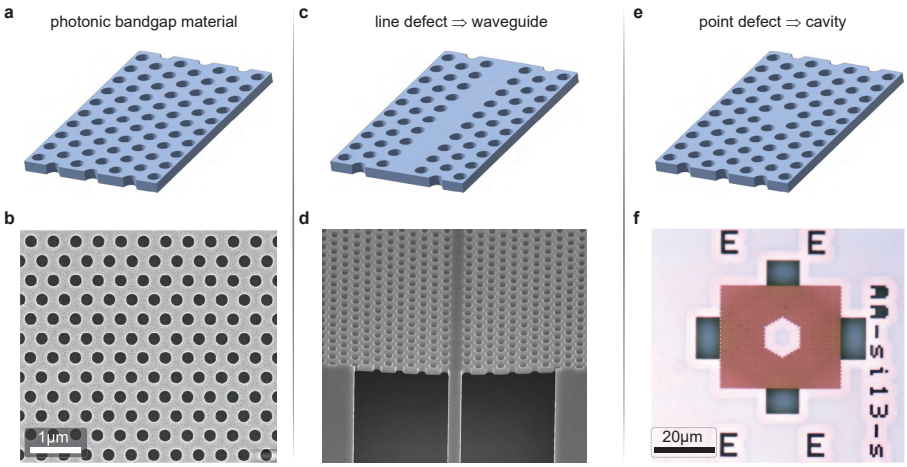

Figure 1.4: Photonic crystal slabs with defect waveguides and cavities. a, Schematic depiction of the geometric starting point for the design of photonic crystal (PhC) defect modes, here, a triangular lattice of circular air holes perforating a silicon PhC slab. The PhC slab constitutes a photonic bandgap material for the transverse-electric-like modes it supports, i.e., a PhC that features a gap in its frequency dispersion where no guided slab modes exist. **b,** Scanning electron microscope image of a fabricated photonic bandgap material. **c,** Introducing a defect row into the triangular lattice creates defect modes that are prohibited from entering the surrounding slab in the frequency range corresponding to the photonic bandgap (photonic bandgap confinement), and a so-called W1 waveguide is formed (see also Chapter 3). **d,** Scanning electron microscope image of a fabricated W1 waveguide that is interfaced with a silicon ridge access waveguide for in-coupling from the side of the sample (see Section 2.1.1). The finite thickness (220 nm) of the suspended silicon slab becomes apparent from the tilted perspective of the image. **e,** When introducing point defects into the lattice, photonic bandgap confinement within the PhC plane leads to the emergence of localized states inside the defect region, forming a cavity. The schematically shown example of a defect in the triangular PhC formed by a single missing lattice site is also known as an H1 cavity. **f,** Optical microscope image of a (much larger) defect cavity inside a honeycomb PhC lattice (see Chapter 4 for more details on the PhC platform).

in the photonic dispersion relation, and the PhC is then said to feature TE-like or TM-like modes, respectively. The dynamics of the system is then, in analogy to the Schrödinger equation, captured by an eigenvalue problem with the 2D Helmholtz equation [13]

$$-\nabla\cdot(\eta(\mathbf{x})\nabla)\psi(\mathbf{x}) = \left(\frac{\omega}{c}\right)^2 \varrho(\mathbf{x})\psi(\mathbf{x}), \tag{1.30}$$

where for TE-like modes $\psi(\mathbf{x}) = H_z(\mathbf{x})$, $\eta(\mathbf{x}) = \frac{\omega}{\epsilon(\mathbf{x})}$, $\varrho(\mathbf{x}) = 1$, and for TM-like modes $\psi(\mathbf{x}) = E_z(\mathbf{x})$, $\eta(\mathbf{x}) = 1$, $\varrho(\mathbf{x}) = \epsilon(\mathbf{x})$. One important consequence of the finite slab thickness is the leakage of light into free space within a certain range of wavevectors around the Γ-point (i.e., $k = 0$) in the BZ, i.e., the out-of-plane leakage of modes at large angles close to the normal direction. This affects the PhC bands that lie within the region above the so-called light-lines of the slab $\omega = k\frac{c}{n}$, where n is the refractive index of the slab and this angular region is referred to as the light cone. Within the light cone, the mode confinement via index guiding breaks down and out-of-plane losses occur upon propagation. Due to reciprocity, however, this also allows for the excitation of PhC modes from the far field.

PhCs offer a playground for emulating a large variety of phenomena originally associated with their electronic counterparts. Among the first were the design and experimental realization of the photonic analog of conducting wires and resonators, i.e., PhC waveguides and cavities [12–14]. By creating defects (disruptions in the periodicity) in a PhC that features a bandgap (see Figure 1.4a,b), light can be localized within the defect region via photonic bandgap confinement, i.e., light cannot penetrate into the surrounding bulk PhC withing the frequency regime of the bandgap since there are no guided states available. Photonic crystal defect waveguides are created by introducing a line defect into the PhC structure (see Figure 1.4c,d). This disruption in the periodicity alters the local band structure and creates states within the bandgap. Consequently, light of frequencies within the bandgap will be confined to the defect region and guided along it, akin to an optical fiber. Contrary to optical fibers, however, PhC defect waveguides do not rely on total internal reflection, which typically causes radiation losses at bends and junctions. They can therefore be bent and twisted in the plane of the PhC with little loss of the confined light, allowing for more compact integrated optical circuits. Furthermore, by introducing point defects, one can create PhC cavities (see Figure 1.4e,f). These defects create localized states within the bandgap, effectively trapping light in a small volume. Photonic crystal cavities can have very high quality (Q) factors, confining light for long periods of time before it dissipates [12]. They find applications in lasers, sensors, and quantum computing [16, 17, 43]. High-Q cavities are particularly important for enhancing light-matter interactions in these fields.

Great efforts have been conducted to optimize the properties of PhC waveguides and cavities, particularly to minimize losses experienced upon propagation through bends and in the presence of impurities, and to increase the lifetime of trapped states with nanometer-sized mode volumes [91]. An exciting recent development that opens up new avenues in the design of integrated photonic devices is the advent of photonic topological insulators. Akin to their solid state counterparts, the topological principles governing the properties of edge state in these systems hold the promise for unprecedented robustness regarding the transport and confinement of energy and information in the optical domain, immune to losses and backscattering from a wide range of impurities and perturbations. We next turn our attention to the fundamental principles of topology underlying these novel functional materials, and how they are implemented as a design principle for PhCs to introduce topological concepts into the realm of photonics.

1.5. TOPOLOGICAL PHOTONIC CRYSTALS

Transferring concepts from band theory such as band structures and bandgaps from the realm of solid-state physics to photonics has had profound impact on our capabilities to control light on vastly smaller scales than previously deemed possible. However, the energy bands, i.e., the eigenvalues of the governing dynamic equations, only tell half the story. The other half lies within the properties of the eigenvectors, i.e., the wavefunctions populating the bands. The closer study of the properties of these waves and their relationship to the bands they occupy has surfaced an intimate link between band theory and the abstract mathematical dis-

cipline of topology. Introducing topological concepts to band theory has provided a deeper understanding of quantum states, which led to the discovery of novel phases of matter like TIs. Likewise, further exploration of these principles in photonics promises to open up new avenues in the control of light in unprecedented ways. In this section, we will elucidate the key concepts of topological band theory and the TI, its relation to the various QHEs, and their realization in PhCs in the form of photonic topological insulators.

1.5.1. TOPOLOGICAL BAND THEORY

In quantum mechanics, the adiabatic theorem describes the evolution of quantum states under slow, time-dependent perturbations [92]. The state of the system remains essentially "constant" in this process, with the change accumulating a dynamical phase and a geometric phase [93]. The latter is independent of the system's dynamical details — a concept which we now understand as the (Pancharatnam-) Berry phase, first evoked by Pancharatnam in classical optics [94], and later formalized by Michael Berry [95].

The concept of parallel transport in differential geometry plays a key role in our understanding of geometric phase [96, 97]. Parallel transport is a way of moving a vector along a curve in a manifold such that it remains "constant" in the local sense along the journey. Let us start with an intuitive understanding using the surface of the unit sphere as the parameter space, as shown in Figure 1.5a. We imagine starting out with a vector at the north pole of the sphere that points to the south pole along an arbitrary longitude, chosen to intersect the x-axis in the displayed example. We then traverse a closed contour along the sphere's surface: first down to the equator, then a certain distance along the equator, and finally returning to the starting point, always keeping the vector pointing towards the south pole (i.e., not changing its direction in a local sense). Strikingly, once we return to the point of origin, we realize that the vector does not point in the original direction anymore, but is rotated by an angle ϕ. This angle ϕ denotes the geometric phase that is acquired when parallel transporting a vector along a closed contour in parameter space. We can determine it by parametrizing a point $|\psi\rangle$ on the sphere with the Dirac notation [98]

$$|\psi\rangle = \cos\left(\frac{\theta}{2}\right)|0\rangle + e^{i\varphi}\sin\left(\frac{\theta}{2}\right)|1\rangle\,, \tag{1.31}$$

where φ and θ denote the azimuthal and polar angles, respectively. The geometric (Berry) phase accumulated after a complete cycle is given by

$$\phi = \oint_{\ell} \langle\psi|\nabla_{\mathbf{R}}|\psi\rangle \,\mathrm{d}\mathbf{R}\,, \tag{1.32}$$

where $\mathbf{R} = (\varphi, \theta)$ describes the generalized coordinates of the parameter space and the integral runs over a closed contour ℓ. In our example, it explicitly reads

$$\phi = \iint \sin(\theta)\,\mathrm{d}\theta\,\mathrm{d}\varphi \equiv \Omega\,, \tag{1.33}$$

which evidences an intimate link between the geometric phase ϕ acquired by the parallel transported vectors upon completing the loop, and the solid angle Ω (area

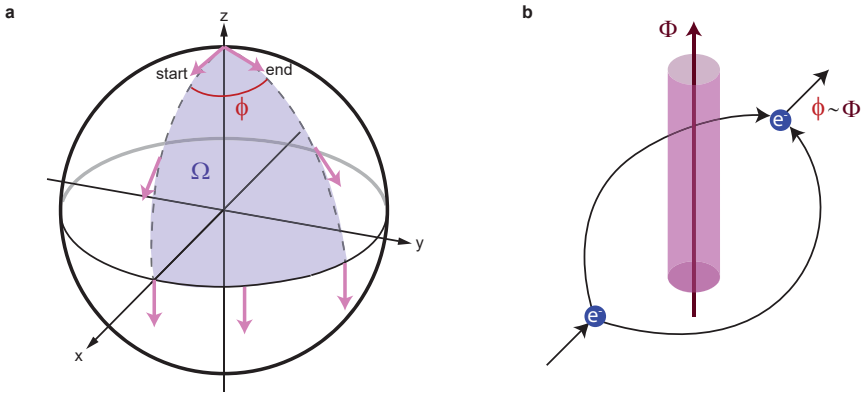

Figure 1.5: Parallel transport and geometric phase. a, Parallel transport on a sphere, illustrating the Berry phase ϕ that is acquired and the geometric connection to the Berry curvature, which can be interpreted as the area enclosed by the chosen transport loop. **b,** Scheme of the Aharonov Bohm effect as a physical example for the manifestation of a geometric phase, acquired by electrons propagating around a solenoid permeated by a flux φ, despite the electrons not directly interacting with the shielded magnetic field.

on the unit sphere) subtended by the loop. In fact, the term "geometric" phase derives from this geometric correspondence between ϕ and Ω in parameter space, and the relation Equation (1.33) can be seen as a manifestation of the Gauss-Bonnet theorem applied to the case of a sphere [99].

The analogy to the evolution of a quantum state is straightforward. The wave function of a quantum system undergoing adiabatic cyclic evolution can be parallel transported along a path in the parameter space. For a Bloch state $\psi_n(\mathbf{k})$, this path corresponds to a closed loop in $\mathbf{k}$-space, i.e., the evolution of $\psi_n(\mathbf{k})$ along an energy band $E_n(\mathbf{k})$ in the BZ. The Berry phase ϕ_n of the wavefunction $\psi_n(\mathbf{k})$ populating the band $E_n(\mathbf{k})$ can then be written as [100–102]

$$\phi_n = \int_l \mathbf{A}_n(\mathbf{k})\, \mathrm{d}\mathbf{k}\,, \tag{1.34}$$

with the Berry connection $\mathbf{A}_n(\mathbf{k})$ defined as

$$\mathbf{A}_n(\mathbf{k}) = i \left\langle \psi_n(\mathbf{k}) \right| \nabla_{\mathbf{k}} \left| \psi_n(\mathbf{k}) \right\rangle . \tag{1.35}$$

The Berry connection $\mathbf{A}_n(\mathbf{k})$ is, in essence, a gauge connection in parameter space. The concept of a connection is fundamental in differential geometry and is the basic ingredient in defining a covariant derivative, allowing to define parallel transport in curved spaces [97, 99]. The term "gauge" in this context refers to the gauge freedom in choosing the phase of the transported state, i.e., under the global transformation $\psi_n(\mathbf{k}) \rightarrow e^{i\zeta(\mathbf{k})}\psi_n(\mathbf{k})$. However, this implies that the Berry connection $\mathbf{A}_n(\mathbf{k})$ is not uniquely defined, i.e., not gauge-invariant. In contrast, the curl of the Berry connection is gauge-invariant, and it is therefore useful to define the so-called Berry curvature

$$\Omega_n(\mathbf{k}) = \nabla_{\mathbf{k}} \times \mathbf{A}_n(\mathbf{k})\,. \tag{1.36}$$

Using Stokes' theorem [103], we can then rewrite Equation (1.34) into an integral over the area S enclosed by the path in parameter space, i.e.,

$$\phi_n = \oiint_S \Omega_n(\mathbf{k})\, \mathrm{d}^2\mathbf{k}\,. \tag{1.37}$$

It is at this point that we can establish the intimate link between band theory and topology [102, 104]. Topology is a branch of mathematics that deals with the properties of objects that are preserved under continuous transformations. At its core, topology is interested in understanding "invariant properties" — those characteristics that do not change even when an object is continuously deformed. Colloquially, topology is often introduced with the example of a coffee mug and a donut which are considered the same, or "topologically equivalent". This is because these objects can be continuously deformed into each other by stretching and bending, and crucially, without tearing the material or creating new holes. While illustrative, this example may also lead to misconceptions, particularly when attempting to force the analogy of real-space objects with holes onto the abstract parameter space that band theory is concerned with. The key notion they have in common, though, is that of the topological invariant.

Topological invariants, mathematical constructs preserved under continuous deformations, play an integral role in band theory. They help classify topological phases of matter and predict their unique properties. A crucial topological invariant in band theory is the Chern number ($\mathcal{C}_n$) [105], which is an integral of the Berry curvature over the full BZ

$$\mathcal{C}_n = \frac{1}{2\pi} \oint_{\mathrm{BZ}} \Omega_n(\mathbf{k})\, \mathrm{d}\mathbf{k}\,. \tag{1.38}$$

We may comprehend the integer nature of $\mathcal{C}_n$ by realizing that, due to the periodicity of the Bloch states, the Berry phase defined by the line integral in Equation (1.34) must be an integer multiple of 2π when integrated over the full BZ. By Stokes' theorem, this implies that Equation (1.37) over the full BZ is also an integer multiple of 2π, which yields Equation (1.38). In this context, $\mathcal{C}_n$ can be thought of as an integer "winding number", i.e., the number of times the Berry phase crosses 2π and "winds" around the BZ.

An alternative, physically more intuitive explanation can be found when realizing the similarity of the abovementioned quantities to electromagnetic phenomena. In particular, the Berry curvature and the Berry connection are related in a way that is analogous to the connection between the magnetic field $\mathbf{B}$ and the magnetic vector potential $\mathbf{A}$, i.e., $\mathbf{B} = \nabla \times \mathbf{A}$. In this picture, while the Berry connection and Berry curvature can be interpreted as momentum-space analogs of the magnetic vector potential and the magnetic field, respectively, the Berry phase takes on the form of a magnetic flux, and the Chern number denotes the integer number of "magnetic monopoles" within the integration area [100, 102].

The terminology is reminiscent of the Aharonov-Bohm effect, in which a magnetic flux enclosed in a solenoid that is shielded from the outside region can affect the interference pattern of electrons propagating around it (see Figure 1.5b) [101, 106]. The Aharonov-Bohm effect is in essence a manifestation of the geometric

phase acquired by the electron, and it only depends (in 2D) on whether the electron trajectory takes a path to the left or to the right of the solenoid before interference, and crucially not on the exact details of the path. In this sense, it represents a robust, global property of the system that only changes when the trajectory crosses to the other side of the solenoid, but is otherwise insensitive to variations of the path. The topological robustness of certain global properties is indeed a key concept in band topology, as it leads to the concept of the TI and the various QHEs this is associated with.

1.5.2. TOPOLOGICAL INSULATORS AND THE QUANTUM HALL EFFECTS

In recent years, the field of condensed matter physics has been revolutionized by the discovery of TIs, materials which are insulating in the bulk (i.e., with a bandgap) but harbor conductive states on their surfaces or edges. The understanding and manipulation of TIs is not only of fundamental scientific interest, but also hold immense potential for applications due to the promise for topologically protected transport of energy and information via the conducting edge currents, which are largely protected from scattering by a broad range of perturbations. Similar to the robustness of the phase differences to changes in the trajectory in the Aharonov-Bohm effect, the robustness of edge states is a characteristic that is not determined by the local atomic details, but rather derives from the bulk topological properties of the system they are associated with. To elucidate this relation, let us first define the concept of a topological bandgap.

As signified by the band index n in Equation (1.38), the topological invariant $\mathcal{C}_n$ is an integer number that is associated with a single band of a material — more accurately, it is only well-defined for the filled bands of a system that lie below the Fermi energy. This also implies that the notion of a topological invariant is only well-defined for systems that possess a bandgap, i.e., where valence and conduction bands (occupied and unoccupied states) do not cross or touch. The bandgap of the system is then typically also assigned a topological index according to [18]

$$\mathcal{C}^{\text{gap}} = \sum_n \mathcal{C}_n \,, \tag{1.39}$$

which is simply the sum of all Chern numbers of the filled bands below the gap. The bandgap is said to be topological if $\mathcal{C}^{\text{gap}} \neq 0$, and it is in this case that topological edge states emerge at the system's boundaries which cross the bulk bandgap and characterize it as a TI.

The concept of edge states is linked to the bulk-boundary correspondence, a fundamental principle in the study of topological phases of matter [18]. The bulk-boundary correspondence states that the topological properties of a bulk system are manifested at its boundaries. More concretely, for a system with a non-trivial topological invariant (e.g., a non-zero Chern number), there will exist protected states at the edges of the system. They are "protected" in the sense that they are robust against perturbations that do not close the energy gap and change the topology. As long as the defining symmetry of the topological phase is retained, these states are robust and immune to disorder and backscattering, which is one of the key features of topological states of matter.

The origin of these interface or edge states is fundamentally tied to the discontinuity in the topological invariants at the edge. In other words, these interface states may be regarded as a way to transition between regions of different topological nature, e.g., the transition from a (topological) Chern insulator to the surrounding (trivial) vacuum. The number of edge states is directly related to the difference in Chern numbers at such a topological interface. Intuitively, this can be understood by considering that the integral of the Berry curvature over the bulk BZ (which gives the Chern number) can be transformed into a line integral along the boundary of the BZ, whereby this line integral effectively counts the number of edge states. The rigorous proof of the bulk-boundary correspondence is rather involved and requires solving the effective Hamiltonian at the edges of the system and considering the wavefunctions' behavior in this region, which changes the effective dispersion relation [107]. It shows that the Hamiltonian becomes gapless at the boundary, i.e., the breaking of translational symmetry at the edges allows the system to undergo a local topological phase transition, which manifests in the emergence of edge states.

When calculated for an arbitrary polarized band over the whole BZ, the Chern number has a non-zero value only in the presence of time-reversal symmetry breaking [29], most commonly achieved by applying an external magnetic field. In this case, the system is often called a Chern insulator. Indeed, Chern insulators where the first type of TIs to be described in the context of the QHE (Figure 1.6a). The QHE, discovered by Klaus von Klitzing in 1980 [81], can be observed when a 2D electron gas is subjected to very low temperatures and strong magnetic fields (see our previous discussion in Section 1.3). When the magnetic field strength is varied, the electrical resistance shows a series of plateaus and the Hall conductance quantizes into exact integer multiples of the fundamental constant $\frac{e^2}{h}$.

The significance of topology in the QHE became evident when David Thouless and collaborators introduced the Chern number to explain the appearance of the Hall conductance in 1982 [108]. Each Landau level can be thought of as a "band" in the system which can be associated with a Chern number, resulting in the appearance of topological edge states at the boundaries, with their number determined by the number of Landau levels below the Fermi level (controlled by the external magnetic field). When the Fermi energy crosses a Landau level, the system transitions from one quantum Hall state to another. Each of these transitions corresponds to a change in the Chern number by 1, leading to the appearance of an additional edge state. These edge states are responsible for the quantized Hall conductance that characterizes the QHE. Reversal of the magnetic field direction reverses the sign of the Chern number, and correspondingly the helicity of the chiral edge states traveling along the edges. It can be shown that the non-trivial topological nature of the bulk is a direct consequence of the time-reversal symmetry breaking by the magnetic field, which also underpins the chirality of the induced edge states [18].

While using a magnetic field is a common way to break time-reversal symmetry, this is also possible by explicitly modulating the parameters of a system periodically in time, known as a Floquet-type TI [25, 29]. Moreover, there are ways to induce topological effects even when time-reversal symmetry is retained, i.e., in reciprocal

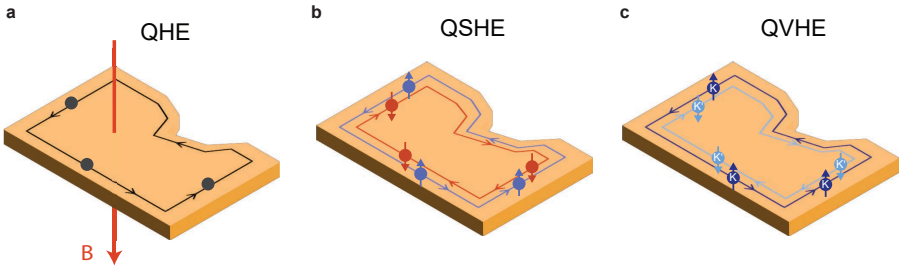

Figure 1.6: Schemes of the quantum Hall effects. Schematic depiction of electron transport in various quantum Hall effects. **a,** In the quantum Hall effect (QHE), an external magnetic field perpendicular to the plane induces chiral edge currents, robust against disorder. **b,** In the quantum spin Hall effect (QSHE), spin-orbit coupling leads to helical edge states where electrons with spin up (blue) and spin down (red) travel in opposite directions. **c,** The quantum valley Hall effect (QVHE), typically achieved by inversion symmetry breaking of the underlying honeycomb lattice which leads to edge currents that are valley-polarized, i.e., electrons that originate from the K' and K valley in the band structures travel in opposite directions.

systems. This is the case for so-called spin TIs and valley TIs that derive from the QSHE and the QVHE, respectively. Despite the reciprocity of such systems which renders them no true isolators, they can still display robust transport in the presence of certain types of perturbations.

In 2005, Kane and Mele proposed the concept of the QSHE, suggesting that it is possible for a 2D system to exhibit the Hall conductance quantization without an external magnetic field, but with spin-orbit coupling instead [84]. These are now known as 2D TIs or quantum spin Hall insulators. The QSHE is a quantum counterpart of the classical spin Hall effect. Spin-orbit coupling is a relativistic effect that couples an electron's spin to its orbital motion. In the context of band theory, this coupling leads to the splitting of energy bands, which results in the non-trivial band topology. If an electric field is applied to a thin strip of a quantum spin Hall TI, spin-polarized currents flow along the edges of the strip that are immune to backscattering and localized impurities, with spins pointing in opposite directions for opposite edges (see Figure 1.6b).

In the QHE, the Chern invariant can in principle assume arbitrary integer values. In contrast, being time-reversal symmetric, the QSHE necessitates a different, so-called $\mathbb{Z}_2$ (or "spin Chern") topological invariant ν. This is essentially a "mod 2" version of the Chern number — it only distinguishes between "even" and "odd" winding numbers of the Berry phase around the BZ. The physical manifestation of this is the difference between normal insulators ($\nu = 0$) and TIs ($\nu = 1$). The key requirements for a system to exhibit the QSHE are two-dimensionality, time-reversal symmetry, and strong spin-orbit coupling. Quantum wells in certain materials like mercury telluride (HgTe) have been shown to exhibit the QSHE, and it was also achieved in suitably modified graphene sheets (e.g., via hydrogen-termination) [109, 110].

The concept of spin-orbit coupling evoking non-trivial topology in the band structure is not exclusively limited to actual electronic spin, but in fact generally

applicable for pseudospins present in a system, i.e., binary degrees of freedom. In this vein, the QVHE constitutes another intriguing pathway to reciprocal TIs. Unlike the QHE or the QSHE, which involve the transport of charge or spin, the QVHE involves the transport of the "valley" degree of freedom (or valley index) [18]. In materials such as graphene, the energy band structure has two inequivalent local maxima or minima, known as K and K' valleys (Section 1.3).

To observe the QVHE, two conditions need to be met: valley polarization and non-zero Berry curvature. Valley polarization refers to a preferential occupation of one valley over the other and can be achieved in graphene by, e.g., applying an in-plane electric field or an out-of-plane magnetic field which couples to the intrinsic magnetic moment associated with the valley index (similar to creating spin polarization via the magnetic moment associated with electronic spin) [85]. Non-zero Berry curvature arises for graphene-like lattices with broken inversion symmetry, which leads to a non-zero mass term in the Dirac equation describing the low-energy excitations (see Equation (1.15)). This mass term opens a bandgap at the Dirac points, giving rise to distinct valence and conduction bands. Crucially, the bandgap and thus the mass term have opposite signs at the K and K' points, which results in opposite Berry curvatures and hence opposite contributions to the valley Chern number from the two valleys. The valley Chern number can be calculated similarly to the Chern number in Equation (1.38), but with the integration area limited to half of the BZ, such that each valley is associated with its own topological invariant. They are exactly opposite for K and K', such that while locally there is a non-zero Berry curvature, globally the contributions of both valleys cancel out, rendering the system reciprocal and topologically trivial. Nevertheless, valley-polarized currents that feature hallmarks of topological protection can be observed along the edges of the system (Figure 1.6c), where the protection from backscattering can be linked to the large momentum mismatch and opposite Berry curvatures at the two valleys.

The inversion symmetry breaking has been theoretically proposed via introduction of a staggered sublattice potential that breaks the symmetry between the two sublattices [85]. In practice, it can be induced by various methods such as applying an external electric field, introducing structural asymmetry (for example, in bilayer graphene), or by selectively doping the system [72, 85, 111, 112]. Another method for inducing valley polarization is by circularly polarized light, which can selectively excite electrons in one valley over the other. Lastly, strain engineering has been proposed as a method to create valley-polarized currents, as it can generate pseudo-magnetic fields that are felt differently by electrons in the different valleys [86].

In summary, the various QHEs represent fascinating facets of the rich tapestry of topological phases of matter, highlighting the diversity of transport phenomena that can arise from the interplay of quantum mechanics and topology in TIs.

1.5.3. PHOTONIC TOPOLOGICAL INSULATORS

After introducing key concepts from solid state band theory and their link to topology, the appeal of emulating these phenomena in the domain of photonics appears

evident. The past years have seen tremendous efforts into designing and demonstrating the photonic equivalents of the TIs we discussed, and lead to the advent of a new class of artificial materials for light — photonic topological insulators (PTIs) [29, 32, 113]. Photonic topological insulators represent a thrilling development at the intersection of optics and topological physics, merging the distinctive properties of both domains to unveil groundbreaking applications. Much like their solid-state counterparts, PTIs are media through which waves travel unhindered at the edge, while their interior acts as an insulator.

Photonic topological states arising from breaking time-reversal symmetry were the first to be conceived [114], with a concrete proposal relying on magneto-optical effects [115] which was shortly after realized experimentally for microwave metamaterials [23]. To bring PTIs into the optical domain, a variety of other approaches were later adopted. Floquet-type PTIs that rely on time periodic modulations have been at the forefront to achieve backscattering-immune light transport in arrays of evanescently coupled optical waveguides [25, 116]. Other notable platforms include arrays of coupled resonators in silicon-based photonic integrated circuits [26, 27], polariton systems that leverage microcavities to shape topologically protected polariton states [28, 117, 118], and bianisotropic metamaterials [24]. Among these diverse implementations, PhCs have emerged as an evermore prominent platform for the realization of PTIs [119, 120].

Topological PhCs with honeycomb lattices, akin to the structure seen in graphene, hold a special place in this exploration [121]. Such structures can exhibit properties similar to the ones observed for the various QHEs in condensed matter, offering a pseudospin degree of freedom for photons that mirrors the spin degree of freedom for electrons. This analogous behavior permits the creation of photonic edge states, leading a path toward unidirectional light propagation that is resilient to backscattering. Herein, we will discuss the main ideas that underpin the systems studied in this thesis and how they relate to the concepts we discussed earlier. While honeycomb-like lattices of Floquet-type PTIs, such as helical bent waveguides where one spatial dimension is mapped to time [25], represent an intriguing domain of PTIs in themselves, herein we will focus on the implementation within honeycomb PhC membranes which is most relevant for the work presented in the following chapters.

As outlined in Section 1.4, the Bloch band formalism can be readily applied to the modes of PhC membranes with the adequate substitutions, and we can similarly introduce the concepts of band topology and topological invariants in terms of the PhCs' eigenstates $|E_z\rangle$ (TM-like) or $|H_z\rangle$ (TE-like) that are governed by Equation (1.30). As a phenomenon that typically requires external magnetic fields, the analog of the QHE cannot be directly induced in arbitrary PhC slabs since photons, as uncharged particles, do not interact with magnetic fields in the same way electrons do. However, such an interaction for photons can be mediated via magneto-optic interactions in gyromagnetic materials. These materials exhibit the Faraday effect [122], which means that their optical properties, specifically the refractive index, changes in response to a magnetic field. By applying a magnetic field to a 2D PhC composed of a gyromagnetic material or placed on

top of a gyromagnetic substrate, time-reversal symmetry can be broken to induce the photonic analog of the QHE [31]. This was experimentally realized [23] in the microwave regime using a lattice of vanadium-doped calcium-iron-garnet rods, and there has also been a successful implementation in the optical regime using a PhC bonded with InGaAsP quantum wells placed on top of a substrate made of the magneto-optical material yttrium iron garnet [123].

The QHE in graphene and in a 2D PhC made from magneto-optic materials draws intriguing parallels but also presents key differences, primarily due to the disparate nature of electrons and photons. In photonic systems, the QHE does not lead to quantized Hall conductance. Instead, the most notable manifestation is the formation of chiral one-way edge states, which are immune to backscattering from defects and where the direction of light propagation is determined by the sign of the external magnetic field [25, 29, 124]. Apart from the specific material requirements, the inherently weak magneto-optical interactions (especially at optical frequencies) pose severe challenges in the achievable bandwidths of such PTIs and their integration into standard lithography processes for on-chip applications. Therefore, there is a strong motivation to realize the magnetic-field-free reciprocal versions of the QHE in PhC membranes, i.e., the QSHE and the QVHE. To gain better understanding for the principles underlying the emulation of the QSHE in our systems, we will first elucidate a central model that is widely used in the realm of topological phases of matter: the Su-Schriefer-Heeger (SSH) model.

The SSH model describes a 1D, periodic chain that advanced our understanding of electronic properties in polymeric systems and offered a profound insight into the broader realm of TIs. The model was first introduced by W. P. Su, J. R. Schrieffer, and A. J. Heeger in 1979 to explain the peculiar electronic properties of polyacetylene, a polymer with alternating single and double carbon bonds [126]. At its core, the SSH model is a tight-binding model that describes electrons in a 1D chain of atoms with alternating bond strengths. Here, the atoms are equally spaced, but the electron hopping amplitudes (t, t') between them vary, leading to two different types of bonds: strong and weak. Each unit cell in this model comprises a pair of atoms, connected by the intra-cell coupling t, and unit cells are connected via their inter-cell couplings t' (see Figure 1.7). Depending on the ratio of intra- to inter-cell coupling, the chain can be in two distinct topological phases, and the band structure features a gap [127].

The transition from the trivial ($t > t'$, Figure 1.7a) to the topological ($t < t'$, Figure 1.7c) phase is characterized by a closing of the bandgap for equal coupling strengths ($t = t'$, Figure 1.7b). Upon reopening of the bandgap, a band inversion occurs, signified by the switching of roles for the modes at the band edges: while in the trivial case, the mode at the upper band edge features a spatially symmetric profile and the mode at the lower band edge an antisymmetric one, the situation is inverted for the topological case. Such a band inversion is often a telltale sign for a topological phase transition. The topological difference between the two phases manifests itself in the edge states of the chain. In contrast to the topologically trivial phase, the topologically nontrivial phase hosts zero-energy edge states that are localized at the ends of the chain. The presence of zero energy edge states is

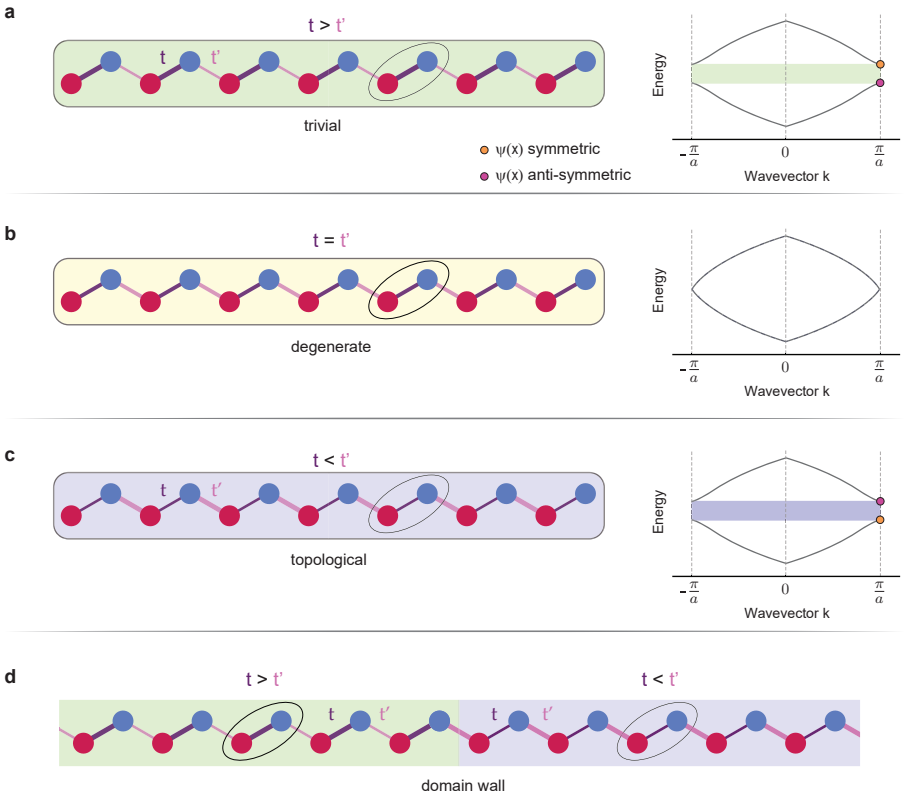

Figure 1.7: Su-Schriefer-Heeger model. Schematic depictions of the Su-Schriefer-Heeger (SSH) model in different phases, determined by the ratio of (t) intra- to (t') inter-cell coupling. The coupling constants are depicted as purple (t) and pink (t') lines that connect the (red and blue) lattice sites within each unit cell (indicated), and the thickness of the lines represents the relative coupling strengths. **a,** Finite SSH chain with stronger intra- than inter-cell couplings ($t > t'$), when the system is in the trivial phase. The band structure features a bandgap at the Brillouin zone boundary, whereby the mode above (below) the gap has a symmetric (antisymmetric) real-space profile. **b,** For equal coupling strengths ($t = t'$), the bandgap vanishes and the system has a degeneracy at the Brillouin zone boundary. **c,** When the inter-cell coupling becomes stronger than the intra-cell coupling ($t < t'$), the bandgap reopens, and the system is in the topological phase that features zero-energy edge states. The transition from the trivial to the topological phase is characterized by a band-inversion, signified by the inversion of symmetric and antisymmetric modes at the band edges. **d,** Infinite SSH chain with a central domain wall, i.e., a transition between the topological and trivial phase. The displayed band diagrams are based on Ref. [125].

robust against small perturbations, i.e., variations of the hopping amplitudes (so long as the ratio of intra- to inter-cell coupling is not inverted) — a hallmark of topological properties. Topological domain walls may be constructed by forming an interface between a topological and a trivial phase of the SSH chain (Figure 1.7d). Since its inception, the SSH model has inspired the discovery of various topological phases of matter in multiple dimensions, and indeed the QSHE-type topological PhC membranes we study in this thesis may be regarded as a generalization of the SSH model to two dimensions.

The PhC design we refer to was initially proposed by Long-Hua Wu and Xiao Hu and takes a honeycomb arrangement of lattice sites as its geometric starting point, i.e., a PhC with Dirac-like crossings in its band structure (Figure 1.8a) [119]. The unit cell is chosen to be hexagonal (rather than the primitive rhombic unit cell), leading to band folding of the inequivalent Dirac cones at the K and K' valleys onto the Γ point in the center of the BZ which results in a four-fold degeneracy. While this band folding thus far simply corresponds to a basis change, i.e., the Bloch modes folded onto the Γ point carry zero weight, this situation changes as soon as we introduce a symmetry breaking mechanism that turns the hexagonal unit cell into the primitive one. This sublattice symmetry breaking consists of either concentrically shrinking or expanding the radius of the lattice sites within a unit cell with respect to its center, changing the ratio of intra- to inter-cell coupling in analogy to the 1D SSH model (Figure 1.8b). In the same vein, this leads to the lifting of the Dirac point degeneracies and the opening of a bandgap which is, crucially, topologically different for the shrunken and expanded case. A band inversion takes place between shrunken and expanded lattices, i.e., the doubly degenerate quadrupolar and dipolar bulk bands below and above the gap switch their roles upon transitioning from one unit cell geometry to the other. The modes at the Γ point thereby acquire finite weight and radiate to the far field if the system is a slab bounded by air, as they are situated within the light cone [128–130]. Akin to a QSHE-type TI, an interface between shrunken and expanded domains supports helical topological edge states [131]. This is mediated by spin-orbit coupling in the PhC platform that results in counterpropagating right-hand circular polarization (RCP) and left-hand circular polarization (LCP) spin states [132]. The role of electronic spin is taken over by the pseudospin that arises from the coupling of the degenerate multipolar bulk bands at the band edges. The pseudospins correspond to the handedness of circularly polarized modes inside a hexagonal unit cell, arising from the coupling of these bands. Each polarization, RCP and LCP, is then associated with its respective $\mathbb{Z}_2$ invariant (see Section 1.5.2), implying that the notion of spin is now encoded in the vectorial nature of the electromagnetic fields.

The origin of the pseudospins in the coupled bulk bands necessitates a domain wall between expanded and shrunken geometries to observe edge states. This is in contrast to electronic TIs where edge states can exist at the physical boundary of the system — a consequence of their origin in the fermionic electron spin that guarantees the existence of these states whenever there is a boundary between a topological and a trivial insulator (or vacuum). Due to the bosonic nature of photons, there is also no Pauli exclusion principle as in the fermionic case that

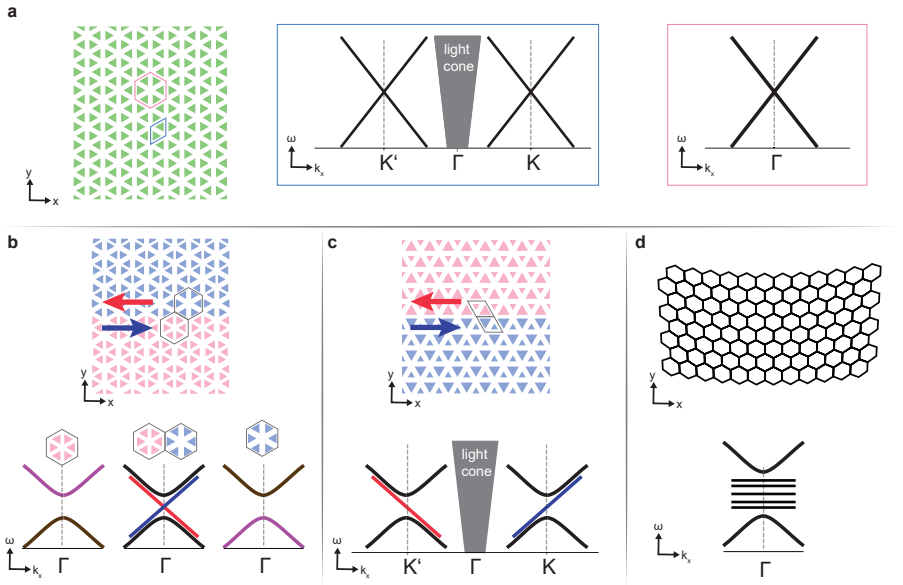

Figure 1.8: Topology and symmetry breaking in honeycomb photonic crystals. a, Schematic of a pristine honeycomb lattice made of triangular lattice sites. Depending on the choice of unit cell, the Dirac cones either reside at the K and K' high symmetry points (rhombic unit cell) or are folded to form a fourfold degeneracy at the Γ point. **b,** Shrinking and expanding the lattice sites within a hexagonal unit cell opens up a band gap, whereby a band inversion occurs upon transformation from shrunken to expanded geometry. The interface between expanded and shrunken domains hosts spin-polarized edge states akin to those in the quantum spin Hall effect. **c,** When breaking the inversion symmetry within a rhombic unit cell, bandgaps open at the K and K' points, with opposite local Berry curvature. This leads to the emergence of valley-polarized edge states, in analogy to the quantum valley Hall effect. **d,** By applying non-uniform strain to the honeycomb lattice, a pseudomagnetic field is generated that lifts the Dirac point degeneracy and induces photonic Landau levels.

would guarantee the existence of pseudospins via Kramer's degeneracy [133], and time-reversal symmetry does not act to protect the pseudospin states from scattering into each other. It is rather the presence of the spatial lattice symmetries that takes over the role of time-reversal symmetry in these PTIs and which grants a certain degree of topological protection so long as these symmetries are not perturbed too strongly. The exact notion and extent of topological protection in this case is an active topic of research. Rigorous calculation of topological invariants has claimed that topological invariants are zero, but that they are finite in a simplified, approximated description of the systems [29]. Interestingly, various effects such as the existence of edge states is nonetheless seen. This increases motivation to study the applications and limitations of these types of material and, in fact, this thesis contributes to the discussion by quantifying the robustness (i.e., amount of backscattering) in the presence of engineered defects in a PTI that mimics the QVHE (see Chapter 3) [134].

This QVHE-type PTI relies on a different type of symmetry breaking, but as before, takes the geometrical starting point of a pristine honeycomb lattice (Fig-

ure 1.8c). A major advantage of PhC TIs over electronic TIs is the immense freedom in tailoring the geometrical properties of the unit cell. It is thus that inversion symmetry breaking can be (contrary to graphene) easily implemented at the fabrication stage by designing the lattice sites within a rhombic unit cell to differ from each other (in size, shape, etc.). This opens up a bandgap in place of the former Dirac point degeneracies, with opposite Berry curvature at the inequivalent valleys (see Section 1.5.2). A boundary formed between mirror-imaged copies of the lattices then effectively creates a domain wall between materials that locally possess an opposite sign of the Berry curvature at the K and K' valleys, resulting in valley-polarized topological photonic edge states guided along the interface [135–139].

We further examined a different flavor of QVHE-type PTI which relies on the engineering of artificial strain, i.e., tailored lattice deformations (Figure 1.8d). It has been shown that strain-engineering in graphene can induce pseudomagnetic fields that make it possible to observe the QVHE [140, 141], sparking great interest into imitating similar mechanism in PhCs due to the unique flexibility in the design and the potential to implement complex strain patterns for the engineering of artificial gauge fields [142–145]. This leads to phenomena formerly only associated with charged particles in magnetic fields, like the formation of Landau levels, and provides a new design paradigm for PTIs to mediate effective magnetic interactions in purely dielectric systems.

In conclusion, the fascinating realm of TIs and QHEs, with their intricate interplay of geometry, topology, and quantum mechanics, provides a vibrant playground for exploring novel states of matter. The intricate coupling of these effects in electronic systems has revolutionized our understanding of condensed matter physics, elucidating new pathways for topological electronics. Their emulation in photonic systems offers a compelling parallel narrative, exhibiting an inspiring convergence of ideas that spans across disciplines. From the fundamental perspective, these phenomena grant a profound understanding of the deep connections between topology and physics. From the practical viewpoint, they hold the promise of robust, energy-efficient, and backscattering-immune devices that could play pivotal roles in future technological advancements. As we turn the page, the chapters ahead will delve into experimental studies that elucidate intriguing phenomena and inherent limitations associated with practical implementations of this field.

1.6. OUTLINE OF THIS THESIS

In this thesis, we explore the possibilities of controlling the flow, confinement, and emission of light in 2D topological PhCs. We identify the hallmarks of the underlying non-trivial band topology in the optical properties of waveguides and resonators operating in the telecom frequency regime, and demonstrate the engineering of mode dispersion, localization, and radiative coupling by virtue of tailored lattice geometries. We put the topological protection that is mediated by the presence of specific lattice symmetries in the PhC platform to the test and study its limitations as well as the potential it offers for the design of nanophotonic devices.

Chapter 2 reports on the techniques employed to fabricate the suspended silicon PhC membranes studied throughout this work, and the experimental char-

acterization of the fabricated devices. The latter covers both the examination of radiative samples via far-field Fourier spectropolarimetry and the polarization and phase-resolved near-field scanning optical microscopy of non-radiative samples. In addition to discussing the components constituting the setup and relevant calibration procedures in detail, we explain the relevant theoretical foundations underlying the measurement techniques that derive from the distinct characteristics of light propagation in the far-field and near-field zones.

In Chapter 3, we present an examination of topological protection in PhCs that emulate the QVHE for light. Supported by phase-sensitive near-field scanning optical microscopy, we resolve forward- and backward-propagating waveguide modes and perform a detailed quantification of the amount of backscattering experienced at engineered defects. The reflection coefficients we estimate with a transfer matrix model are an order of magnitude lower compared to conventional PhC waveguides, evidencing enhanced robustness for transmission.

Chapter 4 examines the signatures of topological light confinement in the far-field emission of cavities in a PhC platform that features the photonic QSHE and supports helical edge states that are weakly coupled to the radiation continuum. The modes of resonators scaling down to single point defects in the surrounding bulk lattice are characterized in terms of spectral position and multipolar nature of the eigenstates. The mapped mode profiles in real- and momentum-space reveal band inversion-induced confinement and inverted scaling behavior of the mode spectra for trivial and topological defect cavities, reflecting on their origin in the topological band structure. Furthermore, hallmarks of topological protection in the loss rates are demonstrated, which are largely insensitive to cavity shape and size. Lastly, we explore the potential of the cavities as components in photonic integrated devices when coupled to topological waveguides, demonstrating a coupling mechanism that is dictated by spin-conservation. Strikingly, while the cavities support both standing-wave and travelling-wave modes, only the latter display the unique spin-conserved coupling behavior, evidencing their origin in the helical topological edge states supported at the PhC's domain boundaries.

In Chapter 5, we explore the possibilities to control light propagation and localization on chip with synthetic gauge fields. As light does not naturally interact with real magnetic fields, we experimentally realize pseudomagnetic fields in 2D PhCs through engineered strain of the lattice. Analogous to strained graphene, this induces flat-band Landau levels at discrete energies, with associated high degeneracy and local density of states. We study the spatial and spectral properties of these modes using far-field spectroscopy and, taking advantage of the PhC's design freedom, realize domains of opposite pseudomagnetic field that host topological edge states at their interface. We reveal that the modes can achieve remarkably high quality factors, despite being inherently coupled to the radiation continuum.

Finally, in Chapter 6, the findings and conclusions of this work are summarized, and prospects and opportunities for the future research and applicability of 2D topological PhCs for applications in integrated photonics are discussed.

2

FABRICATION AND CHARACTERIZATION OF TOPOLOGICAL PHOTONIC CRYSTAL MEMBRANES

This chapter gives an overview over the central methods surrounding the fabrication and experimental characterization of topological silicon photonic crystal membranes that operate in the telecom frequency regime. We describe the lithography procedure in a silicon-on-insulator platform that is used to implement both radiative and non-radiative photonic crystal designs, each calling for a different in-coupling scheme to access the eigenmodes experimentally. We examine the radiative photonic crystals from the far field with a Fourier-spectroscopy setup that allows for position- and polarization-resolved excitation and probing of the mode profiles in real and momentum space. The non-radiative samples are studied via phase- and polarization-resolved near-field scanning optical microscopy, giving us direct access to the vectorial field on subwavelength scales.

2.1. PHOTONIC CRYSTAL FABRICATION

In this section, we will outline the main design principles underlying the photonic crystal (PhC) lattices we study throughout this work, and describe their fabrication in detail. The designs may be broadly subdivided into two categories: layouts for PhCs with (1) radiative and (2) non-radiative modes, where the design is tailored for excitation and probing using experimental (1) far-field and (2) near-field techniques, respectively. The samples are fabricated via standard lithography on a silicon-on-insulator (SOI) platform [129, 146], whereby the non-radiative samples require additional fabrication steps due to their specific requirements on in-coupling and probing in the near field (see Figure 2.1). The fabrication process is based on the procedure described in [129]. Individual steps were further developed (electron beam lithography, wet etch), process parameters tuned over time as needed, and new steps were added (ultraviolet lithography).

2.1.1. SAMPLE DESIGN

The PhC lattice dimensions are determined prior to fabrication using frequency-domain finite-element-method simulations with the commercial numerical solver COMSOL Multiphysics. The exact geometrical parameters for each system we study are given in the respective chapters. All our samples are designed to support modes in the technologically relevant telecom frequency regime, i.e., based on PhCs with bandgaps around 1550 nm. As we aim to implement platforms that emulate Dirac physics for photons, akin to their solid-state counterpart graphene, the starting point of the PhC geometries is a honeycomb lattice of scattering sites (see Figure 2.2a). This offers a playground to study photonic analogues of the various quantum Hall effects initially evoked in the description of electronic systems (Section 1.5). The lattice sites for the topological PhCs in this work are constituted from holes perforating a silicon membrane of thickness 220 nm. Their shape is chosen to be triangular to ensure a complete bandgap for transverse-electric-like (TE-like) mode upon perturbing the pristine lattice symmetries [147] (see insets Figure 2.2b,c). The PhC designs are defined in the Graphic Design System version II format (GDSII), generated via the open-source Python module GDSPY [148]. In electron beam lithography (EBL), GDSII files are often used to define the desired geometries to be patterned (see Section 2.1.4 for more details).

Photonic crystals with modes that radiate to the far field, by reciprocity, may also be excited with (focused) radiation from the far field (see Section 2.2). Therefore, apart from labels and alignment markers to facilitate targeting in the experimental far-field setup (see Section 2.2), the sample design solely consists of the PhC lattice itself (see Figure 2.2b). These structures are fabricated with the steps described in the following sections, excluding the ultraviolet (UV) lithography procedure which only applies to non-radiative samples that we study in the near field (cf Section 2.3). The non-radiative samples additionally contain silicon ridge waveguides at opposite terminations of the PhC lattice (see Figure 2.2c), used for in-coupling from the side of the chip via light that is focused onto the end facet of these access waveguides. An intermediate PhC waveguide with an adiabatic transition region acts as a mode converter to help decrease scattering losses for light entering the topological

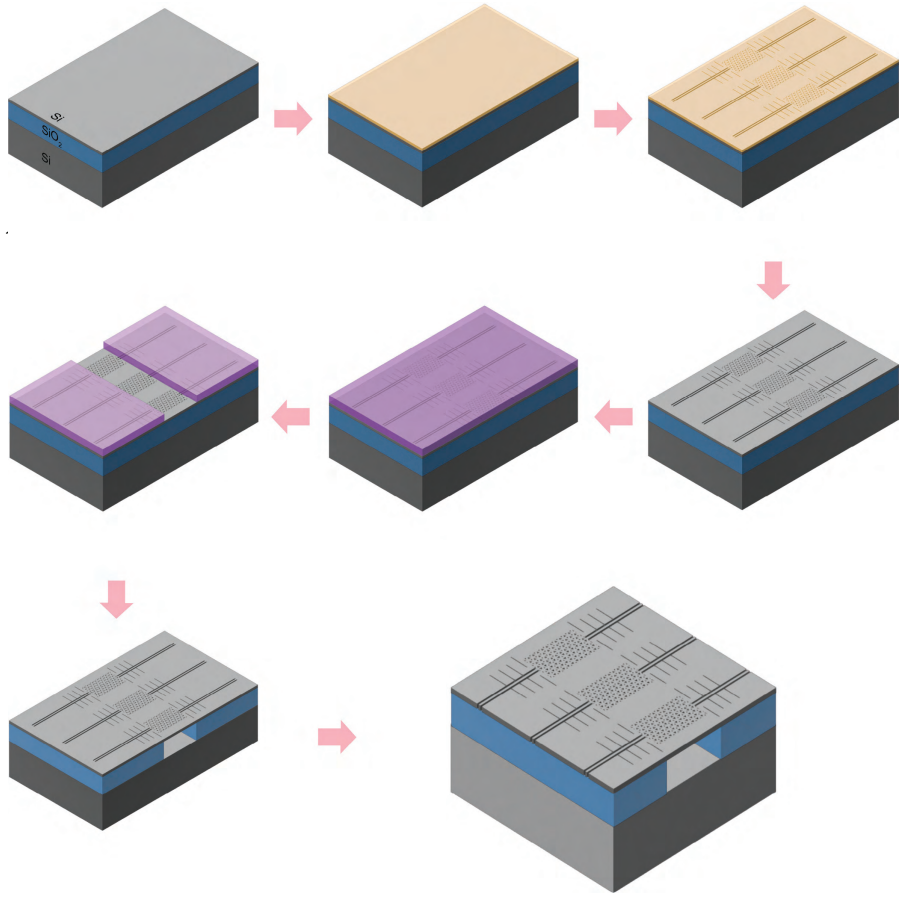

Figure 2.1: Photonic crystal fabrication. Schematic depiction of the lithography procedure used to fabricate suspended two-dimensional photonic crystal membranes with access waveguides for in-coupling from the side of the chip in a silicon-on-insulator platform. For samples without access waveguides, steps 5, 6, and 8 are omitted. See the main text for more details.

PhC [149]. While earlier designs featured tethers to stabilize these macroscopic (millimeters long) waveguides and protect them from collapsing upon under-etching (see Section 2.1.7), the samples in this thesis use the aforementioned UV lithography step to perform selective under-etching. The in-coupled light travels toward the entrance point of the PhC, whereby the access waveguide is tapered toward the lattice, ensuring that the final (partly under-etched) section is only single mode. Furthermore, the PhCs typically feature an adiabatic transition region to reduce scattering losses at the PhC entrance and end facets. Trenches to the sides of the access waveguides in the vicinity of the PhC ensure that guided modes of the silicon bulk layer into which we might couple unintentionally are scattered away and do not interfere with the PhC modes of interest.

After generating the GDSII files that describe the PhC geometry, we perform

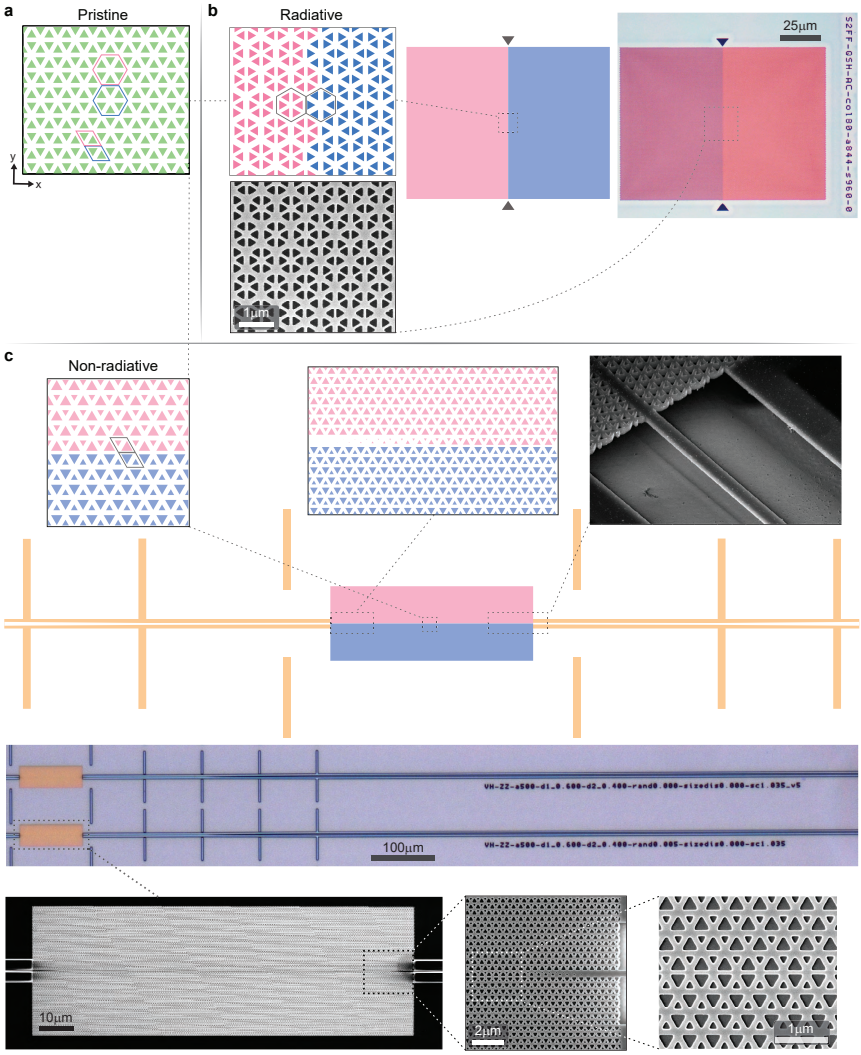

Figure 2.2: Sample designs. a, Starting point of the photonic crystal (PhC) designs studied in this work is a pristine honeycomb lattice of triangular holes in a silicon membrane. The lattice symmetries are perturbed in distinct ways to induce topologically non-trivial bandgaps, with PhC modes that are either radiative or non-radiative. **b,** By perturbing the lattice symmetries in a hexagonal unit cell we create an interface between different domains that hosts radiative topological states. An optical microscope image of a fabricated lattice (right) and a zoomed-in scanning electron microscope (SEM) image (bottom) are shown. **c,** A different type of symmetry breaking within a primitive rhomboid unit cell results in non-radiative topological PhCs. The states are excited via silicon ridge access waveguides (inset, top right: scanning electron microscope (SEM) image) into which we couple light from the side of the chip. An intermediate PhC waveguide (inset, top center) serves as an adiabatic transition region to reduce insertion losses into the PhC. The bottom panels show an optical microscope image of fabricated lattices with access waveguides, together with zoomed-in SEM images of the PhC.

multiple post-processing steps using the software package BEAMER® [150], as we will discuss later in Section 2.1.4.

2.1.2. SUBSTRATE PREPARATION

Starting point of the fabrication procedure is the preparation of the substrate, a commercial 8" SOI wafer with a thin silicon device layer (220 ± 12.5 nm nominal thickness, <100> crystal orientation) with p-type (boron) doping in which the PhC pattern is implemented, atop a layer of buried oxide (3000 ± 70 nm nominal thickness) that is backed by a thick silicon substrate ($725 \pm 15\,\mu$m nominal thickness) for mechanical support. The wafer is cut into pieces of dimensions 20×12 mm with a dicing saw (DISCO DAC-2SP/86 Automated Dicing Saw). Before dicing, the wafers are coated with a thick resist film (MICROPOSIT®S1813®) that protects the surface from scratches and contaminants. During dicing, wafers are fixated by a dicing tape with a sticky backing. The tape glue is weakened after dicing via exposure to UV light.

As every scratch and contamination of the delicate silicon device layer can have a devastating impact on the (comparatively) large-scale PhC lattices we pattern later in the process, it is imperative to handle the chips with extreme care and ensure starting out the lithography procedure with a sample surface that is as clean as possible. Intermittent cross-checks of the surface with a dark-field optical microscope facilitate identifying potential sources of contamination and serve as a cross-check before advancing fabrication.

We remove the protective resist film using multiple cleaning steps. First, the sample is placed in an acetone bath for 5 min before gently wiping it with a microfiber cloth (stained in acetone). It is then submerged in an ultrasonic water bath (Branson 2800 Ultrasonic Cleaner) for 15 min, removing microscopic particles via the implosion of cavitation bubbles induced by high-frequency (40 kHz) pressure waves that agitate the liquid. After a short rinse with isopropanol (IPA), which minimizes the appearance of stains upon blow-drying with a nitrogen gun, it is immersed in hot anisole (60°C) for 10 min and rinsed with IPA once more.

Finally, we clean the sample surface using piranha solution, also known as piranha etch. Piranha solution is a powerful cleaning agent often employed in SEMiconductor fabrication to remove organic residues and contaminants from silicon wafers. The name comes from the solution's voracious ability to clean. The standard piranha solution is a mixture of sulfuric acid (H_2SO_4) and hydrogen peroxide (H_2O_2), usually in a 3:1 ratio. The solution is highly exothermic and will heat up rapidly. We immerse the wafer in the freshly prepared piranha solution for 15 min at 130°C, oxidizing organic residues and effectively removing them from the wafer. Afterwards, the sample is thoroughly rinsed with deionized water (DI-H_2O) and IPA to ensure that all cleaning chemicals have been washed off, before blow-drying with nitrogen.

Another common method to remove organic residues is SC-1 cleaning (also known as RCA-1) [151], a mixture of DI-H_2O, H_2O_2, and ammonium hydroxide (NH_4OH), heated to around 75°C. SC-1 is a step in the RCA wafer clean procedure, another standard cleaning procedure used in SEMiconductor device fabrication.

In the past we employed this step for cleaning at various steps during fabrication, however, the solution has the potential to etch the silicon device layer and increase surface roughness more or less strongly depending on the concentrations of its constituents [152]. This may potentially negatively impact the nanoscale features we fabricate later and reduce the nominal device layer thickness, thereby altering the operating frequency the devices are designed for. To eliminate this risk, we replaced this step by the aforementioned piranha etch.

2.1.3. SPIN COATING

After the cleaning procedure, the sample is prepared to be coated with an electron-sensitive resist for the successive EBL of the PhC design. We subject the SOI chip to a low pressure oxygen plasma (ionized with a 40 kHz radiofrequency generator) inside a quartz vacuum chamber (Sinvacon Diener Pico) for 10 min. This is a recommended procedure before spin coating, as it improves resist adhesion by removing hydrocarbons and activating the surface, i.e., making it hydrophilic. The time between this O_2 descum procedure and application of the resist should be minimized.

The sample is then placed on a hot-plate at 110°C to evaporate any residual water right before spin coating (Suss Delta 80). The spin coating procedure consists of three steps, each involving the deposition of the respective film and successive baking on a hotplate (see Section 2.1.9 for detailed parameters). First, a monolayer of the adhesion reagent hexamethyldisilazane (HMDS) is applied, before spin coating the positive electron-beam resist CSAR 62 (AR-P 6200.09, Allresist GmbH) of thickness 240 nm, which is finally covered with a conductive layer of Electra 92 (AR-PC 5090.02) to mitigate charging effects that could reduce the patterning resolution during EBL.

It has proven to be a good practice to keep a separate stock of (syringe-filtered) resist to avoid cross-contamination by other users. Thereby, it is important to store the filtered liquid in properly sealed glass vials (rather than, e.g., polypropylene tubes), to minimize diffusion and evaporation of the resist's solvent. This could otherwise strongly alter the resist's viscosity and, in the worst case, render it unusable. Still, long-term evaporation of solvents can hardly be avoided, which is why we perform spin coating tests at the beginning of each fabrication round to determine suitable parameters for achieving the desired layer thickness, which is verified by checking the depth of deliberately introduced scratches in the freshly applied resist using a mechanical contact, stylus-based step profiler (KLA Tencor Stylus Profiler P7).

2.1.4. ELECTRON BEAM LITHOGRAPHY

In this step, the PhC design (see Section 2.1.1) is patterned into the resist layer using an EBL machine (Raith VOYAGER). The primary tool in EBL is the electron beam, a focused stream of high-energy electrons (50 kV in our case). When the beam strikes the resist-coated substrate, it can eject electrons from the atoms in the resist, altering its chemical bonds and thereby locally changing the solubility upon immersion in a dedicated developer solution. Electron beam resist can be

grouped into negative and positive-tone resists [153]. While for the former, only the unexposed regions remain undissolved upon development (i.e., a negative of the exposed pattern), for positive resists (such as CSAR 62), the situation is reversed, and only the exposed regions dissolve in the developer. When the high-energy electron beam hits the positive resist, it causes its molecules to break apart in a process called radiolysis, creating smaller, more soluble fragments. The exact mechanism is complex and depends on the specific resist, but it generally involves breaking the long polymer chains into smaller fragments that are soluble in a developer solution.

The electron beam is manipulated and controlled using electromagnetic lenses, allowing for precision in writing patterns onto the resist. The beam's path is typically controlled by a computer, allowing for extremely complex designs to be written. The precision and small spot size of the electron beam is what allows EBL to achieve its high resolution. The principal advantage of EBL lies in its ability to achieve resolution on the nanometer scale, a feat unachievable by traditional photolithography due to the diffraction limit of light. However, EBL also faces several challenges. The patterning is generally slow as it involves writing designs point by point, making it unsuitable for large-scale production. It is also a complex procedure requiring sophisticated equipment and considerable energy due to the need for high-energy electrons. Moreover, the process suffers from problems such as proximity effects, where electrons scatter in the resist and expose nearby areas, causing distortions in the pattern [154].

Before loading the SOI chip into the machine, small scratches are placed at its corners with a diamond pen, resulting in locally deposited nanoscale silicon particles on the surface that will later be useful for calibration of the electron beam. Various alignment and calibration steps are necessary to ensure that the exposure results in structures which are as close as possible to the intended dimensions. The calibration of the electron beam needs to be repeated for each of the employed column modes (see Section 2.1.9), i.e., for each magnitude of the electron beam current used for exposure. The choice of beam current thereby represents a trade-off between the desired patterning resolution and the dwell time, i.e., the time the beam exposes each position in the rasterized design. Lower beam currents in general lead to improved accuracy of patterning at the cost of higher overall exposure times, which is why we employ the lowest available current for the fine features of the PhC lattice, while more coarse features (such as the trenches surrounding the access waveguides, see Section 2.1.1) may be written with higher currents.

The beam calibration comprises astigmatism correction of the electron beam, performed on a reference sample that is part of the wafer holder on which the sample is mounted, and measuring the beam current of the chosen column mode (to exactly determine the required dwell times upon exposure). The sample edges are then aligned with the in-plane Cartesian reference frame, which ensures that the patterned designs are well-aligned with the crystallographic axes of the silicon device layer, crucial for the final cleaving step of samples that contain access waveguides (Section 2.1.1 and Section 2.1.8). The chip also needs to be leveled such that the patterned surface area lies within the focal plane of the electron beam. This is performed by adjusting the height of three piezoelectric actuators supporting

the wafer holder, whereby the particles in the sample corners (obtained from the scratches introduced prior to loading) serve as targets for focusing. Any residual height difference that cannot be corrected by the limited range of the piezoelectric stage is compensated for by mechanical actuators during exposure, using the reflection of a laser beam from the sample surface as a reference signal for constant height feedback. Next, distortion correction of the electron beam is performed using another (checkerboard-pattern) reference sample on the wafer holder. This minimizes the distortion of shapes that are patterned under oblique incidence of the beam, toward the edges of the write field (WF). The WF refers to the field size the electron beam can expose for a fixed sample position, with a maximum of $500 \times 500\,\mu$m. Correction of the WF zoom factor, shape, and rotation constitutes the final alignment step (performed with the same checkerboard-pattern reference sample) and is especially important for designs that span multiple WFs, as to avoid stitching errors along their shared boundaries.

The exposure of the resist is performed following a user-defined position list, i.e., a file that contains references to the GDSII designs to be patterned alongside their relative coordinates and electron beam doses. In GDSII, a design is broken down into reusable blocks, or "cells". Each cell can contain other cells, creating a nested structure, along with various geometric and non-geometric elements. In our layouts, we only use geometric elements, in essence a collection of polygons as defined by their corner coordinates. Each element is associated with a specific layer and datatype, providing a means to differentiate between shapes and, for example, use different beam currents for different layers (depending on the desired accuracy) or use the datatype as an indicator of the exposure dose (as done by default in our EBL system). To determine the optimum exposure dose, a dose test is typically performed prior to fabrication of the actual sample layout. This entails patterning multiple copies of a test design, each with slightly different exposure doses, which are then checked in a SEM (SEM) to find the optimum value.

As mentioned earlier (Section 2.1.1), we do not directly supply the raw generated GDSII files to the EBL system, but first apply some post-processing. The software package BEAMER® offers various modules which aid in optimizing the layout for EBL to improve the accuracy of patterning and obtain fabricated structures that are considerably closer to the design specifications than would be possible using the original GDSII files. In a similar vein as the aforementioned dose tests, prior to fabricating actual samples, we pattern several test lattices to determine good parameters for the post-processing procedure. The main operations we perform are “WF alignment”, “fracturing”, “proximity effect correction”, and “sorting”. Write field alignment thereby simply refers to the centering of the elements within each of the WFs that cover the entire design and are traversed by movements of the stage. This minimizes any potential distortions that become more prominent around the WF boundaries, where the electron beam is incident on the sample surface under shallow angles.

Due to the physical limitations of the EBL process, the polygons defined in the GDSII files must be broken down into simpler, manageable shapes that the EBL system can handle. This process of breaking down or “fracturing” the design into

basic shapes that the EBL system can handle is a critical step in the process [155]. Fracturing of GDSII files for EBL typically involves breaking down the complex patterns into a collection of simple geometric shapes such as rectangles and trapezoids which the electron beam can write effectively. In essence, the fracturing process rasterizes the complex shapes into smaller, simpler ones that can be written sequentially. The quality of the fracturing process has a significant impact on the final written structures. Good fracturing software will aim to minimize the number of shapes, while still preserving the fidelity of the original design. The reduction in the number of shapes is important as it directly affects the writing time: fewer shapes mean less beam movements and thus faster writing times. We further promote the patterning of symmetric features such as the triangular holes of the PhC membranes (see Section 2.1.1) by enforcing symmetric fracturing (see Figure 2.3a, insets).

We can mitigate these deviations by applying proximity effect correction to the fractured design[154]. The proximity effect in EBL refers to the unintentional exposure of resist outside the electron beam focus due to scattered electrons. When the electron beam irradiates the resist, a portion of the electrons scatter laterally and expose regions adjacent to the target area. This leads to overexposure of these areas, causing the structures to differ from their design after development. Proximity effect correction counteract this overexposure based on the system's point spread function (PSF). The PSF is a mathematical function that describes the response of an imaging system to a point source or point object [156]. In the context of EBL, the PSF describes the spatial distribution of energy deposited in the resist by the primary and scattered electrons. This distribution is determined by several factors, including the electron energy, the resist thickness, and the substrate material. Monte Carlo simulations (TRACER® [157]) provide a way to calculate the PSF for a given set of conditions, taking into account both the direct impact of the primary electrons and the contribution from scattered electrons [158]. With a PSF derived from Monte Carlo simulations, one can predict the proximity effect for a given design and then apply corrections to moderate it. This generally involves adjusting the dose of the electron beam for different areas of the design, delivering a higher dose to areas that are predicted to be underexposed due to the proximity effect and a lower dose to areas predicted to be overexposed. An example with color-coded dose factors, i.e., factors that modify the predetermined optimum base dose, is shown in Figure 2.3a.

The next step is sorting of the elements, i.e., defining the order in which the electron beam patterns fractured shapes within a given WF, as well as the order in which the WFs are traversed by stage movements. This essentially boils down to minimizing the movement of the electron beam between successive exposures, avoiding inaccuracies from adjustments to the focusing optics when patterning within a WF and from stage movements between WFs. Write fields are traversed such as to complete an entire PhC design (including potential access waveguides) before starting the next one (see Figure 2.3b). Sorting is typically done in a hierarchical manner, starting from the layers that different parts of the design are associated with. In the case of samples with access waveguides, for example, the waveguides on either side of the PhC are placed in different layers, and so are the PhC's lattice sites and less important features (labels, trenches, etc.). When the stage centers on a

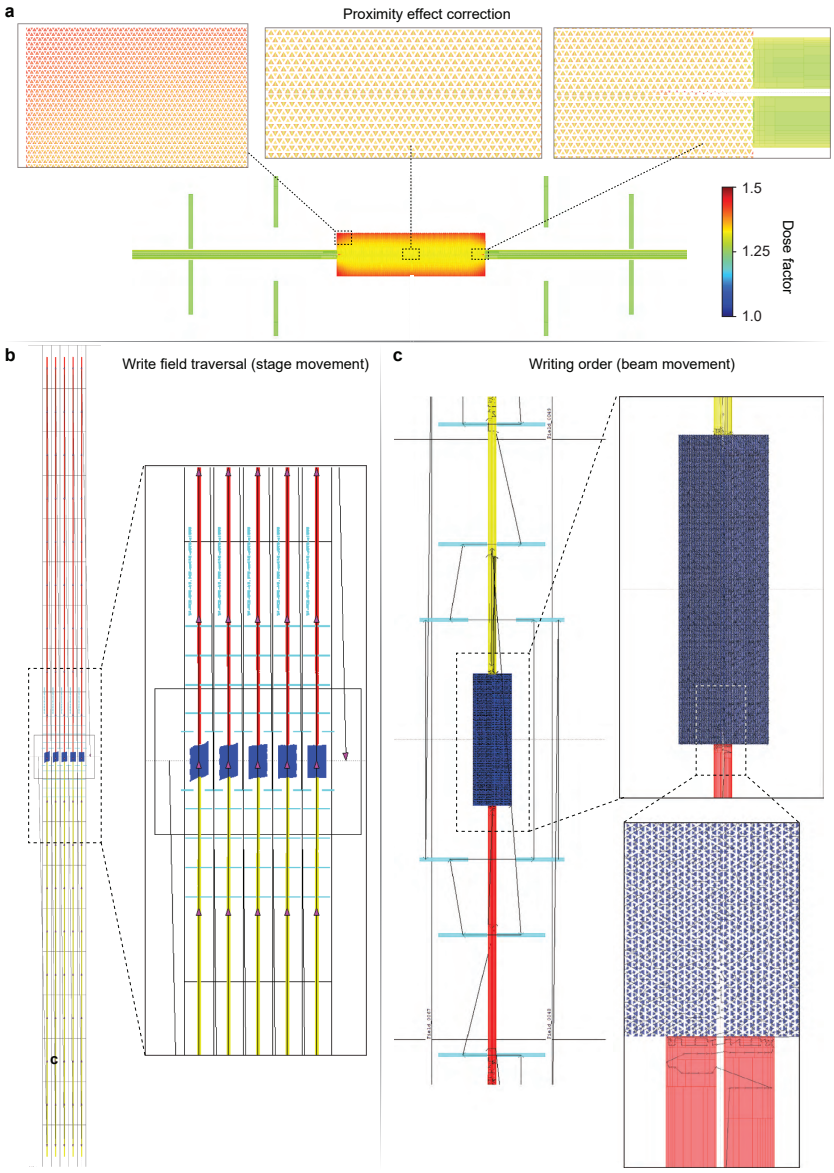

Figure 2.3: Tuning of exposure parameters for improved patterning results. a, Visualization of the spatially varying exposure dose in a photonic crystal lattice with access waveguides after proximity effect correction. The colors signify the dose factor, i.e., the factor with which the predetermined base dose is modified. **b,** Write field traversal during electron beam lithography via movements of the sample stage (magenta arrows). The colors of the elements indicate the layers in the design they are associated with. **c,** Patterning order of elements via deflection of the electron beam within each write field (black arrows).

new WF, the software will guide the patterning of the present layers in a predefined order. This order is designed to ensure that critical elements, and the transitions between them, are exposed with minimal intermediate beam deflections. Within each layer, the elements are further sorted by an algorithm that minimizes beam movements, whereby we can manually optimize parameters such as the sizes of subfields used for sorting. We illustrate this by the example of a WF containing the PhC design and access waveguides in Figure 2.3c. Here, the WF below was just patterned, and the stage moved to the center of the current WF. To reduce stitching errors, it first completes patterning of the bottom waveguide, before carrying on to the PhC, the upper waveguide, and finally the trenches and labels. It will then move the stage upwards to the next field, and continue in a similar fashion.

The post-processed design files are exported in the native file format of our EBL machine that is capable of encoding the performed optimizations. It produces a single file for each WF, which is assigned the proper relative coordinates in side the position list before starting the exposure. After the patterning process, the substrate is developed in multiple steps (see Section 2.1.9): immersion in DI-H_2O to remove the layer of Electra 92, followed by the developer n-amyl acetate that dissolves the exposed areas of the positive resist CSAR 62, a short dip in o-xylene that aids in clearing resist residues, a solution of methyl isobutyl ketone (MIBK) and IPA (1:9) to halt the development, and finally IPA to get rid of chemical residues prior to blow-drying [153]. After this procedure, we are left with the desired PhC pattern in the resist film.

2.1.5. REACTIVE ION ETCHING

The patterned layer of resist covering the sample surface acts as a mask for the subsequent inductively coupled plasma reactive ion etching (ICP-RIE), upon which the design is transferred into the silicon device layer. The sample is placed on a silicon carrier wafer with thermal contact oil in between, and loaded into the reactive ion vacuum chamber (Oxford PlasmaPro 100 Cobra). The fundamental principle of reactive ion etching (RIE) involves the creation of a plasma in a low pressure gas containing a mixture of reactive species and subsequently using it to etch a target material, such as our silicon-based thin films. The high kinetic energy ion bombardment, coupled with chemical reactions from the reactive gas species, gives this process its unique etching capabilities.

In RIE, the plasma is generated using a radio frequency (RF) discharge, and the ions present in the plasma are accelerated towards the target material by an electric field formed between the plasma and the substrate. Since plasma density and ion energy are controlled by the same RF power source, there is a trade-off between etch rate and damage. Increasing the power can increase the etch rate (via increased ion currents), but it might also increase damage due to higher ion energies. In ICP-RIE, on the other hand, a separate RF antenna surrounding the chamber is used to generate the plasma via inductive coupling. The antenna creates an alternating RF magnetic field which induces RF electric fields that ionize the gas molecules in the chamber. The separation between plasma generation and ion acceleration in ICP-RIE allows for more independent control over ion energy and plasma density. This

generally leads to better control over the etch profile, including more anisotropic (vertical) profiles which are desirable for many applications requiring deep etching processes.

The two major components of RIE are physical sputtering and chemical etching. Physical sputtering refers to the physical bombardment of the substrate by the high-energy ions, which knocks off the atoms from the surface. The chemical etching component, on the other hand, involves the reaction of reactive species from the plasma with the surface atoms of the substrate, creating volatile products that are easily removed. The combination of these two etching mechanisms makes RIE an anisotropic process, allowing for the creation of sharp, vertical walls and high aspect ratio structures. The configuration of the device is a laborious process in light of the multitude of optimization parameters (gas composition, RF power, chamber pressure, process times, etc.), aiming to achieve a highly anisotropic etch normal to the substrate surface with minimal sidewall roughness, which could otherwise create undesired scattering sites that negatively impact the sample's optical properties. We use multiple successive etching steps to obtain high-quality PhC lattices with smooth sidewalls. The ICP-RIE is performed at 60°C, whereby the chamber and carrier wafer are pre-conditioned in order to ensure reproducible conditions for the process prior to loading the sample. First, before being able to etch the silicon device layer, we need to remove the thin native oxide layer which rapidly forms on the sample surface under standard room conditions. To this end, a short chlorine gas breakthrough step is performed. This is followed by the main silicon etch which uses a gas mixture of hydrogen bromide (HBr) and O_2. The etching process involves physical sputtering due to ion bombardment (HBr^+, O^+, free electrons) as well as chemical reactions via the neutrals Br and O. Silicon reacts with Br to form silicon tetrabromide ($SiBr_4$), and with O_2 to form silicon dioxide (SiO_2). Both of these products are volatile at the typical etching conditions and can desorb from the surface, effectively removing silicon from the wafer. This particular combination of HBr and O_2 is often used because it can provide high etch rates, good selectivity towards silicon over silicon dioxide, and highly anisotropic profiles. As the selectivity towards the resist layer is rather poor (~1:1), special care has to be taken to not over-etch the sample, which would entirely ablate the protective mask and result in severe damage to the device layer.

While in practice the quality of the anisotropic etch (in terms of selectivity and sidewall roughness) turns out to be fairly stable, the etch rate in our system seems to vary over long time scales (years). It is therefore important to verify that the silicon device layer is thoroughly etched after the process, especially in light of the wet etch performed later (Section 2.1.7). A first indicator is the appearance of the etched holes in an optical microscope, which after (or close to) breakthrough typically appear dark as compared to the surrounding, highly-reflective silicon-covered surface (see Figure 2.4a). Certainty is achieved by imaging the sample in an SEM, where we observe strong charging effects that distort the recorded images if the silicon was removed successfully and the electron beam is incident on the bare surface of the buried oxide layer (see Figure Figure 2.4b).

After successful RIE, the residual resist film is removed by immersion in anisole

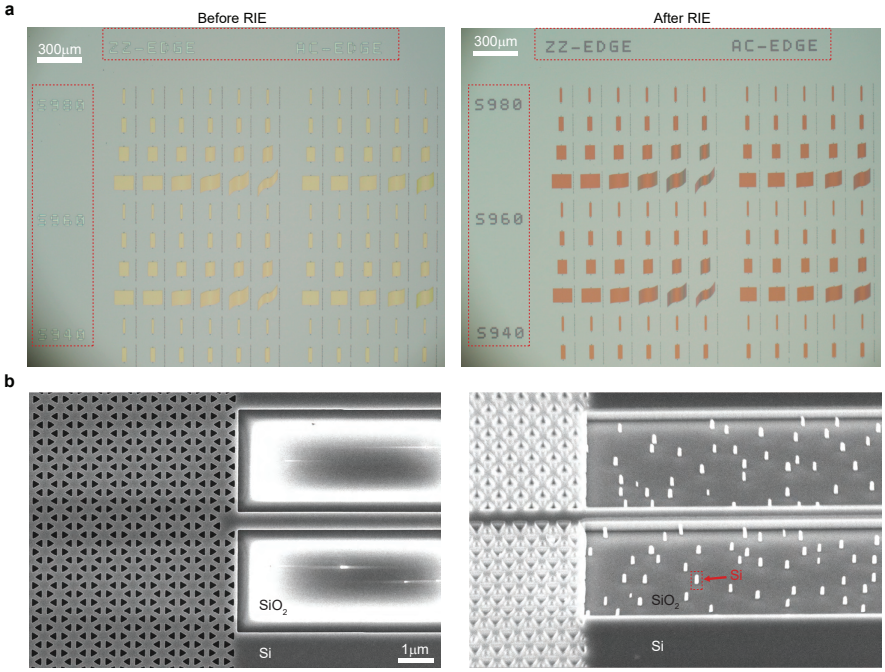

Figure 2.4: Sample appearance after reactive ion etching. a, The dark appearance of structures in optical microscope images after reactive ion etching, most notably for larger trenches such as the labels (red boxes), signifies successful removal of the silicon device layer. **b,** The breakthrough of the etch is verified by the observation of strong charging effects in the uncovered buried oxide layer when imaged in a scanning electron microscope.

(10 min) and acetone (5 min), followed by a rinse with DI-H_2O and a piranha etch (15 min). As the RIE alters the chemical properties of the resist film which renders it more challenging to remove, an additional piranha etch may be required.

2.1.6. ULTRAVIOLET LITHOGRAPHY

The UV lithography procedure described in this section only applies to sample designs with a side-coupling scheme using silicon ridge access waveguides (see Figure 2.2). The aim is to create a wet-etch mask and protect said waveguides from under-etching upon removal of the sacrificial buried oxide layer (see Section 2.1.7).

UV lithography (also known as optical or photolithography) has some parallels to EBL (Section 2.1.4), relying on the exposure of a resist film to create precise patterns. It uses the interaction of UV light with photosensitive materials (photoresists), whereby the exposure is controlled by a mask, which is a template of the desired pattern. The mask, which consists of opaque and transparent regions corresponding to the design, is placed atop the photoresist-coated substrate. When the system is irradiated with UV light, the light passes through the transparent regions of the mask, selectively exposing the photoresist beneath. Since our goal is to selectively under-etch the PhC lattices while protecting the access waveguides from the liquid

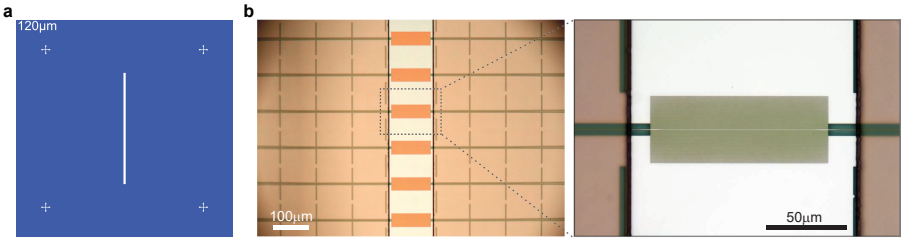

Figure 2.5: Wet etch mask. a, Schematic depiction of the ultraviolet lithography mask used to pattern a narrow (120 μm wide, 6 mm long) window into a positive photoresist covering the sample surface. **b,** Optical microscope images of the patterned wet etch mask after development.

etchant, our design consists of a chromium mask that blocks most of the sample surface from the UV light, while having narrow transparent rectangular windows that are aligned on top of the PhCs (see Figure 2.5a).

In our process, after an O_2 descum and application of HMDS to improve resist adhesion (Section 2.1.3), we spin coat the photosensitive positive resist AZ®1518 (AZ Electronic Materials) that is tailored for use in wet etching processes. We then perform UV exposure (Suss MA/BA6 Mask aligner) using the rectangular mask described earlier, and finally develop the resist in a solution of AZ®400K:DI-H_2O (1:4, AZ Electronic Materials), whereby the development time should be minimized to not expose the bare sample surface to the developer unnecessarily long, as it contains potassium hydroxide (KOH) which may attack the silicon device layer [159]. This process leaves behind well-defined rectangular apertures above the PhC and short stretches of the access waveguides adjacent to it (see Figure 2.5b).

Despite the resolution in this process being constrained by the diffraction limit of light, we use UV lithography as a fast technique with higher throughput than EBL since the rectangular windows have a much larger minimum feature size of $\gtrsim 120\,\mu$m (the window width) than the PhC design itself, requiring far less accuracy of patterning.

2.1.7. WET ETCHING

We create suspended PhC membranes by removing the buried oxide layer which would otherwise cause strongly enhanced mode losses into the slab. To this end, we use a wet etch procedure involving hydrofluoric acid (HF acid), a solution of hydrogen fluoride (HF) in water, particularly effective for etching SiO_2 [160]. Wet etching is a chemical process that involves removing materials from a substrate by dissolving them in a liquid etchant. When the substrate is immersed in the etchant, a chemical reaction occurs, producing soluble products that can be washed away. In the case of HF acid, it reacts with SiO_2 to produce H_2O and hexafluorosilicic acid (H_2SiF_6), a soluble substance that can be easily removed. One of the main advantages of HF wet etching is its high selectivity toward SiO_2, hardly affecting the underlying silicon, which makes it particularly useful in the SEMiconductor industry. However, wet etching with HF acid also has its limitations. It is isotropic, meaning it etches in all directions equally, which can make it challenging to create features with

high aspect ratios or sharp edges. Also, as a highly dangerous substance, handling HF acid requires stringent safety precautions. Moreover, the wet etching process can be hard to control with extreme precision, with the etch rate depending on temperature, substrate material, and (for us most relevant) the concentration of HF. As HF is used up during the etching process in the chemical reaction with the oxide, its concentration drops over time for an ordinary solution of HF in water.

To counter this effect, buffered solutions of HF acid are often employed, also known as buffered oxide etch (BOE) [160]. The purpose of a buffer in chemistry is to maintain a relatively constant pH, even when other substances are added to the solution or when the solution is diluted. The BOE contains a mixture of HF and ammonium fluoride (NH_4F) which helps to maintain a steady concentration of fluoride ions (F^-), even as the HF is consumed by the etching process. The presence of F^- ions in the solution from the dissociation of NH_4F can help replenish the HF by reacting with any available H^+ ions in the solution. This 'replenishing' action helps maintain a constant concentration of HF in the solution, leading to a consistent etching rate, and it allows for a slower, more controllable etch compared to using HF alone. The etching rate can be tuned by adjusting the ratio of HF to NH_4F, as well as the temperature and the agitation of the solution.

In our process, etching is performed at room temperature, leaving the concentration of HF as the main parameter for tuning the etch rate. One of the practical advantages of HF etching is the potential to achieve very high etch rates as compared to other methods like RIE. For samples without access waveguides, we employ a 1:1 solution of 40% HF and DI-H_2O that fully removes the 3 μm thick buried oxide layer below the PhC within 19 min, at an etch rate of ~ 160 nm/min. For samples with access waveguides, however, this comparatively high etch rate poses challenges regarding the wet etch mask we require for protecting the waveguides from under-etching (see Section 2.1.6).

The HF acid can creep under the mask and peel it off, leading to a large-scale suspension of the waveguides beyond the window defined by the wet etch mask (Figure 2.6a). Dark-field images serve as an easy check to estimate the extent of the under-etch, which appears as a margin with bright outlines around the structures and, for unsuccessful etching attempts, extends considerably far along the access waveguides (Figure 2.6b). Moreover, HF acid tends to diffuse more strongly through the protective resist layer at higher concentrations and thus even under-etches features that are initially completely covered by the wet etch mask, also recognizable in optical dark-field and SEM images as broad margins around the scattering trenches (Figure 2.6b,c). Both, diffusion through and creeping under the wet etch mask, ultimately often result in the collapse of the delicate suspended single-mode waveguides around the PhC (see Figure 2.6c). Apart from best practices that aim to improve resist adhesion, using lower HF concentrations turns out to be the most viable way to mitigate this effect (see Figure 2.6d-f). We see that this reduces both creeping under the wet etch mask, i.e, a shorter extent of the side etch along the waveguides, and diffusion through the protective resist layer, i.e., smaller margins around the scattering trenches (Figure 2.6d,e), resulting in nicely suspended access waveguides and PhC membranes (Figure 2.6f).

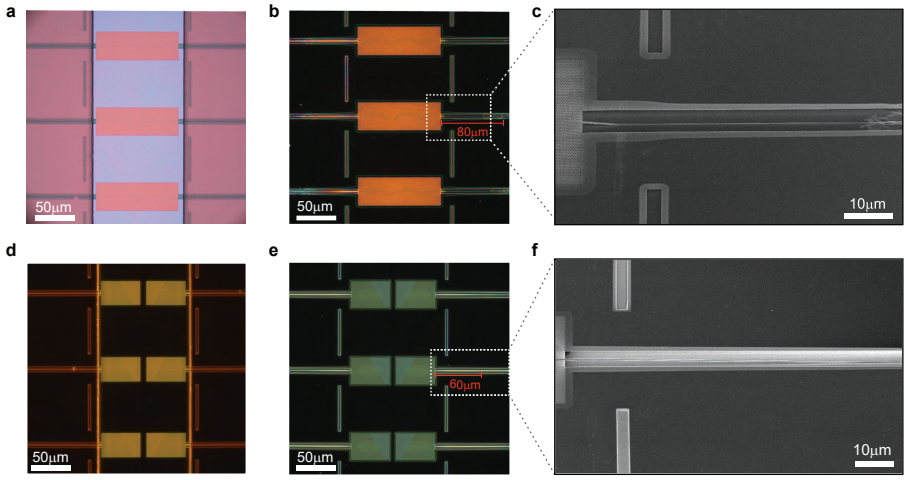

Figure 2.6: Wet etch mask performance. Comparison of **a-c,** unsuccessful and **d-f,** successful under-etches with hydrofluoric acid using a resist wet etch mask. An optical (dark-field) microscope image of the mask before the wet etch is shown in **a** (**d**). After the wet etch, dark-field images (**b, e**) allow to estimate the extent of the under-etch beyond the resist mask via the bright margins around the structures. This is more accurately quantified via scanning electron microscopy (**c, f**), showing the collapse of an access waveguide in the unsuccessful attempt (**c**) due to hydrofluoric acid creeping under and diffusing through the resist.

To etch the samples with access waveguides at low concentrations with controllably low rates, we initially employed a BOE with 1:6 ratio of 49% HF and 40% NH_4F. While this process at first led to satisfactory results, the PhC features turned out to be severely attacked at the end of later fabrication runs, with the issue worsening over time. The structures seemed strongly over-etched (see Figure 2.7a,b), and after excluding other possible culprits such as the SC-1 cleaning step (replaced by piranha solution) and the KOH-based photoresist developer, the buffered HF solution was identified as the problem. It came to light that the solution degrades over long time spans (several years) when exposed to oxygen from the ambient air, likely due to the repeated opening and closing of the storage container upon successive etch runs. For silicon immersed in a solution of buffered HF that contains dissolved O_2, two competing reactions are possible (see Figure 2.7c) [161]. In both cases, the H-terminated silicon surface is oxidized, either anisotropically via OH^- or isotropically via O_2, and the resulting SiO_2 is rapidly dissolved in the HF solution, effectively etching silicon in a two-step process.

An obvious solution to the issue is to replace the degraded BOE solution with a fresh one. Due to time constraints and the anticipated long shelf time of any newly ordered BOE solution in our nanofabrication facility, which would eventually result in the same issues over time, we decided to refrain from using BOE for successive fabrication runs. Instead, we switched to a regular solution of HF in water as for the samples without waveguides, however, using lower concentrations of HF (1:2 HF:DI-H_2O) and only performing a partial under-etch to shorten the process time (20 min

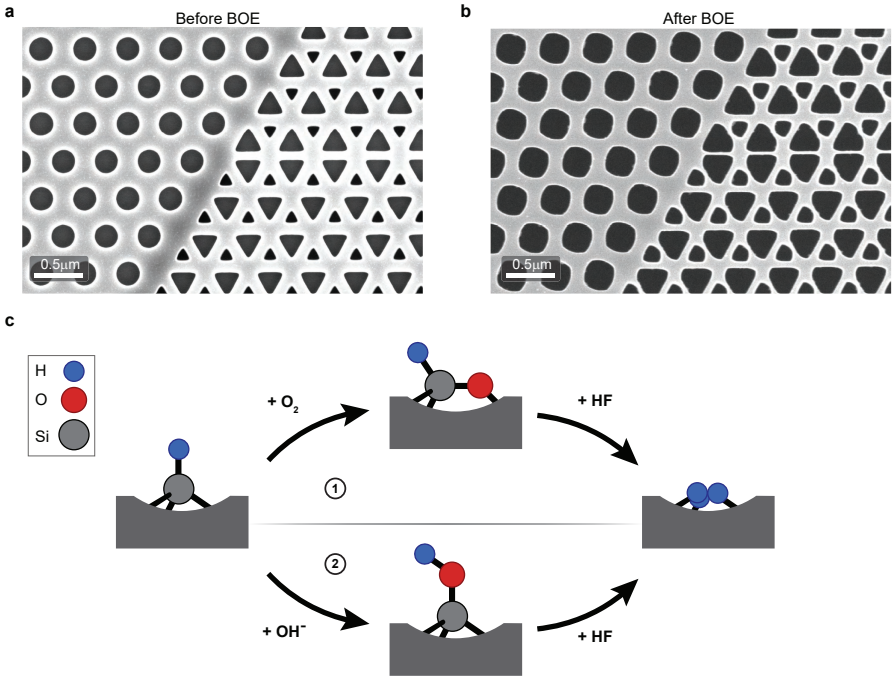

Figure 2.7: Buffered oxide etch issues. Scanning electron microscope images of a photonic crystal **a,** before and **b,** after a buffered oxide etch with a degraded solution, showing attacked (i.e., over-etched) features. **c,** The culprit is most likely oxygen dissolved in the solution which oxidizes the silicon surface following two different chemical pathways. The created oxide is subsequently rapidly dissolved by hydrofluoric acid. Figure adapted from [161].

to remove $\sim 2.5\,\mu$m). The combination of lower HF concentration and shorter process time mitigates the issues of collapsing waveguides due to etching beyond the resist mask, while the elimination of the degraded BOE solved the problem of attacked PhC features, showing a typical 1:100 etch selectivity of Si:SiO_2.

After wet etching, the sample is properly rinsed with water, cleaned with a piranha etch (20 min) to remove any resist residues, and rinsed with DI-H_2O again. If the sample were now left to dry normally under room conditions, surface tension effects upon evaporation of the liquid could be strong enough to result in a collapse of the suspended structures, especially the delicate access waveguides. Instead, we subject the sample to critical point drying. The critical point in thermodynamics refers to the unique set of conditions (temperature and pressure) at which a substance's liquid and gas phases coexist in equilibrium. Beyond this point, there is no distinguishable difference between the liquid and gas phases and the substance becomes a supercritical fluid. Critical point drying leverages this concept by transitioning a substance within a specimen from the liquid to the gas phase without crossing the liquid-gas boundary, thereby avoiding surface tension effects that can cause structural damage.

To this end, the sample is first dehydrated by immersion in ethanol, before being

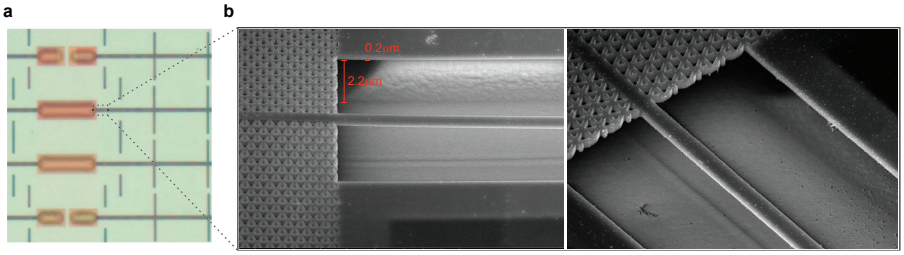

Figure 2.8: HF wet etch. Appearance of photonic crystals after a successful under-etch with hydrofluoric acid. **a,** Under an optical microscope, sagging of the suspended membranes is visible. **b,** Scanning electron microscope images show the formation of a cavity below the photonic crystal and an undercut of the surrounding silicon device layer where the buried oxide is removed.

transferred into an ethanol-filled chamber of a critical point dryer (Autosamdri®-815, Series B). The tightly sealed chamber is then purged with liquid carbon dioxide (CO_2) which has a relatively low critical point, replacing the ethanol. The critical point dryer then increases the temperature and pressure beyond the critical point, where the CO_2 becomes a supercritical fluid. When the supercritical fluid is vented from the dryer, it transitions directly to the gas phase, bypassing the liquid-gas boundary and therefore avoiding the damaging effects of surface tension. The result is a gentle drying process that leaves behind an unharmed sample with delicate suspended structures. After the wet etch, sagging of the PhC membranes can be seen under an optical microscope (see Figure 2.8a). Dark-field images serve as an easy check to estimate the extent of the under-etch (Figure 2.6b,e), and its precise extent is further verified in the SEM (see Figure 2.8b). For samples without access waveguides, this step concludes the fabrication.

2.1.8. CLEAVING

This step is solely performed for samples with access waveguides. While spin coating usually results in a fairly homogeneous film across most of the sample surface, towards the edges, the resist typically bulges and increases in thickness. This makes it challenging to perform EBL reliably in this region, which is why the access waveguides we pattern do not extend to the edges of the chip, but rather span ~ 3 mm on either side of the PhC lattices. As a final step, we therefore cleave the chips from both sides to create end facets for in-coupling (see Figure 2.9a). This is done manually with dedicated pliers, whereby we first apply a small scratch with a diamond pen on one side of the chip that facilitates a clean straight cleave along a crystal axis, where positioning of the scratch is aided by cleaving markers that are patterned during EBL and visible with the naked eye. It is of paramount importance that the original wafer from which the SOI chip is taken was diced in proper orientation, as the cleaved edge might otherwise run under an angle or even through the patterned devices (see Figure 2.9b).

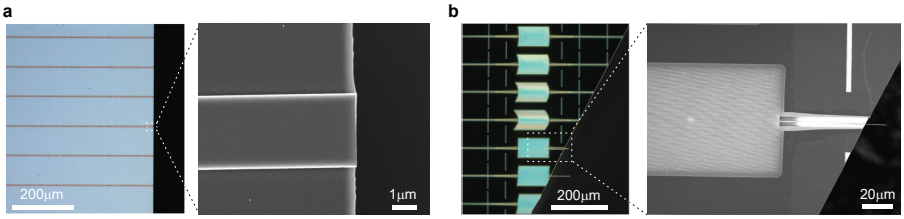

Figure 2.9: Cleaving. a, Optical microscope image showing access waveguides that extend to the edge of the cleaved sample (left) together with an enlarged view of a waveguide end facet under a scanning electron microscope (right). **b,** Same as **a**, for an unsuccessful cleave of the chip under an angle, due to misaligned crystal axes of the original silicon-on-insulator wafer upon dicing.

2.1.9. RECIPE SUMMARY

In the following, to give a concise overview, we provide a summary of the fabrication recipe with the parameters used in the last successful fabrication run performed in the context of this thesis. Please note that while the procedure is rather generally applicable, the exact process and device parameters can be highly variable over time, for different fabrication equipment, and even across different forgeries in spite of using the same equipment.

Sample: 20×12 mm SOI chip (220 nm Si device, 3 μm buried oxide, 725 ± 15 μm Si substrate).

A. Sample preparation

Perform the following steps for cleaning and surface activation of chips taken from a diced (resist-coated) SOI wafer.

1. Acetone (5 min), acetone wipe.
2. Ultrasonic water bath (15 min).
3. Isopropanol (rinse).
4. Anisole (15 min, 60°C).
5. Isopropanol (rinse).
6. Acid piranha (15 min, 130°C).
7. DI-H_2O (rinse).
8. O_2 descum (10min).

B. Spin coating CSAR 62

The spin coater has a bowl that can be attached to the lid with magnets to reduce the air volume around the sample. The confined space of the bowl can help manage solvent evaporation, resulting in resist films that are approximately half as thick as

without bowl. If not specified otherwise, no attached bowl is the default for spinning. Note that spin coating parameters change over time due to variations in viscosity of the resist because of solvent evaporation (older bottle → higher spin speeds). Always perform a spin coating test for CSAR 62 if more than ~ 2 weeks pass between runs or a new resist daughter bottle is used. It is advisable to keep a separate tightly sealed glass flask with syringe-filtered resist to obviate contamination by other users.

Step 1: HMDS

1. Put sample on heater at 110°C for 120 s (water desorption).
2. Transfer substrate to spin coater, cool with N_2 gun.
3. Apply drop of HMDS and wait at least 10 s for spread over surface.
4. Spin coat HMDS:

Step	Rotation (rpm)	Acceleration (rpm/s)	Time (s)	Lid	Function
1	0	20	5	1	Close lid
2	3200	1000	45	1	Spin HMDS
3	0	1500	0	0	Open lid

5. Bake at 150°C for 90 s.

Step 2: CSAR 62

1. Cool with N_2 gun.
2. Apply CSAR 62 (AR-P 6200.09) undiluted with pipette ($20-200\,\mu\ell$, $120\,\mu\ell$ syringe) until at least 2/3 of the sample surface is covered.
3. Spin coat CSAR 62 (parameters for fresh bottle, aim for ~ 240 nm thick layer):

Step	Rotation (rpm)	Acceleration (rpm/s)	Time (s)	Lid	Function
1	0	20	5	1	Close lid
2	2700	1000	45	1	Spin CSAR 62
3	0	1500	0	0	Open lid

4. Bake at 150°C for 3 min.

Step 3: Electra 92

1. Cool with N_2 gun.
2. Apply Electra 92 (AR-PC 5090.02) until at least 2/3 of the sample surface is covered.

3. Spin coat Electra 92:

Step	Rotation (rpm)	Acceleration (rpm/s)	Time (s)	Lid	Function
1	0	20	5	1	Close lid
2	2000	400	40	1	Spin Electra 92
3	0	1500	0	0	Open lid

4. Bake at 150°C for 5 min.

C. Electron beam lithography

Step 1: Exposure
The table below lists some typical exposure parameters for EBL. Note that these parameters can vary considerably depending on the actual design and resist properties.

Parameter	Value	Comment
Column mode - fine	LC 20	Small features in dual-beam exposure
Column mode - coarse	MC 40	Large features in dual-beam exposure
Beam current fine (nA)	0.07	Typical value
Beam current coarse (nA)	1.04	Typical value
Base dose (μC/cm^2)	130	For proximity effect correction
Step size - fine (nm)	2.5	Small features (PhC)
Step size - coarse (nm)	10	Large features (access waveguides, labels, ...)
Write field size (μm)	500	Make sure write field is centered on design
Dwell time (ns)	>60ns	Occasional issues below this threshold

Step 2: Development

1. Remove Electra 92: DI-H_2O (rinse).

2. Develop CSAR 62:

Chemical	Time
n-amyl acetate	75 s
o-xylene	6 s
MIBK:IPA (9:1)	15 s
IPA	15 s

D. Reactive ion etch
Perform RIE of silicon at 60°C using Cl_2 and HBr:O_2.

1. Preconditioning run on empty wafer:
   - Heat up chamber to 60°C.
   - Breakthrough step: Cl_2 - 50.0 sccm (11 s).

- Flush: HBr - 24.0 sccm, O_2 - 1.0 sccm (60 s).
- Pump out (60 s).
- RIE: HBr:O_2 (HBr - 48.0 sccm, O_2 - 2.0 sccm, 5 min).

2. Place sample on wafer (on top of a small droplet of thermal contact oil).
3. Main etch:
   - Breakthrough step: Cl_2 - 50.0 sccm (11 s).
   - Flush: HBr - 24.0 sccm, O_2 - 1.0 sccm (60 s).
   - Pump out (60 s).
   - RIE: HBr:O_2 (HBr - 48.0 sccm, O_2 - 2.0 sccm, 110 s).
     - Typical DC bias: ~ 165 V.
4. Unload the sample.
5. Clean chamber with O_2 plasma, reset temperature.

E. Removing CSAR 62

1. Anisole (10 min).
2. Acetone (5 min), DI-H_2O (rinse).
3. Piranha etch (15 min), perform twice if necessary.

F. Ultraviolet lithography
This step is only for sample designs with access waveguides, to create a wet etch mask for selective under-etching of the PhC.

Step 1: Spin coat AZ® 1518

- O_2 descum (10min).
- Spin coat HMDS.
- Spin coat AZ® 1518 (closed bowl, aim for ~ 2μm thick layer):

Step	Rotation (rpm)	Acceleration (rpm/s)	Time (s)	Lid	Function
1	0	20	5	1	Close lid
2	2000	1500	45	1	Spin AZ® 1518
3	0	1500	0	0	Open lid

- Bake at 100°C for 60 s.

Step 2: Ultraviolet exposure

1. Use mask aligner tape to cover undesired gaps in positive UV mask field. Suboptimal for mask contact, but good enough for our purposes.
    - Alternative solution: use negative resist with corresponding negative mask field.
2. Exposure
    - Lamp: 1000W CP (constant power), $\lambda = 365\,\text{nm}$.
    - Exposure time: 5.5 s.
    - Deposited dose: $137.5\,\text{mJ/cm}^2$.

Step 3: Development

1. Develop with AZ®400K:DI-H_2O (1:4) for 60 s, DI-H_2O (rinse).
2. Post-exposure bake at 110°C for 60 s.

G. HF wet etch

1. Etch 20 min in HF:DI-H_2O (1:2, 40% HF).
2. Rinse samples twice in H_2O.
3. Remove wet etch mask residues: acetone, piranha etch (15min), DI-H_2O (rinse).
4. Transfer to ethanol, critical point drying.

H. Cleaving
If required, cleave the sample using dedicated pliers after making a one-sided scratch with a diamond pen.

2.2. FAR-FIELD MEASUREMENTS

2.2.1. EXPERIMENTAL FAR-FIELD SETUP

The experimental far-field setup is sketched in Figure 2.10 and can be broadly divided into two configurations, operating with either broadband (orange path) or tunable monochromatic (red path) input light. The broadband source is used in conjunction with a Fourier-spectroscopy setup to directly image the angularly resolved reflection spectrum of the sample under study [129]. The monochromatic source, on the other hand, allows for selective addressing of individual modes and imaging of their radiation in real and momentum space. In the first case, a two-dimensional (2D) image is recorded that maps intensity as a function of frequency and one wavevector dimension (pinning the other through spatial filtering). In the second case, the 2D image records the intensity versus both spatial or wavevector dimensions, while instead fixing the frequency through the (tunable)

laser. The setup is an extension of the setup reported in [129], with updated and newly added physical components, as well as newly developed control and analysis scripts for automatization and evaluation of measurements. The following sections aim to provide a concise overview over the components used in the setup, discuss the main principles behind Fourier imaging and Fourier spectroscopy that underpin our far-field experiments, and describe the calibration and measurement procedures central to this work in more detail.

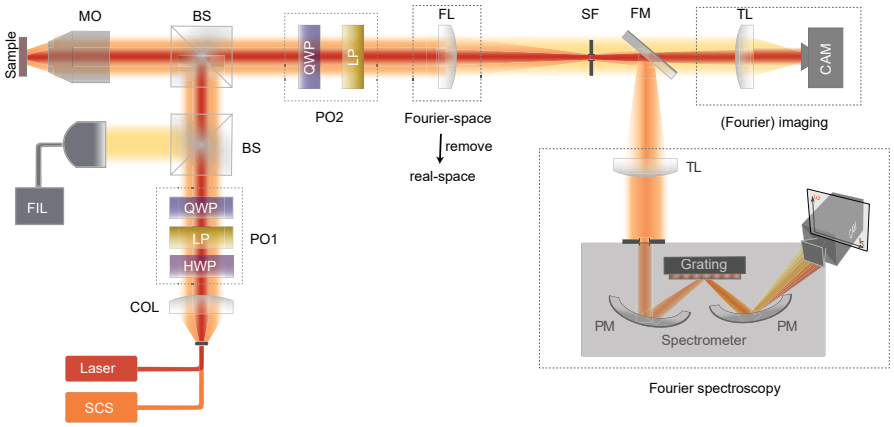

Figure 2.10: Setup configurations. Scheme of the setup configurations used for experimentally probing the optical properties of radiative photonic crystals from the far field. A removable Fourier lens (FL) allows for switching between real-space imaging (yellow path) and angularly resolved Fourier imaging (red path) of the radiation reflected from and emitted by the sample at the (variable) laser excitation frequency. Alternatively, Fourier spectroscopy (orange path) is realized by exciting the sample with a broadband supercontinuum source (SCS) and directing the probe beam to a spectrometer with a flip mirror (FM). See the main text for more details. SCS: supercontinuum source, COL: collimating lens, PO: polarizing optical elements, HWP: half-wave plate, QWP: quarter-wave plate, LP: linear polarizer, FIL: fiber illuminator, BS: beam splitter, MO: microscope objective, FL: Fourier lens, SF: spatial filter, FM: flip mirror, TL: tube lens, CAM: camera, PM: parabolic mirror.

Light Source. To reconstruct the photonic dispersion of our samples in the relevant near-infrared frequency regime, we use a 200 mW supercontinuum source (SCS, Fianium WhiteLase Micro) with a repetition rate of 30 MHz and picosecond pulses that generates light with a broadband spectrum from 400 nm – 2000 nm. The supercontinuum source (SCS) output spectrum is subsequently filtered by a long-pass filter with a cutoff wavelength of 1150 nm. For spatial filtering, the output of the long-pass filter is coupled into a single-mode optical fiber, suppressing higher-order modes upon propagation. The fiber output then passes a collimating lens (COL), ideally resulting in a collimated Gaussian beam at the entrance of the main setup shown in Figure 2.10 (orange path). Another fiber-optical channel may be used to couple in light from a tunable monochromatic laser source (Toptica CTL 1500, Toptica CTL 1550, Velocity TLB-6700) instead of the SCS, enabling measurements at defined frequencies (red path). The input power at the entrance

of the setup is tuned using a variable fiber attenuator. Optionally, incoherent halogen lamp light from a fiber illuminator (FIL, Thorlabs OSL1-EC) is coupled into the setup with a non-polarizing beam-splitter cube (BS) for Koehler illumination of the sample, used for real-space imaging and orientation [162].

Beam Preparation. The collimated Gaussian beam entering the setup passes a set of free-space polarizing optical elements (PO1) which together define the power and polarization state of the light. First, a half-wave plate (HWP) is used to rotate the polarization state and tune the intensity transmitted through the successive linear polarizer (LP). This rotatable LP, in combination with a removable achromatic quarter-wave plate (QWP), oriented at ±45°, allows for generation of arbitrary polarization states [122]. Specifically, we utilize two linear (horizontal, vertical) and both circular (right-/left-handed) polarization states for probing the samples. Right- and left-handedness herein are attributed to clockwise and counter-clockwise rotation, respectively, for an observer facing the source in the direction opposite to the propagation direction.

Focusing and collection. A beam splitter (BS) steers the polarized input light to an aspheric microscope objective (MO, Olympus LCPLN50XIR, 50× magnification, numerical aperture NA = 0.65), which focuses the incident Gaussian beam onto the sample. The focal spot has a typical diameter of ~ 0.5μm at telecom frequencies. The sample is attached to a XYZ-movable piezo actuator (MCL Nano-3D200FT, controlled via MCL ND3-USB163). Together with a custom-developed control software, this enables nanometer-precise scanning and positioning of the sample relative to the excitation beam. The three-dimensional (3D) piezo actuator is itself mounted atop a manual XYZ translation stage with micrometer screw gauges for coarse alignment. Light that is reflected and reradiated from the sample is collected by the same microscope objective (MO) and passed through the BS and a second set of LP and QWP (PO2) to project it onto the desired polarization state.

Imaging and spectroscopy. The light collected by the MO is analyzed either in real or momentum space. The former is achieved by a tube lens (TL) that focuses the real image formed by the MO onto an indium gallium arsenide (InGaAs) infrared camera chip (AVT Goldeye G-008 SWIR). The field of view is about 120 μm, and a typical microscope image of a grating sample under lamp illumination is shown in Figure 2.12a. Alternatively, a Fourier lens (FL) in the beam path permits direct imaging of the sample's angularly resolved emission (Fourier imaging) and angularly resolved photonic bands (Fourier spectroscopy), as we will describe in more detail in the following sections.

2.2.2. FOURIER OPTICS

Fourier optics is the branch of optics treating the propagation of light in reciprocal rather than real space, using Fourier transforms to convert between the two. In

essence, it provides a mathematical framework for understanding how optical systems manipulate the spatial distribution of light, with broad applications in image processing, microscopy, and modern optical communication systems [163]. In the following, we will outline the principles underlying the *Fourier-imaging* and *Fourier-spectroscopy* procedures used to characterize the samples in our experiments.

ANGULAR SPECTRUM REPRESENTATION

In the spatial domain, we denote the complex amplitude of an electric field in a certain plane ($z = 0$) as $E(x, y, 0)$. Using a 2D Fourier transform, we can express it in terms of an angular spectrum of plane waves

$$\widetilde{\mathbf{E}}(k_x, k_y; z = 0) = \frac{1}{4\pi^2} \iint_{-\infty}^{+\infty} \mathbf{E}(x, y, 0) e^{-i(k_x x + k_y y)} \, \mathrm{d}x \, \mathrm{d}y, \tag{2.1}$$

where k_x and k_y are the spatial frequencies (i.e., wavevectors) along the x- and y-axes, respectively. Here, each plane wave component is represented by a point in the spatial-frequency domain (or k-space), and each of these plane waves propagates independently. The propagation in homogeneous, isotropic, linear and source-free media is governed by the vector Helmholtz equation [156]

$$(\nabla^2 + k^2)\mathbf{E} = 0, \tag{2.2}$$

with $k = 2\pi n/\lambda$ denoting the wavevector magnitude, where λ is the free-space wavelength and n is the refractive index of the medium. Upon inserting Equation (2.1) into Equation (2.2), we see that each spatial frequency component, i.e., each angle, accumulates phase according to its wavevector component along the z-axis

$$k_z = \sqrt{k^2 - k_x^2 - k_y^2}. \tag{2.3}$$

Thus, to propagate the wave to a new plane z, we multiply each angular spectrum component by the propagation factor $e^{ik_z z}$ and perform an inverse Fourier transform to arrive at the so-called *angular spectrum representation* of the real-space field distribution in that plane

$$\mathbf{E}(x, y, z) = \iint_{-\infty}^{+\infty} \widetilde{\mathbf{E}}(k_x, k_y, 0) e^{i\left(\sqrt{k^2 - k_x^2 - k_y^2} z\right)} e^{i(k_x x + k_y y)} \, \mathrm{d}k_x \, \mathrm{d}k_y. \tag{2.4}$$

According to Equation (2.3), the wavevector k_z can assume either real ($k_x^2 + k_y^2 < k^2$) or imaginary ($k_x^2 + k_y^2 > k^2$) values, corresponding to two characteristic solutions: propagating oscillatory *plane waves* and exponentially decaying *evanescent waves*, respectively. The field $\mathbf{E}(x, y, z)$ is, in general, a superposition of both components.

The angular spectrum representation can be extended to cover more advanced topics in Fourier optics, such as the propagation of light in inhomogeneous media [164]. Furthermore, it is a powerful tool to describe the action of optical elements on incident fields, such as the effect of a lens. To this end, let us first consider the

far field $\mathbf{E}_\infty$ for a given local field (or near field) at $z = 0$, i.e., Equation (2.4) in the limit of a point at distance $r = \sqrt{x^2 + y^2 + z^2} \to \infty$. We can neglect the contribution of the (exponentially decaying) evanescent waves and restrict the integral in Equation (2.4) to plane waves. An evaluation of the asymptotic behavior of Equation (2.4) [165] shows that only a single plane wave component $\widetilde{\mathbf{E}}(k_x, k_y; 0)$ at $z = 0$ (cf. Equation (2.1)) contributes to a given point in the far field $\mathbf{E}_\infty$, which can be expressed as [156].

$$\mathbf{E}_\infty\left(\frac{k_x}{k}, \frac{k_y}{k}\right) = -2\pi i k_z \frac{e^{ikr}}{r} \widetilde{\mathbf{E}}(k_x, k_y; 0)\,. \tag{2.5}$$

Consequently, we may treat the far field as a collection of independent light rays, and substituting Equation (2.5) into Equation (2.4) yields

$$\mathbf{E}(x, y, z) = \frac{\mathrm{i}r\mathrm{e}^{-\mathrm{i}kr}}{2\pi} \iint\limits_{(k_x^2+k_y^2)\le k^2} \mathbf{E}_\infty\left(\frac{k_x}{k}, \frac{k_y}{k}\right) \mathrm{e}^{\mathrm{i}[k_x x + k_y y \pm k_z z]} \frac{1}{k_z}\, \mathrm{d}k_x\, \mathrm{d}k_y\,. \tag{2.6}$$

This is the framework of *geometrical optics*, which is in general a valid approximation so long as the size of the optical system is much larger than the wavelength. In many practical scenarios we can further make the assumption that the wavevectors contributing to the far-field plane under consideration are almost parallel to the z-axis, i.e., $k_z \approx k$. Under this *paraxial approximation*, Equation (2.6) yields the elegant result that the field at $z = 0$ and its far field form a perfect Fourier transform pair, which is the *limit of Fourier optics*.

FOURIER IMAGING

So far, we asked about the far-field distribution at a large distance for a given near-field distribution. Vice versa, we may ask about the near-field distribution in a local image plane upon focusing a given far field. Consequently, Equation (2.6) may be utilized to describe the action of an aplanatic lens which focuses each spatial frequency component of an incident wave at a different position in its focal plane. In other words, the lens performs a 2D Fourier transform by distributing the various spatial frequency components of the input field across its focal plane.

We use this principle in a custom microscopy setup (see Section 2.2.1) for angularly resolved polarimetry, i.e., polarization-resolved Fourier imaging. The collimated paraxial Gaussian input field may be treated in the formalism of geometric optics, i.e., as a bundle of light rays traveling parallel to the optical axis along z (see Figure 2.11a). The back focal plane (BFP) of the lens is defined as the plane in which parallel rays leaving the focal plane intersect and represents the far-field distribution associated with the focal field. The aplanat converts the real-space distribution $E(x, y)$ of the incident field in the BFP into the angular spectrum of the focal field $\tilde{E}(k_x, k_y)$. Aplanatic lenses are characterized by the sine-condition [156]

$$\rho = n \sin\theta\,, \tag{2.7}$$

which states that an incident ray parallel to the optical axis at a distance ρ is tilted towards the geometric focus under the angle θ. Note that a good MO obeys Equation (2.7) irrespective of the distance ρ from the optical axis (only limited by the

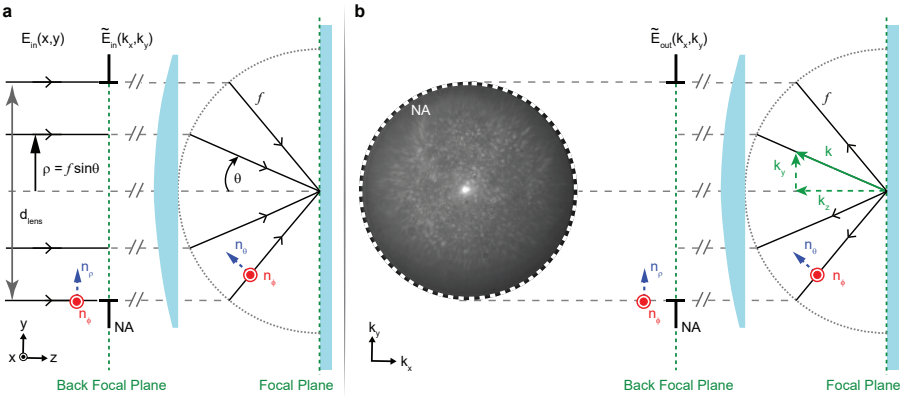

Figure 2.11: Focusing scheme and back focal plane imaging a, Schematic focusing scheme used to perform Fourier reflectometry in our experimental far-field setup. A Gaussian paraxial input field enters the aperture of the aplanatic focusing lens with numerical aperture NA. The action of the lens may be modeled by a reference sphere around the geometric focus with a radius corresponding to its focal length f onto which the field distribution in the back focal plane is projected. A ray incident at a height $\rho = f\sin\theta$ above the optical axis is tilted towards the focus under an angle θ, transforming the spatial input field distribution $E_{\text{in}}(x,y)$ into the angular spectrum $\tilde{E}_{\text{in}}(k_x,k_y)$ of the focal field. **b,** Light reflected and reradiated by the sample in the focal plane is collected by the same lens, and its back focal plane is imaged onto a camera in order to record the angular spectrum of the output field $\tilde{E}_{\text{out}}(k_x,k_y)$ (see also Figure 2.13b). A typical back focal plane image as obtained from reflection off a bare silicon substrate is presented (NA = 0.65).

finite aperture size), i.e., θ is not necessarily a paraxial angle. The focusing process may be modeled by a reference sphere of radius f (the focal length) around the geometric focus, onto which the field distribution in the BFP is projected and refracted according to Equation (2.7), effectively performing a transformation from polar to spherical coordinates (Figure 2.11a). Contrary to Equation (2.6), where every plane wave component contributes to the far field, the finite aperture size of the lens restricts the integral to the maximum aperture angle θ_{max}, which defines the numerical aperture

$$\text{NA} = n\sin\theta_{\text{max}}\,. \tag{2.8}$$

Here, n is the refractive index of the focusing side and θ_{max} is related to the focal length f and the aperture diameter d_{lens} via

$$\sin\theta_{\text{max}} = \frac{d_{\text{lens}}}{2f}\,. \tag{2.9}$$

The angle θ of a ray with respect to the optical axis may be expressed in terms of the Cartesian wavevector components via

$$k_x = k\sin\theta\cos\phi\,, \tag{2.10a}$$
$$k_y = k\sin\theta\sin\phi\,, \tag{2.10b}$$
$$k_z = k\cos\theta\,. \tag{2.10c}$$

To assure energy conservation, the focused field amplitude has to be multiplied by the apodization factor

$$A_{\text{lens}} = \frac{\overline{n}}{n}\sqrt{\cos\theta}, \tag{2.11}$$

where $\overline{n}$ and n are the refractive indices before and after the lens, respectively. A complete vectorial treatment of the focusing process [156, 166, 167] shows that the focal field distribution possesses full vectorial character, i.e., transverse and longitudinal components. Since in our measurements we employ only weakly focused Gaussian beams, the contribution of longitudinal fields to the optical response is assumed to be negligible [168]. After focusing the incident beam onto the sample surface, the directly reflected light as well as the emission of the PhC modes that are excited is collected by the same lens, which performs a back-transformation and maps the angularly resolved emission to a real-space field distribution in the BFP (Figure 2.11b).

We can thus directly access the information encoded in reciprocal space by imaging the BFP onto a charge-coupled device camera, after passing optical elements used for polarization projection. We switch from real-space imaging (Figure 2.12a) to Fourier space imaging by adding a Fourier lens in the analysis arm of the setup, as shown in Figure 2.12b. A correlator, constituted of the Fourier lens and a tube lens, projects the BFP onto the camera chip, possibly with non-unity magnification (Figure 2.12b, inset). Each recorded pixel value in the recorded camera image is proportional to the intensity of light propagating away from the sample with a certain wavevector **k**. A real-space image of the sample is formed in the correlator plane, where we insert a (rectangular) spatial filter to limit the region on the sample surface light is collected from. This aids in suppressing stray light (e.g., scattering at the edges of the PhC) and to improve the signal quality from the modes we target (typically localized around the center of the PhC lattices).

The wavevector axes in the Fourier space image may be calibrated via the known numerical aperture of the MO (Equation (2.8)). For greater accuracy, we perform wavevector calibration using a grating in the sample plane (Figure 2.12b), which under laser illumination produces diffraction orders m as per the grating equation,

$$m\lambda = n\,d\,\sin\theta \quad \longrightarrow \quad k_{\text{j},m} = m\frac{2\pi}{d}, \tag{2.12}$$

where $j = x, y$. These orders appear as bright spots in the Fourier image (Figure 2.12b). The period of the observed pattern corresponds to $\frac{2\pi}{d}$, which for known d determines the scale of the axes in units of $\frac{2\pi}{d}$. This can be mapped to k_{j}/k_0 using the known value of $k_0 = \frac{2\pi}{\lambda}$. For different incident frequency, the grating orders will have a different period, changing the calibration in terms of k_{j}. In terms of k_{j}/k_0, the change in period cancels out. The typical wavevector resolution in our measurements is $\delta k_j/k_0 \approx 0.009$.

FOURIER SPECTROSCOPY

Rather than focussing the tube lens directly onto a camera sensor, it may be imaged onto a spectrometer slit to perform Fourier spectroscopy, i.e., angle- and frequency-resolved examination of the collected radiation (Figure 2.13a). The slit is narrow

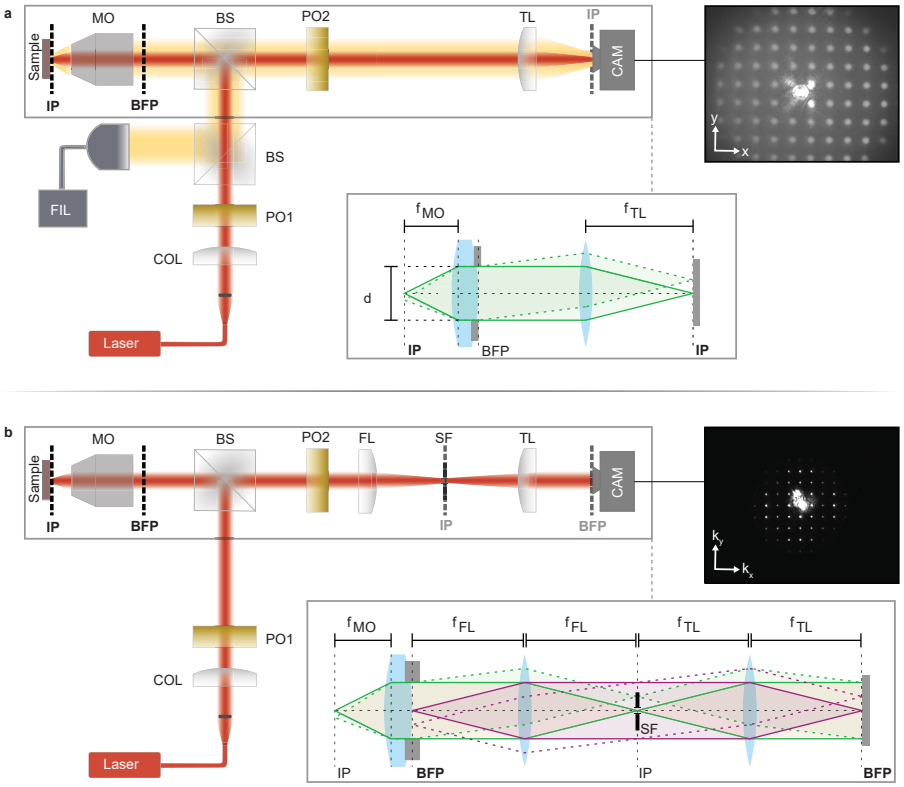

Figure 2.12: Imaging real and momentum space. a, Experimental setup configuration used for real-space imaging of a sample (here: a gold grating) in the image plane (IP) onto a charge-coupled device camera (CAM). A halogen lamp (FIL) is used to illuminate the sample surface and aids in positioning the laser excitation spot. Inset: schematic depiction of the imaging process. **b,** By inserting a Fourier lens (FL) into the beam path, we can switch from real space to reciprocal space by imaging the back focal plane (BFP). The camera image shows the diffraction orders of the grating sample, used to calibrate the wavevector axes in the Fourier plane image. A spatial filter (SF) in the intermediate IP allows for restricting the area on the sample from which light is collected. Inset: schematic depiction of the back focal plane imaging process. See Figure 2.10 for a list of abbreviations.

along the y-axis, selecting a small range of wavevectors along $k_x \approx 0$ within the BFP. With the help of two parabolic mirrors (PMs) for focusing and collection, the spectrometer grating (Acton SpectraPro SP-2300i) then disperses incident broadband infrared light along the orthogonal x-axis, such that in the final InGaAs infrared camera image (AVT Goldeye G-008 SWIR), one axis measures frequency while the other still measures wavevector k_y. This provides a way to directly record images of frequency versus k_y, i.e., photonic band structures. The wavevector axis of the spectrometer camera image is calibrated with a similar procedure as described in Section 2.2.2, with the spectrometer slit being opened as far as possible and the spectrometer grating tilted in a way to produce a smooth reflective surface, i.e., to act as a mirror and directly image the BFP onto the camera. The spectrometer

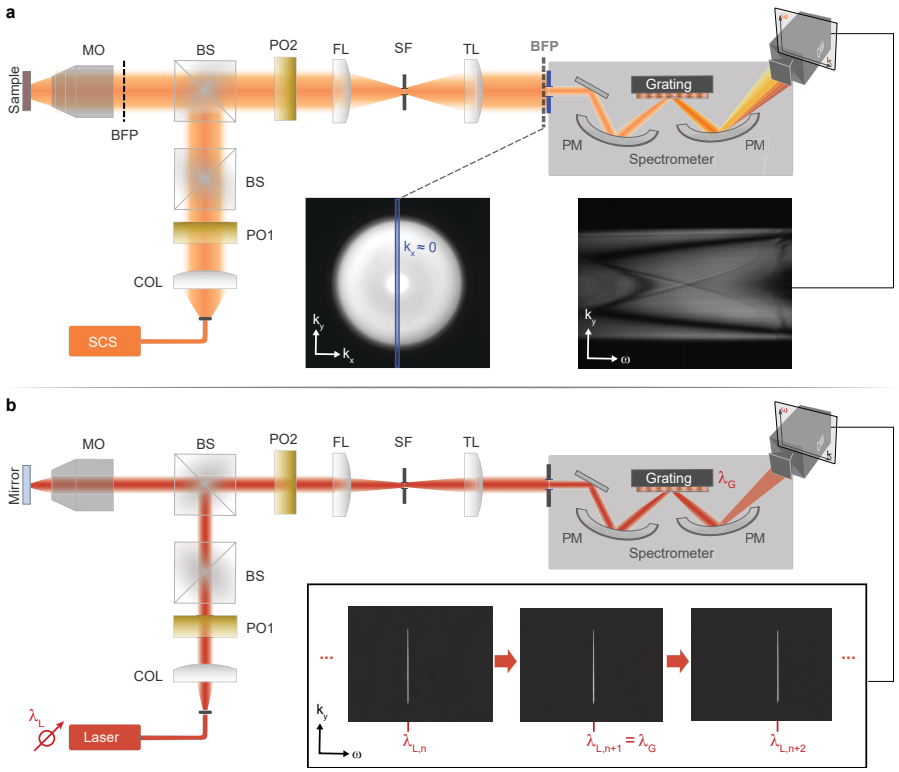

Figure 2.13: Fourier spectroscopy and frequency calibration. a, Experimental setup configuration used for Fourier spectroscopy. A supercontinuum source (SCS) generates broadband light that is focused onto the sample with a microscope objective (MO). The reflected light is collected by the same MO and its back focal plane (BFP) is imaged onto a spectrometer slit, selecting a narrow range of wavevectors around $k_x \approx 0$ (inset). The spectrometer disperses the light orthogonally to the slit, creating an image of wavevector k_y versus frequency, i.e., an image of the photonic dispersion (inset). **b,** The reflection of light from a tunable laser source off a highly reflective (gold-coated) sample is used to calibrate the frequency axis in the spectrometer camera image. See Figure 2.10 for a list of abbreviations.

contains a turret that allows us to switch between two gratings with 150 and 600 grating lines per millimeter, covering a spectral range of about ±100 nm and ±20 nm with frequency resolutions of 87 GHz and 16 GHz per camera pixel, respectively.

The setup configuration for calibration of the frequency axis is depicted schematically in Figure 2.13b. We use a tunable laser source, focused on a highly reflective (gold-coated) surface in the sample plane. The spectrometer components are aligned such that for laser incidence at the central grating wavelength λ_G (adjusted by a control software which tilts the grating) produces a diffraction line that is centered within the camera image. We sweep the laser wavelength λ_L for constant λ_G in discrete steps and record camera images of the diffraction lines for each setting (see inset of Figure 2.13b). We then use the grating line positions to obtain the calibrated frequency axis for a given λ_G by quadratic spline interpolation. This

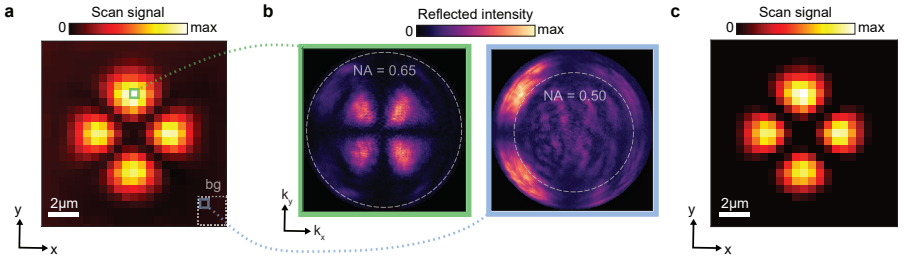

Figure 2.14: Reconstructing real-space mode profiles. a, Spatial excitation maps of photonic crystal modes (left) are recorded by raster-scanning a focused beam over the sample surface, typically in a cross-polarized detection scheme to suppress the strong background of directly reflected light. At each position, we record back focal plane images of the collected emission (right). Each pixel value in the reconstructed spatial map corresponds to the integrated intensity within the back focal plane at the respective position. We perform background correction by restricting the integration region (NA) and subtracting the average pixel value in a region far away from the mode of interest (bg) from the final image, improving the signal-to-background ratio as shown in **b**.

process is repeated for several center grating wavelengths in order to obtain the respective calibrated axes, covering a sufficiently large region in frequency space to cover the photonic bands of interest. Images recorded at differing λ_G may be stitched together in post-processing to cover a larger spectral region.

2.2.3. RECONSTRUCTING REAL-SPACE MODE PROFILES

To reconstruct spatial excitation maps of PhC resonances (e.g. cavity modes, Figure 2.14a), we raster-scan the excitation spot of our laser source over the sample surface by moving the latter in the focal plane using a 3D piezo actuator (see Section 2.2.1). At each position, we record a BFP image of the collected radiation (Figure 2.14b). To eliminate the strong background reflection of the excitation beam, this is typically performed using a cross-polarized setting of polarizer and analyzer. Each pixel value in the reconstructed spatial map then corresponds to the intensity collected at that position, obtained by integrating the signal in the BFP. We can further improve the signal-to-background ratio with filtering methods in real and momentum space. In momentum space, residual background radiation can be filtered by restricting the angular region (NA) we choose to integrate over. This is especially useful to suppress the Maltese cross background pattern that is characteristic for the cross-polarized imaging scheme [169]. An example of such a restricted integration region is shown in the right part of Figure 2.14b. Note that in this image, the asymmetry in the four-lobe pattern is a consequence of sagging of the suspended PhC membrane (Section 2.1). We can further eliminate unwanted reflections by subtracting a background intensity from the real-space maps, as obtained from an average over a pixel region sufficiently far away from the region of interest. Both strategies lead to improved contrast between the reconstructed mode profile and the unwanted background reflection (Figure 2.14c).

2.3. NEAR-FIELD MEASUREMENTS

As we have seen in Section 2.2.2, the far field only contains a limited amount of information about the modes excited in the sample, as the evanescent field components rapidly decay already at distances on the order of one wavelength away from the sample surface and only propagating plane waves, corresponding to the fundamental Bloch harmonic of the PhC dispersion within the light cone, are retained. This effectively represents a low-pass filter where information about the components in the angular spectrum with high spatial frequency is lost irrevocably (Equation (2.6)). Knowledge about the sub-wavelength near-field structure is however crucial for a plethora of nanophotonic applications, such as coupling to (quantum) emitters [131, 170], design of photonic integrated circuits [171, 172], sensing for biomedical and chemical applications [17, 173], and many more. Additionally, in the practical context of on-chip routing and confinement of light, it may be undesirable to work with modes that experience radiative losses. Non-radiative PhCs do not only require a different design of the in-coupling scheme (see Section 2.1.1), but also different ways of probing the fields within the lattice. While methods exist to, for example, measure the transmission through non-radiative PhC waveguides from the far field via gratings for in- and out-coupling [174–176], the most direct and high-fidelity approach to access the information encoded in the near field is achieved by actually probing the modes within this region.

2.3.1. EXPERIMENTAL NEAR-FIELD SETUP

near-field scanning optical microscopy (NSOM) is a microscopy technique for nanostructure investigation that makes use of a very small probe (often a sharp tip or a small aperture) scanning very closely above (within a few nanometers) the sample surface. This breaks the far-field resolution limit by exploiting the proximity of the probe to couple to evanescent waves. The experimental NSOM setup we use, developed and operated by our collaborators in the group of Kobus Kuipers at TU Delft [134, 177–179], is presented schematically in Figure 2.15. It offers unprecedented access to the information encoded within the near field of the structure, not only being able to map the spatial electric and magnetic near-field distributions and thereby provide access to higher order Bloch harmonics [134, 180, 181], but furthermore offering polarization- and phase-resolution at the nanoscale [131, 182–184]. In the following, we will outline the basic principles underlying the experimental implementation of these functionalities.

The PhC modes are excited with a tunable laser source, which is split into a *signal* and a *reference* branch by a polarizing beam splitter cube (PBS1). The signal beam is coupled into the PhC from the side of the chip, where a lensed fiber focuses it onto the entrance facet of a silicon ridge waveguide that extends over several millimeters and eventually couples into the PhC lattice (more details on the design in Section 2.1). A near-field probe is raster-scanned at close distance to the surface (typically in a plane about 20 nm above the PhC) and picks up the evanescent in-plane field components. The probe is manufactured from a pulled optical fiber that is first coated in aluminum, before creating a circular aperture via focused ion beam milling. The aperture has a typical diameter of ~ 100 nm (see inset of Figure 2.15)

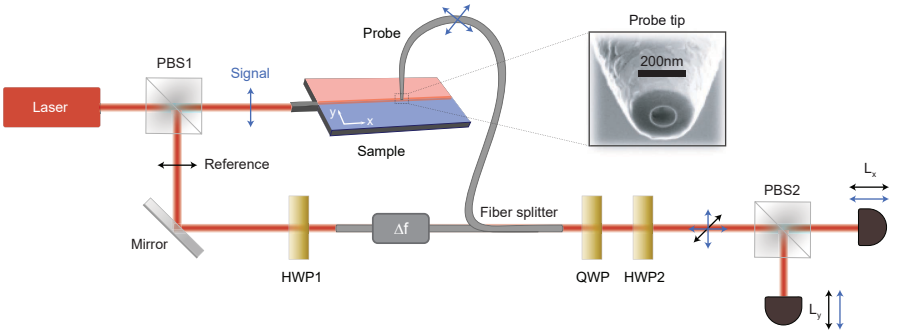

Figure 2.15: Experimental visualization of a topological edge state in a valley photonic crystal. Schematic of the near-field scanning optical microscope used for mapping the in-plane field distribution of photonic crystal modes. Heterodyne phase detection is performed by splitting the input beam into a *signal* and a *reference* branch. An aperture-based near-field probe (inset: scanning electron microscope image) collects part of the evanescent fields while scanning 20 nm above the sample surface and couples the collected light into a single-mode optical fiber. A pair of detectors together with various elements for polarization manipulation allow for simultaneous detection of both Cartesian in-plane field components, symbolized by arrows. See the main text for more details and abbreviations.

and is kept at a constant distance from the sample surface using a shear-force feedback mechanism [177]. The probe picks up the evanescent near-fields close to the sample surface, upon which they are transformed into modes that propagate within the optical fiber, constituting the collected signal. Connecting the fiber to a detector (e.g., a photodiode) then allows for reconstructing the magnitude of the signal at the respective probe position, and a full spatial map of the near-field magnitude may be asSEMbled pixel by pixel. Additional components in the analysis arm of the custom NSOM setup in Figure 2.15 are used to retrieve information about the nanoscale polarization distribution and phase of the signal, and to enhance the sensitivity of detection, as we will discuss in more detail next.

2.3.2. POLARIZATION RESOLUTION

Vectorial mapping of the collected near fields is achieved with polarizing elements in the reference and analysis arm of the setup [184]. This allows for the simultaneous detection of two orthogonal Cartesian polarization components with a pair of photodetectors L_x and L_y [178, 181]. Upon splitting by the first polarizing beam splitter cube (PBS1), the signal and reference light are orthogonally polarized. The first HWP is used to balance the intensity of the reference light on both detectors. The probe picks up the in-plane electric and magnetic field components of the sample's near field, constituting the photodiode signals [181]

$$L_x(\mathbf{r}) = \alpha_x E'_x(\mathbf{r}) + \beta_x H'_y(\mathbf{r}), \tag{2.13a}$$

$$L_y(\mathbf{r}) = \alpha_y E'_y(\mathbf{r}) + \beta_y H'_x(\mathbf{r}), \tag{2.13b}$$

where α_i, β_i $(i = x, y)$ are scalar complex quantities related to the sensitivity of the probe to the respective field components. Since distinguishing the magnetic

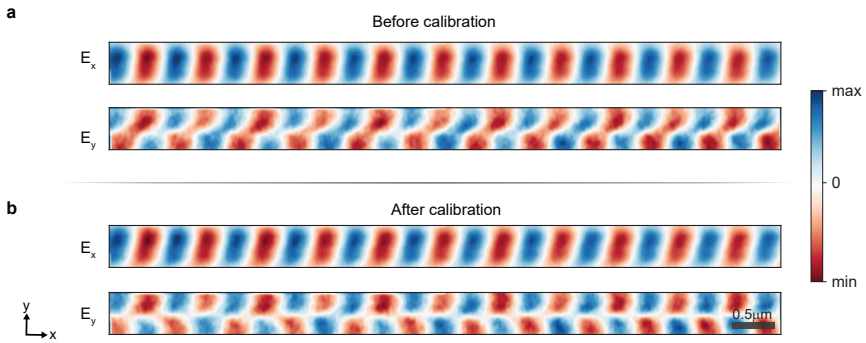

Figure 2.16: Near-field polarization calibration. a, Near-field in-plane electric field amplitude of the fundamental mode in a silicon ridge access waveguide at $\lambda = 1600\,\text{nm}$, as recorded by the detectors L_x and L_y (see Figure 2.15). The improper alignment of the polarization optics in the analysis arm of the setup results in the mixing of the Cartesian in-plane field components, especially visible in the merging lobes of E_y. **b,** Same as **a** after calibration of the polarization optics, resulting in a proper separation of E_x and E_y, inferred from the mode symmetries.

field amplitude is not of relevance in the measurements we perform, we express Equations (2.13) in terms of an effective in-plane electric field [185]

$$\mathbf{E}_{\parallel} = \hat{\mathbf{x}} E_x + \hat{\mathbf{y}} E_y \,, \tag{2.14}$$

with the Cartesian unit vectors $\hat{\mathbf{x}}$, $\hat{\mathbf{y}}$. This constitutes a fair approach since the spatial symmetries of E'_x (E'_y) and H'_y (H'_x) are generally identical, moreover, the contributions of in-plane magnetic fields to the confined modes in the PhCs we study are expected to be miniscule due to their TE-like nature (see Section 1.4). The QWP and second HWP are used to separate the complex in-plane field components E_x and E_y picked up by the probe onto the photodetectors L_x and L_y, respectively. This procedure requires calibration of the polarizing elements for a proper mapping of the fields to the corresponding detectors. The calibration can be performed by imaging fields above a structure with a priori knowledge of the field distribution (e.g., from simulations), such as for the suspended single-mode entrance waveguides or for well-known PhC waveguide modes (see Figure 2.16), where usually HWP2 is rotated until a satisfactory correspondence between measurement and prediction is achieved.

2.3.3. PHASE RESOLUTION

The phase-resolution of the employed NSOM relies on the detection of both quadratures of light in a heterodyne detection scheme. The light of the reference arm is shifted in frequency by about ~ 40kHz with a pair of acousto-optical modulators. The electric fields in the signal (E_{sig}) and reference (E_{ref}) arm under continuous wave excitation can be written as [177]

$$E_{\text{sig}}(x,y,t) = A_{\text{sig}}(x,y)\, e^{i\left[\omega t + \phi_{\text{sig}}(x,y)\right]} \,, \tag{2.15a}$$

$$E_{\text{ref}}(t) = A_{\text{ref}}\, e^{i\left[(\omega+\Delta\omega)\, t + \phi_{\text{ref}}\right]} \,, \tag{2.15b}$$

where A and ϕ denote the respective amplitude and phase. The two fields are recombined in a fiber splitter and, after being polarization-matched with HWP1, interfere to produce a signal on a detector that incorporates the relative phase difference $\phi(x,y) = \phi_{\text{ref}} - \phi_{\text{sig}}(x,y)$ between the two

$$I_{\text{det}}(x,y,t) \propto A_{\text{sig}}(x,y) A_{\text{ref}} \cos\left[\phi(x,y)\right]. \tag{2.16}$$

Apart from yielding access to phase information, the heterodyne detection scheme also largely improves experimental sensitivity, since the detected signal (Equation (2.16)) entails the amplitude of the reference beam. This amplitude can be made orders of magnitude higher than that of the probed fields, strongly improving the signal-to-noise ratio. The phase resolution obtained via this method is an invaluable tool to examine the properties of the topological PhC waveguides studied in this work, giving us access to the full complex near-field mode profiles in real space as well as the information encoded in reciprocal space.

2.3.4. DISPERSION RECONSTRUCTION

Through the phase information obtained via heterodyne detection, we can carry out a Fourier space analysis of the recorded near fields. This gives a powerful tool at hand to perform filtering, separation of individual Bloch harmonics, and reconstruction of the photonic dispersion including the visualization of higher order Bloch harmonics. A 2D spatial Fourier transform $\mathcal{F}(k_x, k_y)$ of the measured complex near-field amplitude yields the intensity distribution in reciprocal space via [134]

$$I(k_x, k_y) = \left(|\mathcal{F}(E_x(x,y))|^2 + |\mathcal{F}(E_y(x,y))|^2\right). \tag{2.17}$$

An example of the procedure for a travelling waveguide mode in a topological PhC at $\lambda = 1600\,\text{nm}$ is shown in Figure 2.17a,b. Operating in reciprocal space offers the possibility of Fourier filtering of undesired signal components, like omitting the fundamental Bloch components inside the light cone associated with radiative far fields (white circle in Figure 2.17b). Moreover, it provides the capacity to independently analyze Fourier components with positive and negative phase velocities, isolate individual Bloch components in reciprocal space, and retrieve the corresponding real-space field distributions by applying an inverse Fourier transform after filtering.

To obtain the photonic band structure, we iterate the near-field scans and corresponding Fourier analysis for a range of frequencies and, for each, integrate $I(k_x, k_y)$ over k_y. This method produces a line-cut of the photonic dispersion at each corresponding laser frequency, which is then used to reconstruct band diagrams similar to Figure 2.17c. The high spatial resolution, coupled with the enhanced signal-to-noise ratio in the heterodyne detection scheme (typically well above $\sim 50\,\text{dB}$), enables the resolution of higher-order Bloch harmonics over multiple Brillouin zones. The signal contrast of a given mode within the fundamental Brillouin zone may further be augmented in post-processing by band-folding of its higher-order Bloch harmonics. The gathered data can be used to isolate components with positive and negative group velocities (as derived from the slope of the reconstructed

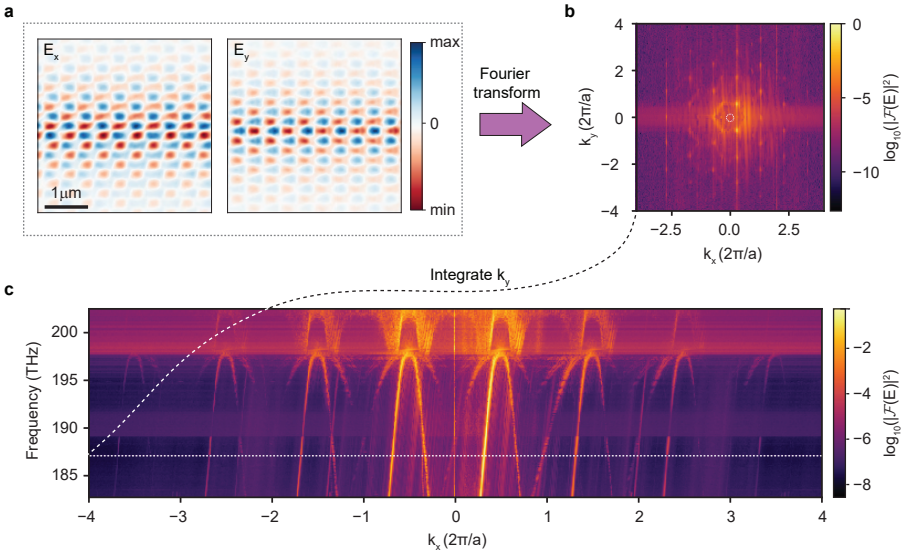

Figure 2.17: Reconstructing the photonic dispersion. a, Spatially resolved near-field amplitude of a topological photonic crystal waveguide (see Chapter 3) for both Cartesian in-plane components of the electric field at a laser wavelength of $\lambda = 1600\,\text{nm}$. **b,** Intensity distribution in reciprocal space as retrieved via a two-dimensional Fourier transform of the real-space amplitude distribution in **a** (Equation (2.17)), in units of the reciprocal lattice vector ($a = 503\,\text{nm}$). The underlying honeycomb real-space lattice symmetry manifests in the symmetry of the high-intensity points in Fourier space. **c,** Integrating the Fourier image in **b** along k_y yields a single isofrequency contour of the photonic dispersion. Reiterating the procedure for a range of laser frequencies allows for a full reconstruction of the photonic bands, where the photonic crystal modes appear as bright lines of varying slopes, and several higher order Bloch harmonics can be resolved. The Fourier intensity for each excitation frequency is normalized to the overall maximum value.

bands) [134, 186, 187], and visualize them in real space or use the relative weight of the harmonics to obtain a direct local measure of backscattering, as detailed in Chapter 3.

To conclude, we have elaborated on the methods that enable the study of the topological PhC membranes presented in the following chapters. The fabrication procedure is relevant for all the samples we examine, with design specifics that are tailored toward the experimental methods employed in each case. In Chapter 3, the non-radiative nature of the PhC waveguides we study calls for access waveguides for in-coupling from the side of the chip and renders probing with NSOM techniques especially appealing, allowing for profound insights into the modes' near-field structure and a quantitative analysis of topological robustness. Chapters 4 and 5, on the other hand, describe experiments on radiative topological PhC platforms, which we conveniently examine with our far-field Fourier-spectroscopy setup to gain insights into the photonic band structure as well as spatially and angularly resolved mode profiles.

3

ROBUSTNESS OF TOPOLOGICAL EDGE STATES AGAINST ENGINEERED DEFECTS

Topological on-chip photonics based on tailored photonic crystals (PhCs) that emulate the quantum valley-Hall effect has recently gained widespread interest owing to its claim of protected helical transport of classical and quantum information. Here, we put this promise to the test by conducting a direct quantitative evaluation of topological photonic edge state transport at telecom wavelengths in the presence of engineered defects, using phase-resolved near-field optical microscopy. By experimentally visualizing the detailed sub-wavelength structure of these modes propagating along the interface between two topologically non-trivial mirror-symmetric lattices we are able to map their dispersion relation and differentiate between the contributions of several higher-order Bloch harmonics. Selective probing of forward- and backward-propagating modes based on their phase velocities allows for direct quantification of topological robustness. Studying near-field propagation in controlled defects allows us to extract upper limits of topological protection in on-chip photonic systems in comparison with conventional PhC waveguides. We find that backscattering at symmetry-protected corners is two orders of magnitude smaller than for conventional PhC waveguides with similar geometry. This direct experimental quantification of topological robustness comprises a crucial step toward the application of topologically protected guiding in integrated photonics.

This chapter is based on Arora, S.,* Bauer, T.,* Barczyk, R.,* Verhagen, E., and Kuipers, L. *Light: Science & Applications* **10**, 9 (2021)

*These authors contributed equally. R.B. contributed to the design and fabrication of the devices, development of the analytical model used for analysis, interpretation of the results, and writing of the manuscript.

3.1. INTRODUCTION

The emergence of photonic topological insulators (PTIs) has led to promising theoretical and experimental approaches for topology-protected light-matter interactions [188] and the integration of robust quantum devices [189]. Topologically protected photonic edge states offer robust energy transport with unprecedented guiding capabilities, providing a cornerstone for the efficient distribution of classical and quantum information in dense networks [190]. Usually, realizing nanophotonic systems with low backscattering at sharp bends is a great design challenge owing to the need to strike a balance between high bandwidth, low reflectance, and modest footprint. The promise of topologically protected photonic states supporting unhindered transport around defects and sharp corners without the need for optimization is thus especially interesting for on-chip applications. In addition to Chern-type PTIs that break time-reversal symmetry [190–193], a time-reversal invariant realization of lossless optical transport was introduced theoretically on a dielectric photonic crystal (PhC) platform at telecom frequencies [194, 195]. Although the existence of these states has been evidenced in the linear [129, 196] and nonlinear regimes [197], and topological robustness has been inferred by high transmission [174, 198], quantifying the defining quality of scattering-free propagation has remained elusive. Potential interference effects and out-of-plane scattering losses at local disorder render this quantification challenging.

Here, we report a rigorous robustness evaluation of valley photonic edge states at telecom wavelengths in the presence of engineered defects that respect the lattice symmetries. Local investigation of the states' transport properties via phase-resolved near-field microscopy provides direct insight into topological protection through the distinction between forward- and backward propagating waves. We find that the examined edge states are two orders of magnitude more robust than modes in conventional waveguides for comparable geometries. This deduction of significantly suppressed back-reflection provides an essential step towards implementing topological guiding in on-chip photonic networks.

3.2. RESULTS AND DISCUSSION

3.2.1. TOPOLOGICAL PHOTONIC CRYSTAL DESIGN AND CHARACTERIZATION

We realize valley-Hall PhCs (VPCs) which possess a valley degree of freedom that is linked to spatial symmetry-breaking within the lattice [174, 199–201] (see also Section 1.5). Similar to the valley-selective polarization caused by spin-orbit coupling in transition metal dichalcogenides [202], these PhC lattices exhibit a non-vanishing Berry curvature at the K and K' points of the Brillouin zone [135]. In contrast to the quantum spin-Hall effect emulating PhCs that support edge states at the Γ point, the edge states in the following VPCs occur below the light line and thus feature negligible radiative losses. As each valley is associated with an intrinsic magnetic moment, the valley Chern invariant $C_{K,K'} = \pm\frac{1}{2}$ signifies a pseudospin [203], rendering the bulk band structure topologically non-trivial. A domain wall formed by two parity-inverted copies of the PhC lattice results in two degenerate and robust

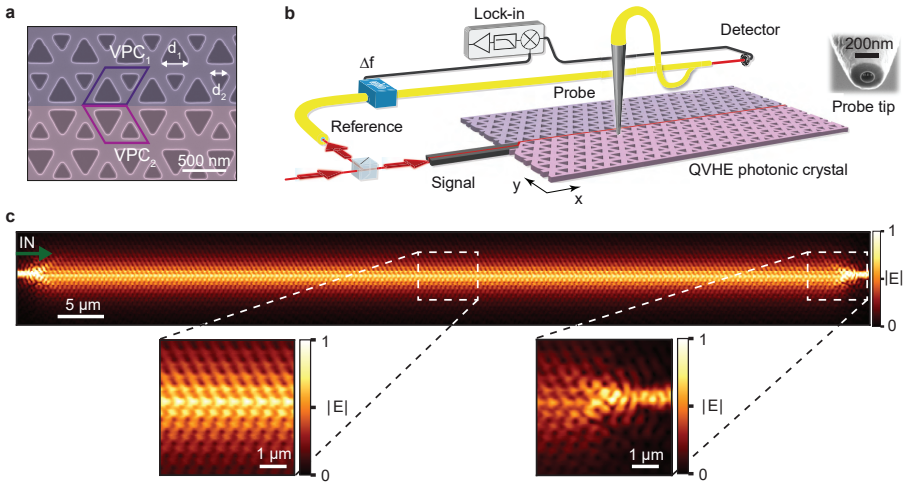

Figure 3.1: Experimental visualization of a topological edge state in a valley photonic crystal. a, SEM of the fabricated structure with two pseudo-colored regions depicting the two lattices VPC_1 and VPC_2 with opposite valley Chern invariants. The unit cell with lattice constant $a = 503\,\text{nm}$ consists of equilateral triangular holes of side lengths $d_1 = 0.7a$ and $d_2 = 0.45a$. Scale bar: 500 nm. **b,** Schematic of the near-field scanning optical microscope used to map the in-plane field distribution of the topologically non-trivial PhC edge mode. To facilitate heterodyne phase detection, the input beam is split into two branches, labeled *signal* and *reference*. An aperture-based near-field probe collects part of the evanescent tail of the in-plane field components while scanning over the crystal at a height of 20 nm and couples the collected light to a single-mode optical fiber. Inset: SEM image of the probe. See Section 2.3.1 and Figure 2.15 for more details on the setup. **c,** Measured normalized amplitude of the in-plane electric field at a laser excitation wavelength of $\lambda = 1600\,\text{nm}$ over the extent of 165 unit cells, with the scale bar corresponding to $5\,\mu\text{m}$. Light is launched from a feed waveguide on the left side of the crystal, with the direction indicated by the green arrow. Left inset: zoomed-in view of the detected field amplitude pattern along the domain wall. Right inset: zoomed-in view of the region around the end facet of the PhC.

edge-state eigenmodes confined to the interface that linearly traverse the photonic bandgap (PBG), each with a unique pseudospin [204]. As long as the lattice symmetry is preserved and no inter-valley scattering occurs to flip the pseudospin, these edge states are predicted to be immune to reflection from local disorder along the domain wall [135, 205].

To determine the experimentally achievable robustness against backscattering, we fabricate a VPC working at telecom wavelengths on a silicon-on-insulator platform (see Section 2.1 for fabrication details), following the design of Shalaev et al. [174] (see Figure 3.1a and Section 3.4.2). Light is coupled into the PhC structure in the $+x$ direction from an access waveguide. This system supports edge modes of opposite group velocity $\pm v_g$ (see also Section 3.5.1 of the appendix) propagating along the domain wall between two parity-transformed lattices (VPC_1 and VPC_2). We visualize the spatial wavefunction of the mode with a phase-sensitive near-field scanning optical microscope (NSOM, Figure 3.1b), described in detail in Section 2.3 [206, 207]. Figure 3.1c shows the measured two-dimensional in-plane field amplitude map at a wavelength of $\lambda = 1600\,\text{nm}$, which lies well within the bulk

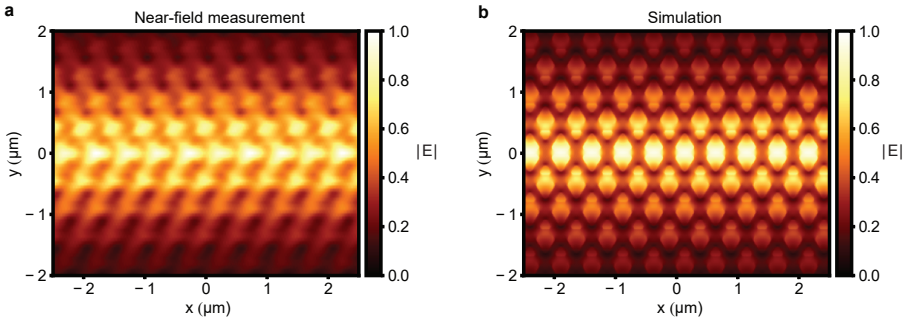

Figure 3.2: Measured near-field profile versus simulation. Comparison between **a,** the experimentally retrieved near-field electric field amplitude map for $\lambda = 1600\,\text{nm}$ ($f = 187.4\,\text{THz}$) and **b,** the numerically calculated in-plane electric field distribution of the edge mode at $k_x/(2\pi/a) = 0.32$ ($f = 187.0\,\text{THz}$). See Section 3.4.1 for more details on simulations.

3

bandgap and inside the linear regime of the edge mode for the particular fabricated device (cf. Figure 3.3). The detected transverse-electric (TE)-like field pattern that is confined to the interface of VPC_1 and VPC_2 extends laterally over roughly five unit cells, revealing an intricate sub-wavelength mode structure. At the locations of the access and exit waveguides, the influence of the broken lattice symmetry and the adjacent feed waveguide becomes evident in distorted field patterns (right inset of Figure 3.1c). Away from the end facets, however, the measured periodic near-field patterns displays a highly uniform amplitude across the whole extent of the lattice (left inset of Figure 3.1c), with good correspondence to numerical calculations (Figure 3.2). Deviations may likely be attributed to a non-ideal (asymmetric) probe tip shape that leads to different coupling efficiencies of the two in-plane field components (see Section 2.3.2 for details on the polarization resolution) and different pick-up efficiencies of forward and backward propagating modes.

The heterodyne detection configuration of the employed NSOM gives access to the complex in-plane optical fields of the edge mode [208] (see Section 2.3.3 for details on the phase resolution). As a direct consequence of Bloch's theorem, the two-dimensional spatial Fourier transform $\mathcal{F}(k_x, k_y)$ of the measured field amplitude allows for separate analysis of Fourier components with positive and negative phase velocities. An example for a Fourier map at $\lambda = 1600\,\text{nm}$ is displayed in Figure 3.3a. By repeating the near-field scans and corresponding Fourier analysis for $\lambda = [1480\,\text{nm} - 1600\,\text{nm}]$ and integrating $\mathcal{F}(k_x, k_y)$ over k_y, we extract the mode dispersion shown in Figure 3.3b (see Section 2.3.4 for a detailed description). We resolve at least six parallel lines due to the excellent signal-to-background ratio (S/B) of $\sim 56\,\text{dB}$. The numerically simulated edge and bulk bands show excellent overlap with the experimentally measured dispersion, as seen in the overlaid enlarged view presented in Figure 3.3c. The achieved spatial resolution, combined with the high S/B, enables us to resolve higher-order Bloch harmonics over multiple Brillouin zones. The lines with a positive slope correspond to a single forward propagating mode with group velocity $v_g = c/6$. Closer inspection reveals negatively sloped lines corresponding to a single backward propagating mode with group velocity $-v_g$

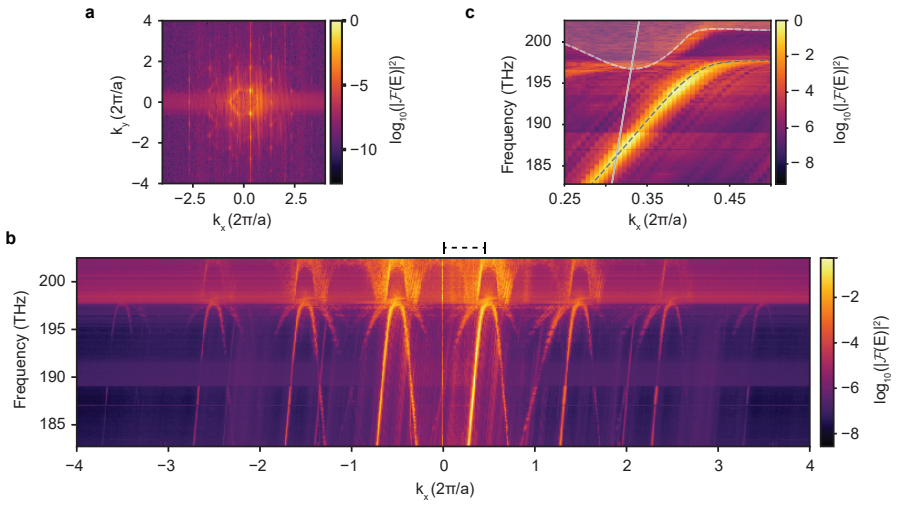

Figure 3.3: Momentum space of the VPC edge state. **a,** Two-dimensional Fourier transform of the real-space amplitude distribution of the VPC mode. High-intensity points are periodically separated by the reciprocal lattice vector $2\pi/a$ in the direction of propagation k_x along the edge and by $4\pi/\sqrt{3}/a$ in the transverse direction k_y, representing the bulk reciprocal symmetry. **b,** Experimentally retrieved dispersion diagram. Bright lines of positive slope indicate positive group velocity (forward propagating modes), while lines with negative slope indicate a negative group velocity (backward propagating modes). Consecutive Bloch harmonics are separated by the size of a single Brillouin zone ($2\pi/a$). Frequencies above 197.5 THz correspond to bulk bands. The Fourier intensity for each excitation frequency is normalized to the overall maximum value. In addition to the dominant modes in the forward and backward directions, lines with half and a third of the dispersion slope appear. These are attributed to a nonlinear interaction with the scanning near-field probe (see Section 3.5.2). **c,** A close-up of the experimentally retrieved dispersion diagram limited to the first Brillouin zone, denoted by black dashed brackets in **b**. The black dashed lines indicate the numerically simulated values for the edge state (see Section 3.4.1 and Section 3.5.1 for details). The solid gray line denotes the light line and the gray dashed lines with grayed-out regions indicate the onset of the bulk bands.

[186, 187]. This separation of forward- and backward propagating Bloch modes allows to locally probe backscattering along the domain wall.

Using this local phase and amplitude information, we probe a straight edge domain wall, as shown in Figure 3.1c. We obtain the quantities F and B representing the forward and backward propagating energy, respectively, through integration of their corresponding Fourier intensities. The ratio $\eta_e = B/F \approx 0.03$ unambiguously yields the conversion from forward to backward propagating modes, a result of scattering events occurring within the VPC as well as at and beyond its end facet. Thus, η_e includes coupling of the forward to backward propagating modes away from the topologically protected regime. This initial examination of the straight edge shows that backscattering is dominated by contributions of the end facet, calling for a more intricate analysis of topological protection within the PhC.

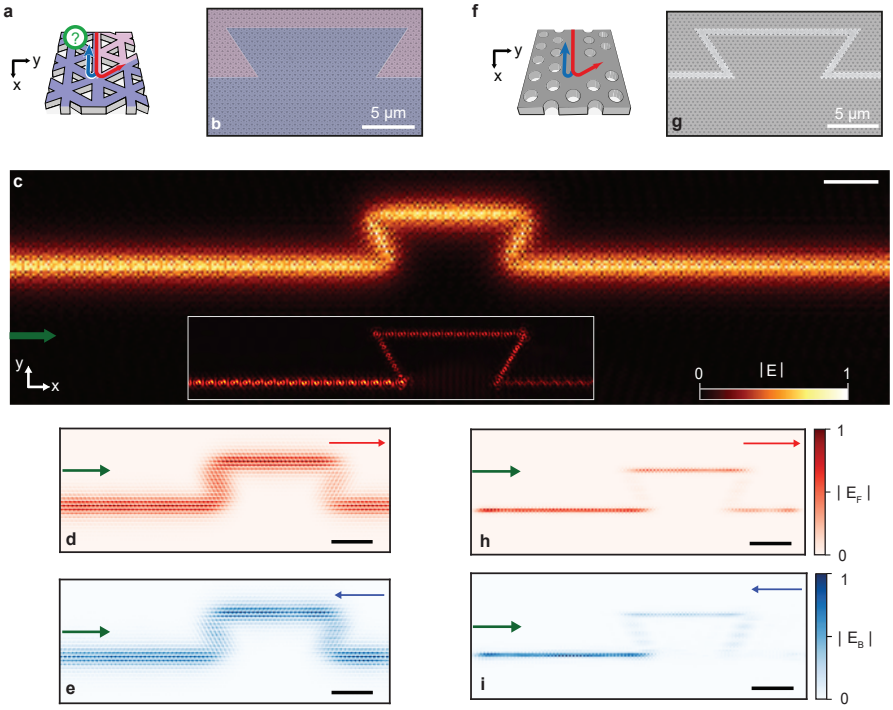

Figure 3.4: Directional transport along defects. a, Schematic of the probed 120° corner for the topologically non-trivial VPC waveguide. **b,** Top-view SEM image of the fabricated Ω-shaped defect. We record two-dimensional real-space amplitude maps showing the **c,** full mode amplitude distribution (inset: $W1$ waveguide), **d,** forward propagating mode amplitude only, and **e,** backward propagating mode amplitude only. The amplitude maps are normalized to their respective maximum. **f,** Schematic of transmission along a 120° bend for a topologically trivial $W1$ waveguide, where **g** shows a top-view SEM image of the device and the two-dimensional amplitude maps of the filtered forward- and backward propagating modes are shown in **h** and **i**, respectively. The direction of in-coupling is indicated by green arrows. All scale bars correspond to 5 μm.

3.2.2. DIRECT QUANTIFICATION OF TOPOLOGICAL PROTECTION

To quantify protection without the aforementioned contributions, we introduce a trapezoidal (Ω-shaped) structure along the domain wall, comprising four sharp corners (Figure 3.4). This structure is expected to be topologically protected, as $n \times 120°$ bends respect the underlying C_3 lattice symmetry. Reflections characterized by energy coupled between the degenerate forward (F) and backward (B) propagating modes are indicated by red and blue arrows, respectively, in schematic Figure 3.4a, with the fabricated structure displayed in Figure 3.4b. Figure 3.4c shows a map of the measured in-plane electric field amplitude of the VPC edge mode. We perform Fourier filtering in k-space based on the sign of the phase velocity before applying an inverse Fourier transform to separate the real-space profiles of forward and backward propagating edge modes. Figure 3.4d qualitatively demonstrates that the forward propagating mode exhibits a near-unity transmission through the

bend. The constant amplitude of the backward propagating mode (Figure 3.4e) also indicates near-unity transmission. This establishes that we may attribute the coupling of the forward and backward propagating modes to the termination of the exit PhC waveguide. In other words, light is almost perfectly guided around the Ω-shaped domain wall, with the transmission being independent of the presence of the defect itself.

This observation is quantified by deriving mode energy ratios from the locally measured amplitudes. We filter the Fourier intensity distribution to obtain the forward and backward propagating mode energy density before (F_1, B_1) and after (F_2, B_2) the Ω-bend (see Figure 3.5a). Locally probing the Fourier filtered based on group velocity allows for This local probing of forward and backward propagating modes within the PhC lattice allows to get rid of the frequency-dependent in-coupling efficiency and to unambiguously determine the transmission through the defect $\eta_T = F_2/F_1$. The results for the linear part of the dispersion are shown in Figure 3.5b, yielding a mean value of $\langle \eta_T \rangle = 0.92$ for the chosen frequency range of ~ 4 THz. In addition, Figure 3.5c shows the mode energy ratios calculated for the regions before ($\eta_{R1} = B_1/F_1$) and after ($\eta_{R2} = B_2/F_2$) the defect in the same spectral regime. We notice that the spectra of η_{R1} and η_{R2} are almost indistinguishable. This strongly suggests that, compared to the end facet, the contribution of the four symmetry-protected corners to the backscattered energy is insignificant.

Although expected, one can appreciate that the remarkably large transmission over the mode's full frequency range is reasonably atypical in comparison with a topologically trivial standard $W1$ PhC waveguide (see Section 3.4.2 for details on the geometry) [135, 198, 209]. We introduce a similar trapezoidal structure in this trivial PhC waveguide (Figure 3.4f,g). It is worth mentioning that the fabricated $W1$ waveguide corners are not optimized for unity transmission at any given frequency [210]. In stark contrast to the VPCs edge state, the $W1$ mode (Figure 3.4c, inset) experiences significant losses across the defect. The mode intensity displays a significant drop-off after each bend, both for the forward and for the backward propagating fields (Figure 3.4h,i), and the mode profile is clearly affected by the presence of the corners. Moreover, the normalized amplitude map of the backward propagating mode in Figure 3.4i demonstrates that the dominant reflections already occur at the first 120° corner. The mode energy here is converted to a back-reflected wave and additionally experiences out-of-plane scattering loss. The value of η_T measured through the Ω-structure in the $W1$ PhC, shown in Figure 3.5d, is on average one-third of the value η_T observed in the VPC. Figure 3.5e confirms the strong reflection from the first corner, with η_{R1} being four times higher than η_{R2} for certain frequencies in the $W1$ PhC waveguide.

3.2.3. QUANTIFICATION OF CORNER REFLECTIVITY AND LOSS

In addition to the back-reflection from individual corners, the direct evaluation of the Ω-shaped defect is affected by other aspects: out-of-plane scattering losses, scattering at the end facet, and interference owing to multiple reflections along the domain wall. We notice rapid oscillations in the spectra of $\eta_{R1,2}$ before and after the defect (Figure 3.5c,e). To disentangle the backscattering contributions from

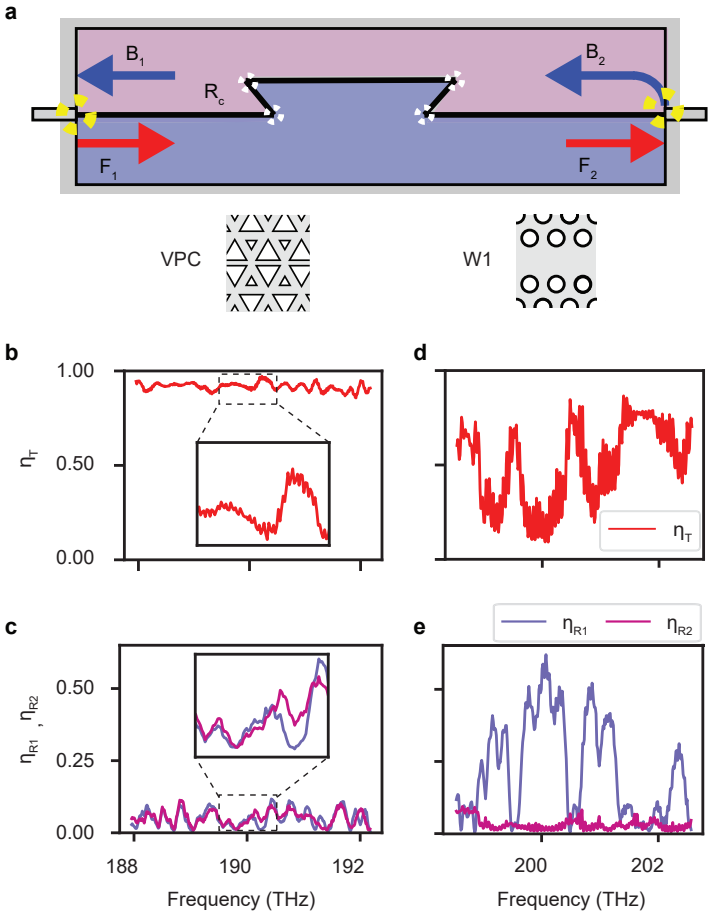

Figure 3.5: Degree of topological protection. a, Schematic of the mode contributions in an Ω-shaped defect VPC waveguide. Red arrows indicate the forward propagating modes, with F_1 and F_2 denoting the modes before and after the defect, respectively. Blue arrows indicate backward propagating modes before (B_1) and after (B_2) the defect. Yellow dashed circles show the locations of in- and out-coupling facets. White dashed circles indicate the four 120° corners. **b,** Plot of the transmission coefficient η_T, with the inset demonstrating transmission over a small region (189.5 THz – 190.5 THz). **c,** Backward-to-forward energy ratio before (η_{R1}) and after (η_{R2}) the Ω-shaped defect in the VPC domain wall. The inset shows how the backward propagating energies before and after the defect are almost indistinguishable over the considered frequency range. **d,** and **e,** show the corresponding plots of **b** and **c**, respectively, for the $W1$ waveguide.

the aforementioned effects, we consider the complex scalar mode amplitude of the Bloch wave at different points along the domain wall. With the assumption of a perfectly mirror-symmetric device, we treat the defect as a single effective interface in a transfer-matrix model (TMM), using η_R and η_T as input parameters. As a quantitative measure of backscattering, we estimate the mean reflectance $\bar{R}_c$ and loss $\bar{A}_c$ (predominantly out-of-plane scattering) of the full defect, as well as the

respective contributions of individual corners in the waveguide (R_c^{single}, A_c^{single}).

We start from Bloch's theorem for a photonic crystal domain wall (or waveguide) with periodicity a along the x direction, resulting in the Bloch state

$$\mathbf{E}_{k_x}(\mathbf{r}) = e^{\imath k_x x} \cdot \mathbf{u}_{k_x}(\mathbf{r}), \quad \text{with} \mathbf{u}_{k_x}(\mathbf{r} + a\hat{\mathbf{x}}) = \mathbf{u}_{k_x}(\mathbf{r}), \tag{3.1}$$

where k_x is the Bloch wavevector along the mode's propagation direction (unit vector $\hat{\mathbf{x}}$) and $\mathbf{u}_{k_x}(\mathbf{r})$ represents its full spatial field distribution. To compare the mode at different positions along the domain wall, we separate a complex scaling amplitude a_k from the mode's periodic field distribution, resulting in

$$\mathbf{E}_{k_x}(\mathbf{r}) = a_k e^{\imath k_x x} \cdot \mathbf{u'}_{k_x}(\mathbf{r}), \tag{3.2}$$

with $\mathbf{u'}_{k_x}$ a fixed function, independent of the unit cell or time at which the mode field is evaluated. The full spatial information in each unit cell is thus effectively reduced to the scalar complex amplitude value a_k. The complex amplitude together with the reciprocal nature of the employed photonic crystals enable us to describe backscattering sites along the domain wall as interfaces with complex amplitude reflection and transmission coefficients r_c and t_c, respectively. Furthermore, we introduce a loss channel A_c, incorporating out-of-plane scattering, via

$$R_c + T_c = 1 - A_c\,, \tag{3.3}$$

where $R_c = |r_c|^2$, $T_c = |t_c|^2$.

Without loss of generality, we consider the forward and backward propagating field amplitudes f_1, f_2 and b_1, b_2 to denote the value of a_k at specific positions on the sample as shown in Figure 3.6a, and get

$$b_1 = r_c f_1\, e^{i2\delta} + t_c b_2\, e^{i\delta} \tag{3.4a}$$

$$f_2 = t_c f_1\, e^{i\delta} + r_c b_2\,, \tag{3.4b}$$

with the propagation phase $\delta = k \cdot d$ given by the wavenumber k and distance d between the two detection points 1 and 2, which are placed immediately after an interface. Equations (3.4a) and (3.4b) can be cast into the compact form

$$\begin{pmatrix} f_1 \\ b_1 \end{pmatrix} = \mathbf{M}_c \begin{pmatrix} f_2 \\ b_2 \end{pmatrix}, \tag{3.5}$$

where

$$\mathbf{M}_c = \frac{1}{t_c} \begin{pmatrix} e^{-i\delta} & 0 \\ 0 & e^{i\delta} \end{pmatrix} \begin{pmatrix} 1 & -r_c \\ r_c & t_c^2 - r_c^2 \end{pmatrix} \tag{3.6}$$

is the transfer matrix describing light propagation from position 1 to 2 in the multilayer stack. The propagation through a series of N layers can then be written as a single matrix $\tilde{M}$, given by

$$\tilde{\mathbf{M}} = \prod_{i=1}^{N} \mathbf{M}_i\,. \tag{3.7}$$

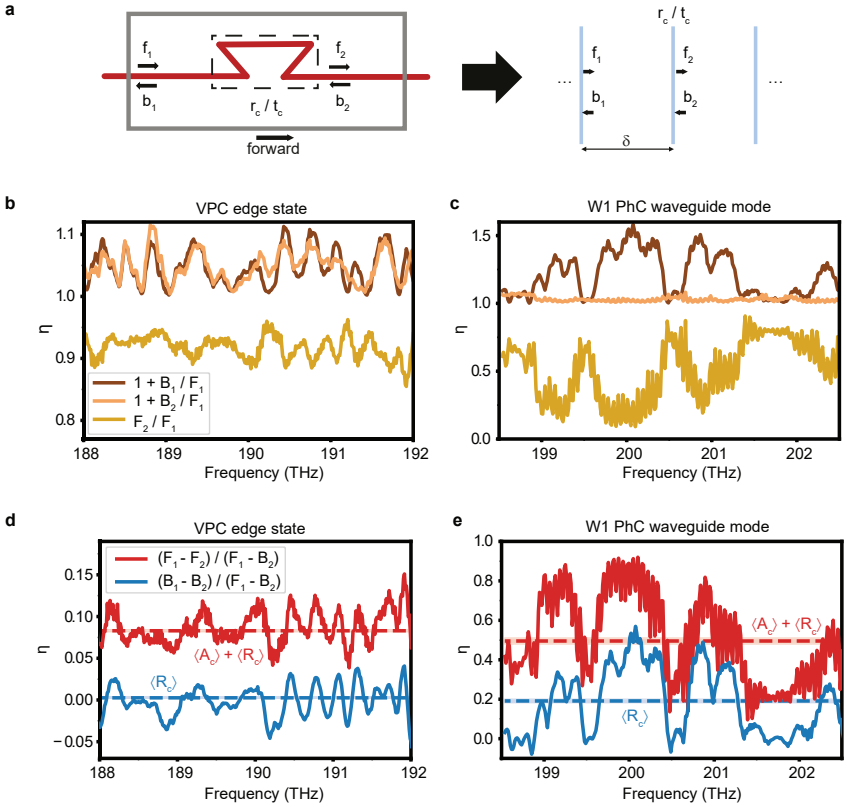

Figure 3.6: Transfer matrix model. a, Sketch of the experimentally investigated VPC with an Ω-shaped domain wall defect, as well as its representation within a transfer matrix model. The effect of the Ω-shaped defect onto the field amplitudes is approximated by complex reflection and transmission coefficients r_c and t_c, and the distance between the detection points is associated with a propagation phase δ. **b,** Experimentally retrieved energy of the forward (F_2) and backward (B_1, B_2) propagating VPC edge states before and after the Ω-shaped defect, normalized to F_1. The backward mode intensities are shifted by 1 for better visibility. **c,** Same as **b**, for the $W1$ waveguide. **d,** Evaluation of Equations (3.9a) and (3.9b) for the VPC edge state data, where $\langle R_c \rangle$ and $\langle R_c \rangle + \langle A_c \rangle$ according to Equations (3.10a) and (3.10b) are indicated as red and blue dashed lines, respectively. The shaded region around the lines corresponds to the standard deviation of the extracted mean values. **e,** Same as **d**, for the $W1$ waveguide.

Here, $\mathbf{M}_i$ are the transfer matrices of the individual layers, with their respective distances and reflection/transmission coefficients.

It is straightforward to relate any field amplitudes in a TMM to each other by appropriate transfer matrix multiplications. The experimentally determined energy densities on which we base our analysis are given by $F_n = |f_n|^2$ and $B_n = |b_n|^2$ ($n = 1, 2$) in Figure 3.6b,c, and derived from the same data as Figure 3.5b-e. If we want to achieve a full overlap of these energy densities with predictions from the TMM model, we not only need to take into account the four 120° corners of the tailored topologically protected defect, but additionally all scattering sites after the defect. These include scattering at the transition from the VPC domain wall

to an intermediate PhC waveguide, the subsequent transition to a silicon ridge waveguide, and scattering at potential fabrication defects. Since these additional interfaces are not protected by the mirror symmetry of the VPC lattice, it is expected that their reflection coefficients dominate the entire system.

3.2.4. EFFECTIVE CORNER REFLECTIVITY

Our aim is to arrive at a relation between the measured energy densities before and after the defect, and the intensity reflection coefficient R_c and loss A_c. If we, in fair approximation, assume our devices to possess mirror symmetry (as by design), reciprocity dictates equal coefficients for forward and backward propagation through the full Ω-shaped defect. We can thus combine the four individual corners into a single effective interface with complex amplitude reflection and transmission coefficients r_c and t_c (see Figure 3.6a). We divide Equations (3.4a) and (3.4b) by f_1 and take the absolute square to obtain

$$\begin{aligned}\frac{B_1}{F_1} &= R_c + \frac{B_2}{F_1}\,T_c + \left(\sqrt{R_c}e^{-i\theta_{r_c}}\,\sqrt{T_c}e^{i\theta_{t_c}}\,\sqrt{\frac{B_2}{F_1}}e^{i\theta_{b_2}}e^{-i\theta_{f_1}} + c.c.\right)\\ &= R_c + \frac{B_2}{F_1}\,T_c + 2\sqrt{R_c\,T_c\,B_2\,F_1}\cos(\theta_c-\theta) \qquad (3.8a)\\ \frac{F_2}{F_1} &= T_c + \frac{B_2}{F_1}\,R_c + 2\sqrt{R_c\,T_c\,\frac{B_2}{F_1}}\;\cos(\theta_c+\theta)\,. \qquad (3.8b)\end{aligned}$$

Here, *c.c.* denotes the complex conjugate, and we express complex quantities in their polar form ($z=\sqrt{Z}e^{i\theta_z}$), with the phase differences $\theta_c=\theta_{r_c}-\theta_{t_c}$ and $\theta=\theta_{b_2}-\theta_{f_1}$. Using Equation (3.3), we cast Equations (3.8a) and (3.8b) into the form

$$\begin{aligned}\frac{B_1-B_2}{F_1-B_2} &= R_c - \frac{A_cB_2-2\sqrt{R_c(1-R_c)F_1B_2}}{F_1-B_2}\cos(\theta_c-\theta) \qquad (3.9a)\\ \frac{F_1-F_2}{F_1-B_2} &= R_c + \frac{A_cF_1-2\sqrt{R_c(1-R_c)F_1B_2}}{F_1-B_2}\cos(\theta_c+\theta) \qquad (3.9b)\end{aligned}$$

Equations (3.9a) and (3.9b) represent the central result of the TMM analysis, and the corresponding data is presented in Figure 3.6d,e.

Due to the expected strong influence of scattering events from outside the topological photonic crystal, as seen by the strong correlation between the signals B_1/F_1 and B_2/F_1 in Figure 3.6b, we utilize an effective averaging approach. Such an approach is based on the linear slope of the VPC edge state dispersion. We can then disentangle the reflection at the tailored Ω-shaped defect from any subsequent backscattering events by averaging over a frequency range where the interference effects between the latter lead to cosine-like intensity modulations with multiple full periods. Both θ_c and θ in Equations (3.9a) and (3.9b) are oscillatory functions of frequency since they incorporate the propagation phases (see Equations (3.4a) and (3.4b)). Therefore, by applying a frequency average over the experimental range of ~ 4 THz (denoted by $\langle\cdot\rangle$) to Equations (3.9a) and (3.9b), we average out the cosine

modulation and solve for the mean effective defect reflectivity and loss

$$\langle R_c \rangle = \frac{(\overline{B_1 - B_2})\overline{F_1} - (\overline{F_1 - F_2})\overline{B_2}}{\overline{F_1} + \overline{B_2}} \tag{3.10a}$$

$$\langle A_c \rangle = \frac{(\overline{F_1 - F_2}) - (\overline{B_1 - B_2})}{\overline{F_1} - \overline{B_2}}, \tag{3.10b}$$

where we defined the operator

$$\bar{\cdot} \equiv \left\langle \frac{\cdot}{F_1 - B_2} \right\rangle, \tag{3.11}$$

and assume no correlation in the spectral behavior of A_c and F_1, B_2. The resulting averages are displayed as straight lines in Figure 3.6d,e, with shaded regions indicating the standard deviation. By applying the model to the data for the VPC edge states, we associate a mean effective reflectance $\bar{R}_c = 0.002 \pm 0.001$ and an out-of-plane scattering loss $\bar{A}_c = 0.080 \pm 0.002$ with the full defect. The same approach applied to the data for the $W1$ PhC waveguide reveals a reflectance of $\bar{R}_c = 0.191 \pm 0.010$, two orders of magnitude larger than the value observed in the VPC, and an out-of-plane scattering coefficient $\bar{A}_c = 0.304 \pm 0.017$. These values for the $W1$ structure are in close agreement with literature [211–213].

3.2.5. SINGLE CORNER REFLECTIVITY

From the mean effective interface values $\langle R_c \rangle$ and $\langle A_c \rangle$ obtained via Equations (3.10a) and (3.10b), we infer an estimate for the coefficients of the individual corners, i.e., when representing each of the four waveguide bends by a single interface in the TMM. The distances between the interfaces are set to the design parameters, as indicated in Figure 3.6a. We model a waveguide with four identical corners, then search for a single corner reflectivity $\left\langle R_c^{\text{single}} \right\rangle$ such that the mean effective $\langle R_c \rangle$ given by Equation (3.10a) reproduces the value extracted from the experiment. The single corner absorption is subsequently given by

$$\left\langle A_c^{\text{single}} \right\rangle = 1 - \left\langle R_c^{\text{single}} \right\rangle - \sqrt[4]{1 - \langle R_c \rangle - \langle A_c \rangle}. \tag{3.12}$$

The mean effective parameters extracted from our measurements of the VPC domain wall and $W1$ waveguide are displayed in Figure 3.6d,e and listed together with the single corner parameters in Table 3.1. For the VPC edge state defect, we obtain $\left\langle R_c^{\text{single}} \right\rangle \approx 0.1\%$ and $\left\langle A_c^{\text{single}} \right\rangle \approx 2\%$. While the value of $\left\langle A_c^{\text{single}} \right\rangle$ might seem large for a topological photonic insulator, topological protection is only given for in-plane propagation, with out-of-plane confinement in the silicon slab solely provided by total internal reflection. If we apply the described model to the experimentally measured mode amplitudes of a topologically trivial $W1$ photonic crystal waveguide, we obtain a corner reflectivity that is two orders of magnitude higher with respect to the topologically protected system ($\left\langle R_c^{\text{single}} \right\rangle \approx 5\%$), alongside a roughly four-fold increase in out-of-plane scattering ($\left\langle A_c^{\text{single}} \right\rangle \approx 11\%$). Such an

	VPC edge state	$W1$ waveguide
$\langle R_c \rangle$	0.0026 ± 0.0010	0.191 ± 0.010
$\langle A_c \rangle$	0.0804 ± 0.0014	0.304 ± 0.017
$\left\langle R_c^{\text{single}} \right\rangle$	0.0007	0.052
$\left\langle A_c^{\text{single}} \right\rangle$	0.0208	0.105

Table 3.1: Comparison of extracted effective mean corner reflectivity and loss for the Ω-shaped defect within the studied photonic crystal waveguides, as well as the estimates for single corners.

increase in losses matches well with the expected scaling behavior of the modes' group velocity as v_g^{-2} [214], with $v_g \approx c/5.8$ for the VPC edge state and $v_g \approx c/10.1$ for the $W1$ waveguide mode. A topologically protected PhC lattice thus reduces the experimentally achievable back-reflection from individual sharp corners by two orders of magnitude over the entire frequency range of the edge state. We confirm this finding and the applicability of the introduced TMM using finite-difference time-domain simulations for the same lattice designs with increasing numbers of corners.

3.2.6. INFLUENCE OF AMOUNT OF CORNERS ON BACKSCATTERING

In order to validate the experimentally retrieved estimate for the corner reflectivity via the TMM, we calculate the back-reflected energy densities for different numbers of corners using finite difference time domain simulations (Lumerical FDTD). We construct a VPC interface and $W1$ photonic crystal waveguide with the same dimensions and a similar in-coupling scheme as used in the experiment. The lattice constant a and sizes of the triangular holes in the unit cell of the VPC were chosen as $a = 500\,\text{nm}$, $d_1 = 0.70a$ and $d_2 = 0.45a$, while the $W1$ waveguide was constructed with a lattice constant of $a' = 420\,\text{nm}$ and hole radius of $r = 120\,\text{nm}$. To reduce the computational demand, we simulate an effective 2D model where we adapt the refractive indices to approximately match the experimentally retrieved bandgaps around 190 THz – 200 THz. In this configuration, out-of-plane scattering is absent in the simulations, in contrast to the experiment. We utilize a broadband source in the feed waveguide to launch a pulse with a spectral range of 1450 nm – 1650 nm and temporal width of $\Delta t \approx 40\,\text{fs}$. The simulation domain is encapsulated by perfectly matched layers (PMLs) with sufficient thickness to minimize unwanted reflections at the domain boundaries, and the simulation is performed for 10 ps to allow for the pulse energy to adequately decay inside the PMLs.

The in-plane electric field components over an area of 20×20 unit cells along the interface/waveguide before the corner(s) were subsequently extracted (see Figure 3.7a-c for the different defect configurations) and used to calculate the mode energy of the forward (F_1) and backward (B_1) traveling edge state or waveguide mode via their dispersion relation, analog to the experimental realization. The resulting energy ratio η_{R_1} is shown for the three different configurations in Figure 3.7a-c on a logarithmic scale to compare the QVHE-emulating VPC and $W1$ PhC waveguide for each configuration, as well as in Figure 3.7d,e on a linear scale

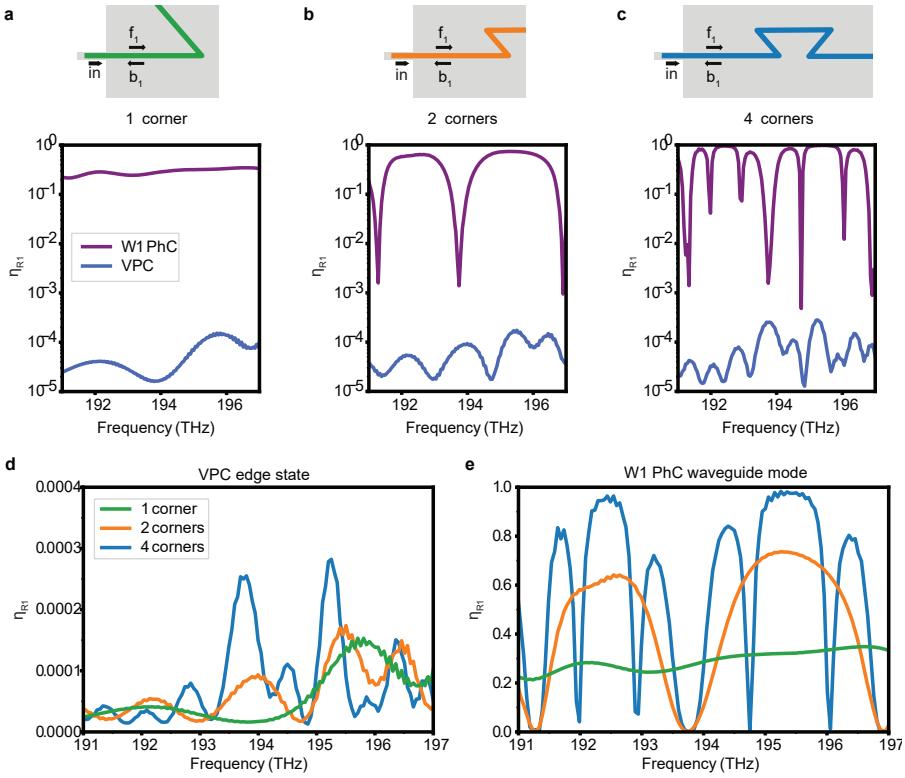

Figure 3.7: Backscattering from various defect geometries in trivial and topological waveguides. Numerically calculated energy ratio $\eta_{R_1} = B_1/F_1$ of the backward (B_1) and forward (F_1) propagating mode for different configurations of the guiding channel. A schematic of the simulation setup is shown above the corresponding ratio of a VPC edge state and $W1$ waveguide mode for **a,** a single 120° corner, **b,** two corners (Z-shaped defect) and **c,** four corners (Ω-shaped defect), where the mode amplitudes f_1 and b_1 are extracted from an area of 20×20 unit cells. To visualize the four orders of magnitude difference, the retrieved energy ratio is plotted in logarithmic scale. **d,** Comparison between the three different scenarios in **a-c** for the VPC edge state, and **e,** the $W1$ PhC waveguide mode.

to follow the evolution of the two modes with increasing amount of corners. In the case of two and four 120° corners, the field energies F_2, B_2 were additionally extracted from a similar area after the defect.

Looking at the variation in the energy ratio, we see that the oscillation amplitude of the back-reflected mode energy increases as the amount of interface corners is increased. In addition, the interference between the different corners leads to a distinct Fabry-Perot type modulation pattern for the $W1$ waveguide (Figure 3.7e), while an increase of contributing oscillation periods can be seen for the VPC edge (Figure 3.7d). The almost flat reflection coefficient for a single corner in the $W1$ waveguide of $\langle \eta_{R_c} \rangle = 0.288$ highlights the dominating influence of the $W1$ corner over other sources of backscattering, while the modulation seen in the VPC edge data for a single corner hints at a comparable backscattering strength from the

corner and the PMLs terminating the simulation domain.

Evaluating the shown energy ratios via the transfer matrix model of Section 3.2.2, we get an effective full reflectivity of $\langle R_c \rangle = [0.2, 1.4, 3.9] \cdot 10^{-5}$ for a system containing 1, 2 and 4 corners along the VPC interface, respectively. The $W1$ waveguide system exhibits $\langle R_c \rangle = [0.288, 0.443, 0.571]$ for the same configurations. The relatively low reflectivity for the VPC suggests that, in addition to backscattering caused by the introduced defects, the backward propagating mode energy is affected by numerical as well as meshing artifacts in the simulations. These are negligible for the $W1$ simulations, which show a clear trend of increasing system reflectivity with number of corners. Using the reflectivity $\langle R_c \rangle$ for the $W1$ waveguide structures with 2 and 4 corners, we can estimate the single-corner reflectivity with the approach of Section 3.2.5, resulting in $\langle R_c^{\text{single}} \rangle = [0.285, 0.284]$ for the two- and four-corner system, respectively. This is in good agreement with the reflectivity $\langle R_c \rangle = 0.288$ that was calculated directly for a single-corner system, corroborating the approach of Section 3.2.2 to estimate the single-corner reflectivity from the properties of the full-defect.

The extracted four orders of magnitude difference in reflectivity between the VPC edge state and the $W1$ waveguide mode highlights the robustness of the former against the designed corner defects. While these 2D simulations achieve an additional two orders of magnitude decrease in backscattering as compared to the experiment, we want to emphasize here that no disorder in the position and size of the triangles constituting the VPC unit cells was taken into account in the simulations. Typical state-of-the-art manufacturing techniques allow for disorder as small as $\sigma \approx 1\,\text{nm}$ [215], which is an order of magnitude larger than the grid size chosen in the shown numerical calculations. The discrepancy between experimentally determined and numerically extracted corner reflectivity can thus be understood as an indirect measure of the C_3 symmetry-breaking disorder in the experimental system. In future studies it thus may be of interest to more closely study and compare losses not only due to designed defects within the lattice, but also due to disorder and other scattering sites along the full extent of the device, including the in- and out-coupling facets and the taper transition region.

3.3. CONCLUSION

In summary, we achieved a direct experimental quantification of topological protection in VPC-based PTIs at telecom frequencies by accessing the full complex wavefunction of the edge state via phase-resolved near-field microscopy. This allows for the determination of back-reflection from topologically protected defects as well as for the quantification of experimentally unavoidable out-of-plane scattering losses. We unambiguously determined an experimental upper limit to the backscattering contribution from symmetry-protected defects in PhC-based topological edge states. This evaluation opens a direct pathway towards topological photonic networks for on-chip applications.

3.4. METHODS

3.4.1. SIMULATIONS

Numerical simulations were performed using MIT Photonic Bands [216], with the retrieved dispersion relation shown in Section 3.5.1. The refractive index of silicon was chosen as $n = 3.36$ to match the calculated edge state dispersion to measurements. To account for the corner roundness arising from fabrication, a fillet of 42 nm radius was added to the triangular holes of lattice constant $a =$ 503 nm. The unit cell consisted of equilateral triangles, with larger triangle side length $d_1 = 0.7a$ and smaller triangle side length $d_2 = 0.45a$. The plotted near-field distributions were extracted from the simulation in a plane located 20 nm above the silicon membrane. In addition, finite-difference time-domain calculations (FDTD Solutions by Lumerical) were used to verify the intrinsic transmittance spectra through 120° bends in a $W1$ PhC waveguide.

3.4.2. SAMPLE DESIGN

The PhC lattice featured a honeycomb configuration of two equilateral triangles in a unit cell of lattice constant $a = 503$ nm. One triangle was scaled up ($d_1 = 0.7a$), and the other down ($d_2 = 0.45a$), while preserving C_3 lattice symmetry. A domain wall was created along VPC_1 and VPC_2 by applying a parity operation along the spatial y-coordinate. Two different VPC domain walls were fabricated to facilitate transmission and backscattering comparisons. The straight edge VPC had dimensions $195a \times 55a$, designed such that the PBG fell within the tunable laser wavelength range of 1480 nm–1640 nm. For the trapezoidal edge VPC domain wall, the two diagonals extended over 12 unit cells, whereas the horizontal extent of the defect between the second and third corners was 34 unit cells. The standard $W1$ waveguide was formed from a honeycomb lattice of circular holes, with a lattice constant $a' = 420$ nm and hole radius $r = 120$ nm, where one row of circular holes was removed. The PhCs featured an intermediate PhC waveguide at the end facets, acting as an adiabatic transition region with the Si-ridge access waveguides to enable better index matching for efficient in-coupling [174]. The design was implemented in a silicon-on-insulator platform with a 220 nm thick silicon layer on a 3 μm buried oxide layer. The fabrication process is described in detail in Section 2.1.

3.5. APPENDICES

3.5.1. NUMERICAL CALCULATION OF EDGE STATE DISPERSION

The edge state eigenfrequencies $f(k)$ as well as eigenmodes $\mathbf{E}_k(\mathbf{r})$ that are localized at the domain wall between two mirror-symmetric valley photonic crystals (VPCs) were calculated for an in-plane wavevector k with the freely available MIT Photonic Bands solver [216]. It determines the Bloch eigenmodes of the full three-dimensional photonic crystal structure using a plane-wave basis set and periodic boundary conditions. We used a simulation supercell of dimensions $a \times 28a \times 10h$, where h is the thickness of the freestanding silicon slab and a is the lattice constant of the VPC patterned therein. This supercell was sufficiently large to avoid interactions between neighboring supercells in y and z. The calculations used an in-plane

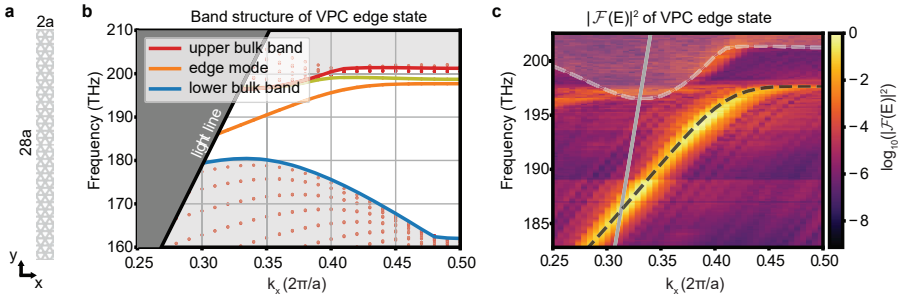

Figure 3.8: Band structure calculations. a, Geometry of the photonic crystal membrane used in the eigenmode calculations, with gray and white representing silicon and air, respectively. For better visibility, two unit cells are shown along the domain wall. **b,** Numerically calculated band structure of the edge state eigenmode (orange) as well as the upper and lower bulk bands (red and blue, respectively) of the photonic crystal. The light cone is displayed as dark gray shading, while the bulk band region has been shaded light gray. In addition to the topologically non-trivial edge mode, there exists a second mode confined to the edge at large k_x, shown in ocher. **c,** Comparison of the fundamental Brillouin zone of the experimentally retrieved dispersion relation and the numerically calculated edge state eigenfrequencies (black dashed line) as well as bulk bands (gray dashed line and shaded region), highlighting the excellent overlap between experiment and simulation. The light line is given by the solid gray line.

grid size of $a/32$ and out-of-plane grid size of $a/16$, which ensured convergence of the eigenvalues to better than 0.1%. To account for surface passivation effects of the experimentally employed silicon membrane of height $h = 220\,\text{nm}$ and to adapt the resulting eigenfrequencies to the experimentally determined dispersion relation, the effective refractive index of silicon was modelled to be 3.36. The lattice constant was chosen as $a = 503\,\text{nm}$, and the base length of the triangular holes in each unit cell, determined from SEM images, was $d_1 = 0.70a$ and $d_2 = 0.45a$ for the large and small triangle, respectively. Both triangular holes were modeled with a corner rounding of $r = 42\,\text{nm}$ to account for fabrication-related deviations from their ideal structure. We construct a bridge-type domain wall between two mirror-symmetric sub-lattices VPC_1 and VPC_2 in the supercell, with the base of the large triangles facing each other. The periodic nature of the simulation subsequently dictates the additional occurrence of the complementary domain wall (base of small triangles facing each other) at the boundary of the supercell (see Fig. Figure 3.8a).

The calculated edge state eigenmodes located at this complementary domain wall were filtered out, and the resulting band structure for the topologically protected edge state as well as the bulk VPC eigenfrequencies determining the system's bandgap are shown in Figure 3.8b. The latter were calculated for a single unit cell of one of the sub-lattices and subsequently mapped to the chosen interface orientation by projecting the resulting bulk frequencies onto the k_x direction.

In addition to the edge state traversing the bandgap with a linear dispersion around the K-point, a second mode confined to the central domain wall is found branching off the top bulk band for high in-plane k-values (shown in ocher in Figure 3.8b). Within the fundamental Brillouin zone, we see an excellent agreement between the measured and simulated edge state dispersion, which extends into the

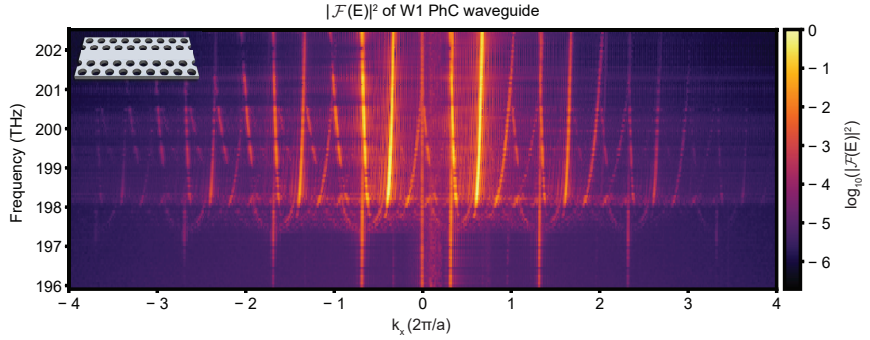

Figure 3.9: W1 waveguide dispersion. Dispersion relation of the fundamental mode of a $W1$-type photonic crystal waveguide (inset: schematic geometry), retrieved from Fourier transforms of the measured near-field mode profile for varying excitation frequency. The lattice constant of the investigated photonic crystal is $a' = 420\,\text{nm}$, with a hole of radius $r = 120\,\text{nm}$ constituting the unit cell of the hexagonal lattice.

light cone for $k_x < 0.31 \cdot 2\pi/a$ (see Figure 3.8c).

3.5.2. DISPERSION RELATION OF W1 PHOTONIC CRYSTAL WAVEGUIDE

To compare the robustness against reflections from a corner defect between the VPC edge state and a $W1$-type photonic crystal waveguide, both modes need to be considered at comparable group velocities v_g, since loss scales with v_g^{-2} [214]. Thus, we experimentally determine the dispersion relation of the $W1$-type photonic crystal waveguide (analogous to the VPC edge state dispersion shown in Figure 3.3b), and show the bands of forward and backward propagating Bloch modes spanning several Brillouin zones in Figure 3.9. One key observation here is that the forward propagating mode in the fundamental Brillouin zone is located at negative k_x, in accordance with the mode's expected behavior [214].

In addition to the predicted band in forward and backward direction, bands with half and a third of the dispersion slope of the fundamental mode appear. These were already observed in GaAs-based PhCs and attributed to nonlinear interactions with the scanning near-field probe [217].

4

INTERPLAY OF LEAKAGE RADIATION AND PROTECTION IN TOPOLOGICAL PHOTONIC CRYSTAL CAVITIES

The introduction of topological concepts to the design of photonic crystal cavities holds great promise for applications in integrated photonics due to the prospect of topological protection. These concepts have, however, conventionally been defined for conservative, non-radiative systems that are relatively large. This study examines the signatures of topological light confinement in the leakage radiation of two-dimensional topological photonic crystal cavities. The cavities are implemented in an all-dielectric platform that features the photonic quantum spin Hall effect at telecom wavelengths and supports helical edge states that are weakly coupled to the radiation continuum. The modes of resonators scaling down to single point defects in the surrounding bulk lattice are characterized via spectral position and multipolar nature of the eigenstates. The mode profiles in real- and momentum space are mapped using far-field imaging and Fourier spectropolarimetry, revealing how certain properties of the cavity modes reflect on their origin in the topological band structure. This includes band-inversion-induced confinement and inverted scaling of mode spectra for trivial and topological defect cavities. Furthermore, hallmarks of topological protection in the loss rates are demonstrated, which are largely unaffected by cavity shape and size. The results constitute an important step toward the use of radiative topological cavities for on-chip confinement of light, control of emitted wave fronts, and enhancing light-matter interactions.

This chapter is based on Barczyk et al., *Laser & Photonics Reviews* **16**, 2200071 (2022)

4.1. INTRODUCTION

Photonic crystal (PhC) resonators represent versatile building blocks for the control and manipulation of light on wavelength scales [13], offering highly desirable functionality for on-chip integration such as sensing [17], delay lines [218], and quantum information processing [219]. Since the confinement of light to small mode volumes renders resonators more prone to radiative losses, i.e., scattering and out-of-plane leakage, extensive effort has been conducted to realize miniaturized whispering-gallery-mode (WGM) and lattice-defect PhC cavities with various quality factors and mode volumes through optimization of design down to the nanometer level [220–223]. In this context, the concept of topological insulators provides an interesting new paradigm for photonic design, including that of PhC resonators, as it offers inherent robustness to specific forms of imperfections [18, 96, 127].

Topological insulators are characterized by a non-trivial topology of the material's band structure, originating from the geometrical structure of the associated wavefunctions in momentum space. While being insulating in the bulk, the boundary of a topological insulator supports propagating edge states [127, 224], constituting a transmission line resilient to backscattering by a wide range of perturbations which respect the symmetry that underlies the topological protection. The transfer of topological ideas from the electronic to the photonic domain lead to the advent of photonic topological insulators (PTIs) with unprecedented light-guiding capabilities, as we described in Section 1.5.3. Apart from Chern-type PTIs that break time-reversal symmetry [114], time-reversal invariant PTIs that rely on certain spatial symmetries for a protection mechanism were proposed and successfully implemented in passive dielectric PhCs [147, 194, 196, 225, 226]. Due to a lack of fermionic Kramer's doubling in bosonic systems, PTIs that mimic the quantum valley-Hall effect (QVHE) [134–136] or quantum spin-Hall effect (QSHE) [129, 196, 226] take a geometrical approach to construct pseudospins and corresponding spin-momentum locking [227, 228], a luring proposition for chiral quantum optics [170, 196].

Building upon the light-guiding capabilities of PTIs, one can design ring-like PhC cavities based on the photonic QVHE [229–233] and QSHE [26, 234–240] by folding the edge between domains with different topological order into a closed contour. It is worth noting that, apart from cavities that derive from edge states and topological bulk properties as in our case [234, 241], cavities based on corner states have also been realized in 2D PhCs that can host a second-order topological phase [121, 242]. While QVHE-type PTIs operate below the light line, edge states in QSHE-type PTIs are intrinsically leaky [128], providing a direct near-to-far-field interface. Control over far-field radiation properties of PhC cavities is highly relevant for applications relying on efficient emission (photoluminescence, lasing) or in-coupling (optical pumping, add-drop functionality) of light from and into nanophotonic devices, respectively. Various studies on conventional PhC cavities are therefore dedicated to the optimization of far-field coupling for e.g. light-matter interfaces, sensors, and surface-emitting lasers [241, 243–246]. With its inherent coupling to radiation, QSHE-type cavities could thus provide an interesting platform for such applications.

At the same time, as the leakage is not contained in the topological description of the system, intriguing fundamental questions arise: how do the cavities' radiation losses affect topological robustness and, conversely, how does the PhC's band structure control the emitted radiation? The fact that intrinsic loss and topological protection naturally coalesce in QSHE-type PhC cavities calls for an examination on the consequences of the mutual presence of these seemingly opposing features.

Here, we present an experimental study of the radiative optical properties of Si nanocavities using a topological PhC platform featuring the photonic QSHE at telecom frequencies. Contrary to earlier theoretical [234] and experimental studies [235–237, 241, 246, 247], we investigate resonators that are coupled to the radiation continuum and scale down to the size of a single point defect in the surrounding bulk lattice, where the common interpretation of the interface as a ring-like topological waveguide breaks down. We find that the origin of the cavity modes in the topological band structure is still manifested in the mode properties. It must be noted that the word 'topological' is usually meant to describe properties of band structures of (semi-) infinite PhCs, and thus cannot be rigorously linked to finite-sized systems. Nevertheless, for simplicity, we use the term 'topological cavity' in this chapter to refer to any finite-sized regions that are derived from combining the unit cells corresponding to two PhCs with different bulk topological nature [229, 232–238, 241, 246]. To acquire full knowledge over the cavities' spectral, angular, spatial, and polarimetric characteristics, we employ Fourier spectropolarimetry of the cavity far-field radiation. We elucidate the modes' multipolar nature and scaling with cavity size, and identify hallmarks of topological behavior such as band-inversion-induced confinement, inverted mode spectra for shrunken and expanded cavities, and directional emission in vortex beam modes. We demonstrate that, in contrast to regular PhC cavities and WGM resonators, the mode quality factors are largely insensitive to the cavity size, and examine the robustness of mode spectra against strong deformations of the cavity shape.

4.2. RESULTS AND DISCUSSION

4.2.1. TOPOLOGICAL PHOTONIC CRYSTAL DESIGN AND CHARACTERIZATION

Our implementation of a topological PhC platform follows the symmetry-based approach outlined by Wu & Hu [194]. The scheme relies on the geometric properties of the PhC which, in our case, is formed by equilateral triangular air holes perforating a silicon membrane [147]. We fabricate these structures via electron beam lithography and reactive ion and wet etching of a silicon-on-insulator substrate (see Section 2.1 for more details on fabrication) [146].

Figure 4.1a shows a top view scanning electron micrograph of a fabricated nanocavity, next to a pictorial representation illustrating the two lattice types constituting the system. The inset represents a three-dimensional cross-cut of the sample, displaying a suspended PhC membrane. The relation between unit cell geometry and photonic dispersion for TE-polarized bulk crystal modes is presented in Figure 4.1b. Considering a six-site unit cell of a perfect triangular lattice, a

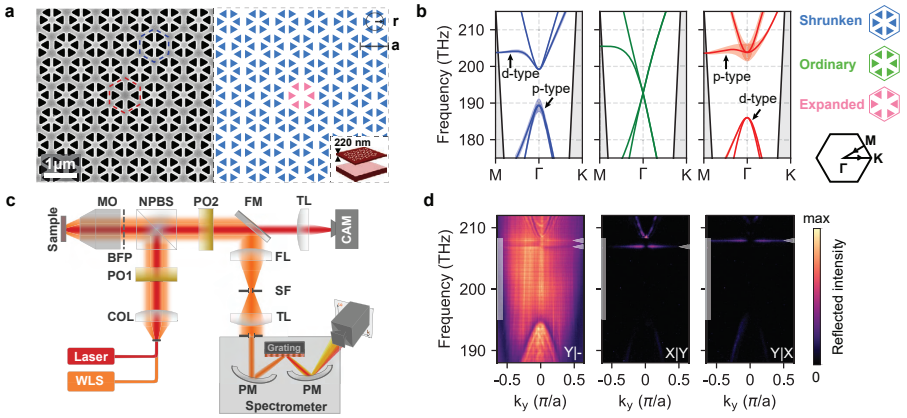

Figure 4.1: System, setup, and typical measurements. a, Topological photonic crystal cavity in a silicon membrane. Left: scanning electron micrograph of a defect cavity made from a single topologically non-trivial (expanded) unit cell, surrounded by a trivial (shrunken) bulk, with unit cells indicated by red and blue dashed hexagons, respectively. Right: schematic illustration of the system with an inset of the suspended photonic crystal membrane geometry. The distance r of the scattering sites to the unit cell center and the lattice constant a are indicated. **b,** Numerically obtained photonic bands for an expanded (blue), ordinary C_6-symmetric (green), and shrunken (red) bulk. We denote the dipolar (p-type) and quadrupolar (d-type) nature of the bulk bands and indicate the associated linewidths by colored shadings (scaled up 5× for visibility). Regions outside the light cone are shaded in gray. Inset: computed trajectory within the fundamental Brillouin zone. **c,** Mode spectrum of the system shown in **a** for various settings of polarizer and analyzer (denoted as 'polarizer|analyzer'). Recognizable cavity modes as well as the bulk bandgaps are highlighted by white pointers and light shaded bars, respectively.

Dirac-like linear dispersion is found at the Γ point in the center of the Brillouin zone (Figure 4.1b, center panel) [194]. It is four-fold degenerate, as it originates from band folding of the Dirac points in the dispersion of a graphene-like lattice at the K and K' points when considering a fundamental two-site rhombic unit cell. Spatial symmetry breaking creates bandgaps with non-trivial topological nature through the lifting of this Dirac-point degeneracy [127]. Bandgaps of different topological order are created by continuously deforming the unit cell, radially shifting the holes while preserving C_6 symmetry to obtain either the 'shrunken' (Figure 4.1b, left) or the 'expanded' (Figure 4.1b, right panel) design. The size of the bandgap is an important parameter for resonators as it relates to spatial confinement, i.e., the mode volume [13]. For our sample geometry (see Section 4.4.2 for detailed parameters), we numerically obtain relative bandgap sizes of $\Delta\omega/\omega_0 \approx 5.0\,\%$ and $7.4\,\%$ for the shrunken and expanded case, centered around 194.3 THz and 196.5 THz, respectively. The bandgap size may be tuned by varying lattice parameters such as the expansion factor r/r_0, where r describes the radius of the centroids of the triangular air holes, with $r = r_0$ for the ordinary lattice. Larger deviations $|r/r_0 - 1|$ are associated with smaller mode volumes [237]. Without detailed optimization of the design to minimize the leakage rate through interference [220, 221, 248], in regular PhC cavities a smaller mode volume is generally accompanied by larger radiative loss. In our case, $r/r_0 = 0.91$ and 1.09 for the shrunken and expanded unit

cells, respectively [129].

The topological nature of the system is associated with band inversion, like in the one-dimensional Su-Schrieffer-Heeger chain [127]: a continuous transformation from shrunken to expanded geometry inverts the ratio of intra- to inter-cell coupling of scattering sites, necessarily accompanied by intermediate closing of the bandgap. In consequence, the nature of the states populating the band edges is inverted. While the states of the bottom (top) bulk bands in the shrunken (expanded) lattice possess an out-of-plane magnetic field H_z that resembles dipolar p-orbitals, responsible for the radiative loss, the top (bottom) bands feature sub-radiant quadrupolar d-orbitals [128, 129, 147, 194]. The difference in leakiness is also reflected in the radiative linewidths (Figure 4.1b, colored shading), which is about an order of magnitude larger for p-type bands [128, 129].

Although the true topological character of the platform has been a topic of debate [249, 250], recent studies [251] support the argument that the bulk topology of the lattices is indeed analogous to a $\mathbb{Z}_2$ topological insulator in the QSHE [127], with the expanded lattice being in a non-trivial phase [147]. Bulk-edge correspondence then implies the existence of two counter-propagating edge states at the PhC's boundaries that cross the bandgap linearly [129, 147, 194]. While any lattice defect in a PhC potentially hosts localized states, the promise of topologically protected edge states makes it especially interesting to study localized states of defects in PTIs [234–238]. As previous theoretical and experimental studies demonstrate, the helicity of the radiation emitted from both edge states is coupled to their unique (and opposing) pseudospins, allowing for spin-dependent excitation and probing of counterpropagating modes from the far field [128, 147, 194, 226]. In consequence, we can examine the optical and topological properties of the system via Fourier reflectometry (see Figure 2.10) [128, 129], whereby we employ two different beam paths to retrieve the cavity mode spectra and the individual modes' profiles in real- and momentum space (see Section 2.2 for more details).

Figure 4.1c shows a measurement of reflected intensity (obtained with the orange beam path in Figure 2.10, see also Figure 2.13a) for a cavity that consists of a single unit-cell expanded defect within a shrunken bulk (see Figure 4.1a). Without analyzer (Figure 4.1c, left panel), the recorded signal has a bright background of directly reflected light and spectrally broad fringes (apparent at large k_y). The latter are a consequence of the sample geometry, which forms a Fabry-Pérot-like cavity between the suspended membrane and the underlying substrate (see Figure 4.1a, inset) [129]. On top of this background, sharper resonant features appear, exhibiting Fano-type lineshapes along k_y due to interference with the background radiation. These features include the dispersive bulk bands of the PhC surrounding the bandgap [128, 129], as well as flat bands at specific frequencies within the gap. We associate the latter with the cavity modes of the system in Figure 4.1a, demonstrating that a single expanded unit cell supports a pair of confined modes around 208 THz with quality factors $Q \approx 600$. To obtain the measurements in the center and right panel of Figure 4.1c, we illuminate the sample with light linearly polarized along X (Y) and detect the reflected signal with an orthogonal linear polarizer in the beam path, denoted by $X|Y$ ($Y|X$). This cross-polarization scheme allows us to

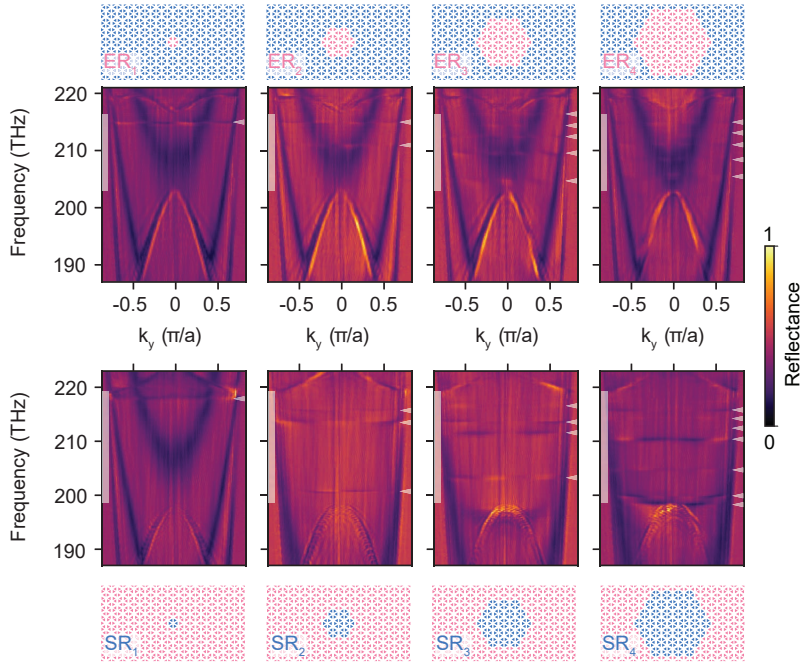

Figure 4.2: Dispersion vs. cavity size. Experimentally retrieved dispersion diagrams of hexagonal cavities formed by patches of expanded-in-shrunken (ER_n, upper row) or shrunken-in-expanded (SR_n, lower row) unit cells, where n denotes the cavity's side length and the input is Y-polarized (no analyzer). Recognizable cavity modes as well as the bulk bandgaps are highlighted by white pointers and light shaded bars, respectively, and the cavity geometries are depicted schematically.

better resolve the individual modes by suppressing background radiation, such that the resonances assume a typical Lorentzian lineshape. It relies on the cavity modes converting polarization of the incident to outgoing light fields, which as we will show is always possible for well-chosen alignment of the focused incident beam with respect to the cavity center.

4.2.2. RADIATION PROFILES OF TOPOLOGICAL CAVITY MODES

We employ reflectometry measurements to study the mode spectra for cavities of varying size and type. Figure 4.2 displays the experimentally measured reflection of X-polarized light for expanded and shrunken defect cavities labeled ER_n and SR_n, respectively, where n denotes the hexagon's side length in terms of unit cells ($n = 1 \ldots 4$). The number of states within the bandgap increases with n, whereby the expanded (Figure 4.2, top row) and shrunken (Figure 4.2, bottom row) resonators follow the same trend of decreasing free spectral range (FSR), exhibiting a comparable number of modes for a given cavity size. A reduction of FSR with cavity size is qualitatively expected as it generally scales inversely proportional to the mode volume. It must be noted that the modes we excite strongly depend on the vectorial field overlap with the focused input beam, hence, only a single mode is visible

for ER_1 in Figure 4.2 (as opposed to Figure 4.1c, left panel). Looking at the bands' intensity variations for different k_y, the resonant states at discrete frequencies display a distribution of emission angles characteristic of their multipolar nature. The latter is especially relevant in the context of topological lasing and generation of vortex beams, since it determines the symmetries and the amount of orbital angular momentum carried by the radiated fields [238]. As a consequence of reciprocity, the multipolar order also determines the symmetries of the incident fields that can efficiently couple to the modes.

We therefore study the radiation patterns of individual modes by selectively addressing the resonances with a monochromatic light source (red beam path in Figure 2.10, see also Figure 2.12b). We tune the wavelength of the incident light on resonance with the cavity mode of interest and record the reflected and re-radiated intensity in the back focal plane (BFP) of the microscope objective used for focusing and collection. In Figure 4.3a, we compare the experimental $(X|Y)$ BFP patterns for selected modes in ER_2 and SR_2 cavities to numerical calculations. The latter are determined by analytically propagating the near fields obtained from finite-element-method calculations to the far field (see Section 4.4.1 for details on the numerical model). The orthogonal polarization projection as well as additional modes are shown in Figure 4.9 of the appendix. It must be noted that, due to the experimental focusing scheme, the cross-polarized configuration cannot suppress all incident light, which is present as a 4-fold symmetric background in the BFP [252]. On top of this background, we see an excellent correspondence between calculated and recorded fields, sharing all characteristic symmetries (e.g. nodal lines). The number of radial nodal lines, together with the phase information shown in Figure 4.10 of the appendix, serves as an indicator for the topological charge of the emitted vector beam, implying the possibility to generate light with a certain amount of orbital angular momentum. Experimental deviations in the intensity distributions may be attributed to the structural imperfections in the fabricated device as well as reflected stray light. Certain modes display considerably directional emission into a narrow spectrum of wavevectors around the normal direction (see also Figure 4.9 of the appendix) as a consequence of the topological edge state transport that involves Bloch components with well-defined, near-zero in-plane wavevectors, in contrast to trivial WGM resonators that rely on total internal reflection.

The exact modes we excite strongly depend on the position and polarization of the focused input beam, which is of particular relevance for applications that rely on the addressing of individual resonances. Therefore, we record polarization-resolved spatial cavity mode profiles and compare them to numerical predictions in Figure 4.3b (see also Section 2.2 for more details on the procedure). In experiment, we raster-scan the input beam over a grid of positions whilst recording BFP images, similar to the ones in Figure 4.3a. Each pixel in the reconstructed map then corresponds to the radiated intensity at that position, integrated over the BFP. In these maps, the cavity is centered around the origin. The numerical results are obtained by propagating the simulated near field to the far field, restricting the angular spectrum to the experimentally accessible range, and then performing the back-transformation. We present the results for excitation with X-polarized light (and

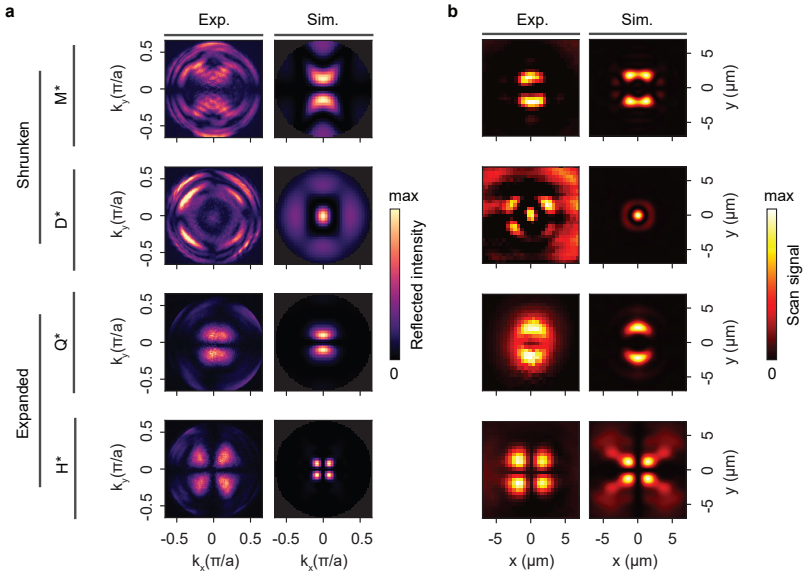

Figure 4.3: Angular and spatial cavity mode profiles. a, Comparison of experimentally retrieved and numerically calculated radiation patterns for the M^* (monopole), D^* (dipole), Q^* (quadrupole), and H^* (hexapole) modes indicated in Figure 4.4a,b. In the experimental images, the polarizer and analyzer are aligned along Y and X, respectively, and the simulated X-polarized field is shown. **b,** Spatial cavity mode profiles with polarizer and analyzer aligned along Y and X, respectively, and the simulated Y-polarized field is shown.

cross-polarized detection) which, as can be inferred from reciprocity, correspond to the X-polarized radiation patterns in Figure 4.3a and hence display the same symmetries (see Section 4.5.1 and Figure 4.9 of the appendix for a more detailed discussion of this argument and additional maps of other modes and polarization projections).

Measurements and numerical predictions correspond well to each other, successfully recovering all characteristic symmetries. It is worth noting that, apart from the dipolar modes, the radiated fields and spatial mode profiles possess a node at the origin. This implies that an angled, off-center excitation is essential to efficiently couple light into the system from the far field. We achieve this by focusing a Gaussian beam to obtain a broad spectrum of incident wavevectors which we translate across the sample plane. More efficient in-coupling could be achieved by means of structured illumination with input beams that are precisely tailored toward the cavity mode field of interest [253]. The good agreement between experiment and calculations allows for a straightforward categorization of the modes in terms of their multipolar nature, which we infer from the simulated out-of-plane magnetic field component H_z in the symmetry plane of the PhC (see Figure 4.10 of the appendix). The simulations show that the cavity modes are spatially localized at the cavities' edges or within its bulk region, having their origin in the topological edge states and in the band-inversion-induced confinement at the topological

boundary [234, 241]. This is in contrast to corner states that exist in 2D PhCs with a second-order topological phase and which also attract broad interest in the context of topological resonators [121, 242]. We identify the modes in Figure 4.3 as monopolar (M), dipolar (D), quadrupolar (Q) and hexapolar (H). To elucidate their origin and scaling behavior, we continue by identifying all modes observed in the ER_n and SR_n cavities (up to $n = 3$).

4.2.3. SCALING BEHAVIOR OF MODE SPECTRA

The experimentally extracted center mode frequencies and multipolar orders are displayed in Figure 4.4a. We highlight the bandgaps in the region between the p- and d-like bulk bands. For the shrunken and expanded case, the gaps have relative sizes of 5.7 % and 10.9 %, centered around 202.5 THz and 201.4 THz, respectively. This is quantitatively well reproduced by numerical calculations. We notice a constant offset on the order of $\sim 5-8$ THz that is attributed to deviations of the real device from the ideal design.

The spatial symmetries of the PhC determine the symmetries of the modes it potentially hosts. Our cavities can be regarded as defects in an otherwise unperturbed TE-like PhC slab, where the surrounding lattice as well as the defect obey a C_6 rotational symmetry. Solving the electromagnetic eigenvalue equation governing the system shows that such a lattice supports precisely the types of modes shown in Figure 4.3 (M, D, Q and H), whereby the spherical multipoles are named according to the respective rotational symmetries of the H_z field [13]. Rotations of 60° transform eigenstates into each other and may be used to construct two mutually orthogonal bases for D and Q. This implies double degeneracy and is in contrast to M and H, which are singlet states [254]. The degenerate D and Q modes can be interpreted as traveling-wave WGMs, i.e., a superposition of two counter-propagating edge states traveling along the resonator's perimeter with equal amplitude but different phase. The M and H modes, however, have no traveling-wave analogue, and the system is better described as a PhC defect cavity that supports collective resonances extending throughout its bulk. These standing-wave modes (SWMs) appear due to the reduced spatial symmetry of the resonators [255]. While conventional ring cavities may be designed perfectly circular to only feature WGMs and no SWMs, cavities in the PTI platform, regardless of their size, inevitably break continuous rotational symmetry and display both types of modes. To control and reduce the appearance of SWMs, we match the symmetries of the cavities to the C_6 symmetry of the unit cell by a hexagonal design [247].

The consequences of these spatial symmetry considerations for the mode spectra are nicely corroborated by the ideal numerical model presented in Figure 4.4b, displaying doubly degenerate Q and D WGMs as well as non-degenerate M and H SWMs. In contrast to simulations, we observe splitting on the order of $\lesssim 1$ THz for D and Q modes in the fabricated device. It is known that a small splitting in straight QSHE-type topological PhC edge state waveguides exists as a consequence of C_6 symmetry being only approximately fulfilled at a straight interface between shrunken and expanded unit cells, causing the two pseudospin states to mix and a small spin-spin-scattering gap to open up [194]. However, since a hexagonal cavity

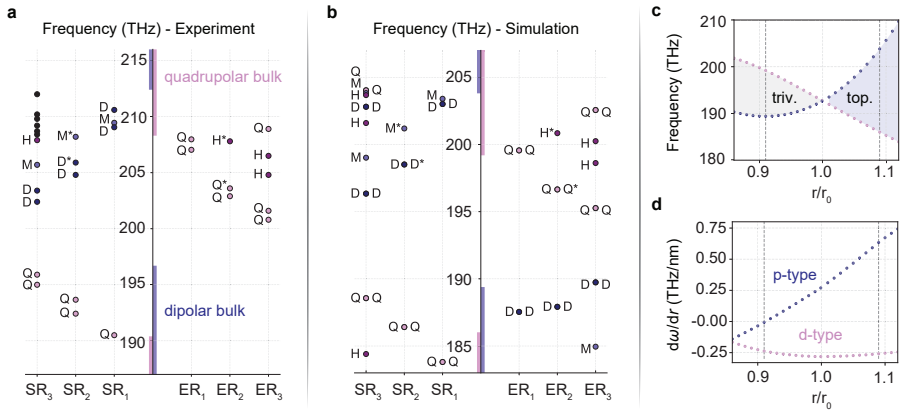

Figure 4.4: Nature of cavity modes. a, Experimentally and **b,** numerically retrieved mode spectra for shrunken and expanded cavities of different sizes. Cavity modes are labeled according to their multipolar order, i.e. monopolar (M), dipolar (D), quadrupolar (Q) and hexapolar (H). Mode colors indicate the bulk bands from which they detach: quadrupolar for Q and H modes (pink shades), dipolar for M and D modes (purple shades). Vertical bars indicate the dipolar (p-type, purple) and quadrupolar (d-type, pink) bands of the bulk lattice surrounding the cavity (expanded for SR_n, shrunken for ER_n). **c,** Numerically retrieved frequency of the top and bottom bulk bands as a function of the unit cell expansion factor (r/r_0). Band inversion takes place upon transformation from shrunken (trivial) to expanded (topological) geometry. The distance of the triangular air holes' centroids from the unit cell center is denoted by r, with $r = r_0$ for an ordinary lattice (see Figure 4.1b). Our choice of the unit cell expansion factor for the shrunken (0.91) and expanded (1.09) case are indicated by dashed lines in **c** and **d**. **d,** Frequency change for an infinitesimal expansion, as obtained from first-order perturbation theory.

obeys C_6 symmetry, a strict degeneracy between modes of different polarization is expected in theory [254]. Notably, numerical simulations of larger hexagonal cavities have not always confirmed this degeneracy [234], possibly due to simulation imperfections. In finite-element-method calculations where we ensure C_6 symmetry is obeyed in all aspects of the simulation, we indeed observe that splitting is negligibly small (see Figure 4.4b).

If we compare the spectra for increasingly large expanded or shrunken resonators, we observe that, while additional modes emerge in the bandgap, their frequencies shift in qualitatively and quantitatively different ways. It furthermore becomes evident, especially for the simulation results in Figure 4.4b, that these modes originate and detach from the bulk bands upon increasing the cavity size. Strikingly, if we consider their multipolar order, we observe an inverted scaling behavior of the modes for the shrunken and expanded case. For SR cavities, M and D modes appear to originate from the top bulk bands and decrease in energy with cavity size, while Q and H modes emerge from the bottom bulk and shift upwards. The situation is reversed for the expanded case, where instead Q and H modes shift downwards and M and D upwards, as evidenced by simulations. We attribute the lack of M and D modes for ER cavities in experiments to their frequencies falling into the lower bulk region, causing hybridization with extended PhC slab modes and thus increasing in-plane radiation losses, making these resonances harder to resolve

in measurements. Apart from ordinary photonic bandgap confinement, band inversion induced confinement in the topological PhC contributes to the localization of cavity modes in the bulk band region (e.g. M in ER_3, or Q in SR_1) [241].

The scaling of mode frequencies becomes more clear if we trace the upper and lower band edges for a continuous transformation from shrunken to expanded geometry, as shown in Figure 4.4c. We vary the unit cell expansion factor r/r_0 and thus track the process of band inversion upon which p- and d-type bands switch their role and become degenerate for the perfectly triangular lattice with $r = r_0$. We indicate the radii of our realizations of shrunken and expanded geometry and denote the trivial or topological nature of the bandgap, which the p-type bands cross linearly while the d-type modes feature a rather parabolic progression. The curves for the degenerate pairs lie exactly on top of each other. This behavior implies that, if we start out with a lattice of a specific type and introduce defects in the shape of unit cells of the other type, we effectively dope it with a material with inverted band structure. If we, for instance, consider an infinite shrunken lattice ($r < r_0$) into which we introduce a point defect in the shape of an expanded cell (ER_1), this defect "pulls" and "pushes" modes from the upper and lower bulk bands, respectively. In the limit where we replace every shrunken unit cell by an expanded one, this process ultimately inverts the band structure. For finite patches of increasing size however, as in our case, we observe discrete modes (with decreasing FSR) whose frequencies evolve in opposite directions for ER and SR systems.

To support this argument, we employ first order perturbation theory [13, 256] and determine the frequency shift $d\omega$ upon infinitesimal variation of the radius of the triangular air holes' centroids dr through suitable integration of the mode fields. We treat an expanded (shrunken) cavity as a defect inside the surrounding shrunken (expanded) bulk lattice, constituted of perturbed unit cells with an increased (decreased) radius r. Altering the unit cell expansion factor r/r_0 may be viewed as a perturbation $\Delta\epsilon$ of the dielectric function. The frequency shift $\Delta\omega$ for an eigenmode of a system subject to such a perturbation may be written as [13]

$$\Delta\omega = -\frac{\omega}{2}\frac{\int \mathrm{d}^3\mathbf{r}\,\Delta\epsilon(\mathbf{r})\,|\mathbf{E}(\mathbf{r})|^2}{\int \mathrm{d}^3\mathbf{r}\,\epsilon(\mathbf{r})\,|\mathbf{E}(\mathbf{r})|^2} + \mathcal{O}(\Delta\epsilon^2)\,, \tag{4.1}$$

where E and ω denote the electric field distribution and frequency, respectively, of the unperturbed dielectric function ϵ. Although this expression is applicable for a wide range of small perturbations, small displacements of dielectric boundaries with high refractive index contrast such as in our system represent moving discontinuities to which the formula cannot be applied. In this case, if we consider a dielectric boundary shifting from ϵ_1 toward ϵ_2 by a distance Δr perpendicular to the interface (see Figure 4.5), the correct expression is given by [256]

$$\Delta\omega = -\frac{\omega}{2}\frac{\int \mathrm{d}^2\mathbf{r}\,\left[(\epsilon_1-\epsilon_2)|\mathbf{E}_\parallel(\mathbf{r})|^2 - (\epsilon_1^{-1}-\epsilon_2^{-1})|\epsilon\mathbf{E}_\perp(\mathbf{r})|^2\right]}{\int \mathrm{d}^3\mathbf{r}\,\epsilon(\mathbf{r})\,|\mathbf{E}(\mathbf{r})|^2}\cdot\Delta r + \mathcal{O}(\Delta r^2)\,. \tag{4.2}$$

Here, $\mathbf{E}_\parallel$ and $\mathbf{E}_\perp$ are the electric field components parallel and orthogonal to the boundary, respectively.

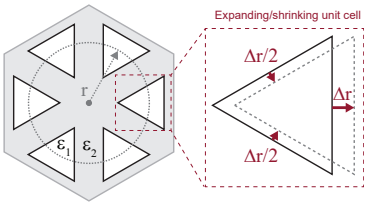

Figure 4.5: Unit cell perturbation. Sketch of an infinitesimal expansion/contraction of the unit cell, displaying the geometrical parameters used for the perturbative approach of Equation (4.2) to calculate the scaling behavior of cavity mode frequencies with size, as shown in Figure 4.4d.

We use Equation (4.2) up to first order to calculate the frequency shift upon variation of the unit cell expansion factor. The result is shown in Figure 4.4d and, as expected, represents the derivative of the graphs in Figure 4.4c with respect to r. While the p-type modes display a fairly constant rate of energy change, corresponding to the linear crossing of the bandgap in Figure 4.4c, the parabolic progression of the d-type modes therein manifests as linear slope of the respective curves in Figure 4.4d (the degenerate mode pairs lie on top of each other again). The frequency scaling of the bands underlines the importance of choosing sufficiently different expansion factors for the defect and bulk unit cells in order to achieve comparable bandgap sizes and sufficient mode confinement, especially visible for the frequencies of the d-type bands which vary only weakly around $r/r_0 = 0.91$ (shrunken lattice). The sign of $\mathrm{d}\omega/\mathrm{d}r$ is reflected in the direction of frequency change for the various multipoles in Figure 4.4a,b, further underlining the qualitatively different behavior in expanded and shrunken systems. The inversion of mode scaling behavior results from the band inversion underlying the topological phase transition in the platform and represents a design advantage over trivial PhC lattice defect or WGM resonators, as it offers an additional degree of freedom to strongly tailor cavity mode spectra by small variations to the unit cell geometry while preserving the overall footprint.

4.2.4. SIZE- AND SHAPE-DEPENDENCE OF LEAKAGE RADIATION

Another key advantage of topological platforms with respect to conventional systems is considered to be their enhanced robustness against defects. In Figure 4.6, we investigate the influence of cavity size and shape on the mode spectra to search for hallmarks of topological protection. An obvious point to study is the radiative loss, which we compare for cavities of increasing size. To this end, we choose to examine the higher energy quadrupolar mode (Q^*) which all expanded cavities (ER_{1-4}) have in common (see Figure 4.2, Figure 4.3, and Figure 4.4a,b), as well as the common dipolar mode (D^*) of the shrunken cavities (SR_{1-4}). For each resonator, we fit a model of a general resonance lineshape (see Equation (4.4) in Section 4.4.3) to the normalized reflection in order to extract the mode frequency and linewidth from seven cross-cuts along k_y. The average extracted quality factors alongside the standard error of the mean are shown in Figure 4.6a and Table 4.1 of the appendix. Albeit being slightly lower for the shrunken than for the expanded defect, in both

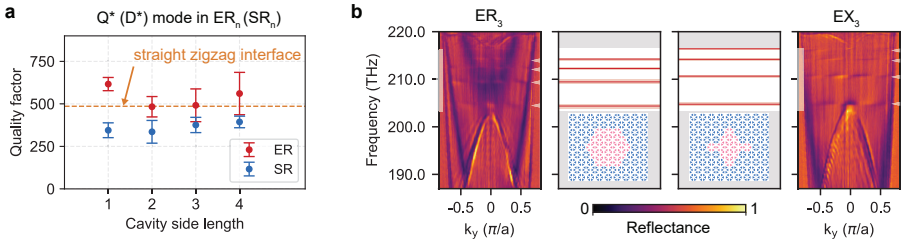

Figure 4.6: Fingerprints of non-trivial topology. a, Experimentally extracted quality factors for the Q^* (D^*) mode common to all investigated ER$_n$ (SR$_n$) cavities, averaged from seven line cuts to the angularly resolved mode spectra and given alongside with the standard error. The red dashed line indicates the radiative quality factor for a straight zigzag-type topological interface [129]. **b,** Comparison of modes for cavities of similar perimeter but strongly differing shape, as indicated by pictograms. In measurements, the cavity modes and bulk bandgaps are highlighted by white pointers and light shaded bars, respectively. Extracted center mode frequencies and corresponding linewidths are presented in the central panels as shaded horizontal lines.

cases we observe no significant variation of the quality factor with size, suggesting that scattering due to the curvature of the perimeters is not the dominant loss mechanism for these cavities, not even for the smallest ones. Since the experimental linewidths are comparable to those of regular edge state dispersion curves along a straight zigzag-type interface (Figure 4.6a, red dotted line) [129], the states' intrinsic leakage radiation seems largely unaffected by the curvature of the interface and is likely to be the dominant loss-mechanism for our resonators.

If we, for comparison, consider the same situation in topologically trivial WGM cavities, there is in general a trade-off between mode volume and radiative losses [13]. In small cavities (i.e., cavities with small mode volumes), light is forced onto a strongly curved path; a ring-shaped waveguide that is dominated by bending losses. The latter are expected to disappear in the limit of infinitely large cavities, as the perimeter effectively approaches a straight waveguide. In absence of any other loss mechanisms the quality factor continuously increases with mode volume. However, in practice it is limited by processes such as scattering from fabrication imperfections and intrinsic material losses. Therefore, we expect the quality factor to increase with size until eventually converging to the value for a straight waveguide. In the QSHE-type PhC cavities, however, the fairly constant quality factor implies that non-trivial topology protects the edge states from scattering at the cavities' corners, to within the precision given by the intrinsic radiation quality factor. We refer to Section 4.5.2 of the appendix for a comparison between the cavity mode properties of the topological PhC at hand and of a commonly used trivial PhC.

The robustness of cavity modes can also be studied by deliberately introducing more corners whilst keeping the size constant. Figure 4.6b shows a comparison between the dispersion of the hexagonal ER$_3$ cavity and another cavity EX$_3$, with same perimeter but drastically different shape. If we compare the extracted mode frequencies and linewidths, we notice that, apart from an overall increase in FSR, the mode spectra look fairly similar and the number of modes remains the same.

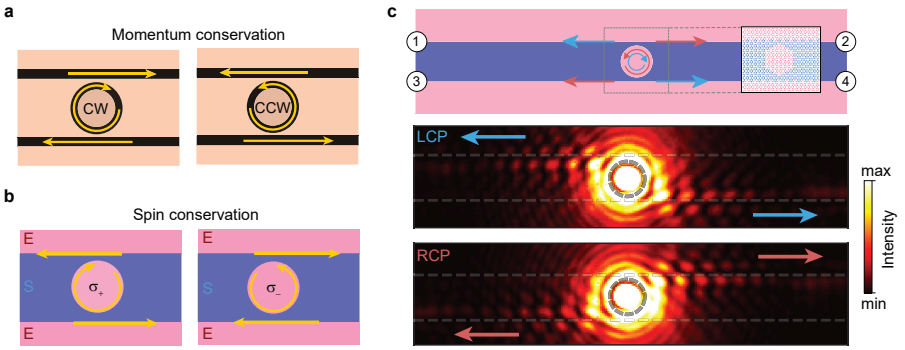

Figure 4.7: Spin-conserved coupling of light. Schematic depiction of **a,** momentum-conserved coupling of clockwise (CW) and counter-clockwise (CCW) modes in a conventional ring-cavity waveguide coupler, as opposed to **b,** spin-conserved coupling in the QSHE-type photonic crystal platform. **c,** Schematic experimental coupling scheme and experimentally retrieved real-space images of coupling of circularly polarized light at 1475 nm. Light is coupled into port 1 and 4 (2 and 3) for left-hand (right-hand) circularly polarized input. The locations of excitation spot and waveguides are indicated by dashed lines.

4

Furthermore, while all quality factors for ER_3 are slightly lower than for the perturbed cavity EX_3 (see Table 4.2 of the appendix), they remain on the same order of magnitude. The number of modes as well as their lifetime is considerably well retained even for a significant perturbation of the resonator's shape, which can be regarded as a further hallmark of topological protection. Moreover, the leakage radiation rate is a fundamental property that is not significantly affected by cavity size and shape.

4.2.5. COUPLING OF CAVITIES TO WAVEGUIDES

Lastly, we explore the potential of the QSHE-type PhC cavities as components in more complex nanophotonic devices when coupled to the topological edge states of a straight interface between expanded and shrunken lattices, and study the unique coupling behavior that originates from the helical nature of these states. Coupled systems of cavities and waveguides allow implementing desirable on-chip functionality such as directional coupling and add-drop filtering. Here, we consider a geometry that resembles a conventional ring resonator coupled to two waveguide channels on opposite ends. The cavity supports degenerate, clockwise (CW) and counter-clockwise (CCW) propagating modes that each couple differently to the traveling waveguide modes of the four-port system.

As sketched in Figure 4.7a, the coupling mechanism in conventional ring cavity-waveguide couplers typically relies on momentum conservation within the finite evanescent coupling region where waveguide and cavity boundary are in close proximity and run approximately parallel to each other. The CW (CCW) cavity mode only couples to waveguide modes with positive (negative) group velocity in the upper (lower) transmission channel. The situation is drastically different for coupled systems of QSHE-type PhC cavities and topological waveguides, outlined in Figure 4.7b exemplary for an ER_n cavity. Contrary to conventional systems,

the coupling behavior is dictated by spin conservation rather than momentum conservation, owing to the spin-momentum locking of the topological edge states that propagate along the interfaces constituting the waveguides and the cavity perimeter. Modes with positive (negative) pseudospin σ_+ (σ_-) only couple to modes with negative (positive) group velocity in the upper (lower) waveguide, precisely the reverse case as for the conventional coupler in Figure 4.7a. The coupling of CW and CCW WGMs (e.g., due to imperfections in the cavity) is largely suppressed in the topological PhC platform owing to the protection against backscattering that is effective so long as there are no spin-flipping defects admixing the pseudospin states. Moreover, due to the unique correspondence between edge state pseudospin and helicity of emitted radiation, it is possible to selectively excite either of the pseudospin states constituting the CW and CCW cavity modes from the far field by means of focused CP light. Polarimetric probing of straight domain walls evidences that the σ_+ pseudospin (corresponding to the CW WGM) is associated with LCP far-field radiation, while the σ_- pseudospin (corresponding to the CCW WGM) couples to RCP far-field radiation [129].

In Figure 4.7c, we demonstrate the selective excitation and spin-conserved coupling behavior of the pseudospins experimentally by focusing CP light at 1475 nm onto an ER_4 cavity that is coupled to two topological waveguides formed by armchair interfaces between expanded and shrunken domains. A clear switching of coupling directions is observed when changing the spin of the incident CP light from left- to right-hand. Light is coupled into ports 1 and 4 when we excite the CW WGM with LCP light, while incident RCP light excites the CCW WGM and results in coupling into ports 2 and 3.

It is important to stress that this type of chiral coupling behavior in which the spin is conserved is fundamentally linked to the origin of the doubly degenerate WGMs in the pair of helical edge states of the QSHE-type PhC platform. The chirality that the incident CP light carries manifests in the excitation of one of these two edge states and its helical propagation. The spin is conserved when coupling from waveguide to cavity and vice versa, and no spin-flipping occurs in either of the components. Despite the reduced rotational symmetry of the cavity (i.e., it is not circular) which would lead to coupling of CW and CCW modes in conventional ring resonators (e.g., via scattering at corners), there is little to no backscattering into the other pseudospin state within the cavity of the QSHE-type PhC platform. This hallmark of topological protection in which the spin is conserved across the cavity-waveguide coupler assures that the CW and CCW WGM do not admix if either of them is excited, and results in the chiral coupling behavior we observe. The SWMs, however, being non-degenerate and not originating from traveling waves, cannot exhibit the same chiral coupling behavior. In contrast to the doubly degenerate WGM modes which are protected from (back-) scattering into each other, the pseudospin states admix within the cavity when a SWM is excited and spin is thus not conserved across the cavity-waveguide coupler [247].

To demonstrate the different behavior of WGMs and SWMs, we study a coupler of similar geometry as in Figure 4.7c via numerical simulations (see Figure 4.8), details of which can be found in Section 4.5.3 of the appendix. An edge state

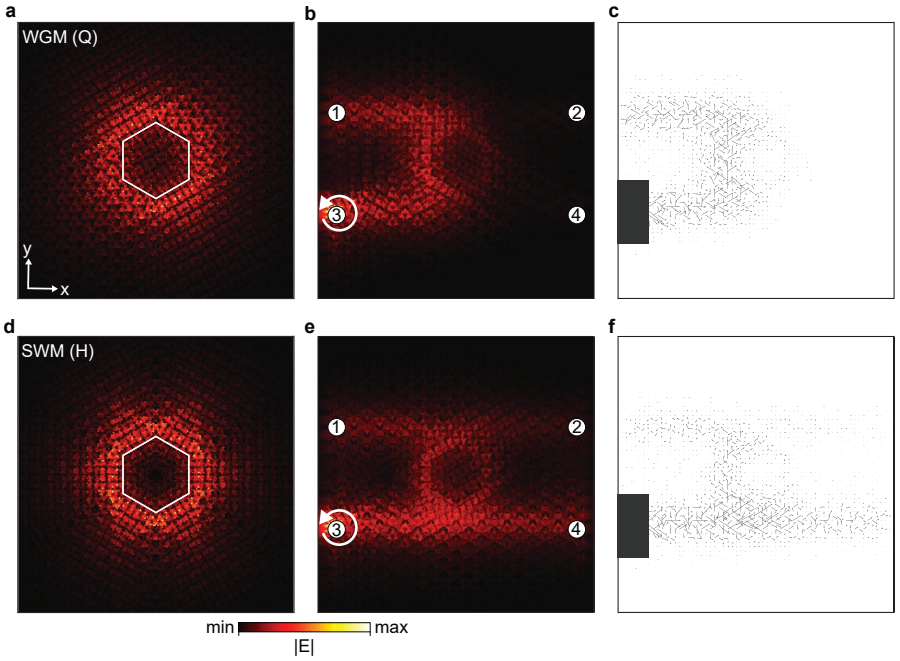

Figure 4.8: Coupling via traveling-wave and via standing-wave modes. a, Numerical simulation of the in-plane electric field magnitude of a quadrupolar (Q) whispering-gallery mode (WGM) of an ER_4 cavity. The cavity perimeter is indicated by white hexagonal outlines. **b,** Simulated device with similar geometry as in Figure 4.7, whereby the system is excited by a left-hand circularly polarized dipole source from port 3 at frequencies that couple to the WGM. **c,** Same as **b**, with arrows indicating the Poynting vector distribution. For reasons of visibility, the region containing the source is excluded from plotting (dark rectangle). **d-f,** Same as **a-c**, for a hexapolar (H) standing-wave mode (SWM) of the cavity.

with positive group velocity (σ_+) is excited at port 3 with an LCP dipole source, at frequencies that couple into either a quadrupolar WGM (Q) or a hexapolar SWM (H) of the ER_4 cavity (see also Figure 4.12c of the appendix). In the case of the Q mode (Figure 4.8a-c), we see that almost all light is coupled from port 3 to port 1 via the cavity. Moreover, this coupling takes place under the conservation of pseudospin. The left/right-asymmetry of the intensity distribution inside the cavity suggests that a rightward propagating mode launched in the bottom waveguide at port 3 couples to the CW WGM of the cavity, which then couples to a leftward propagating mode in the top waveguide toward port 1. This is also evidenced by considering the local flow of energy that is illustrated in Figure 4.8c by arrows with a length that is proportional to the time-averaged Poynting vector [257]

$$\langle \mathbf{S} \rangle = \frac{1}{2} \mathrm{Re}\left[\mathbf{E}^* \times \mathbf{H}\right], \tag{4.3}$$

where $\mathbf{E}$ ($\mathbf{H}$) is the electric (magnetic) field vector, Re[·] (Im[·]) refers to the real (imaginary) part of the argument, and * denotes the complex conjugate. This behavior is coherent with our schematic depiction of the σ_+ pseudospin coupling behavior

in Figure 4.7b. Since all the mode energy is coupled from port 3 to port 1 via the cavity under preservation of pseudospin (i.e., no backscattering), and considering that both waveguides are coupled to the cavity at comparable rates, the depicted scenario may be viewed as critical coupling regime. The simulation further serves to verify that the absorbing boundary conditions at the waveguide terminations work effectively, showing no significant backscattering (and associated spin-flipping) of the mode incident on the boundary at port 1, which would otherwise lead to noticeable signals reaching ports 2 and 4.

The situation looks different, however, for coupling to the H mode (Figure 4.8d-f). Firstly, a significant share of the mode energy launched with σ_+ pseudospin at port 3 reaches port 4. Considering the intensity distributions in the waveguide and the cavity, most of this energy seems to propagate past the cavity without being coupled to it (i.e., no critical coupling), while a smaller part is likely coupled back from the cavity into the lower waveguide toward port 4 due to the absence of spin-conservation for the SWM. The presence of notable mode energy propagating rightward in the top waveguide toward port 2, which corresponds to the pseudospin state σ_- (cf. also Figure 4.7b), is a strong indicator for the absence of spin-conservation in the coupler geometry when targeting SWMs. This is in contrast to the situation observed for the WGMs and highlights the different nature of these modes.

4.3. CONCLUSION

In conclusion, we experimentally investigate the optical confinement and radiation of telecom light in leaky topological PhC cavities mimicking the QSHE via Fourier spectropolarimetry and corroborate our measurements with full-wave finite-element-method calculations. The cavities support both traveling WGMs and extended PhC defect SWMs, corresponding to the ideally degenerate D/Q and non-degenerate M/H multipoles. We elucidate the origin and scaling behavior of the multipolar modes supported by the system and relate it to the angularly resolved radiation patterns and spatial cavity mode profiles, providing a route toward selectively addressing individual modes by spectral, spatial, angular, and polarimetric means. We discuss the implications of the simultaneous presence of radiative loss and non-trivial topology onto the modes' properties, demonstrating the robustness of cavity spectra and quality factors with respect to alterations of shape and size, in sharp contrast to conventional, topologically trivial micro- and nanocavities. Finally, we examine the different coupling behaviors of the cavities' SWMs and WGMs to topological waveguides. Due to their origin in the propagating helical topological edge states, only the doubly degenerate WGMs conserve the pseudospin within the cavity and display a chiral critical coupling behavior, while the non-degenerate SWMs generally admix both pseudospin states. The key advantage of robustness alongside other inherent properties like radiation in vortex beam modes make them promising building blocks for applications in integrated passive and active nanophotonic devices [31]. The helical edge state transport and associated spin-conserved coupling behavior, together with the possibility to selectively excite pseudospin states from the far field, represents an attractive feature for applications in chiral (quantum) optics. Although our study focuses

on the technologically relevant telecommunication band, these findings may be applied more broadly in the context of lossy topological bosonic systems, including other frequency regimes as well as mechanical and phononic platforms. As such, we envision the results of our study to advance the development of novel functional devices that aim to manipulate and control classical and quantum information.

4.4. METHODS

4.4.1. SIMULATIONS

Full-wave finite-element-method simulations in 3D were performed using the COMSOL Multiphysics RF Module [258]. The refractive index of silicon was set to $n = 3.48$, with a slab thickness of 220 nm. The unit cell consisted of equilateral triangular air holes, with a triangle side length of $s = 250$ nm and a lattice constant of $a = 800$ nm. By adding perfectly matched layers above the simulation box, we retrieve the linewidth of the (quasinormal) eigenmodes, defined as two times the imaginary part of the complex eigenfrequency. The simulation domain was chosen to be hexagonal to match the C_6 symmetry of the system, and terminated by scattering boundary conditions. We extract the near-field profiles on a regular grid in a plane located 20 nm above the slab. The near-field phase enables us to classify the cavity modes according to their multipolar nature, and the full field information is used to retrieve the far-field radiation patterns and spatial cavity mode profiles, as detailed in the main text of this chapter.

4.4.2. SAMPLE DESIGN

The PhC lattice design featured a honeycomb configuration of equilateral triangles (side length $s = 0.3125 \cdot a$) in a hexagonal unit cell with lattice constant a. The unit cell expansion factor r/r_0 was chosen to be 0.91 and 1.09 for the shrunken and expanded case, respectively, whereby r is the distance of the centroids of the triangular air holes from the unit cell center, with $r = r_0$ for a perfectly triangular lattice. Two samples were fabricated, with $a = 800$ nm in Figure 4.2 and Figure 4.6, and $a = 852$ nm in all other experimental images. The design was implemented in a silicon-on-insulator platform with a 220 nm thick silicon layer on a 3 μm buried oxide layer. The fabrication process is described in detail in Section 2.1.

4.4.3. EXTRACTION OF CAVITY MODE FREQUENCIES AND QUALITY FACTORS

In order to extract the center frequencies and quality factors of the cavity modes from cross-cuts of the normalized reflection, we fit a set of general (Fano) resonance lineshapes of the form

$$R(\omega) = \left| A_0 + \sum_{j=1}^{n} A_j e^{i\phi_j} \frac{\gamma_j}{\omega - \omega_{0_j} + i\gamma_j} \right|^2, \tag{4.4}$$

where A_0 is a constant background amplitude; and A, ϕ, and $\omega_0 - i\gamma$ are the amplitude, phase, and complex frequency of individual Lorentzians, respectively. For

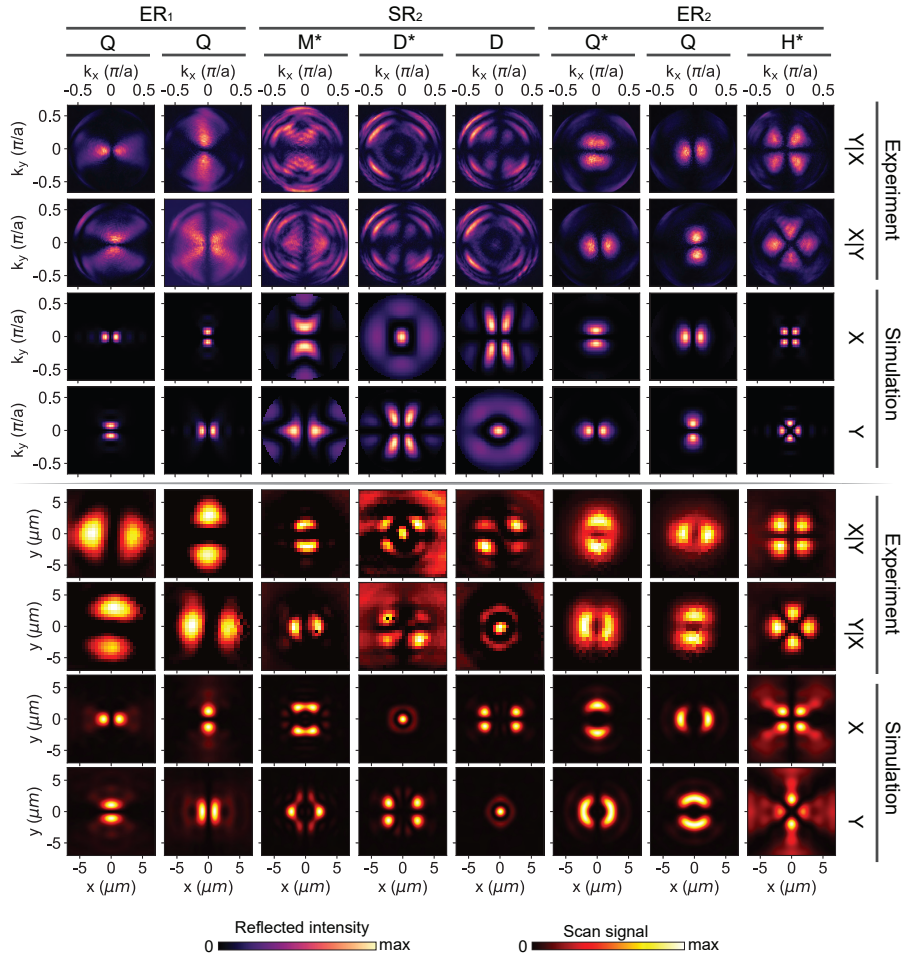

Figure 4.9: Cavity mode profiles in real and momentum space. Radiation patterns and spatial cavity mode profiles for various cavity modes in ER_1, SR_1, ER_2, and SR_2 (see Figure 4.3 and Figure 4.4a,b). The settings of polarizer and analyzer in experiments and the linear polarization of the numerically retrieved fields are indicated, as well as the monopolar (M), dipolar (D), quadrupolar (Q), and hexapolar (H) nature of the modes. M^*, D^*, Q^*, and H^* denote the same modes as in Figure 4.3 and Figure 4.4a,b. Each panel is normalized to its respective maximum for reasons of visibility.

cross-polarized measurements $n = 1$, i.e., the lineshape is well reproduced by a single Lorentzian due to negligible A_0. For reflection measurements recorded without analyzer $n = 2$, whereby one of these Lorentzians models the cavity mode, while the second (broad) Lorentzian accounts for the slowly varying background reflection. Quality factors are defined as $Q_j = \omega_0/(2\gamma_j)$.

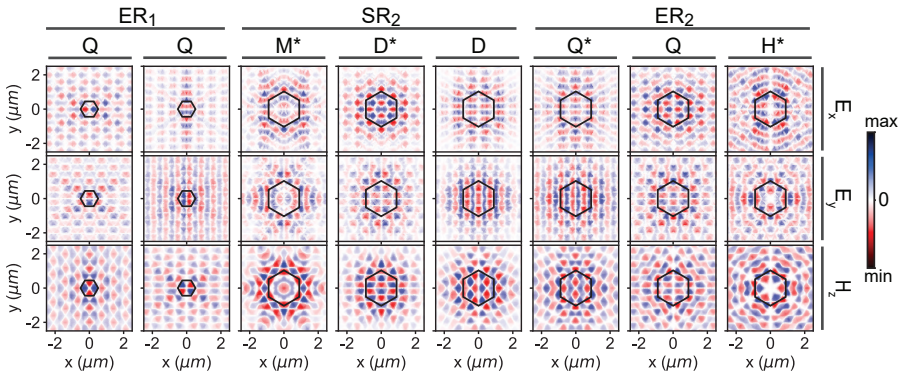

Figure 4.10: Simulated cavity mode near-fields. Simulated real parts of the non-zero field components (E_x, E_y, H_z) in the symmetry plane of the TE-type photonic crystal, for the cavity modes shown in Figure 4.9. The cavities' perimeters are indicated by black hexagonal outlines.

4.5. APPENDICES

4.5.1. RADIATION PATTERNS AND SPATIAL CAVITY MODE PROFILES

In the top panel of Figure 4.9, we compare experimentally and numerically retrieved polarization-resolved radiation maps (see also Figure 4.2) for a selection of modes that is partly included in Figure 4.3, encompassing every multipole present in our system. The measured back focal plane patterns correspond well to the simulated radiation profiles, retrieving all characteristic symmetries of the individual multipolar resonances. By comparing these to the numerically obtained near-field maps of the out-of-plane magnetic field component H_z in the symmetry plane of the TE-type photonic crystal shown in Figure 4.10, we can infer the multipolar order of the probed cavity modes. Apart from the dipolar resonances (D/D^*), both in-plane components of the modes' far fields feature radial nodal lines which, together with the phase information in Figure 4.10, shows that they represent vector beams that carry one (monopoles M and quadrupoles Q) or two (hexapoles H) quanta of orbital angular momentum. As such, reciprocity implies most efficient excitation of these modes with similar vectorial input beams, such as higher order Laguerre-Gaussian beams. Reciprocity also dictates the relation between the symmetries of the angularly resolved far-field radiation and the spatial profiles of the cavity modes shown in the bottom panel of the figure.

The spatial mode profile is determined by calculating the excitation efficiency η of a cavity mode $\mathbf{E}_{\text{cav}}$ under illumination with the incident field $\mathbf{E}_{\text{in}}$ propagating along z. We notice that, if the wavefronts of both fields have the same frequency and the complex field profiles are well-matched in a certain z-plane, they remain well-matched during further propagation (i.e., η is conserved during free-space propagation). We can thus, without loss of generality, consider the mode overlap in the symmetry-plane of the photonic crystal ($z = 0$) and omit the z-dependence in the observables. For the TE-polarized guided modes in our photonic crystal it holds that $\mathbf{E}_{\text{cav},z} = 0$ in the symmetry-plane, i.e., the cavity mode is purely transverse for

$z = 0$. Furthermore, our radially symmetric focusing scheme does not admix the orthogonally polarized field components along x and y. In our calculations of η we can therefore decompose the vectorial observables into their Cartesian in-plane components along $j = x, y$ and consider them separately. In experiments, we record the spatially resolved $\eta_j(x, y)$ by sweeping the position of the incident beam while assuming the cavity mode to remain centered around the origin, i.e.,

$$\eta_j(x, y) = \left| \iint \mathrm{d}x' \mathrm{d}y' \, E^*_{\mathrm{cav},j}(x', y') \, E_{\mathrm{in},j}(x' - x, y' - y) \right|^2 . \tag{4.5}$$

Note that, for simplicity, we omit the commonly performed normalization of η w.r.t. the total power. To gain further insight into the symmetry relations between the fields and the recorded signal let us first consider the complex quantity

$$\eta'_j(x, y) = \iint \mathrm{d}x' \mathrm{d}y' \, E^*_{\mathrm{cav},j}(x', y') \, E_{\mathrm{in},j}(x' - x, y' - y) , \tag{4.6}$$

such that $\eta_j = |\eta'_j|^2$. By applying a two-dimensional Fourier transform in consideration of the convolution theorem, taking the absolute squared of the resulting equation, and performing a back-transformation to the spatial domain, we finally arrive at an expression for the excitation efficiency

$$\eta_j(x, y) = \mathcal{F}^{-1} \left\{ \left| \hat{E}^*_{\mathrm{cav},j}(k_x, k_y) \, \hat{E}_{\mathrm{in},j}(k_x, k_y) \right|^2 \right\} , \tag{4.7}$$

where $\hat{E}_{\mathrm{cav},j}$, $\hat{E}_{\mathrm{in},j}$ are the spectral representations of the cavity mode and input field, respectively, and $\mathcal{F}^{-1}$ denotes the two-dimensional inverse Fourier transform. The Fourier transform (and its inverse) commutes with orthogonal symmetry transformations such as rotations and reflections, and we can thus directly infer that η_j has the same symmetries as the intensity of the product of $\hat{E}_{\mathrm{cav},j}$ and $\hat{E}_{\mathrm{in},j}$. Since in our case the input field is represented by a rotationally invariant Gaussian beam, η_j retains the discrete symmetries of $\hat{E}_{\mathrm{cav},j}$. This fact is corroborated by the back focal plane patterns and spatial cavity mode profiles presented in Figure 4.9.

4.5.2. COMPARISON WITH TRIVIAL PHOTONIC CRYSTAL CAVITIES

After establishing the scaling behavior of cavity mode frequencies (see Figure 4.3a,b) and quality factors (see Figure 4.6 of the main text and Table 4.1, Table 4.2) in the topological photonic crystal platform, it is natural to ask how this compares to conventional photonic crystal cavities.

To this end, we perform numerical studies on a commonly used two-dimensional topologically trivial photonic crystal platform, constituted of a triangular lattice of circular air holes (radius $r = 120\,\mathrm{nm}$) perforating a silicon slab (see Figure 4.11a, inset). The silicon slab has the same thickness $d = 220\,\mathrm{nm}$ as for the topological PhC (see Section 4.4.2), and we choose a lattice period of $a = 420\,\mathrm{nm}$ to obtain a bandgap in the telecom regime (see Figure 4.11a). By selectively removing holes, we introduce hexagonal defects H_n with side length $n = 1 \ldots 4$ into the trivial lattice and obtain cavities that are similar in shape to the ones studied in the

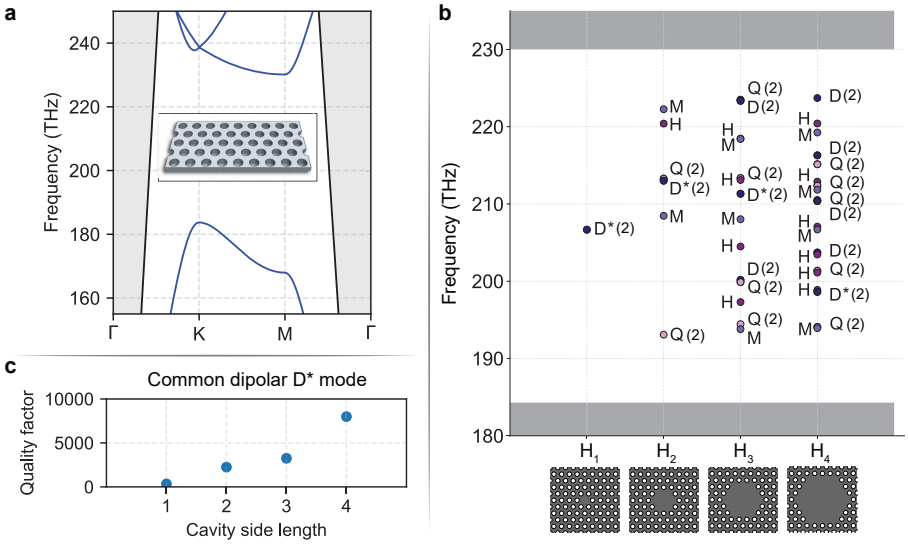

Figure 4.11: Cavity modes in a topologically trivial platform. a, Band structure of the topologically trivial photonic crystal schematically depicted in the inset. Regions inside the light cone are shaded in gray. **b,** Mode structure of PhC defect cavities of increasing size. The bulk band regions are shaded in gray, doubly degenerate modes are denoted by '(2)'. **c,** Quality factors of the dipolar D^* mode common to all cavities in **b**.

4

topological PhC platform. The mode spectra, however, show significantly different behavior (see Figure 4.11b). Since the mode localization is based exclusively on photonic bandgap confinement, we observe modes that are distributed around the bandgap center, with no (or very lossy) modes close to the band edges. The mode spectra feature no simple scaling behavior of the multipolar resonances as in the topological case, where band-inversion dictates the frequency shift with varying cavity size. One of the hallmark properties that our cavities derive from their origin in a topological bulk band structure and edge states is the insensitivity of the quality factor toward cavity size (see Figure 4.6a). This is strikingly different for the trivial defects, where we observe a dramatic increase in the quality factor of the dipolar D^* mode with size (see Figure 4.11c). Note that, except for the H_1 cavity, the quality factors here significantly exceed those of the topological cavities due to the absence of leakage radiation.

In conclusion, the cavity mode spectra and their scaling behavior in the QSHE-type PhC platform, as well as their insensitivity toward variations of size and shape, are properties that derive from the origin in a topological bulk band structure and are distinct from trivial PhC cavities.

4.5.3. EFFECTIVE TWO-DIMENSIONAL MODEL

Due to the large model domain size that would be too computationally intensive to simulate in 3D, we use an effective 2D model to perform the numerical calculations of coupled cavity-waveguide-systems shown in Figure 4.8. In order to reproduce the

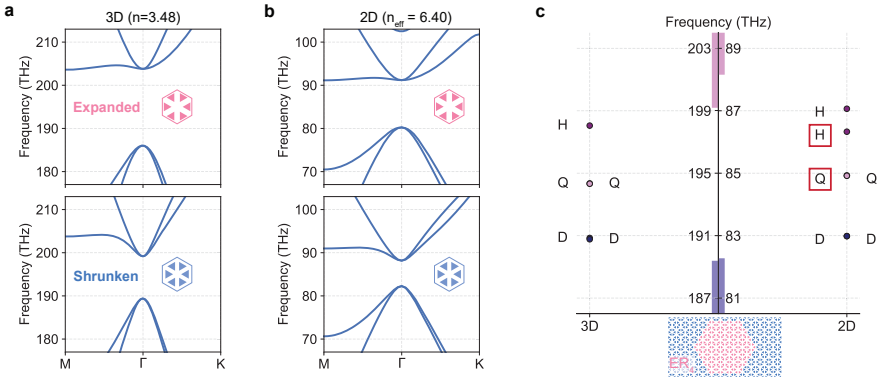

Figure 4.12: 3D vs 2D bulk bands and cavity modes. a, Bulk bands of an expanded (top) and a shrunken (bottom) unit cell, with a refractive index of silicon $n_{Si} = 3.48$ (as throughout the main text of this chapter). **b,** Same as **a** for an effective 2D model with refractive index $n_{eff} = 6.4$. **c,** Comparison of ER_4 cavity modes within the surrounding bulk bandgap (indicated by colored bars, see Figure 4.4) for the case of 3D and 2D simulations. Vertical bars indicate the dipolar (p-type, purple) and quadrupolar (d-type, pink) bands of the bulk lattice surrounding the cavity. The quadrupolar (*Q*) and hexapolar (*H*) modes shown in Figure 4.8 are highlighted by red frames.

optical properties in 2D simulations, we need to adapt an effective refractive index n_{eff} in place of the real refractive index $n_{Si} = 3.48$ of silicon at telecom wavelengths. Values of n_{eff} smaller than n_{Si} turn out to only feature an indirect bandgap at the Γ point, strongly affecting the spectral properties of the edge states and cavity modes we intend to simulate. We therefore choose a value of $n_{eff} = 6.4$ that, despite a considerable shift in frequency, results in a similar bulk band structure (Figure 4.12a,b) with direct bandgaps and similar cavity mode spectra (Figure 4.12c) and localization (Figure 4.10 and Figure 4.8) as in the 3D case.

Table 4.1: Quality factors of the photonic crystal cavity modes analyzed in Figure 4.6a, whereby the straight zigzag edge in reference [129] has $Q = 486$.

Cavity	Quality factor
ER_1	616 ± 39
ER_2	483 ± 61
ER_3	492 ± 97
ER_4	561 ± 125
SR_1	345 ± 44
SR_2	336 ± 67
SR_3	376 ± 45
SR_4	394 ± 35

Table 4.2: Quality factors of the photonic crystal cavity modes analyzed in Figure 4.6b, in descending order of frequency.

Mode	Quality factor ER_3	Quality factor EX_3
1	492 ± 72	626 ± 85
2	405 ± 63	581 ± 86
3	248 ± 21	380 ± 31
4	238 ± 31	271 ± 19

5

OBSERVATION OF LANDAU LEVELS AND CHIRAL EDGE STATES IN PHOTONIC CRYSTALS VIA STRAIN-INDUCED PSEUDOMAGNETIC FIELDS

The control over light propagation and localization in photonic crystals offers wide applications from sensing and on-chip routing to lasing and quantum light-matter interfaces. While in electronic crystals magnetic fields can be used to induce a multitude of unique phenomena, the uncharged nature of photons necessitates alternative approaches to bring about similar control over photons at the nanoscale. Here, we experimentally realize pseudomagnetic fields in two-dimensional photonic crystals through engineered strain of the lattice. Analogous to strained graphene, this induces flat-band Landau levels at discrete energies. We study the spatial and spectral properties of these states in silicon photonic crystals at telecom wavelengths with far-field spectroscopy. Moreover, taking advantage of the photonic crystal's design freedom, we realize domains of opposite pseudomagnetic field and observe chiral edge states at their interface. We reveal that the strain-induced states can achieve remarkably high quality factors despite being phase-matched to the radiation continuum. Together with the high density of states and high degeneracy associated with flat bands, this provides powerful prospects for enhancing light-matter interactions, and demonstrates a design principle to govern both on-chip and radiating light fields.

This chapter is based on Barczyk et al., *arXiv:2306.03860* (2023)

5.1. INTRODUCTION

In condensed matter physics, magnetic fields provide a versatile mechanism to control the behavior of electrons in materials. For example, a magnetic field piercing a two-dimensional electron gas induces flat bands at discrete energies known as Landau levels, which can be viewed as the quantization of the electrons' cyclotron motion in the magnetic field. Moreover, at the system's boundaries, the magnetic field implies the existence of chiral edge states associated with the quantum Hall effect. In photonics, the idea of controlling light in a similar way has been a tantalizing prospect. While at microwave frequencies magneto-optic effects may be strong enough to effectively mediate interactions between photons and real magnetic fields [23], this approach is unfeasible for optical frequencies. Realizing an effective magnetic control over photons in dielectric photonic systems without relying on actual external magnetic fields represents an especially luring proposition for on-chip, nanophotonic systems.

In graphene, pseudomagnetic fields (PMFs) can be induced for electrons via mechanical strain of the lattice, as the corresponding perturbation to inter-atomic hopping mimics the action of a magnetic gauge potential [86, 140, 141, 259]. Contrary to real magnetic fields that break time-reversal symmetry, strain-induced PMFs carry opposite signs for the two non-equivalent Dirac cones at the K and K' valleys. Nevertheless, they still give rise to intriguing phenomena including Landau-level quantization and chiral edge states. Analogously, suitable lattice deformations can act as magnetic gauge potentials in bosonic systems. Their effects have been studied in lattices of coupled waveguides [142, 260], arrays of microwave resonators [261, 262], microcavity exciton-polaritons [118, 263], and in acoustic platforms [264–268].

Recently, Guglielmon and coworkers predicted that inhomogeneous deformations in honeycomb photonic crystal (PhC) membranes can act as a magnetic gauge potential, creating synthetic strain through a designed perturbation of the dielectric function $\epsilon(\mathbf{x})$ [143]. Strain-induced pseudomagnetism in photonic crystals is nontrivial because of inherent long-range interactions. It would however be highly appealing as it provides a new paradigm for the on-chip routing and confinement of light [269, 270], and a path to enhance light-matter interactions and nonlinearities through the high degeneracy and high local density of states of photonic Landau levels, associated with their nature as flat bands [271–275].

Here, we realize pseudomagnetic fields in silicon photonic crystals at telecom wavelengths, and demonstrate the emergence of photonic Landau levels. Using far-field Fourier spectropolarimetry [128–130], we study the characteristic energy scaling of Landau levels with strain, their delocalization, and loss mechanisms. We reveal that they can exhibit remarkably high quality factors, even though they exist within the radiation continuum. We finally demonstrate the creation of inhomogeneous pseudomagnetic fields by spatial tailoring of the strain field. This allows observing signatures of the chiral edge states that are predicted to exist at the boundaries of domains with opposite magnetic fields [276] and which are distinct from other crystal symmetry-based implementations of chiral edge states in photonic crystals [119, 270, 277, 278]. Our findings illustrate the applicability of

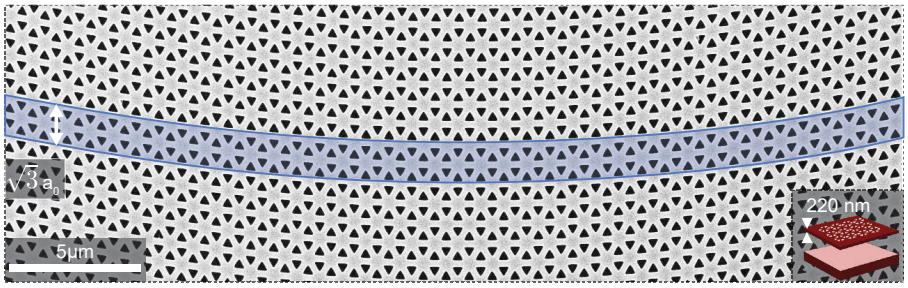

Figure 5.1: Sample geometry. Scanning electron micrograph of a fabricated photonic crystal membrane, with the sample geometry depicted in the inset. The supercell of the strained honeycomb lattice is highlighted in blue, with periodicity $a = \sqrt{3}a_0$ along the y-direction, and a_0 denoting the lattice constant of the underlying pristine honeycomb lattice.

synthetic strain engineering for the control of light and its interaction with matter at the nanoscale.

5.2. RESULTS AND DISCUSSION

5.2.1. OBSERVATION OF PHOTONIC LANDAU LEVELS

We fabricate suspended silicon membranes perforated by triangular air holes using electron-beam lithography and wet etching of a silicon-on-insulator substrate with a 220 nm thick silicon layer on a 3 μm buried oxide layer [146, 147]. The fabrication process is described in detail in Section 2.1. The PhC lattice design features a honeycomb configuration of equilateral triangles (side length $s = 0.3125a$) in a hexagonal unit cell with lattice constant $a = 827$ nm. Figure 5.1 shows a scanning electron micrograph of a fabricated strained PhC lattice, where the inset depicts a three-dimensional cross-cut of the slab. We follow the approach outlined in [143] to induce a uniform pseudomagnetic field $\mathbf{B}_{\text{eff}}$ piercing the PhC plane. The starting point is a pristine TE-type honeycomb PhC with lattice constant a_0 and dielectric distribution $\epsilon(\mathbf{x})$ ($\mathbf{x} = (x, y)$). The lattice is oriented with the zigzag and armchair directions along the x and y axes, respectively. The PhC's frequency spectrum features a Dirac-type crossing (Figure 5.2a) and is governed by the scalar Helmholtz equation for the out-of-plane magnetic field $\mathbf{H}(\mathbf{x}) = H_z(\mathbf{x})\hat{\mathbf{z}}$ (cf. also Equation (1.30) in Section 1.4)

$$-\nabla \cdot (\epsilon^{-1}(\mathbf{x})\, \nabla) H_z(\mathbf{x}) = (\omega/c)^2\, H_z(\mathbf{x})\,. \tag{5.1}$$

The calculated dispersion is plotted in Figure 5.2a for the k_y direction, with the Dirac point appearing at $k_y = 0$ for a lattice constant of $a = \sqrt{3}a_0$, which is the minimal periodicity when implementing the strain profile.

This uniaxial strain is realized by displacing each point $\mathbf{x}$ in the PhC plane via $T(\mathbf{x}) = \mathbf{x} + \mathbf{u}(\mathbf{x})$, with quadratic displacement function $\mathbf{u}(\mathbf{x}) = (0, a^{-1}(\kappa x)^2)$ and the parameter κ representing the strain magnitude. The displacement thus breaks the x-periodicity but preserves the larger super-cell periodicity a along y. In the vicinity of the K and K' valleys the eigenfunctions' dynamics are captured by a 2D Dirac-type

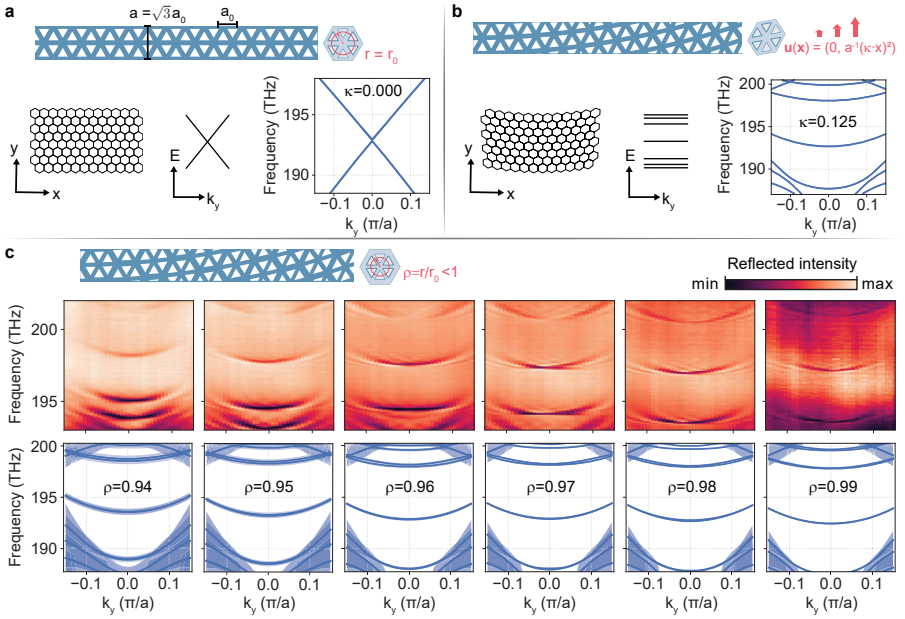

Figure 5.2: Strain-induced Landau levels. a, Schematic real-space geometry and dispersion of a pristine honeycomb lattice, together with simulated photonic bulk bands. The dispersion is characterized by a Dirac-type linear crossing. **b,** A bandgap is opened in place of the original Dirac-type crossing due to strain, and flat Landau levels emerge symmetrically distributed around the bandgap center. The applied displacement function is given by $\mathbf{u}(\mathbf{x})$. **c,** Experimentally (top) and numerically (bottom) retrieved angularly resolved spectra showing photonic Landau levels in strained photonic crystal lattices for increasing $\rho = r/r_0$ ($\kappa = 0.125$ in all cases), where ρ denotes the relative displacement of holes within a hexagonal unit cell with respect to a pristine lattice ($\rho = 1$). The linewidth in simulations is scaled by a factor two for enhanced visibility.

Hamiltonian (cf. also Section 1.3) [86]

$$H_{\text{eff}} = v_D[-i\nabla_{\mathbf{x}} - \mathbf{A}_{\text{eff}}(\mathbf{x})] \cdot \sigma\,, \tag{5.2}$$

figure with Dirac velocity v_D, Pauli matrices $\sigma = (\sigma_1, \sigma_2)$, and effective magnetic vector potential $\mathbf{A}_{\text{eff}}$ that is related to the displacement function $\mathbf{u}$ via

$$\mathbf{A}_{\text{eff}} \propto \begin{pmatrix} u_{x,x} - u_{y,y} \\ -(u_{x,y} + u_{y,x}) \end{pmatrix}, \tag{5.3}$$

where $u_{i,j} = \frac{\partial u_i}{\partial x_j}$. The solutions to the eigenvalue problem associated with Equation (5.2), up to first order $\mathcal{O}(\kappa)$, correspond to flat states at discrete frequencies that are symmetrically distributed around the original Dirac-cone frequency ω_D (Figure 5.2b). These constitute Landau levels that follow the square-root law (cf. also Equation (1.27))

$$\omega_n = \omega_D \pm \frac{v_D c^2}{\sqrt{2}\omega_D} \sqrt{n|\mathbf{B}_{\text{eff}}(\kappa)|}, \quad n = 0, 1, 2, ldotsc, \tag{5.4}$$

where the effective magnetic field amplitude is given by $|\mathbf{B}_{\text{eff}}(\kappa)| = |\nabla_{\mathbf{x}} \times \mathbf{A}_{eff}(\kappa)| = B_0\kappa^2$, and B_0 is a constant parameter specific to the (meta)material [143, 276]. To make the strain-induced photonic Landau levels experimentally accessible via far-field Fourier spectroscopy (see Section 2.2 for details on the setup), we enhance their radiative coupling by applying an additional type of sub-lattice symmetry breaking via concentrically shrinking the radial position r of six air holes within a hexagonal unit cell by a factor of $\rho = r/r_0$ (Figure 5.2c), where $r = r_0$ for the pristine honeycomb PhC [119, 128–130].

Figure 5.2c presents the wavevector- and frequency-resolved reflectance for two shrinking factors $\rho = 0.99$ and 0.97, highlighting the substantial enhancement in band visibility achieved through the symmetry breaking mechanism. Here, we recognize pronounced, largely horizontal bands in the photonic dispersion, in a striking departure from the linear Dirac-cone dispersion of the unperturbed lattice. This constitutes the first result of our study — the experimental observation of photonic Landau levels in a strained PhC membrane. The clarity with which these states can be resolved is testament to the low loss and large scale of the PhC implementation. The Landau levels are unaffected by the shrinking factor (Figure 5.2c). They are distributed around the $n = 0$ Landau level at $\omega_D \approx 2\pi \cdot 197\,\text{THz}$ and exhibit Fano lineshapes due to interference with the broad reflection background (see Section 2.2). In the following, if not stated otherwise, the presented reflection measurements are of PhCs with $\rho = 0.98$ that have bands which are well visible whilst keeping the symmetry breaking weak.

The strain magnitude, as controlled by the parameter κ, largely affects the energy landscape of the PhC (Figure 5.3a). We see that the bandgap size increases with κ, and successively more flat states emerge around ω_D. Extracting their center mode frequencies at the Γ point from fits to the experimental lineshape (see Equation (5.5) in Section 5.4.2), we recognize that the retrieved level separation follows the expected square root scaling that is unique to massless Dirac particles in an increasingly strong external (pseudo-)magnetic field — see Equation (5.4). This characteristic energy scaling is further supported by eigenfrequency simulations (Figure 5.3b). Together, the results of Figure 5.3 underline the origin of the resolved states in the strain-induced PMF.

5.2.2. LOCALIZATION AND RADIATION

Long-range interactions in the PhC lattice render the photonic Landau levels weakly dispersive away from the Γ point, increasing in frequency with $|k_y|$ (Figure 5.4a) [143]. Coupling beyond next-nearest-neighbors corresponds to higher order contributions ($\mathcal{O}(\kappa^2)$) in Equation (5.4). It thus represents a feature specific to the photonic platform, differentiating it from the tight-binding graphene analogue. The spatial localization of the states also displays a clear dependence on k_y. Figure 5.4b shows the simulated fields of the $n = 0$ Landau level at three different k_y values. All bands are doubly degenerate, with fields that are even and odd with respect to the mirror symmetry axis of the lattice along $x = 0$ — or an orthogonal pair of superpositions thereof, as we plot in Figure 5.4b. While the states' transverse extent for $k_y = 0$ — where the group velocity vanishes — spans many unit

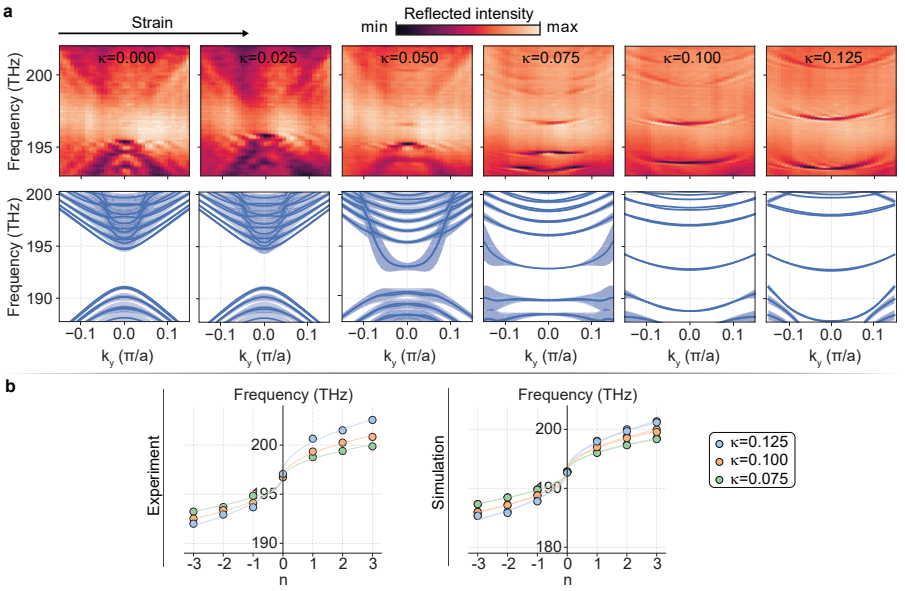

Figure 5.3: Photonic Landau levels in increasingly strong pseudomagnetic fields. a, Far-field reflection spectra displaying the evolution of photonic bands with increasing strain magnitude κ, alongside numerical simulations of the photonic bands. The gap at small κ is due to the sub-lattice symmetry breaking ($\rho = 0.98$). **b,** Experimentally and numerically extracted center mode frequencies of photonic Landau levels for varying κ, fitted respectively with a square-root scaling law. The small mode splitting of the (ideally doubly degenerate) modes in simulations is a finite-size effect and not resolvable in our far-field measurements.

5

cells, it appears finite nonetheless. For finite wavevector k_y, the fields are localized further away from the center, eventually transforming into trivial chiral states that propagate along the armchair edges of the lattice (Figure 5.4b) [143, 279, 280].

We see this behavior confirmed in experiment when scanning the excitation focus along x, as shown in Figure 5.4c. In Figure 5.4c, we plot the measured states for two pairs of orthogonal incident polarizations, i.e., x/y-linear and right-/left-circular, respectively. Interestingly, we recognize that a mode with positive k_y can be excited either with right-circular polarization to the left of the center ($x = -3\ \mu$m) or with left-circular polarization to the right ($x = 3\ \mu$m). Thus, these states form a degenerate pair with opposite pseudospin (encoded as far-field helicity) linked to transverse localization. We note that an equivalent pair with opposite handedness exists in the backwards direction, owing to time-reversal symmetry. For excitation near the center $x = 0$, the flat part of the band near $k_y = 0$ is probed for any polarization.

The transverse localization is also linked to the losses of the states, manifested in their resonance linewidths. We distinguish four possible sources of loss: (i) intrinsic far-field radiation, due to the fact that the states inherently reside within the radiation continuum, (ii) losses associated with the edge of the lattice at large $|x|$, due to either scattering or leakage into slab modes, (iii) losses due to scattering

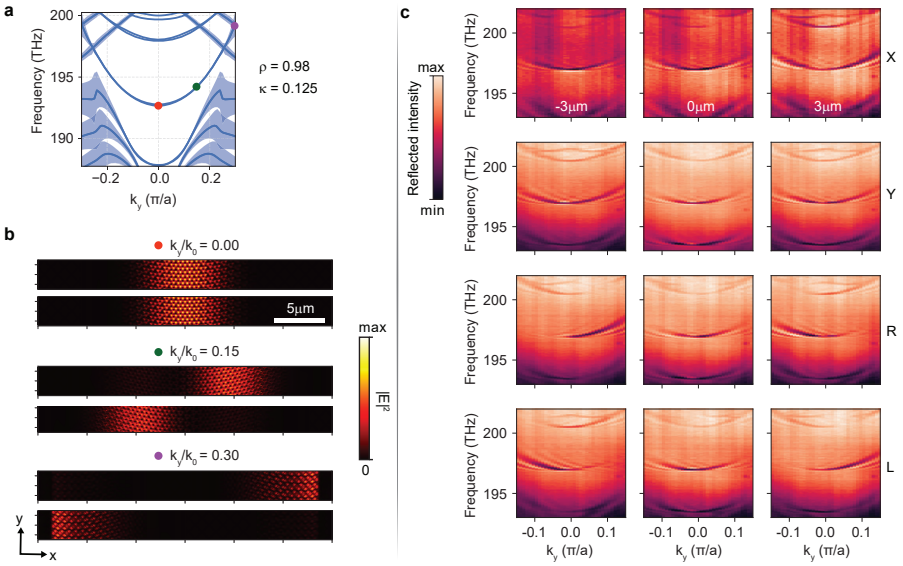

Figure 5.4: Landau level localization and polarization. a, Simulated bands of a shrunken strained lattice. **b,** Simulated mode profiles of the in-plane electric field intensity for selected values of k_y (indicated in **a**). **c,** Position- and polarization-dependent excitation of photonic Landau levels, where the displacement in x relative to the lattice center and the x/y-linear (X/Y) and right-/left-circular (R/L) polarization state of the incident beam are indicated.

at random disorder, and finally (iv) the radiation losses associated with non-unity shrinking factor ρ, which are intentionally introduced to facilitate the free-space measurements. At the Γ point, we determine the quality factors of the $n = 0$ level from linewidth fits (Figure 5.5a). The measured quality factors reach $Q \approx 7000$ for the weakest symmetry breaking $\rho = 0.99$, close to the spectral resolution limit (see Section 2.2). The fact that losses increase strongly with smaller ρ shows that at $k_y = 0$ they are limited by the non-intrinsic losses due to non-unity ρ. In fact, the linearly decreasing trend of linewidth with ρ shows that losses are negligibly small when extrapolated to $\rho = 1$. Numerical simulations with and without absorbing boundary conditions (see Section 5.4.1) indeed show that radiative losses dominate (Figure 5.5b, top), and the intrinsic quality factor ($\rho = 1$) is calculated to be on the order of $Q \sim 10^7$ (Figure 5.5b, bottom). This is a remarkably high value, given that the photonic Landau levels are inherently residing within the free-space radiation continuum, as can also be seen from numerical simulations of the complex mode frequencies (Figure 5.5c). So while the strain perturbation strongly alters the real parts of the spectrum, transforming the linear Dirac dispersion into flat Landau levels, it leaves the imaginary parts close to zero. From the k_y-dependent reflection spectra in Figure 5.4c, we see that resonance linewidths increase away from the Γ point. This can be related to the shift in localization away from the lattice center toward the edges, accompanied by increased in-plane losses (ii) that dominate for large wavevectors (Figure 5.5d), reducing the visibility of the bands in experiment

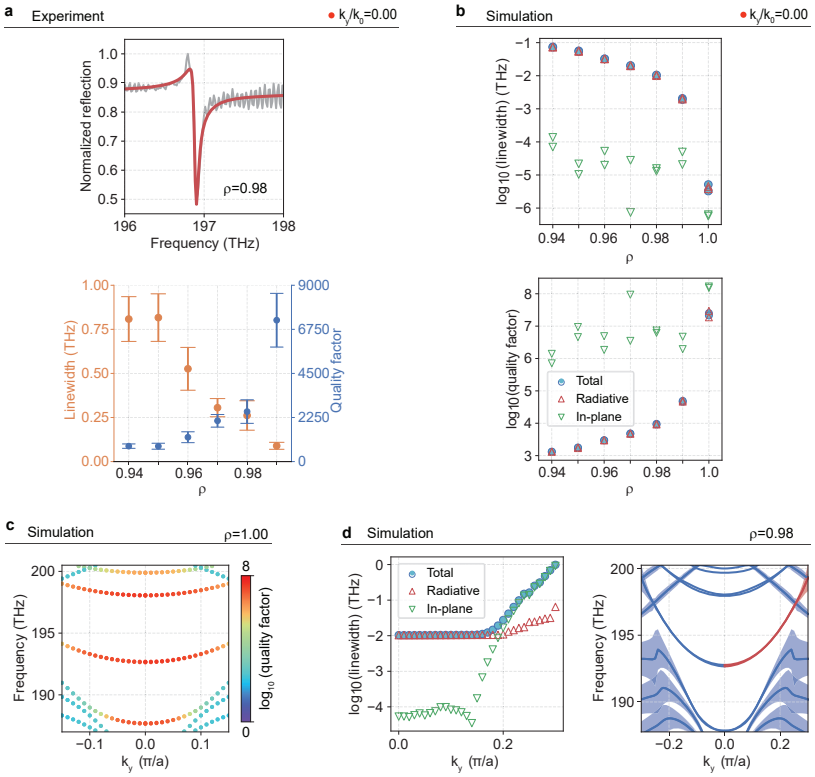

Figure 5.5: Landau level losses. a, Fano-fits to the measured lineshapes (top) yield the experimentally extracted linewidths and quality factors of the $n = 0$ Landau level at the Γ point as a function of ρ (bottom). The linewidths are averaged over seven cross-cuts of the recorded dispersion along k_y (around $k_y \approx 0$) and given alongside the standard error. **b,** Numerically retrieved linewidths (top) and quality factors (bottom), showing the respective contributions of radiative and in-plane losses to the total mode loss. **c,** Numerically retrieved bands of a pristine strained photonic crystal featuring Landau levels, with color-coded quality factors. **d,** Numerically retrieved contributions of radiative and in-plane losses to the total linewidth of the zeroth Landau level (left), corresponding to the section of the band highlighted in red (right). The strain magnitude is $\kappa = 0.125$ for all panels.

as they become under-coupled to free-space radiation.

5.2.3. CHIRAL EDGE STATES AT DOMAIN WALLS

A defining advantage of the PhC platform is the ease with which optical potentials can be tailored at will as a function of position. Indeed, different gauge potentials (Equation (5.3)) can be realized through different deformations $\mathbf{u}(\mathbf{x})$. By choosing $\mathbf{u}(\mathbf{x}) = (0, a^{-1}(\kappa x)^2 \operatorname{sgn} x)$, i.e., enforcing inversion- rather than mirror-symmetry in the $x = 0$ plane of the PhC, we obtain two oppositely strained domains that feature a domain wall between oppositely oriented PMFs at $x = 0$ (Figure 5.6a,b). Numerical simulations predict the emergence of non-degenerate chiral edge states at the interface, connecting the former Landau levels of the individual half-domains

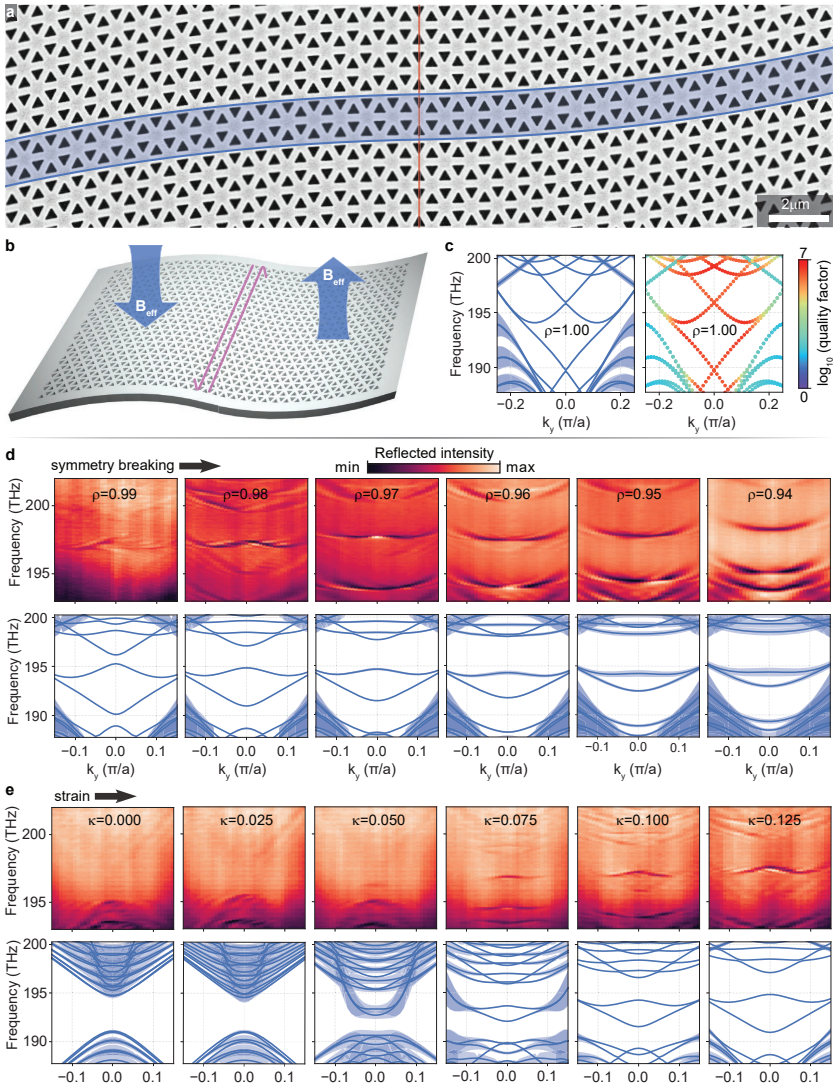

Figure 5.6: Chiral edge states through inhomogeneous pseudomagnetic fields. a, Scanning electron micrograph and **b,** schematic illustration of a photonic crystal membrane composed of inversely strained domains sharing an armchair interface. The opposing pseudomagnetic fields $\pm B_{\text{eff}}$ penetrating both domains (blue arrows) lead to the emergence of counterpropagating, spin-polarized chiral edge states guided along their mutual boundary (magenta arrows) **c,** Simulated bands for the pristine case (left), with color-coded quality factors (right). **d,** Measured (top) and simulated (bottom) bands of chiral edge states in PhCs with varying unit cell shrinking factor ρ, all at $\kappa = 0.125$. The linewidth is scaled by a factor two for enhanced visibility. The sub-lattice symmetry breaking leads to avoided crossings around the Γ-point in the edge state dispersion. **e,** Measured (top) and simulated (bottom) bands of chiral edge states in PhCs with increasing strain magnitude κ, all at $\rho = 0.98$.

(Figure 5.6c, left) [276]. The edge states are localized at the central boundary for $k_y/k_0 = 0$ but now feature finite group velocity there. Like the Landau levels, they are largely protected from diffraction loss at the PhC terminations, resulting in similarly narrow linewidths and theoretical quality factors up to 10^6 (Figure 5.6c, right). The symmetry breaking $\rho < 1$ we induce to enhance radiative coupling now alters the chiral edge state dispersion, introducing avoided crossings at the Γ point. Nonetheless, much of the characteristic features of the predicted chiral edge states can be recognized in the dispersion bands, as compared to the numerical prediction in Figure 5.6d.

Away from the Γ point, the edge states are increasingly displaced from the central domain wall and slowly restore their degeneracy and the photonic Landau level nature, before eventually also turning into trivial propagating states at the PhC boundaries (Figure 5.7a,b), accompanied by enhanced losses and a broadened linewidth (Figure 5.6c, right). The mode localization and associated losses can be broadly tuned by means of changing the PMF magnitude (see Figure 5.7e) or by realizing more complex strain patterns. Figure 5.7c shows Fourier spectroscopy measurements for different excitation positions and polarizations. For right- and left-handed circularly polarized light, we see signatures of spin-orbit coupling in the chiral edge states. At a fixed frequency, one can selectively couple into forward or backward propagating modes by changing the helicity (pseudospin) of the incident beam. However, we note that the same state can be launched with opposite helicity at the other side of the center. Moreover, Figure 5.7c shows that two edge states can be excited at the same location with equal helicity, despite having opposite group velocity. Thus, contrary to other implementations of chiral edge states in PhCs based on the quantum spin Hall effect [119, 129], there is no unique correspondence between the states' pseudospin and the far-field helicity of the emitted radiation.

5.3. CONCLUSION

We demonstrated the experimental realization of pseudomagnetic fields in PhC membranes via engineered synthetic strain, and employed it to induce photonic Landau levels and chiral edge states in the photonic band structure. We studied these states in the far field by introducing radiative coupling through sub-lattice symmetry breaking. The latter could however be readily removed, leaving remarkably high quality factors despite the states being coupled to the radiation continuum. In fact, these PhC Landau levels share some traits with bound states in the continuum [281], combining low radiation coupling and spatial delocalization. While the predicted extreme ($\sim 10^7$) quality factors may not be reached in practice due to random fabrication disorder, the low loss augments the high interest of these states for applications that benefit from strong field enhancement. Together with the slow group velocity and large delocalization, it makes the flat Landau level bands extremely appealing for quantum interfaces, nonlinear nanophotonics, lasers, etc. Moreover, it provides an intriguing testbed to study the physics of Anderson localization. The reliance on artificial rather than mechanical strain allows for broad engineering of the PhCs' localization and propagation properties, and offers extensive control over dispersion through tailoring of the lattice. For instance, the flatness

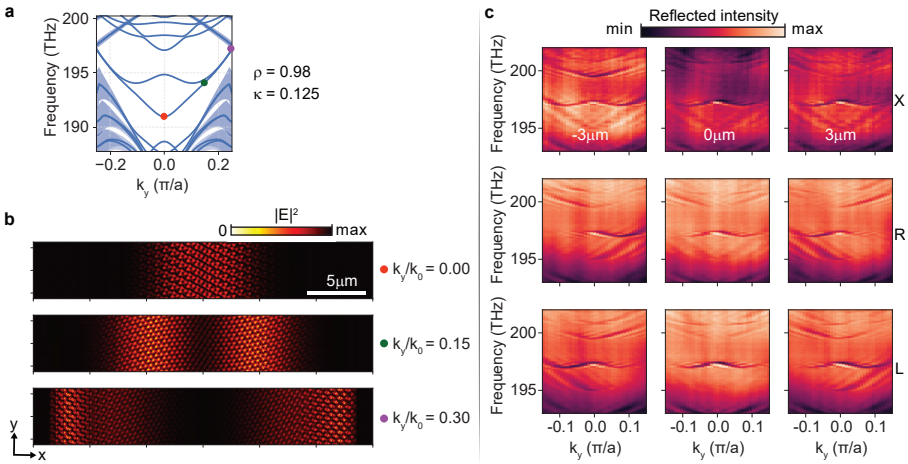

Figure 5.7: Chiral edge state localization and losses. a, Simulated bands of a shrunken lattice with two inversely strained domains. **b,** Real-space edge state mode profiles of the in-plane electric field intensity for the values of k_y marked in **a**. **c,** Position- and polarization-dependent edge state spectra, where the incident polarization state is denoted as X (linear horizontal), R (right-hand circular), or L (left-hand circular). The strain magnitude is $\kappa = 0.125$ for all panels.

of the Landau level bands could be readily improved by engineering an effective pseudoelectric field through additional transverse strain along x when exploring applications of light-matter enhancement [143]. Overall, the demonstrated strain-induced gauge fields provide a new, highly flexible paradigm for the exploration of novel photonic phenomena and the potential development of new photonic devices.

5.4. METHODS

5.4.1. NUMERICAL SIMULATIONS

Full-wave finite-element-method simulations in three dimensions were performed using the COMSOL Multiphysics RF Module [258]. The refractive index of silicon was set to $n = 3.48$, with a slab thickness of 220 nm. The unstrained primitive rhombic unit cell consisted of equilateral triangular air holes with side length $s = 0.3125 \cdot \sqrt{3}a_0$ and lattice constant $\sqrt{3}a_0 = 800$ nm. Perfectly matched layers above and to the transverse (x) sides of the simulation domain provide us with an estimate for the total loss and associated linewidth of the (quasinormal) eigenmodes, defined as two times the imaginary part of the complex eigenfrequency. We also perform simulations in which the transverse perfectly matched layers are replaced by perfect electric conducting boundaries to eliminate in-plane loss, and thus separately quantify the in-plane and out-of-plane (radiative) contributions to the total loss through comparison. We extract the displayed near-field profiles on a regular grid in a plane located 20 nm above the slab.

5.4.2. EXTRACTION OF RESONANCE FREQUENCIES AND QUALITY FACTORS

In order to extract the center mode frequencies and quality factors from the reflection spectra, we fit a set of general (Fano) resonance lineshapes of the form

$$R(\omega) = \left| A_0 + \sum_{j=1}^{n} A_j e^{i\phi_j} \frac{\gamma_j}{\omega - \omega_{0_j} + i\gamma_j} \right|^2, \tag{5.5}$$

where A_0 is a constant background amplitude; and A_j, ϕ_j, and $\omega_{0_j} - i\gamma_j$ are the amplitude, phase, and complex frequency of $n = 2$ individual Lorentzians, respectively. One of these Lorentzians models the photonic crystal mode, while the second (broad) Lorentzian accounts for the slowly varying background reflection. Quality factors are defined as $Q_j = \omega_{0_j}/(2\gamma_j)$.

6

CONCLUSION AND OUTLOOK

This work demonstrated the experimental realization of topological phenomena in silicon photonic crystal (PhC) slabs, and characterized the properties and limitations of the photonic states that emerge. We explored different types of judicious symmetry breaking, and correspondingly found analogs of effects known from condensed matter physics as the quantum spin Hall effect (QSHE) and the quantum valley Hall effect (QVHE). Using both near- and far-field techniques, we probed in particular radiative and scattering properties, revealing topological signatures as well as inherent limitations.

The experimental results presented in Chapter 3 have provided compelling evidence for the robustness of topological PhCs against backscattering in the presence of engineered defects. By emulating the quantum valley Hall effect for light, we have demonstrated that topological PhC waveguides with sharp bends which respect the symmetry of the underlying honeycomb PhC lattice exhibit significantly reduced backscattering. In fact, the observed backscattering was an order of magnitude lower than that for comparable trivial PhC waveguides. This finding underscores the potential of topological PhCs to provide a design paradigm for integrated photonics that can be readily implemented, without the need for extensive a priori optimizations of the geometry to minimize losses upon routing of light across each and every bend in a circuit. Importantly, the defects we studied here conserve the C_3 crystal symmetry that is essential to the topological mechanism. It would be highly interesting to also study the resilience to random disorder such as that related to fabrication imperfections, which could, at least in part, break that spatial symmetry. Indeed, experimental studies have observed significant backscattering in a specific type of valley-Hall waveguide [282]. Numerical studies suggested that while all passive topological PhCs exhibit backscattering, its strength subtly depends on the type and magnitude of such disorder [249, 283]. Further detailed investigation, especially in real-world experimental systems, is thus warranted. At the same time, the fact that topological PhCs are never fully robust against any type of disorder motivates the continued study of other kinds of topological insulators, that rely for

example on nonlinearities or time-reversal symmetry breaking, especially in on-chip, nanoscale systems. Particularly in the context of slow light, which is inherently more susceptible to the tiniest of imperfections, topological robustness represents an alluring prospect for a plethora of applications due to the possibility of covering genuinely macroscopic distances and the associated strong enhancement of light-matter interactions in this regime.

Our study also highlights the powerful tool that near-field scanning optical microscopy (NSOM), especially when equipped with phase resolution, provides for the accurate quantification and visualization of light transport in nanoscale structures. The imaging of higher order Bloch harmonics and ability to filter modes according to their direction is an invaluable capability for assessing the potential advantages such systems may display with respect to their trivial PhC counterparts. Especially in light of applications such as spin-selective coupling of single emitters in chiral quantum optics (e.g., cold atoms, trapped ions, quantum dots), it is of paramount importance to consider the highly structured nature of the mode's near fields, as it gives deep insights into properties inaccessible from the far field. To give an example, in another study we probed the near fields of edge states in the QSHE-type PhC platform of Chapter 4 [131], which displays a unique correspondence between edge state pseudospin and the circular polarization of the associated far-field radiation [128, 129]. The detailed examination via phase- and polarization resolved NSOM, however, reveals a breakdown of this spin-to-helicity locking in the modes' near-field distribution and evidences the highly structured nature of the spin angular momentum density, containing regions of opposite helicity within each unit cell. The breakdown can be attributed to the contributions of higher order Bloch harmonics, an experimental result which would have been impossible to infer solely from the properties of the fundamental Bloch harmonic that radiates to the far field. This illustrates the importance of detailed studies into the structure of topological states for possible applications as chiral quantum optical interfaces [170].

In addition to the accurate assessment of losses in the presence of random disorder, the mitigation of, at times, substantial insertion and out-coupling losses when interfacing topological devices with other on-chip components also necessitates further research efforts. For the QVHE-type waveguides we study it is in fact the transition region to the trivial silicon ridge waveguides used for in- and out-coupling that leads to, by far, the largest contribution to scattering losses light experiences upon propagation. In our case, this is also attributed to the fact that we were not concerned with these scattering sites in the experimental context that the topological PhCs were examined in. However, it is a crucial factor for any real-world applications of integrated photonics that relies on the resilient transport of energy and information, especially in the realm of quantum optics where topological waveguides could serve as low-loss optical interconnects. There are several potential routes toward reducing the amount of scattering in these scenarios, among which the most common, already used extensively in trivial photonic devices, is the design of adiabatic transition regions akin to the (unoptimized) intermediate PhC waveguides we employ (see Section 2.1.1), e.g., adiabatic and topological tapers [149, 284].

Terminations of topological systems can also be smartly designed to minimize the scattering light experiences, such as by using zigzag terminations which respect the lattice symmetry in honeycomb topological PhCs [135]. This approach may even turn the former problem into a feature, as it has been shown theoretically that suitably designed lattice terminations in a QVHE-type PhC may act as an effective single-port cavity due to the near-conservation of the valley degree of freedom [285]. In the absence of other loss channels, light becomes localized at the end of a topological waveguide by virtue of the strongly-suppressed inter-valley backscattering provided by the topological PhC platform, for which in-situ probing by near-field microscopy could form a suitable investigative tool. Another potential pathway is to more extensively integrate topological functionalities across several on-chip devices, taking full advantage of the offered protection simply by minimizing the amount of trivial components. Topological waveguides may be smoothly interfaced with topological cavities to create more complex nanophotonic circuits, not only broadening the extent of on-chip topological protection, but also offering confinement and coupling mechanisms that are unparalleled in comparable trivial devices, as we showcase in the subsequent chapter of this thesis.

Chapter 4 provides an in-depth experimental investigation into radiative PhC defect cavities that originate from a topological PhC bulk lattice displaying the quantum spin Hall effect for light. The topological bulk band structure, characterized by a band inversion between two lattices with slightly different unit cell geometries ('shrunken' and 'expanded') [119], shows intriguing signatures in the cavity mode spectra of hexagonal cavities made of shrunken unit cells within an expanded bulk lattice, and vice versa.

The band inversion leads to a unique mode confinement, distinct from the typical photonic bandgap confinement observed in trivial defect cavities. This band-inversion-induced confinement is clearly manifested in the mode spectra, with an inverted scaling behavior of multipolar resonances observed between the cases of shrunken cavities in an expanded bulk and expanded cavities in a shrunken bulk, respectively. The observation that radiative quality factors are insensitive to variations in cavity size and shape departs from the usual convention observed in trivial PhCs. This, together with the unique spin-conserved coupling behavior of the cavities' travelling wave modes to topological waveguides could be useful for a variety of integrated devices that benefit from the enhanced robustness and helicity of the underlying topological edge states, such as lasing and spin-selective coupling to emitters. The findings from this chapter pave the way for future research into the design and fabrication of topological photonic devices with tunable properties that can act as near-to-far field interfaces. The robustness of the cavity modes against variations in size and shape, coupled with the ability to selectively couple into specific modes, could lead to the development of more flexible and efficient photonic integrated circuits. The non-Hermitian nature of the topological PhC platform represents an intriguing juxtaposition of a system that is, on the one hand, celebrated for its suppressed losses in the face of perturbations and, on the other hand, features an inherent radiative loss-mechanism. For example, an additional observation made in this chapter is the occurrence of mode splitting in the cavities.

This phenomenon, likely related to fabrication imperfections, suggests potential limitations of topological protection in the system which does not guard against this splitting. Further research is needed to fully understand the mechanisms underlying the observed phenomena and to explore their potential applications in various fields, and indeed the research into non-Hermitian photonic topological insulators is a rapidly growing field [286].

However, it is crucial to note that topological protection is not the only significant property of the cavities under study. The system also introduces rich physics to the field of photonics, enabling mechanisms such as band-inversion-induced confinement and spin-conserved coupling, which are unparalleled in comparable trivial PhC defect cavities. These unique properties open up new possibilities for the design and fabrication of photonic devices and highlight the potential of topological photonics to introduce novel functionalities to the field. As we transition to the next section of this conclusion, we delve into another fascinating phenomenon that is being transferred from the realm of solid-state physics to PhCs: artificial gauge fields. This concept, with its potential to transform the design of nanocavities and mode confinement, sets the stage for exciting developments to follow.

In Chapter 5, we experimentally realized pseudomagnetic fields in two-dimensional PhCs through the engineered strain of the lattice. This approach has allowed us to induce flat-band Landau levels at discrete energies, a phenomenon typically observed in electronic systems under the influence of a magnetic field. Our study delves into the spatial and spectral properties of these states in silicon PhCs at telecom wavelengths, using far-field spectroscopy. We have also successfully created domains of opposite pseudomagnetic fields, leading to the observation of topological edge states at their interface. Remarkably, these strain-induced states can achieve high quality factors, despite being phase-matched to the radiation continuum. This finding opens up new avenues for enhancing light-matter interactions and offers a novel design principle to govern both on-chip and radiating light fields.

Looking ahead, our findings lay the groundwork for more intensive efforts to study artificial gauge fields in PhCs. The appeal of these fields for fundamental research and the emulation of phenomena known from solid-state physics is clear. The ability to control and manipulate light in such a precise manner could have far-reaching implications for a range of real-world technologies and applications, from telecommunications to more robust and error-resistant quantum information processing. Especially with regard to the coupling of quantum emitters, photonic Landau levels offer unique possibilities due to the simultaneous strong delocalization and extremely long lifetime of these states. In contrast to the confined mode volumes of typical defect cavities (such as in Chapter 4), the Landau levels are strongly delocalized and combine high degeneracy, high quality factors, and slow light in a way that can lead to large Purcell enhancement over extended areas, benefitting from the topological robustness they inherit from their origin in the strain-induced effective magnetic field. The observation of topological edge states that emerge within the same design paradigm highlights the untapped potential that pseudomagnetic (and pseudoelectric [142, 145]) fields enfold as we continue to explore and understand these artificial pendants of condensed matter systems.

In closing, let us consider a more overarching perspective on the field of topological photonics and its transformative potential, as well as the challenges it may face along the path of continued research efforts and permeation into new technologies that find their way into practical applications. We ask ourselves: what are the potential real-world applications of topological photonics, and how can they revolutionize existing technologies? How can the inherent challenge of truly unidirectional, backscattering-free transport be overcome? Lastly, how can the integration of topological lattices into practical applications be improved?

From a fundamental perspective, topological photonics serves as a rich platform for delving into the intricacies of topological physics, potentially unlocking discoveries of new materials and particles. The field is partly driven by sheer scientific curiosity, with researchers eager to push the boundaries of our understanding of light and challenge conventional wisdom. Topological photonics diverges from traditional optical systems from a fundamental and theoretical standpoint. Instead of focusing primarily on geometric parameters, it delves deep into the unique properties of photonic platforms and emphasizes functionalities rooted in topological phenomena. The allure of this field lies in the intertwining of abstract mathematical concepts with the tangible behavior of light. These topological principles manifest in real-world scenarios, producing topologically protected edge states that can seamlessly navigate around obstacles without any backscattering. There is still a lot of untapped potential in emulating condensed matter phenomena and realizing some other of its intriguing predictions. To give an example, the fractional quantum Hall effect which relies on strong electron-electron interactions is inherently challenging to implement for photons since they do not naturally interact with each other. While there has been some theoretical work on realizing similar effects in photonic systems via artificial gauge fields and nonlinear interactions [287, 288], this is still largely unexplored territory. It would however pave the way for the realization of anyonic statistics for photons, a luring proposition in the context of topological quantum computing [20].

On the application front, topological photonics heralds a new era of design possibilities, and significant transformative potential has been identified in reshaping optical technologies [289–292]. This domain promises solutions to challenges inherent to traditional optical systems, introducing functionalities that might have been deemed challenging or outright impossible using traditional methods, such as the realization of unidirectional three-dimensional routing, advanced switching, and the development of high-performance sensors utilizing truly long-distance slow light. The robust nature of topological photonics is especially pivotal in integrated photonics, where even minor fabrication imperfections can disrupt light propagation.

This robustness, combined with the field's foundational mathematical considerations, offers groundbreaking opportunities for wavefront engineering, laser systems, terahertz devices, and fault-tolerant quantum information systems, to name a few. In principle, any field that could benefit from integrated photonic devices would itself benefit from the successful introduction of topological design

concepts. The potential impact of this research on various industries could be multifold. It would be interesting to see how topological PhCs could assist the development of fast and energy-efficient optical circuits, for instance in the form of optical interconnects in (quantum) computing scenarios. In medicine, the creation of advanced imaging and sensing systems for more accurate diagnoses and treatments could be facilitated, and the enhanced sensing capabilities could also benefit chemical and metrology applications. Looking ahead, topological photonics may one day be seamlessly integrated into various technologies, from communication infrastructures to consumer products [290]. As this field matures, it is anticipated to play an important role in advancing the landscape of optical and quantum innovations.

However, it is important to acknowledge the challenges that lie ahead, of which the main one likely is overcoming the aforementioned problem of truly unidirectional transport. The main difficulty lies in breaking time-reversal symmetry at optical frequencies, given the weak response of magnetic materials in this regime. While in this work we have presented various reciprocal topological PhC devices that introduce rich physics to photonics and also quantitatively outperform their trivial counterparts in terms of robustness, topological photonics needs to exceed the performance of mature technologies that have been optimized using conventional techniques in real-life settings. Crucially, the advantages it offers need to be significant outside of lab conditions, in the presence of realistic imperfections and in various integrated environments, all while retaining the key property of topological robustness. Merging true nonreciprocity with topological states is a large step into cementing this supremacy in practical scenarios, and indeed, an increasing effort is devoted to achieving this feat for compact systems that can be readily integrated on a chip.

For instance, the emerging field of nonlinear topological photonics transcends the constraints of linear photonic systems, achieving magnet-free nonreciprocity and unveiling a plethora of untapped physical phenomena. This innovation paves the way for advanced functionalities, including active tunability, self-interaction effects, frequency conversion, topological lasing, and beyond [273]. Time-modulated (i.e., Floquet-type) quasicrystals present another intriguing approach to achieve magnet-free nonreciprocity in topological insulators [289]. Despite their lack of periodicity and absence of a unit cell, these quasicrystals, under periodic modulation, can function as topological insulators with edge states that exhibit all the hallmark features of topological edge states. Similarly, fractal structures, like the Sierpinski gasket, can become topological insulators under periodic modulation [293]. Intriguingly, these fractal geometries inherently lack a bulk — every site is essentially an edge, be it external or internal.

This approach can help to solve another serious issue on the route toward practical applications of topological PhCs: their comparatively large footprint, which poses severe challenges in the design of integrated circuits, as real-estate on microchips is a scarce resource. Overcoming this issue is further aided by identifying concrete realizations of topological systems that improve the performances of classical optical components, including a new holistic approach to photonic design

where the requirement of lattices is viewed as a feature rather than a nuisance. This could mean, for example, leveraging the advantages lattice effects introduce to many scenarios, such as employing large arrays of coupled waveguides and cavities for lasing and quantum computation applications rather than focusing on singular components. Additionally, in the same vein as for current state-of-the art electronic microprocessors, the density of photonic components can be vastly enhanced by increasing their packing density in a three-dimensional configuration.

This, however, highlights the next major challenge in the field, not exclusive to topological systems, but rather concerning integrated photonics in its entirety: precise nanofabrication. Despite the compatibility of fully dielectric topological PhCs with large-volume semiconductor manufacturing processes, the fabrication of low-cost and large-area optical components with nanometer-scale precision presents considerable obstacles, making scalability a serious concern. Future research will need to focus on developing topological PhC designs that are not only robust against defects but also compliant with large-scale fabrication. This includes the development of reliable and scalable three-dimensional nanolithography techniques. These would, akin to the introduction of advanced two-dimensional lithography techniques which strongly propelled the whole field of research on PhCs, represent a true revolution for the step of topological photonics out of the laboratory and into convenient technologies that we rely on and use on a daily basis, without even noticing.

The journey from the lab to real-world applications will certainly be challenging, but the potential rewards undoubtedly make it a journey worth undertaking.

BIBLIOGRAPHY

1. Jalali, B. & Fathpour, S. Silicon Photonics. *Journal of Lightwave Technology* **24,** 4600–4615 (2006).
2. Heck, M. J. R., Bauters, J. F., Davenport, M. L., Doylend, J. K., Jain, S., Kurczveil, G., Srinivasan, S., Tang, Y. & Bowers, J. E. Hybrid Silicon Photonic Integrated Circuit Technology. *IEEE J. Sel. Top. Quantum Electron.* **19,** 6100117–6100117 (2013).
3. Rickman, A. The Commercialization of Silicon Photonics. *Nat. Photonics* **8,** 579–582 (2014).
4. Thomson, D. *et al.* Roadmap on Silicon Photonics. *J. Opt.* **18,** 073003 (2016).
5. Shalaev, V. M. Optical Negative-Index Metamaterials. *Nat. Photonics* **1,** 41–48 (2007).
6. Liu, Y. & Zhang, X. Metamaterials: A New Frontier of Science and Technology. *Chem. Soc. Rev.* **40,** 2494–2507 (2011).
7. Hess, O., Pendry, J. B., Maier, S. A., Oulton, R. F., Hamm, J. M. & Tsakmakidis, K. L. Active Nanoplasmonic Metamaterials. *Nat. Mater.* **11,** 573–584 (2012).
8. Zheludev, N. I. & Kivshar, Y. S. From Metamaterials to Metadevices. *Nat. Mater.* **11,** 917–924 (2012).
9. Poddubny, A., Iorsh, I., Belov, P. & Kivshar, Y. Hyperbolic Metamaterials. *Nat. Photonics* **7,** 948–957 (2013).
10. Chen, H.-T., Taylor, A. J. & Yu, N. A Review of Metasurfaces: Physics and Applications. *Rep. Prog. Phys.* **79,** 076401 (2016).
11. Kadic, M., Milton, G. W., van Hecke, M. & Wegener, M. 3D Metamaterials. *Nat. Rev. Phys.* **1,** 198–210 (2019).
12. Joannopoulos, J. D., Villeneuve, P. R. & Fan, S. Photonic Crystals: Putting a New Twist on Light. *Nature* **386,** 143–149 (1997).
13. Joannopoulos, J. D., Johnson, S. G., Winn, J. N. & Meade, R. D. *Photonic Crystals: Molding the Flow of Light* 2nd ed. (Princeton University Press, Princeton, NJ, 2008).

14. Krauss, T. F. & De La Rue, R. M. Photonic Crystals in the Optical Regime — Past, Present and Future. *Prog. Quantum Electron.* **23,** 51–96 (1999).

15. Busch, K., Lölkes, S., Wehrspohn, R. B. & Föll, H. *Photonic Crystals: Advances in Design, Fabrication, and Characterization* (John Wiley & Sons, Hoboken, NJ, 2004).

16. Soljačić, M. & Joannopoulos, J. D. Enhancement of Nonlinear Effects Using Photonic Crystals. *Nat. Mater.* **3,** 211–219 (2004).

17. Pitruzzello, G. & Krauss, T. F. Photonic Crystal Resonances for Sensing and Imaging. *J. Opt.* **20,** 073004 (2018).

18. Hasan, M. Z. & Kane, C. L. Colloquium: Topological Insulators. *Rev. Mod. Phys.* **82,** 3045–3067 (2010).

19. Haldane, F. D. M. Nobel Lecture: Topological Quantum Matter. *Rev. Mod. Phys.* **89,** 040502 (2017).

20. Freedman, M., Kitaev, A., Larsen, M. & Wang, Z. Topological Quantum Computation. *Bull. Amer. Math. Soc.* **40,** 31–38 (2003).

21. Bernevig, B. A. *Topological Insulators and Topological Superconductors* (Princeton University Press, Princeton, NJ, 2013).

22. Shen, S.-Q. *Topological Insulators: Dirac Equation in Condensed Matter* (Springer, Singapore, 2017).

23. Wang, Z., Chong, Y., Joannopoulos, J. D. & Soljačić, M. Observation of Unidirectional Backscattering-Immune Topological Electromagnetic States. *Nature* **461,** 772–775 (2009).

24. Chen, W.-J., Jiang, S.-J., Chen, X.-D., Zhu, B., Zhou, L., Dong, J.-W. & Chan, C. T. Experimental Realization of Photonic Topological Insulator in a Uniaxial Metacrystal Waveguide. *Nat. Commun.* **5,** 1–7 (2014).

25. Rechtsman, M. C., Zeuner, J. M., Plotnik, Y., Lumer, Y., Podolsky, D., Dreisow, F., Nolte, S., Segev, M. & Szameit, A. Photonic Floquet Topological Insulators. *Nature* **496,** 196–200 (2013).

26. Hafezi, M., Mittal, S., Fan, J., Migdall, A. & Taylor, J. M. Imaging Topological Edge States in Silicon Photonics. *Nat. Photonics* **7,** 1001–1005 (2013).

27. Mittal, S., Fan, J., Faez, S., Migdall, A., Taylor, J. M. & Hafezi, M. Topologically Robust Transport of Photons in a Synthetic Gauge Field. *Phys. Rev. Lett.* **113,** 087403 (2014).

28. Karzig, T., Bardyn, C.-E., Lindner, N. H. & Refael, G. Topological Polaritons. *Phys. Rev. X* **5,** 031001 (2015).

29. Ozawa, T., Price, H. M., Amo, A., Goldman, N., Hafezi, M., Lu, L., Rechtsman, M. C., Schuster, D., Simon, J., Zilberberg, O. & Carusotto, I. Topological Photonics. *Rev. Mod. Phys.* **91,** 015006 (2019).

30. Wang, H., Gupta, S. K., Xie, B. & Lu, M. Topological Photonic Crystals: A Review. *Front. Optoelectron.* **13,** 50–72 (2020).

31. Iwamoto, S., Ota, Y., Arakawa, Y., Ota, Y. & Arakawa, Y. Recent Progress in Topological Waveguides and Nanocavities in a Semiconductor Photonic Crystal Platform [Invited]. *Opt. Mater. Express* **11,** 319–337 (2021).

32. Tang, G.-J., He, X.-T., Shi, F.-L., Liu, J.-W., Chen, X.-D. & Dong, J.-W. Topological Photonic Crystals: Physics, Designs, and Applications. *Laser Photonics Rev.* **16,** 2100300 (2022).

33. Noda, S., Fujita, M. & Asano, T. Spontaneous-Emission Control by Photonic Crystals and Nanocavities. *Nat. Photonics* **1,** 449–458 (2007).

34. Sukhoivanov, I. A. & Guryev, I. V. *Photonic Crystals: Physics and Practical Modeling* (Springer, Berlin, Heidelberg, 2009).

35. Nair, R. V. & Vijaya, R. Photonic Crystal Sensors: An Overview. *Prog. Quantum Electron.* **34,** 89–134 (2010).

36. Chen, H., Lou, R., Chen, Y., Chen, L., Lu, J. & Dong, Q. Photonic Crystal Materials and Their Application in Biomedicine. *Drug Delivery* **24,** 775–780 (2017).

37. Zhao, Y., Zhao, X. & Gu, Z. Photonic Crystals in Bioassays. *Adv. Funct. Mater.* **20,** 2970–2988 (2010).

38. Fenzl, C., Hirsch, T. & Wolfbeis, O. S. Photonic Crystals for Chemical Sensing and Biosensing. *Angew. Chem. Int. Ed.* **53,** 3318–3335 (2014).

39. Lee, K. & Asher, S. A. Photonic Crystal Chemical Sensors: pH and Ionic Strength. *J. Am. Chem. Soc.* **122,** 9534–9537 (2000).

40. Lončar, M., Scherer, A. & Qiu, Y. Photonic Crystal Laser Sources for Chemical Detection. *Appl. Phys. Lett.* **82,** 4648–4650 (2003).

41. Arsenault, A. C., Puzzo, D. P., Manners, I. & Ozin, G. A. Photonic-Crystal Full-Colour Displays. *Nat. Photonics* **1,** 468–472 (2007).

42. Bello, M., Platero, G., Cirac, J. I. & González-Tudela, A. Unconventional Quantum Optics in Topological Waveguide QED. *Sci. Adv.* **5,** eaaw0297 (2019).

43. Carusotto, I., Houck, A. A., Kollár, A. J., Roushan, P., Schuster, D. I. & Simon, J. Photonic Materials in Circuit Quantum Electrodynamics. *Nat. Phys.* **16,** 268–279 (2020).

44. Xie, X., Zhang, W., He, X., Wu, S., Dang, J., Peng, K., Song, F., Yang, L., Ni, H., Niu, Z., Wang, C., Jin, K., Zhang, X. & Xu, X. Cavity Quantum Electrodynamics with Second-Order Topological Corner State. *Laser Photonics Rev.* **14,** 1900425 (2020).

45. Wang, C. F., Hanson, R., Awschalom, D. D., Hu, E. L., Feygelson, T., Yang, J. & Butler, J. E. Fabrication and Characterization of Two-Dimensional Photonic Crystal Microcavities in Nanocrystalline Diamond. *Appl. Phys. Lett.* **91,** 201112 (2007).

46. Bayn, I., Meyler, B., Lahav, A., Salzman, J., Kalish, R., Fairchild, B. A., Prawer, S., Barth, M., Benson, O., Wolf, T., Siyushev, P., Jelezko, F. & Wrachtrup, J. Processing of Photonic Crystal Nanocavity for Quantum Information in Diamond. *Diam. Relat. Mater.* **20,** 937–943 (2011).

47. Arcari, M., Söllner, I., Javadi, A., Lindskov Hansen, S., Mahmoodian, S., Liu, J., Thyrrestrup, H., Lee, E. H., Song, J. D., Stobbe, S. & Lodahl, P. Near-Unity Coupling Efficiency of a Quantum Emitter to a Photonic Crystal Waveguide. *Phys. Rev. Lett.* **113,** 093603 (2014).

48. Wan, N. H., Mouradian, S. & Englund, D. Two-Dimensional Photonic Crystal Slab Nanocavities on Bulk Single-Crystal Diamond. *Appl. Phys. Lett.* **112,** 141102 (2018).

49. Yan, Q., Hu, X., Fu, Y., Lu, C., Fan, C., Liu, Q., Feng, X., Sun, Q. & Gong, Q. Quantum Topological Photonics. *Adv. Opt. Mater.* **9,** 2001739 (2021).

50. Goi, E., Zhang, Q., Chen, X., Luan, H. & Gu, M. Perspective on Photonic Memristive Neuromorphic Computing. *PhotoniX* **1,** 3 (2020).

51. Shastri, B. J., Tait, A. N., Ferreira de Lima, T., Pernice, W. H. P., Bhaskaran, H., Wright, C. D. & Prucnal, P. R. Photonics for Artificial Intelligence and Neuromorphic Computing. *Nat. Photonics* **15,** 102–114 (2021).

52. Bloch, F. Über Die Quantenmechanik Der Elektronen in Kristallgittern. *Z. Phys.* **52,** 555–600 (1929).

53. Kittel, C. *Introduction to Solid State Physics* 8th ed. (Wiley, Hoboken, NJ, 2005).

54. Schrödinger, E. An Undulatory Theory of the Mechanics of Atoms and Molecules. *Phys. Rev.* **28,** 1049–1070 (1926).

55. Planck, M. Ueber Das Gesetz Der Energieverteilung Im Normalspectrum. *Ann. Phys.* **309,** 553–563 (1901).

56. De Broglie, L. XXXV. A Tentative Theory of Light Quanta. *Lond. Edinb. Dubl. Philos. Mag. J. Sci.* **47,** 446–458 (1924).

57. Wigner, E. *Gruppentheorie Und Ihre Anwendung Auf Die Quantenmechanik Der Atomspektren* (Vieweg+Teubner Verlag, Wiesbaden, 1931).

58. Wehling, T., Black-Schaffer, A. & Balatsky, A. Dirac Materials. *Adv. Phys.* **63,** 1–76 (2014).

59. Armitage, N. P., Mele, E. J. & Vishwanath, A. Weyl and Dirac Semimetals in Three-Dimensional Solids. *Rev. Mod. Phys.* **90,** 015001 (2018).

60. Katsnelson, M. I. Graphene: Carbon in Two Dimensions. *Mater. Today* **10,** 20–27 (2007).

61. Dirac, P. A. M. & Fowler, R. H. The Quantum Theory of the Electron. *Proc. R. Soc. Lond. A* **117,** 610–624 (1928).

62. Weissbluth, M. *Atoms and Molecules* (Academic Press, Cambridge, MA, 1978).

63. Pauli, W. Zur Quantenmechanik Des Magnetischen Elektrons. *Z. Phys.* **43,** 601–623 (1927).

64. Semenoff, G. W. Condensed-Matter Simulation of a Three-Dimensional Anomaly. *Phys. Rev. Lett.* **53,** 2449–2452 (1984).

65. Haldane, F. Model for a Quantum Hall Effect without Landau Levels: Condensed-matter Realization of the "Parity Anomaly". *Phys. Rev. Lett.* **61,** 2015–2018 (1988).

66. Castro Neto, A. H., Guinea, F., Peres, N. M. R., Novoselov, K. S. & Geim, A. K. The Electronic Properties of Graphene. *Rev. Mod. Phys.* **81,** 109–162 (2009).

67. Laird, E. A., Kuemmeth, F., Steele, G. A., Grove-Rasmussen, K., Nygård, J., Flensberg, K. & Kouwenhoven, L. P. Quantum Transport in Carbon Nanotubes. *Rev. Mod. Phys.* **87,** 703–764 (2015).

68. Wallace, P. R. The Band Theory of Graphite. *Phys. Rev.* **71,** 622–634 (1947).

69. Geim, A. K. & Novoselov, K. S. The Rise of Graphene. *Nat. Mater.* **6,** 183–191 (2007).

70. Novoselov, K. S., Geim, A. K., Morozov, S. V., Jiang, D., Zhang, Y., Dubonos, S. V., Grigorieva, I. V. & Firsov, A. A. Electric Field Effect in Atomically Thin Carbon Films. *Science* **306,** 666–669 (2004).

71. Novoselov, K. S., Geim, A. K., Morozov, S. V., Jiang, D., Katsnelson, M. I., Grigorieva, I. V., Dubonos, S. V. & Firsov, A. A. Two-Dimensional Gas of Massless Dirac Fermions in Graphene. *Nature* **438,** 197–200 (2005).

72. Vozmediano, M. A. H., Katsnelson, M. I. & Guinea, F. Gauge Fields in Graphene. *Phys. Rep.* **496,** 109–148 (2010).

73. Landau, L. Diamagnetismus Der Metalle. *Z. Phys.* **64,** 629–637 (1930).

74. Zhang, Y., Tan, Y.-W., Stormer, H. L. & Kim, P. Experimental Observation of the Quantum Hall Effect and Berry's Phase in Graphene. *Nature* **438,** 201–204 (2005).

75. Zheng, Y. & Ando, T. Hall Conductivity of a Two-Dimensional Graphite System. *Phys. Rev. B* **65,** 245420 (2002).

76. Zhang, Y., Jiang, Z., Small, J. P., Purewal, M. S., Tan, Y.-W., Fazlollahi, M., Chudow, J. D., Jaszczak, J. A., Stormer, H. L. & Kim, P. Landau-Level Splitting in Graphene in High Magnetic Fields. *Phys. Rev. Lett.* **96,** 136806 (2006).

77. McClure, J. W. Diamagnetism of Graphite. *Phys. Rev.* **104,** 666–671 (1956).

78. Guinea, F., Castro Neto, A. H. & Peres, N. M. R. Electronic States and Landau Levels in Graphene Stacks. *Phys. Rev. B* **73,** 245426 (2006).

79. Jiang, Z., Henriksen, E. A., Tung, L. C., Wang, Y.-J., Schwartz, M. E., Han, M. Y., Kim, P. & Stormer, H. L. Infrared Spectroscopy of Landau Levels of Graphene. *Phys. Rev. Lett.* **98,** 197403 (2007).

80. Laughlin, R. B. Quantized Hall Conductivity in Two Dimensions. *Phys. Rev. B* **23,** 5632–5633 (1981).

81. v. Klitzing, K., Dorda, G. & Pepper, M. New Method for High-Accuracy Determination of the Fine-Structure Constant Based on Quantized Hall Resistance. *Phys. Rev. Lett.* **45,** 494–497 (1980).

82. v. Klitzing, K. in *Highlights in Condensed Matter Physics and Future Prospects* (ed Esaki, L.) 7–22 (Springer US, Boston, MA, 1991).

83. Novoselov, K. S., Jiang, Z., Zhang, Y., Morozov, S. V., Stormer, H. L., Zeitler, U., Maan, J. C., Boebinger, G. S., Kim, P. & Geim, A. K. Room-Temperature Quantum Hall Effect in Graphene. *Science* **315,** 1379–1379 (2007).

84. Kane, C. L. & Mele, E. J. Quantum Spin Hall Effect in Graphene. *Phys. Rev. Lett.* **95,** 226801 (2005).

85. Xiao, D., Yao, W. & Niu, Q. Valley-Contrasting Physics in Graphene: Magnetic Moment and Topological Transport. *Phys. Rev. Lett.* **99,** 236809 (2007).

86. Guinea, F., Katsnelson, M. I. & Geim, A. K. Energy Gaps and a Zero-Field Quantum Hall Effect in Graphene by Strain Engineering. *Nat. Phys.* **6,** 30–33 (2010).

87. Yablonovitch, E. Inhibited Spontaneous Emission in Solid-State Physics and Electronics. *Phys. Rev. Lett.* **58,** 2059–2062 (1987).

88. John, S. Strong Localization of Photons in Certain Disordered Dielectric Superlattices. *Phys. Rev. Lett.* **58,** 2486–2489 (1987).

89. Yablonovitch, E. & Gmitter, T. J. Photonic Band Structure: The Face-Centered-Cubic Case. *Phys. Rev. Lett.* **63,** 1950–1953 (1989).

90. Bragg, W. H. & Bragg, W. L. The Reflection of X-rays by Crystals. *Proc. R. Soc. Lond. A* **88,** 428–438 (1997).

91. Li, W., Meng, F., Chen, Y., fan Li, Y. & Huang, X. Topology Optimization of Photonic and Phononic Crystals and Metamaterials: A Review. *Adv. Theory Simul.* **2,** 1900017 (2019).

92. Griffiths, D. J. & Schroeter, D. F. *Introduction to Quantum Mechanics* 3rd ed. (Cambridge University Press, Cambridge, NY, 2018).

93. Wilczek, F. & Shapere, A. *Geometric Phases in Physics* (World scientific, Singapore, 1989).

94. Pancharatnam, S. Generalized Theory of Interference, and Its Applications. *Proc. Indian Acad. Sci.* **44,** 247–262 (1956).

95. Berry, M. V. Quantal Phase Factors Accompanying Adiabatic Changes. *Proc. R. Soc. Lond. A* **392,** 45–57 (1997).

96. Qi, X.-L. & Zhang, S.-C. Topological Insulators and Superconductors. *Rev. Mod. Phys.* **83,** 1057–1110 (2011).

97. Horsley, S. A. R. Tutorial: Topology, Waves, and the Refractive Index. *Int. J. Theor. Phys* **62,** 135 (2023).

98. Dirac, P. a. M. A New Notation for Quantum Mechanics. *Math. Proc. Camb. Philos. Soc.* **35,** 416–418 (1939).

99. Singer, I. M. & Thorpe, J. A. *Lecture Notes on Elementary Topology and Geometry* (Springer, New York, NY, 1976).

100. Hassani Gangaraj, S. A., Silveirinha, M. G. & Hanson, G. W. Berry Phase, Berry Connection, and Chern Number for a Continuum Bianisotropic Material From a Classical Electromagnetics Perspective. *IEEE J. Multiscale Multiphysics Comput. Tech.* **2,** 3–17 (2017).

101. Cohen, E., Larocque, H., Bouchard, F., Nejadsattari, F., Gefen, Y. & Karimi, E. Geometric Phase from Aharonov–Bohm to Pancharatnam–Berry and Beyond. *Nat. Rev. Phys.* **1,** 437–449 (2019).

102. Bisharat, D., Davis, R., Zhou, Y., Bandaru, P. & Sievenpiper, D. Photonic Topological Insulators: A Beginner's Introduction [Electromagnetic Perspectives]. *IEEE Antennas Propag. Mag.* **63,** 112–124 (2021).

103. Hecht, E. *Optics* 5th ed. (Pearson Education, Inc, Boston, 2017).

104. Bansil, A., Lin, H. & Das, T. Colloquium: Topological Band Theory. *Rev. Mod. Phys.* **88,** 021004 (2016).

105. Chern, S.-s. Characteristic Classes of Hermitian Manifolds. *Ann. Math.* **47,** 85–121 (1946).

106. Aharonov, Y. & Bohm, D. Significance of Electromagnetic Potentials in the Quantum Theory. *Phys. Rev.* **115,** 485–491 (1959).

107. Mong, R. S. K. & Shivamoggi, V. Edge States and the Bulk-Boundary Correspondence in Dirac Hamiltonians. *Phys. Rev. B* **83,** 125109 (2011).

108. Thouless, D. J., Kohmoto, M., Nightingale, M. P. & den Nijs, M. Quantized Hall Conductance in a Two-Dimensional Periodic Potential. *Phys. Rev. Lett.* **49,** 405–408 (1982).

109. Bernevig, B. A., Hughes, T. L. & Zhang, S.-C. Quantum Spin Hall Effect and Topological Phase Transition in HgTe Quantum Wells. *Science* **314,** 1757–1761 (2006).

110. Balakrishnan, J., Kok Wai Koon, G., Jaiswal, M., Castro Neto, A. H. & Özyilmaz, B. Colossal Enhancement of Spin–Orbit Coupling in Weakly Hydrogenated Graphene. *Nat. Phys.* **9,** 284–287 (2013).

111. Gorbachev, R. V., Song, J. C. W., Yu, G. L., Kretinin, A. V., Withers, F., Cao, Y., Mishchenko, A., Grigorieva, I. V., Novoselov, K. S., Levitov, L. S. & Geim, A. K. Detecting Topological Currents in Graphene Superlattices. *Science* **346,** 448–451 (2014).

112. Moon, P. & Koshino, M. Electronic Properties of Graphene/Hexagonal-Boron-Nitride Moir\'e Superlattice. *Phys. Rev. B* **90,** 155406 (2014).

113. Raghu, S. & Haldane, F. D. M. Analogs of Quantum-Hall-effect Edge States in Photonic Crystals. *Phys. Rev. A* **78,** 033834 (2008).

114. Haldane, F. D. M. & Raghu, S. Possible Realization of Directional Optical Waveguides in Photonic Crystals with Broken Time-Reversal Symmetry. *Phys. Rev. Lett.* **100,** 013904 (2008).

115. Wang, Z., Chong, Y. D., Joannopoulos, J. D. & Soljačić, M. Reflection-Free One-Way Edge Modes in a Gyromagnetic Photonic Crystal. *Phys. Rev. Lett.* **100,** 013905 (2008).

116. Maczewsky, L. J., Zeuner, J. M., Nolte, S. & Szameit, A. Observation of Photonic Anomalous Floquet Topological Insulators. *Nat. Commun.* **8,** 13756 (2017).

117. Basov, D. N., Fogler, M. M. & García de Abajo, F. J. Polaritons in van Der Waals Materials. *Science* **354,** aag1992 (2016).

118. Jamadi, O., Rozas, E., Salerno, G., Milićević, M., Ozawa, T., Sagnes, I., Lemaître, A., Le Gratiet, L., Harouri, A., Carusotto, I., Bloch, J. & Amo, A. Direct Observation of Photonic Landau Levels and Helical Edge States in Strained Honeycomb Lattices. *Light Sci. Appl.* **9,** 144 (2020).

119. Wu, L.-H. & Hu, X. Scheme for Achieving a Topological Photonic Crystal by Using Dielectric Material. *Phys. Rev. Lett.* **114,** 223901 (2015).

120. Yves, S., Fleury, R., Berthelot, T., Fink, M., Lemoult, F. & Lerosey, G. Crystalline Metamaterials for Topological Properties at Subwavelength Scales. *Nat. Commun.* **8,** 16023 (2017).

121. Kim, M., Jacob, Z. & Rho, J. Recent Advances in 2D, 3D and Higher-Order Topological Photonics. *Light: Sci. Appl.* **9,** 130 (2020).

122. Goldstein, D. H. & Collett, E. *Polarized Light* 2nd revised and expanded ed. (Marcel Dekker, New York, 2003).

123. Bahari, B., Ndao, A., Vallini, F., Amili, A. E., Fainman, Y. & Kanté, B. Nonreciprocal Lasing in Topological Cavities of Arbitrary Geometries. *Science* **358,** 636–640 (2017).

124. Lu, L., Joannopoulos, J. D. & Soljačić, M. Topological Photonics. *Nat. Photonics* **8,** 821–829 (2014).

125. Esmann, M. & Lanzillotti-Kimura, N. A Topological View on Optical and Phononic Fabry–Perot Microcavities through the Su–Schrieffer–Heeger Model. *Appl. Sci.* **8,** 527 (2018).

126. Su, W. P., Schrieffer, J. R. & Heeger, A. J. Solitons in Polyacetylene. *Phys. Rev. Lett.* **42,** 1698–1701 (1979).

127. Asbóth, J. K., Oroszlány, L. & Pályi, A. *A Short Course on Topological Insulators* (Springer Cham, Cham, 2016).

128. Gorlach, M. A., Ni, X., Smirnova, D. A., Korobkin, D., Zhirihin, D., Slobozhanyuk, A. P., Belov, P. A., Alù, A. & Khanikaev, A. B. Far-Field Probing of Leaky Topological States in All-Dielectric Metasurfaces. *Nat. Commun.* **9,** 909 (2018).

129. Parappurath, N., Alpeggiani, F., Kuipers, L. & Verhagen, E. Direct Observation of Topological Edge States in Silicon Photonic Crystals: Spin, Dispersion, and Chiral Routing. *Sci. Adv.* **6,** eaaw4137 (2020).

130. Barczyk, R., Parappurath, N., Arora, S., Bauer, T., Kuipers, L. & Verhagen, E. Interplay of Leakage Radiation and Protection in Topological Photonic Crystal Cavities. *Laser Photonics Rev.* **2022,** 2200071 (2022).

131. Arora, S., Bauer, T., Parappurath, N., Barczyk, R., Verhagen, E. & Kuipers, L. Breakdown of Spin-to-Helicity Locking at the Nanoscale in Topological Photonic Crystal Edge States. *Phys. Rev. Lett.* **128,** 203903 (2022).

132. Petersen, J., Volz, J. & Rauschenbeutel, A. Chiral Nanophotonic Waveguide Interface Based on Spin-Orbit Interaction of Light. *Science* **346,** 67–71 (2014).

133. Kramers, H. A. L'interaction Entre les Atomes Magnétogènes dans un Cristal Paramagnétique. *Physica* **1,** 182–192 (1934).

134. Arora, S., Bauer, T., Barczyk, R., Verhagen, E. & Kuipers, L. Direct Quantification of Topological Protection in Symmetry-Protected Photonic Edge States at Telecom Wavelengths. *Light Sci. Appl.* **10,** 9 (2021).

135. Ma, T. & Shvets, G. All-Si Valley-Hall Photonic Topological Insulator. *New J. Phys.* **18,** 025012 (2016).

136. Dong, J.-W., Chen, X.-D., Zhu, H., Wang, Y. & Zhang, X. Valley Photonic Crystals for Control of Spin and Topology. *Nat. Mater.* **16,** 298–302 (2017).

137. He, X.-T., Liang, E.-T., Yuan, J.-J., Qiu, H.-Y., Chen, X.-D., Zhao, F.-L. & Dong, J.-W. A Silicon-on-Insulator Slab for Topological Valley Transport. *Nat. Commun.* **10,** 872 (2019).

138. Collins, M. J., Zhang, F., Bojko, R., Chrostowski, L. & Rechtsman, M. C. Integrated Optical Dirac Physics via Inversion Symmetry Breaking. *Phys. Rev. A* **94,** 063827 (2016).

139. Shalaev, M. I., Walasik, W., Tsukernik, A., Xu, Y. & Litchinitser, N. M. Robust Topologically Protected Transport in Photonic Crystals at Telecommunication Wavelengths. *Nat. Nanotechnol.* **14,** 31–34 (2019).

140. Levy, N., Burke, S. A., Meaker, K. L., Panlasigui, M., Zettl, A., Guinea, F., Neto, A. H. C. & Crommie, M. F. Strain-Induced Pseudo–Magnetic Fields Greater Than 300 Tesla in Graphene Nanobubbles. *Science* **329,** 544–547 (2010).

141. Gomes, K. K., Mar, W., Ko, W., Guinea, F. & Manoharan, H. C. Designer Dirac Fermions and Topological Phases in Molecular Graphene. *Nature* **483,** 306–310 (2012).

142. Rechtsman, M. C., Zeuner, J. M., Tünnermann, A., Nolte, S., Segev, M. & Szameit, A. Strain-Induced Pseudomagnetic Field and Photonic Landau Levels in Dielectric Structures. *Nat. Photonics* **7,** 153–158 (2013).

143. Guglielmon, J., Rechtsman, M. C. & Weinstein, M. I. Landau Levels in Strained Two-Dimensional Photonic Crystals. *Phys. Rev. A* **103,** 013505 (2021).

144. Barczyk, R., Kuipers, L. & Verhagen, E. Observation of Landau Levels and Topological Edge States in Photonic Crystals through Pseudomagnetic Fields Induced by Synthetic Strain. arXiv: 2306.03860 (2023).

145. Barsukova, M., Grisé, F., Zhang, Z., Vaidya, S., Guglielmon, J., Weinstein, M. I., He, L., Zhen, B., McEntaffer, R. & Rechtsman, M. C. Direct Observation of Landau Levels in Silicon Photonic Crystals. arXiv: 2306.04011 (2023).

146. Reardon, C. P., Rey, I. H., Welna, K., O'Faolain, L. & Krauss, T. F. Fabrication And Characterization Of Photonic Crystal Slow Light Waveguides And Cavities. *J. Vis. Exp.* **69,** 50216 (2012).

147. Barik, S., Miyake, H., DeGottardi, W., Waks, E. & Hafezi, M. Two-Dimensionally Confined Topological Edge States in Photonic Crystals. *New J. Phys.* **18,** 113013 (2016).

148. Gabrielli, L. H. *Gdspy: Python Module for Creating GDSII Stream Files* version 1.6.13. GitHub, 2023.

149. Dutta, H. S., Goyal, A. K., Srivastava, V. & Pal, S. Coupling Light in Photonic Crystal Waveguides: A Review. *Photonics Nanostructures — Fundam. Appl.* **20,** 41–58 (2016).

150. BEAMER® v6.3.0. *GenISys GmbH* (2021).

151. *Handbook of Silicon Wafer Cleaning Technology* 3rd ed. (eds Reinhardt, K. A. & Kern, W.) (William Andrew Publishing, Norwich, NY, 2018).

152. Yamamoto, K., Nakamura, A. & Hase, U. Control of Cleaning Performance of an Ammonia and Hydrogen Peroxide Mixture (APM) on the Basis of a Kinetic Reaction Model. *IEEE Trans. Semicond. Manuf.* **12,** 288–294 (1999).

153. Gangnaik, A. S., Georgiev, Y. M. & Holmes, J. D. New Generation Electron Beam Resists: A Review. *Chem. Mater.* **29,** 1898–1917 (2017).

154. Tseng, A., Chen, K., Chen, C. & Ma, K. Electron Beam Lithography in Nanoscale Fabrication: Recent Development. *IEEE Trans. Compon. Packag. Manuf.* **26,** 141–149 (2003).

155. Pan, D. Z., Yu, B. & Gao, J.-R. Design for Manufacturing With Emerging Nanolithography. *IEEE Trans. Comput.-Aided Des. Integr. Circuits Syst.* **32,** 1453–1472 (2013).

156. Novotny, L. & Hecht, B. *Principles of Nano-Optics* 2nd ed. (Cambridge University Press, Cambridge, NY, 2012).

157. TRACER® v2.11.0. *GenISys GmbH* (2021).

158. Zhou, J. & Yang, X. Monte Carlo Simulation of Process Parameters in Electron Beam Lithography for Thick Resist Patterning. *J. Vac. Sci. Technol. B* **24,** 1202–1209 (2006).

159. Bean, K. Anisotropic Etching of Silicon. *IEEE Trans. Electron Devices* **25,** 1185–1193 (1978).

160. Bühler, J., Steiner, F.-P. & Baltes, H. Silicon Dioxide Sacrificial Layer Etching in Surface Micromachining. *J. Micromech. Microeng.* **7,** R1 (1997).

161. Garcia, S. P., Bao, H. & Hines, M. A. Understanding the pH Dependence of Silicon Etching: The Importance of Dissolved Oxygen in Buffered HF Etchants. *Surf. Sci.* **541,** 252–261 (2003).

162. Köhler, A. Ein Neues Beleuchtungsverfahren Für Mikrophotographische Zwecke. *Z. Wiss. Mikrosk.* **10,** 433–440 (1893).

163. Goodman, J. W. *Introduction to Fourier Optics* 4th ed. (W.H. Freeman, Macmillan Learning, New York, 2017).

164. Friberg, A. T. & Wolf, E. Angular Spectrum Representation of Scattered Electromagnetic Fields. *J. Opt. Soc. Am.* **73,** 26–32 (1983).

165. Mandel, L. & Wolf, E. *Optical Coherence and Quantum Optics* (Cambridge University Press, Cambridge, NY, 1995).

166. Wolf, E. & Gabor, D. Electromagnetic Diffraction in Optical Systems - I. An Integral Representation of the Image Field. *Proc. R. Soc. Lond. A* **253,** 349–357 (1997).

167. Richards, B., Wolf, E. & Gabor, D. Electromagnetic Diffraction in Optical Systems, II. Structure of the Image Field in an Aplanatic System. *Proc. R. Soc. Lond. A* **253,** 358–379 (1997).

168. Zhao, Y., Edgar, J. S., Jeffries, G. D. M., McGloin, D. & Chiu, D. T. Spin-to-Orbital Angular Momentum Conversion in a Strongly Focused Optical Beam. *Phys. Rev. Lett.* **99,** 073901 (2007).

169. Foreman, M. R. & Török, P. Computational Methods in Vectorial Imaging. *J. Mod. Opt.* **58,** 339–364 (2011).

170. Lodahl, P., Mahmoodian, S., Stobbe, S., Rauschenbeutel, A., Schneeweiss, P., Volz, J., Pichler, H. & Zoller, P. Chiral Quantum Optics. *Nature* **541,** 473–480 (2017).

171. Wu, Y., Li, C., Hu, X., Ao, Y., Zhao, Y. & Gong, Q. Applications of Topological Photonics in Integrated Photonic Devices. *Adv. Opt. Mater.* **5,** 1700357 (2017).

172. Bogaerts, W., Pérez, D., Capmany, J., Miller, D. A. B., Poon, J., Englund, D., Morichetti, F. & Melloni, A. Programmable Photonic Circuits. *Nature* **586,** 207–216 (2020).

173. Altug, H., Oh, S.-H., Maier, S. A. & Homola, J. Advances and Applications of Nanophotonic Biosensors. *Nat. Nanotechnol.* **17,** 5–16 (2022).

174. Shalaev, M. I., Walasik, W., Tsukernik, A., Xu, Y. & Litchinitser, N. M. Robust topologically protected transport in photonic crystals at telecommunication wavelengths. *Nat. Nanotechnol.* **14,** 31–34 (2019).

175. Cheng, L., Mao, S., Li, Z., Han, Y. & Fu, H. Grating Couplers on Silicon Photonics: Design Principles, Emerging Trends and Practical Issues. *Micromachines* **11,** 666 (2020).

176. Wang, Y., Shi, W., Wang, X., Lu, Z., Caverley, M., Bojko, R., Chrostowski, L. & Jaeger, N. A. F. Design of Broadband Subwavelength Grating Couplers with Low Back Reflection. *Opt. Lett.* **40,** 4647–4650 (2015).

177. Sandtke, M., Engelen, R. J. P., Schoenmaker, H., Attema, I., Dekker, H., Cerjak, I., Korterik, J. P., Segerink, F. B. & Kuipers, L. Novel Instrument for Surface Plasmon Polariton Tracking in Space and Time. *Rev. Sci. Instrum.* **79,** 013704 (2008).

178. Burresi, M., Engelen, R. J. P., Opheij, A., van Oosten, D., Mori, D., Baba, T. & Kuipers, L. Observation of Polarization Singularities at the Nanoscale. *Phys. Rev. Lett.* **102,** 033902 (2009).

179. Rotenberg, N. & Kuipers, L. Mapping Nanoscale Light Fields. *Nat. Photonics* **8,** 919–926 (2014).

180. Gersen, H., Karle, T. J., Engelen, R. J. P., Bogaerts, W., Korterik, J. P., van Hulst, N. F., Krauss, T. F. & Kuipers, L. Real-Space Observation of Ultraslow Light in Photonic Crystal Waveguides. *Phys. Rev. Lett.* **94,** 073903 (2005).

181. Le Feber, B., Rotenberg, N., Beggs, D. M. & Kuipers, L. Simultaneous Measurement of Nanoscale Electric and Magnetic Optical Fields. *Nat. Photonics* **8,** 43–46 (2014).

182. Balistreri, M. L. M., Korterik, J. P., Kuipers, L. & van Hulst, N. F. Local Observations of Phase Singularities in Optical Fields in Waveguide Structures. *Phys. Rev. Lett.* **85,** 294–297 (2000).

183. Engelen, R. J. P., Sugimoto, Y., Gersen, H., Ikeda, N., Asakawa, K. & Kuipers, L. (Ultrafast Evolution of Photonic Eigenstates in K-Space. *Nat. Phys.* **3,** 401–405 (2007).

184. Le Feber, B., Sipe, J. E., Wulf, M., Kuipers, L. & Rotenberg, N. A Full Vectorial Mapping of Nanophotonic Light Fields. *Light. Sci. Appl.* **8,** 28 (2019).

185. De Angelis, L., Alpeggiani, F. & Kuipers, L. Spatial Bunching of Same-Index Polarization Singularities in Two-Dimensional Random Vector Waves. *Phys. Rev. X* **8,** 041012 (2018).

186. Engelen, R. J., Sugimoto, Y., Gersen, H., Ikeda, N., Asakawa, K. & Kuipers, L. Ultrafast evolution of photonic eigenstates in k-space. *Nat. Phys.* **3,** 401–405 (2007).

187. Burresi, M., Engelen, R. J., Opheij, A., Van Oosten, D., Mori, D., Baba, T. & Kuipers, L. Observation of polarization singularities at the nanoscale. *Phys. Rev. Lett.* **102,** 033902 (2009).

188. Klembt, S., Harder, T. H., Egorov, O. A., Winkler, K., Ge, R., Bandres, M. A., Emmerling, M., Worschech, L., Liew, T. C., Segev, M., Schneider, C. & Höfling, S. Exciton-polariton topological insulator. *Nature* **562,** 552–556 (2018).

189. Carusotto, I. & Ciuti, C. Quantum fluids of light. *Rev. Mod. Phys.* **85,** 299–366 (2013).

190. Wang, Z., Chong, Y. D., Joannopoulos, J. D. & Soljačić, M. Reflection-Free One-Way Edge Modes in a Gyromagnetic Photonic Crystal. *Phys. Rev. Lett.* **100,** 013905 (2008).

191. Haldane, F. D. M. & Raghu, S. Possible realization of directional optical waveguides in photonic crystals with broken time-reversal symmetry. *Phys. Rev. Lett.* **100,** 013904 (2008).

192. Raghu, S. & Haldane, F. D. Analogs of quantum-Hall-effect edge states in photonic crystals. *Phys. Rev. A* **78,** 033834 (2008).

193. Plotnik, Y., Rechtsman, M. C., Song, D., Heinrich, M., Zeuner, J. M., Nolte, S., Lumer, Y., Malkova, N., Xu, J., Szameit, A., Chen, Z. & Segev, M. Observation of unconventional edge states in 'photonic graphene'. *Nat. Mater.* **13,** 57–62 (2014).

194. Wu, L.-H. & Hu, X. Scheme for Achieving a Topological Photonic Crystal by Using Dielectric Material. *Phys. Rev. Lett.* **114,** 223901 (2015).

195. Khanikaev, A. B., Hossein Mousavi, S., Tse, W. K., Kargarian, M., MacDonald, A. H. & Shvets, G. Photonic topological insulators. *Nat. Mater.* **12,** 233–239 (2013).

196. Barik, S., Karasahin, A., Flower, C., Cai, T., Miyake, H., DeGottardi, W., Hafezi, M. & Waks, E. A Topological Quantum Optics Interface. *Science* **359,** 666–668 (2018).

197. Smirnova, D., Kruk, S., Leykam, D., Melik-Gaykazyan, E., Choi, D. Y. & Kivshar, Y. Third-Harmonic Generation in Photonic Topological Metasurfaces. *Phys. Rev. Lett.* **123,** 103901 (2019).

198. He, X. T., Liang, E. T., Yuan, J. J., Qiu, H. Y., Chen, X. D., Zhao, F. L. & Dong, J. W. A silicon-on-insulator slab for topological valley transport. *Nat. Commun.* **10,** 872 (2019).

199. Lu, L., Joannopoulos, J. D. & Soljačić, M. Topological photonics. *Nat. Photonics* **8,** 821–829 (2014).

200. Lu, M.-H., Wang, Z. D., Wang, H.-F., Xie, B.-Y., Zhu, X.-Y. & Chen, Y.-F. Photonics meets topology. *Opt. Express* **26,** 24531 (2018).

201. Dubrovkin, A. M., Chattopadhyay, U., Qiang, B., Buchnev, O., Wang, Q. J., Chong, Y. & Zheludev, N. I. Near-field mapping of the edge mode of a topological valley slab waveguide at $\lambda = 1.55\ \mu$m. *Appl. Phys. Lett.* **116,** 191105 (2020).

202. Schaibley, J. R., Yu, H., Clark, G., Rivera, P., Ross, J. S., Seyler, K. L., Yao, W. & Xu, X. Valleytronics in 2D Materials. *Nat. Rev. Mater.* **1,** 1–15 (2016).

203. Xiao, D., Yao, W. & Niu, Q. Valley-contrasting physics in graphene: Magnetic moment and topological transport. *Phys. Rev. Lett.* **99,** 236809 (2007).

204. Zak, J. Berry's Phase for Energy Bands in Solids. *Phys. Rev. Lett.* **62,** 2747–2750 (1989).

205. Cheng, X., Jouvaud, C., Ni, X., Mousavi, S. H., Genack, A. Z. & Khanikaev, A. B. Robust Reconfigurable Electromagnetic Pathways within a Photonic Topological Insulator. *Nat. Mater.* **15,** 542–548 (2016).

206. Gersen, H., Karle, T. J., Engelen, R. J. P., Bogaerts, W., Korterik, J. P., van Hulst, N. F., Krauss, T. F. & Kuipers, L. Direct observation of Bloch harmonics and negative phase velocity in photonic crystal waveguides. *Phys. Rev. Lett.* **94,** 123901 (2005).

207. Rotenberg, N. & Kuipers, L. Mapping nanoscale light fields. *Nat. Photonics* **8,** 919–926 (2014).

208. Balistreri, M. L. M., Korterik, J. P., Kuipers, L. & van Hulst, N. F. Local Observations of Phase Singularities in Optical Fields in Waveguide Structures. *Phys. Rev. Lett.* **85,** 294–297 (2000).

209. Ma, T., Khanikaev, A. B., Mousavi, S. H. & Shvets, G. Guiding electromagnetic waves around sharp corners: Topologically protected photonic transport in metawaveguides. *Phys. Rev. Lett.* **114,** 127401 (2015).

210. Krauss, T. F., O'Faolain, L., Schulz, S., Beggs, D. M., Morichetti, F., Canciamilla, A., Torregiani, M., Melloni, A., Mazoyer, S., Lalanne, P., Samarelli, A., Sorel, M. & Rue, R. D. L. Understanding the rich physics of light propagation in slow photonic crystal waveguides. in *Advances in Slow and Fast Light III* (SPIE, Bellingham, WA, 2010).

211. Kuang, W. & O'Brien, J. D. Strategy for Reducing the Out-of-Plane Radiation Loss in Photonic Crystal Waveguides on High-Index Substrates. in *Conference on Lasers and Electro-Optics/International Quantum Electronics Conference and Photonic Applications Systems Technologies* (Optica Publishing Group, Washington, D.C., 2004).

212. Chow, E., Lin, S. Y., Wendt, J. R., Johnson, S. G. & Joannopoulos, J. D. Quantitative analysis of bending efficiency in photonic-crystal waveguide bends at λ = 1.55 μm wavelengths. *Opt. Lett.* **26,** 286 (2001).

213. Chutinan, A., Okano, M. & Noda, S. Wider bandwidth with high transmission through waveguide bends in two-dimensional photonic crystal slabs. *Appl. Phys. Lett.* **80,** 1698–1700 (2002).

214. Engelen, R. J. P., Mori, D., Baba, T. & Kuipers, L. Two Regimes of Slow-Light Losses Revealed by Adiabatic Reduction of Group Velocity. *Phys. Rev. Lett.* **101,** 103901 (2008).

215. Mazoyer, S., Lalanne, P., Rodier, J., Hugonin, J., Spasenović, M., Kuipers, L., Beggs, D. & Krauss, T. Statistical fluctuations of transmission in slow light photonic-crystal waveguides. *Opt. Express* **18,** 14654 (2010).

216. Johnson, S. G. & Joannopoulos, J. D. Block-Iterative Frequency-Domain Methods for Maxwell's Equations in a Planewave Basis. *Opt. Express* **8,** 173–190 (2001).

217. Singh, A., Ctistis, G., Huisman, S. R., Korterik, J. P., Mosk, A. P., Herek, J. L. & Pinkse, P. W. H. Observation of nonlinear bands in near-field scanning optical microscopy of a photonic-crystal waveguide. *J. Appl. Phys.* **117,** 033104 (2015).

218. Hafezi, M., Demler, E. A., Lukin, M. D. & Taylor, J. M. Robust Optical Delay Lines with Topological Protection. *Nat. Phys.* **7,** 907–912 (2011).

219. Dietrich, C. P., Fiore, A., Thompson, M. G., Kamp, M. & Höfling, S. GaAs Integrated Quantum Photonics: Towards Compact and Multi-Functional Quantum Photonic Integrated Circuits. *Laser Photonics Rev.* **10,** 870–894 (2016).

220. Srinivasan, K. & Painter, O. Momentum Space Design of High-Q Photonic Crystal Optical Cavities. *Opt. Express* **10,** 670–684 (2002).

221. Akahane, Y., Asano, T., Song, B.-S. & Noda, S. High-Q Photonic Nanocavity in a Two-Dimensional Photonic Crystal. *Nature* **425,** 944–947 (2003).

222. Akahane, Y., Asano, T., Song, B.-S. & Noda, S. Fine-Tuned High-Q Photonic-Crystal Nanocavity. *Opt. Express* **13,** 1202–1214 (2005).

223. Foreman, M. R., Swaim, J. D. & Vollmer, F. Whispering Gallery Mode Sensors. *Adv. Opt. Photonics* **7,** 168–240 (2015).

224. Ren, Y., Qiao, Z. & Niu, Q. Topological Phases in Two-Dimensional Materials: A Review. *Rep. Prog. Phys.* **79,** 066501 (2016).

225. Fu, L. Topological Crystalline Insulators. *Phys. Rev. Lett.* **106,** 106802 (2011).

226. Anderson, P. D. & Subramania, G. Unidirectional Edge States in Topological Honeycomb-Lattice Membrane Photonic Crystals. *Opt. Express* **25,** 23293 (2017).

227. Bliokh, K. Y., Smirnova, D. & Nori, F. Quantum Spin Hall Effect of Light. *Science* **348,** 1448–1451 (2015).

228. Sala, V. G., Solnyshkov, D. D., Carusotto, I., Jacqmin, T., Lemaître, A., Terças, H., Nalitov, A., Abbarchi, M., Galopin, E., Sagnes, I., Bloch, J., Malpuech, G. & Amo, A. Spin-Orbit Coupling for Photons and Polaritons in Microstructures. *Phys. Rev. X* **5,** 011034 (2015).

229. Barik, S., Karasahin, A., Mittal, S., Waks, E. & Hafezi, M. Chiral Quantum Optics Using a Topological Resonator. *Phys. Rev. B* **101,** 205303 (2020).

230. Ji, C.-Y., Zhang, Y., Zou, B. & Yao, Y. Robust Fano Resonance in the Photonic Valley Hall States. *Phys. Rev. A* **103,** 023512 (2021).

231. Kim, K.-H. & Om, K.-K. Multiband Photonic Topological Valley-Hall Edge Modes and Second-Order Corner States in Square Lattices. *Adv. Opt. Mater.* **9,** 2001865 (2021).

232. Mehrabad, M. J., Foster, A. P., Dost, R., Clarke, E., Patil, P. K., Fox, A. M., Skolnick, M. S. & Wilson, L. R. Chiral Topological Photonics with an Embedded Quantum Emitter. *Optica* **7,** 1690–1696 (2020).

233. Zeng, Y., Chattopadhyay, U., Zhu, B., Qiang, B., Li, J., Jin, Y., Li, L., Davies, A. G., Linfield, E. H., Zhang, B., Chong, Y. & Wang, Q. J. Electrically Pumped Topological Laser with Valley Edge Modes. *Nature* **578,** 246–250 (2020).

234. Siroki, G., Huidobro, P. A. & Giannini, V. Topological Photonics: From Crystals to Particles. *Phys. Rev. B* **96,** 041408 (2017).

235. Yang, Y. & Hang, Z. H. Topological Whispering Gallery Modes in Two-Dimensional Photonic Crystal Cavities. *Opt. Express* **26,** 21235–21241 (2018).

236. Gao, X., Yang, L., Lin, H., Zhang, L., Li, J., Bo, F., Wang, Z. & Lu, L. Dirac-Vortex Topological Cavities. *Nat. Nanotechnol.* **15,** 1012–1018 (2020).

237. Jalali Mehrabad, M., Foster, A. P., Dost, R., Clarke, E., Patil, P. K., Farrer, I., Heffernan, J., Skolnick, M. S. & Wilson, L. R. A Semiconductor Topological Photonic Ring Resonator. *Appl. Phys. Lett.* **116,** 061102 (2020).

238. Sun, X.-C. & Hu, X. Topological Ring-Cavity Laser Formed by Honeycomb Photonic Crystals. *Phys. Rev. B* **103,** 245305 (2021).

239. Dong, J., Hu, Q., Ji, C.-Y., Zou, B. & Zhang, Y. Exceptional Points in a Topological Waveguide-Cavity Coupled System. *New J. Phys.* **23,** 113025 (2021).

240. Dong, J., Zou, B. & Zhang, Y. Theoretical Study of Transparent Peaks in a Topological Waveguide-Cavity Coupled System. *Appl. Phys. Lett.* **119,** 251101 (2021).

241. Shao, Z.-K., Chen, H.-Z., Wang, S., Mao, X.-R., Yang, Z.-Q., Wang, S.-L., Wang, X.-X., Hu, X. & Ma, R.-M. A High-Performance Topological Bulk Laser Based on Band-Inversion-Induced Reflection. *Nat. Nanotechnol.* **15,** 67–72 (2020).

242. Kim, H.-R., Hwang, M.-S., Smirnova, D., Jeong, K.-Y., Kivshar, Y. & Park, H.-G. Multipolar Lasing Modes from Topological Corner States. *Nat. Commun.* **11,** 5758 (2020).

243. Jágerská, J., Zhang, H., Diao, Z., Thomas, N. L. & Houdré, R. Refractive Index Sensing with an Air-Slot Photonic Crystal Nanocavity. *Opt. Lett.* **35,** 2523–2525 (2010).

244. Hamel, P., Haddadi, S., Raineri, F., Monnier, P., Beaudoin, G., Sagnes, I., Levenson, A. & Yacomotti, A. M. Spontaneous Mirror-Symmetry Breaking in Coupled Photonic-Crystal Nanolasers. *Nat. Photonics* **9,** 311–315 (2015).

245. Iwahashi, S., Kurosaka, Y., Sakai, K., Kitamura, K., Takayama, N. & Noda, S. Higher-Order Vector Beams Produced by Photonic-Crystal Lasers. *Opt. Express* **19,** 11963–11968 (2011).

246. Yang, Z.-Q., Shao, Z.-K., Chen, H.-Z., Mao, X.-R. & Ma, R.-M. Spin-Momentum-Locked Edge Mode for Topological Vortex Lasing. *Phys. Rev. Lett.* **125,** 013903 (2020).

247. Yu, S.-Y., He, C., Sun, X.-C., Wang, H.-F., Wang, J.-Q., Zhang, Z.-D., Xie, B.-Y., Tian, Y., Lu, M.-H. & Chen, Y.-F. Critical Couplings in Topological-Insulator Waveguide-Resonator Systems Observed in Elastic Waves. *Natl. Sci. Rev.* **8,** nwaa262 (2021).

248. Portalupi, S. L., Galli, M., Reardon, C., Krauss, T., O'Faolain, L., Andreani, L. C. & Gerace, D. Planar Photonic Crystal Cavities with Far-Field Optimization for High Coupling Efficiency and Quality Factor. *Opt. Express* **18,** 16064 (2010).

249. Orazbayev, B. & Fleury, R. Quantitative Robustness Analysis of Topological Edge Modes in C6 and Valley-Hall Metamaterial Waveguides. *Nanophotonics* **8,** 1433–1441 (2019).

250. de Paz, M. B., Vergniory, M. G., Bercioux, D., García-Etxarri, A. & Bradlyn, B. Engineering Fragile Topology in Photonic Crystals: Topological Quantum Chemistry of Light. *Phys. Rev. Res.* **1,** 032005 (2019).

251. Palmer, S. J. & Giannini, V. Berry Bands and Pseudo-Spin of Topological Photonic Phases. *Phys. Rev. Res.* **3,** L022013 (2021).

252. Hong, X., van Dijk, E. M. P. H., Hall, S. R., Götte, J. B., van Hulst, N. F. & Gersen, H. Background-Free Detection of Single 5 Nm Nanoparticles through Interferometric Cross-Polarization Microscopy. *Nano Lett.* **11,** 541–547 (2011).

253. Rubinsztein-Dunlop, H. *et al.* Roadmap on Structured Light. *J. Opt.* **19,** 013001 (2016).

254. Kim, S.-H. & Lee, Y.-H. Symmetry relations of two-dimensional photonic crystal cavity modes. *IEEE J. Quantum Electron.* **39,** 1081–1085 (2003).

255. Lu, X., Rogers, S., Jiang, W. C. & Lin, Q. Selective Engineering of Cavity Resonance for Frequency Matching in Optical Parametric Processes. *Appl. Phys. Lett.* **105,** 151104 (2014).

256. Johnson, S. G., Ibanescu, M., Skorobogatiy, M. A., Weisberg, O., Joannopoulos, J. D. & Fink, Y. Perturbation Theory for Maxwell's Equations with Shifting Material Boundaries. *Phys. Rev. E* **65,** 066611 (2002).

257. Poynting, J. H. The Wave Motion of a Revolving Shaft, and a Suggestion as to the Angular Momentum in a Beam of Circularly Polarised Light. *Proc. R. Soc. Lond. A* **82,** 560–567 (1909).

258. COMSOL Multiphysics® v. 5.2. *www.comsol.com COMSOL AB* (Stockholm, Sweden, 2015).

259. Kane, C. L. & Mele, E. J. Size, Shape, and Low Energy Electronic Structure of Carbon Nanotubes. *Phys. Rev. Lett.* **78,** 1932–1935 (1997).

260. Song, W., Li, T., Wu, S., Wang, Z., Chen, C., Chen, Y., Huang, C., Qiu, K., Zhu, S., Zou, Y. & Li, T. Dispersionless Coupling among Optical Waveguides by Artificial Gauge Field. *Phys. Rev. Lett.* **129,** 053901 (2022).

261. Bellec, M., Poli, C., Kuhl, U., Mortessagne, F. & Schomerus, H. Observation of Supersymmetric Pseudo-Landau Levels in Strained Microwave Graphene. *Light Sci. Appl.* **9,** 146 (2020).

262. Jia, H., Wang, M., Ma, S., Zhang, R.-Y., Hu, J., Wang, D. & Chan, C. T. Experimental Realization of Chiral Landau Levels in Two-Dimensional Dirac Cone Systems with Inhomogeneous Effective Mass. *Light: Sci. Appl.* **12,** 165 (2023).

263. Lledó, C., Carusotto, I. & Szymanska, M. Polariton Condensation into Vortex States in the Synthetic Magnetic Field of a Strained Honeycomb Lattice. *SciPost Phys.* **12,** 068 (2022).

264. Duan, G., Zheng, S., Zhang, J., Jiang, Z., Man, X., Yu, D. & Xia, B. Synthetic Gauge Fields and Landau Levels in Acoustic Moiré Superlattices. *Applied Physics Letters* **123,** 021702 (2023).

265. Wen, X., Qiu, C., Qi, Y., Ye, L., Ke, M., Zhang, F. & Liu, Z. Acoustic Landau Quantization and Quantum-Hall-like Edge States. *Nat. Phys.* **15,** 352–356 (2019).

266. Yang, Z., Gao, F., Yang, Y. & Zhang, B. Strain-Induced Gauge Field and Landau Levels in Acoustic Structures. *Phys. Rev. Lett.* **118,** 194301 (2017).

267. Abbaszadeh, H., Souslov, A., Paulose, J., Schomerus, H. & Vitelli, V. Sonic Landau Levels and Synthetic Gauge Fields in Mechanical Metamaterials. *Phys. Rev. Lett.* **119,** 195502 (2017).

268. Peri, V., Serra-Garcia, M., Ilan, R. & Huber, S. D. Axial-Field-Induced Chiral Channels in an Acoustic Weyl System. *Nat. Phys.* **15,** 357–361 (2019).

269. Salerno, G., Ozawa, T., Price, H. M. & Carusotto, I. How to Directly Observe Landau Levels in Driven-Dissipative Strained Honeycomb Lattices. *2D Mater.* **2,** 034015 (2015).

270. Salerno, G., Ozawa, T., Price, H. M. & Carusotto, I. Propagating Edge States in Strained Honeycomb Lattices. *Phys. Rev. B* **95,** 245418 (2017).

271. Borregaard, J., Sørensen, A. S. & Lodahl, P. Quantum Networks with Deterministic Spin–Photon Interfaces. *Adv. Quantum Technol.* **2,** 1800091 (2019).

272. Krauss, T. F. Why Do We Need Slow Light? *Nat. Photonics* **2,** 448–450 (2008).

273. Smirnova, D., Leykam, D., Chong, Y. & Kivshar, Y. Nonlinear Topological Photonics. *Appl. Phys. Rev.* **7,** 021306 (2020).

274. Schomerus, H. & Halpern, N. Y. Parity Anomaly and Landau-Level Lasing in Strained Photonic Honeycomb Lattices. *Phys. Rev. Lett.* **110,** 013903 (2013).

275. Yang, Y., Roques-Carmes, C., Kooi, S. E., Tang, H., Beroz, J., Mazur, E., Kaminer, I., Joannopoulos, J. D. & Soljačić, M. Photonic Flatband Resonances for Free-Electron Radiation. *Nature* **613,** 42–47 (2023).

276. Huang, Z.-T., Hong, K.-B., Lee, R.-K., Pilozzi, L., Conti, C., Wu, J.-S. & Lu, T.-C. Pattern-Tunable Synthetic Gauge Fields in Topological Photonic Graphene. *Nanophotonics* **11,** 1297–1308 (2022).

277. Kiriushechkina, S., Vakulenko, A., Smirnova, D., Guddala, S., Kawaguchi, Y., Komissarenko, F., Allen, M., Allen, J. & Khanikaev, A. B. Spin-Dependent Properties of Optical Modes Guided by Adiabatic Trapping Potentials in Photonic Dirac Metasurfaces. *Nat. Nanotechnol.* **18,** 875–881 (2023).

278. Ren, B., Wang, H., Belić, M. R., Li, Y., Zhu, X. & Zhang, Y. Zero-Energy Edge States and Solitons in Strained Photonic Graphene. *Phys. Rev. A* **107,** 043504 (2023).

279. Akhmerov, A. R. & Beenakker, C. W. J. Boundary Conditions for Dirac Fermions on a Terminated Honeycomb Lattice. *Phys. Rev. B* **77,** 085423 (2008).

280. Kohmoto, M. & Hasegawa, Y. Zero Modes and Edge States of the Honeycomb Lattice. *Phys. Rev. B* **76,** 205402 (2007).

281. Hsu, C. W., Zhen, B., Stone, A. D., Joannopoulos, J. D. & Soljačić, M. Bound States in the Continuum. *Nat. Rev. Mater.* **1,** 1–13 (2016).

282. Rosiek, C. A., Arregui, G., Vladimirova, A., Albrechtsen, M., Vosoughi Lahijani, B., Christiansen, R. E. & Stobbe, S. Observation of Strong Backscattering in Valley-Hall Photonic Topological Interface Modes. *Nat. Photon.* **17,** 386–392 (2023).

283. Arregui, G., Gomis-Bresco, J., Sotomayor-Torres, C. M. & Garcia, P. D. Quantifying the Robustness of Topological Slow Light. *Phys. Rev. Lett.* **126,** 027403 (2021).

284. Flower, C. J., Barik, S., Mehrabad, M. J., Martin, N. J., Mittal, S. & Hafezi, M. Topological Edge Mode Tapering. *ACS Photonics* (2023).

285. Li, Y., Yu, Y., Liu, F., Zhang, B. & Shvets, G. Topology-Controlled Photonic Cavity Based on the Near-Conservation of the Valley Degree of Freedom. *Phys. Rev. Lett.* **125,** 213902 (2020).

286. Parto, M., Liu, Y. G. N., Bahari, B., Khajavikhan, M. & Christodoulides, D. N. Non-Hermitian and Topological Photonics: Optics at an Exceptional Point. *Nanophotonics* **10,** 403–423 (2021).

287. Umucalılar, R. O. & Carusotto, I. Fractional Quantum Hall States of Photons in an Array of Dissipative Coupled Cavities. *Phys. Rev. Lett.* **108,** 206809 (2012).

288. Kapit, E., Hafezi, M. & Simon, S. H. Induced Self-Stabilization in Fractional Quantum Hall States of Light. *Phys. Rev. X* **4,** 031039 (2014).

289. Segev, M. & Bandres, M. A. Topological Photonics: Where Do We Go from Here? *Nanophotonics* **10,** 425–434 (2021).

290. Getting Topological Photonics out of the Laboratory. *Nat. Commun.* **13,** 2249 (2022).

291. Price, H. *et al.* Roadmap on topological photonics. *J. Phys. Photonics* **4,** 032501 (2022).

292. Kumar, A., Gupta, M., Pitchappa, P., Wang, N., Fujita, M. & Singh, R. Terahertz Topological Photonic Integrated Circuits for 6G and beyond: A Perspective. *J. Appl. Phys.* **132,** 140901 (2022).

293. Yang, Z., Lustig, E., Lumer, Y. & Segev, M. Photonic Floquet Topological Insulators in a Fractal Lattice. *Light. Sci. Appl.* **9,** 128 (2020).

SUMMARY

TOPOLOGICAL CONTROL OF LIGHT IN PHOTONIC CRYSTALS

Light, both fascinating and fundamental, intricately shapes our perception of the world around us. It has become a pivotal element in a multitude of technological advancements, from the mere illumination of our homes to the development of cutting-edge imaging techniques and advanced optical communication systems. The crux of these innovations lies in our ever-increasing ability to exert control over light. As light and matter are inherently intertwined, gaining greater control over matter invariably translates to enhanced control over light. Venturing into the realm of the nanoscale unveils a myriad of opportunities for precisely tailoring the interaction of light and matter, creating a platform where the common wave nature of light and electrons allows for the transference of many analogies and concepts from condensed matter physics. Particularly compelling is the introduction of topological concepts, initially formulated for electronic systems, into the realm of photonics.

In condensed matter physics, topology has played an indispensable role in the discovery of novel phases of matter. Topology provides a framework to describe and understand the global features of systems that remain invariant under continuous transformations. This theoretical approach has been pivotal in explaining phenomena like the quantum Hall effect, where coupling of the charge degree of freedom to an external magnetic field that breaks time-reversal-symmetry leads to quantized electron transport. The requirement of magnetic fields is technologically challenging, especially in the context of miniaturized devices. In the quantum spin Hall effect and the quantum valley Hall effect, time-reversal-symmetry is replaced by spatial lattice symmetries that are associated with (pseudo-) spin degrees of freedom and which can be broken at will to induce topological phases, waiving the need for external magnetic fields. Explaining these phenomena in the context of topology has paved the way for understanding topological insulators — materials that are insulating in their interior but feature highly conductive states on their surface. Intriguingly, these surface or edge states are protected by the underlying topology of the bulk material, which renders them inherently robust to a broad range of perturbations.

Motivated by the advancements in condensed matter physics, topological ideas where soon introduced as a design paradigm to photonics. While being studied in a diverse set of systems, photonic crystals are especially appealing as they can bring topological protection to small scales and on-chip applications. Photonic crystals are structures featuring a periodic arrangement of materials with different dielectric constants, patterned on subwavelength scales. As such, they act like an effective material through which light propagates in a way that is largely analogous to how electrons propagate through the atomic lattice of a crystal. Topological insulators described in the framework of the quantum spin Hall effect and the quantum valley Hall effect represent an especially promising class of materials to emulate in photonic crystals due their reliance on spatial symmetries rather than magnetic fields. Moreover, many intriguing topological phenomena have been observed in two-dimensional solid state systems such as graphene, a geometry which may be readily emulated in photonic lattices.

It is within this fascinating context that this thesis explores the potential and limitations of transferring topological concepts from the domain of matter to light, with a focus on experimental investigations within the field of two-dimensional photonic crystals operating in the telecom frequency regime. We aim to explore ways to introduce topological phenomena in photonic crystals, identify the hallmarks of non-trivial band topology in the states that emerge, and study their impact on the flow and confinement of light in waveguides and cavities. We elaborate in detail on the theoretical concepts underlying topological photonic crystals in Chapter 1. The discussion spans the arc between the vectorial properties of light, the physics of condensed matter systems with emphasis on the Bloch wave formalism and Dirac physics, its relation to the abstract mathematical field of topology, and finally the synthesis of all these concepts in the form of topological photonic crystals.

The research on photonic crystals was largely propelled by the development of advanced nanofabrication techniques, wherefrom two-dimensional photonic crystals benefit especially due to the compatibility with widespread semiconductor fabrication processes. This enabled the realization of complex and large scale photonic crystal lattices with intricate features at operating frequencies up to the optical regime. In Chapter 2, we report on our own fabrication procedure used to obtain the suspended silicon photonic crystal membranes studied throughout this work, and the experimental techniques employed to characterize the fabricated devices. Radiative photonic crystal modes may be conveniently probed from the far-field, whereby we use a Fourier spectropolarimetry setup to characterize the modes spectral, spatial, and polarimetric properties in real- and momentum space. Complementary near-field techniques are used to characterize non-radiative modes, performed via phase- and polarization-resolved near-field scanning optical microscopy.

While there are many analogies to condensed matter systems, photons also exhibit striking differences to electrons, most notably their bosonic rather than fermionic character. Further, due to their reliance on spatial symmetries, topological insulators based on the quantum spin Hall effect and quantum valley Hall

effect are in fact reciprocal systems. It is thus especially intriguing to study the extent and robustness of topological protection for light that these systems offer in practical experiments. In Chapter 3, we put the topological protection in a photonic crystal platform emulating the quantum valley Hall effect for light to the test This system is non-radiative and thus appealing in the context of low-loss waveguides. Using phase-sensitive near-field scanning optical microscopy, we resolve forward- and backward-propagating waveguide modes and accurately quantify the amount of backscattering experienced at engineered defects. We develop a transfer matrix model to estimate the reflection coefficients, which turn out to be an order of magnitude lower compared to conventional photonic crystal waveguides, demonstrating enhanced protection against back-scattering.

In Chapter 4, we study the far-field emission of cavities in a photonic crystal platform that features the photonic quantum spin Hall effect and supports helical edge states that are weakly coupled to the radiation continuum, examining the signatures of topological light confinement. We characterize the mode spectra and multipolar nature of cavities scaling down to the size of single point defects within the surrounding photonic crystal lattice by mapping their mode profiles in real- and momentum-space. Hallmarks of the topological bulk band structure such as band inversion-induced confinement and inverted scaling behavior of the mode spectra for trivial and topological defect cavities are revealed. We also evidence signatures of topological protection in the cavities' loss rates, which are largely unaffected by cavity shape and size. Lastly, we explore the behavior of the cavities as components in integrated devices when interfaced with topological waveguides, demonstrating a coupling mechanism that is dictated by spin-conservation, a property rooted in the helicity of the topological edge states underlying the modes in the platform.

As light does not naturally interact with real magnetic fields, several proposals have been put forward on how to effectively mediate magnetic interactions for photons. In Chapter 5, we explore the possibilities to control light propagation and localization on chip via synthetic gauge fields that are induced by engineered strain of a photonic crystal lattice, analogous to strained graphene. Akin to the formation of Landau levels for electrons in an external magnetic field, we observe a discretization of the photonic dispersion into flat bands due to the strain-induced pseudomagnetic fields, with associated high degeneracy and local density of states. The large design freedom of the photonic crystal platform opens up unprecedented flexibility for strain engineering, which we evidence by realizing domains of opposite pseudomagnetic fields that host topological edge states at their interface. The pseudomagnetic-field-induced states feature remarkably high quality factors, despite being inherently coupled to free-space radiation.

The findings and conclusions of this work contribute to a better assessment of the prospects and opportunities for future research and applicability of two-dimensional topological photonic crystals in integrated photonic devices.

SAMENVATTING

TOPOLOGISCHE CONTROLE VAN LICHT IN FOTONISCHE KRISTALLEN

Licht, zowel fascinerend als fundamenteel, vormt op complexe wijze onze perceptie van de wereld om ons heen. Het is een essentieel element geworden in tal van technologische ontwikkelingen, van de eenvoudige verlichting van onze huizen tot de ontwikkeling van geavanceerde beeldvormingstechnieken en geavanceerde optische communicatiesystemen. De kern van deze innovaties ligt in onze steeds grotere mogelijkheid om controle uit te oefenen over licht. Aangezien licht en materie onlosmakelijk met elkaar verbonden zijn, leidt het verkrijgen van een grotere controle over materie onvermijdelijk tot verbeterde controle over licht. Het betreden van het domein van de nanometerschaal onthult tal van mogelijkheden om de interactie tussen licht en materie nauwkeurig af te stemmen, waardoor er een platform ontstaat waarop de gemeenschappelijke golfachtige aard van licht en elektronen het mogelijk maakt om veel analogieën en concepten uit de fysica van de gecondenseerde materie over te dragen. Bijzonder boeiend is de introductie van topologische concepten, oorspronkelijk geformuleerd voor elektronische systemen, in het domein van de fotonica.

In de fysica van de gecondenseerde materie heeft topologie een onmisbare rol gespeeld bij de ontdekking van nieuwe fasen van materie. Topologie biedt een kader om de globale kenmerken van systemen te beschrijven en te begrijpen die welke onveranderd blijven onder continue transformaties. Deze theoretische benadering is cruciaal geweest bij het verklaren van fenomenen zoals het kwantum-hall-effect, waarbij de koppeling van de elektrische lading aan een extern magnetisch veld waarbij tijdomkeersymmetrie verbreekt leidt tot gekwantiseerd elektronentransport. De vereiste van magnetische velden is technologisch uitdagend, vooral in de context van geminiaturiseerde apparaten. In het kwantum-spin-hall-effect en het kwantum-valley-hall-effect wordt tijdsomkeersymmetrie vervangen door ruimtelijke rooster symmetrieën die geassocieerd zijn met (pseudo-) spin-toestandendie opzettelijk verbroken kunnen worden om topologische fasen te induceren zonder de noodzaak van externe magnetische velden. Door deze fenomenen uit te leggen in de context van topologie is de weg geëffend voor het begrijpen van topologische isolatoren -

materialen die van binnen isolerend zijn, maar zeer geleidende toestanden hebben aan het oppervlak. Intrigerend genoeg worden deze oppervlakte- of randtoestanden beschermd door de onderliggende topologie van het bulkmateriaalwaardoor ze inherent robuust zijn tegen een breed scala aan verstoringen.

Gemotiveerd door de vooruitgang in de fysica van de gecondenseerde materie, werden topologische ideeën al snel geïntroduceerd als een ontwerpparadigma voor fotonica. Terwijl ze bestudeerd worden in een divers scala aan systemen, zijn fotonische kristallen vooral aantrekkelijk omdat ze topologische bescherming kunnen bieden op kleine schaal en voor on-chip toepassingen. Fotonische kristallen zijn structuren met een periodieke rangschikking van materialen met verschillende dielektrische constanten, geprofileerd op sub-golflengte schalen. Als zodanig gedragen ze zich als een effectief materiaal waar licht doorheen kan propageren op een manier die grotendeels analoog is aan hoe elektronen zich voortbewegen door het atomaire rooster van een kristal. Topologische isolatoren die beschreven worden in het kader van het kwantum-spin-Hall-effect en het kwantum-valley-Hall-effect vormen een bijzonder veelbelovende klasse van materialen om na te bootsen in fotonische kristallen vanwege de afhankelijkheid van ruimtelijke symmetrieën in plaats van magnetische velden. Bovendien zijn er veel intrigerende topologische fenomenen waargenomen in tweedimensionale vaste-stofsystemen zoals grafeen - een geometrie die gemakkelijk kan worden nagebootst in fotonische roosters.

In deze fascinerende context onderzoekt deze scriptie het potentieel en de beperkingen van het overbrengen van topologische concepten van het materiedomein naar licht, waarbij de nadruk ligt op experimenteel onderzoek binnen het vakgebied van tweedimensionale fotonische kristallen die werken in het telecomfrequentiebereik. We streven ernaar manieren te verkennen om topologische verschijnselen in fotonische kristallen te introduceren, de kenmerken van niettriviale bandtopologie in de ontstane toestanden te identificeren, en hun invloed op de stroming en beperking van licht in golfgeleiders en trilholtes te bestuderen. We gaan in detail in op de theoretische concepten die ten grondslag liggen aan topologische fotonische kristallen in hoofdstuk 1. De discussie omvat de vectoriële eigenschappen van licht, de natuurkunde van gecondenseerde materiesystemen met een nadruk op de Bloch-golfformalisme en Dirac-fysica, de relatie tot het abstracte wiskundige vakgebied van topologie, en tot slot de synthese van al deze concepten in de vorm van topologische fotonische kristallen.

Het onderzoek naar fotonische kristallen werd grotendeels aangedreven door de ontwikkeling van geavanceerde nanofabricagetechnieken. Vooral tweedimensionale fotonische kristallen profiteerden hiervan vanwege de compatibiliteit met veelgebruikte halfgeleiderfabricageprocessen. Dit maakte het mogelijk om complexe en grootschalige fotonische kristalroosters te realiseren met ingewikkelde kenmerken met operationele frequenties bedrijfsfrequenties tot in het optische regime. In hoofdstuk 2 rapporteren we over onze eigen fabricageprocedure die wordt gebruikt om de opgehangen silicium fotonische kristalmembranen te verkrijgen die in dit werk zijn bestudeerd, en benoemen we de experimentele technieken die worden gebruikt om de gefabriceerde apparaten te karakteriseren. Radiatieve fotonische kristalmodi kunnen handig worden onderzocht vanuit het verre veld,

waarbij we een Fourier-spectropolarimetrie-opstelling gebruiken om de spectrale, ruimtelijke en polarimetrische eigenschappen van de modi in reële- en impulsmomentruimte te karakteriseren. Aanvullende nabijveldtechnieken worden gebruikt om niet-radiatieve modi te karakteriseren, en zijn uitgevoerd via een fase- en polarisatieresolved nabijveldscanning optische microscopie.

Hoewel er veel analogieën zijn met systemen van gecondenseerde materie, vertonen fotonen ook opvallende verschillen met elektronen, met name hun bosonische karakter in plaats van fermionisch. Bovendien zijn topologische isolatoren gebaseerd op het kwantumspin-Hall-effect en het kwantum-valley-Hall-effect feitelijk reciproque systemen vanwege hun afhankelijkheid van ruimtelijke symmetrieën. Het is dus bijzonder intrigerend om de omvang en robuustheid van de topologische bescherming voor licht die deze systemen bieden in praktische experimenten te bestuderen. In hoofdstuk 3 testen we de topologische bescherming in een fotonische kristalplatform dat het kwantum-valley-Hall-effect voor licht nabootst. Dit systeem is niet-radiatief en daardoor aantrekkelijk in het kader van weinig verlies van golfgeleiders. Met fasegevoelige nabij-veld-scanning optische microscopie kunnen we voorwaarts- en achterwaarts voortplantende golfgeleidermodi onderscheiden en nauwkeurig de mate van terugkaatsing bij geconstrueerde defecten kwantificeren. We ontwikkelen een overdrachtsmatrixmodel om de reflectiecoëfficiënten in te schatten, welke een orde van grootte lager blijken te zijn in vergelijking met conventionele fotonicakristal golfgeleiders en wat wijst op een verbeterde bescherming tegen terugverstrooiing.

In hoofdstuk 4 bestuderen we de verre-veld emissie van trilholtes in een fotonisch kristalplatform wat het fotonische kwantum-spin-Hall-effect ondersteunt en helicale randstaten heeft die zwak gekoppeld zijn aan het stralingscontinuüm. We onderzoeken de kenmerken van topologische lichtbeperking. We karakteriseren de modusspectra en de multipolaire aard van trilholtes. Dezezijn verkleind tot de grootte van enkele puntdefecten binnen het omliggende fotonisch kristalrooster door hun modusprofielen in de reële en momentumspace in kaart te brengen. Kenmerken van de topologische bulkbandstructuur zoals bandinversie-geïnduceerde beperking en omgekeerd schalend gedrag van de modusspectra voor triviale en topologische defect trilholtes worden onthuld. We tonen ook bewijs van kenmerken van de topologische bescherming in de verliespercentages van de trilholtesdie grotendeels onaangetast blijven door de vorm en grootte van de trilholte. Ten slotte onderzoeken we het gedrag van de trilholtes als componenten in geïntegreerde apparaten bij het gebruik van topologische golfgeleiders, waarbij we een koppelingsmechanisme demonstreren dat wordt bepaald door spinbehoud, een eigenschap die geworteld is in de heliciteit van de topologische randstaten die ten grondslag liggen aan de modi in het platform.

Aangezien licht van nature niet reageert op echte magnetische velden, zijn er verschillende voorstellen gedaan over hoe men magnetische interacties met fotonen effectief kan interfereren.magnetische interacties effectief kunnen worden geïnterfereerdworden bemiddeld voor fotonen. In hoofdstuk 5 onderzoeken we de mogelijkheden om lichtpropagatie en lokalisatie op een chip te controleren via synthetische meetvelden die worden opgewekt door kunstmatige vervorming van

een fotonisch kristalrooster -analoog aan vervormd grafeen. Net zoals de vorming van Landau-niveaus voor elektronen in een extern magnetisch veld, observeren we een discretisering van de fotonische dispersie in vlakke banden als gevolg van de pseudomagnetische velden die worden veroorzaakt door de vervormingen de bijbehorende hoge degeneratie en lokale dichtheid van toestanden. De grote ontwerpvrijheid van het fotonische kristalplatform biedt ongekende flexibiliteit voor vervormingsengineering, wat blijkt uit het realiseren van domeinen met tegenovergestelde pseudomagnetische velden die topologische randtoestanden hebben aan hun interface. De met pseudomagnetische velden geïnduceerde toestanden hebben opmerkelijk hoge kwaliteitsfactorenondanks dat ze inherent gekoppeld zijn aan straling in vrije ruimte.

De bevindingen en conclusies van dit werk dragen bij aan een betere beoordeling van de vooruitzichten en mogelijkheden voor toekomstig onderzoek en toepasbaarheid van tweedimensionale topologische fotonische kristallen in geïntegreerde fotonische apparaten.

ACKNOWLEDGEMENTS

Smooth seas do not make skillful sailors. An adequate metaphor to capture the process that culminated in this book, and topographically accurate for the environment in which this happened. Navigating through the process of crafting this thesis was indeed a significant voyage. In addition to the scientific endeavor, this adventure also involved moving to the Netherlands, a transition that came with its own set of nuances and opportunities to learn. The global pandemic further rendered my experience —– and that of many others —– rather unconventional. While there were challenges, the journey was made far smoother and enjoyable thanks to the support of many incredible individuals. Over the years, it became increasingly evident that AMOLF I had the chance to work in a uniquely encouraging and inspiring environment, and I will remember my time here fondly. Therefore, I would like to extend my sincere gratitude to everyone who has, knowingly and unknowingly, greatly supported me in the completion of my PhD.

Ewold, it goes without saying that this thesis would not exist without your guidance. The strongest advice I received in regard to my search for a PhD position was to pick my group leader wisely, and I am glad to say that this worked out splendidly. Your ability to adeptly juggle numerous responsibilities while maintaining an open and attentive ear to your group members, even during the busiest times (which are frequent), is truly admirable. The mentoring and counsel you have provided over the years have been instrumental to my development and success. Thank you for your dependability, your enthusiasm, and the trust you have placed in me since day one in your group.

Speaking of supervision, I would also like to thank my second promotor, **Kobus**, for the steadfast support throughout several projects. The input you provided during our numerous discussions over the years has been invaluable. I greatly appreciate the expertise and wit you consistently brought to our weekly meetings, especially when you assumed your tailor-made role as the devil's advocate. Importantly, you have maintained a sense of humor and light-hearted spirit throughout, which I believe positively influences your group members with whom I had the pleasure to collaborate extensively over the past years.

Sonakshi, I remember the first time we met in person at the AMOLF summer school all green behind the ears, and suddenly four years have passed and we both are at the end of this journey. It was fun doing the PhD in synchrony, not only thanks

to the fruitful collaboration, but also since this meant that we could relate to each other's successes and struggles quite directly. I appreciate your diligence in the work we did, and the humorous and well-dosed sarcastic way of dealing with things along the way. Best of luck for whatever the future holds for you. **Thomas**, our paths seem destined to cross, first at MPL in Erlangen, then at TU Delft, and again at AMOLF with your new role at UvA. Working with you has always been a pleasure due to your calm demeanor and approachability. Yet, below the calm surface you possess scientific skills and a driving force that has been of inestimable value to our collaboration, thank you for that. **Daniël**, though our time working together was brief, it was great to see your skills develop over the course of our joint project. I am confident that you will excellently carry on the legacy in Kobus' group. I wish you all the best in this endeavor and in the pursuit of your PhD.

Joining the Photonic Forces group was a rewarding experience, offering the privilege of witnessing two generations of PhDs. Each member brought unique traits while maintaining an open, friendly atmosphere intrinsic to the group. **Jente**, thank you for being a great colleague, neighbor, paranymph, and friend. I admire your jolly nature, camaraderie, resilience, and your exquisite taste in Belgian beer, which expanded my palate beyond familiar Bavarian brews. **Jesse**, sharing an office with you often felt like a seamless continuation of my life in Germany. Your outstanding impersonations and endless Dutch and German trivia enriched my experience. Thank you for that and hopefully "auf Wiederschnitzel". **Roel**, you were my first contact in the group and a welcoming presence during my solicitation, and I enjoyed our shared moments inside and outside the lab ever since. Your well-timed jabs at German customs were a delightful contrast to my comments on Dutch bread and other peculiarities. Best wishes for your next life chapter. **Javier**, your charisma and grounded demeanor defy the stereotypical image of a theoretical physicist. It has been wonderful seeing you and Bruna in Amsterdam and Zürich, witnessing your continuous thrive. **Cesare**, during the year you were part of our group, your potential as a great scientist and your deeply social streak became abundantly clear. Thank you for the memorable evenings at DUWO during the lockdown, I enjoyed your ironic and sharp-witted comments, and watching you spar with Andrea over essentially every topic. **Giada**, your outspokenness and passion for science and art are admirable. Best wishes for your continued success in merging these two domains. **Nikhil**, thank you for guiding me early in my PhD and passing the topological torch to me. **Robin**, your unique wit added a delightful dynamic to our group and I typically remember (and see) you with a smirk on your face. It is always pleasant to bump into you in- and outside AMOLF, even long after your departure from the group. **Daniël**, thank you for all the fun chats and for keeping the group afloat from the technical side of things, it is great to see how quickly you grew into your new role and even manage to combine it with your own experimental work. **Pascal**, I think fondly of the time we had you in our group, thank you for many pleasant conversations and for your characteristic dry humor that made me laugh on many occasions. **Alejandro**, your visits to Amsterdam were always a delight, where your presence and calm demeanor enriched many of our fancy lunches. **Giorgios**, sharing an office while grappling with the intricacies of

topology in photonic crystals was a pleasure. **Karel**, your charisma and humor made every conversation enjoyable, both before and after sharing a few drinks. **Lars**, you were a kind presence in the group and I enjoyed our chats, I wish you continued success in your PhD. **Menno**, your transition from junior to senior in our group was swift, and it feels like you have been part of it much longer than is actually the case. Remarkably, you are ahead of me in the immersion into various aspects of German culture (Bagger 288, visiting Oktoberfest, owning Lederhosen), a commendable achievement. **Fons**, you are a seamless fit for our group and the AMOLF environment, a pleasant person to chat with while cracking just the right amount of silly jokes per unit of time. **Johneph**, you were not only an enthusiastic and dedicated colleague but also a kind-hearted friend with clear career goals, something many of us strive for. Conversations about fabrication, life in India and Germany, and various other topics were always enlightening and enjoyable. You are sorely missed. Last but not least, **Jonne**, **Giorgios**, and **Tuoyu**, our most recent members of the Photonic Forces, though our time together was brief, extrapolating from the status quo makes me confident that you will have no issues in carrying on the group spirit and succeeding on your academic trajectory.

Several individuals within and related to AMOLF deserve my acknowledgement. My journey began with meeting **Femius** at a Rome conference in 2018. Despite the absence of immediate openings, your invitation for a solicitation enabled me to pursue my PhD project with Ewold —– thank you, Femius. I also extend gratitude to **Said** and **Imran** for constructive feedback and engaging questions during colloquia and poster sessions. **Sergey**, your encouragement to pursue a PhD at AMOLF, coupled with your exceptional mentorship during my Master's tenure at MPL in Erlangen, significantly influenced my career trajectory. Your support was invaluable. Looking back, I spent most of my first year in the cleanroom, and many more weeks in the years to follow. **Bob**, **Dimitry**, **Igor**, and **Hans**, thank you for the great support over this period, magically fixing problems with devices that seemed unsolvable, and always picking up the phone even if it was the gazillionth call for help in a day. Without your dedication, none of the photonic crystals in this thesis would have seen the laser light of day. My extended gratitude goes to all the support departments that keep AMOLF running so smoothly. In particular, thanks to the precision manufacturing team led by **Jan** for their help with wafer dicing, to **Jan-Bonne** and **Marko** for support in the lab, **Henk-Jan** and **Max** from mechanical design for manufacturing an updated sample stage and holder, **Rutger** for IT support, and **Clyde** for support with facilities.

Andrea, thank you for the many cheerful moments inside and outside of work, I was particularly glad to have you there as a knowledgeable local during the conference in Siena. Your sociable nature —– what Germans would perhaps describe as "bekannt wie ein bunter Hund" —– is admirable, and all the while, you have excelled in science. Whether within academia or beyond, I am confident in your bright future. Thanks are also due to **Paweł** and **Alex**, for shared moments during the lockdown. **Giorgio**, it is always great fun to cross your path, thank you for your kind nature and all the nice conversations. **Ariane**, thank you for the times spent together following our first encounter at AMOLF during your Master's, and after you

returned to start your PhD. I extend my best wishes for your career and personal life's next phases. Many others at AMOLF contributed to making my time enjoyable — through coffee chats, kind gestures, outings, and various events (kudos to the PV for organizing!). Each interaction added value to my experience, and for that, I am thankful to a long list of people, including (but not exclusively): **Agustín**, **Alex L.**, **Annemarie**, **Arno**, **Balázs**, **Carolyn**, **Christian**, **Daphne**, **Davide**, **Debapriya**, **Dominique**, **Eitan**, **Evelijn**, **Evgenia**, **Falco**, **Giel**, **Hongyu**, **Ilan**, **Isabelle**, **Jaime**, **Jeroen**, **Kelly**, **Kevin P.**, **Kévin C.**, **Kian**, **Lukas**, **Magda**, **Manuel**, **Mareike**, **Marloes**, **Matthias**, **Moritz**, **Nasim**, **Nelson**, **Nick**, **Nika**, **Olivier**, **Parisa**, **Radosław**, **Ruslan**, **Saeed**, **Stefan**, **Sven**, **Tom V.**, **Tom W.**, **Vashist**, **Verena**, **Wessel**, **Xuan**, **Yorick**, **Yvonne**, **Zabreen**, **Zhou**.

When not absorbed in work at my desk, the optical table, or the chemical bench, I had the fortune of enjoying delightful distractions and unforgettable moments with dear friends. Over the course of my regular visits back home to Germany, and the reciprocal visits to Amsterdam, I was glad to realize that many of the friendships I built earlier in life remained undiminished by the miles that separated us. **Tobias**, **Philipp**, **David**, and **Fabian**, our biannual gatherings were events I eagerly anticipated. Whether we were skiing in Austria during the winter or hiking through the splendid landscapes around Aufseß (complemented by its exquisite local breweries) in summer, each moment was a cherished highlight of my year. David, it was a joy having you in Amsterdam following your move. I extend my gratitude to both you and **Mareen** for the delightful events we have celebrated together, with the promise of many more to come. **Florian**, I am glad that we maintained our friendship ever since our wild times in Stein, thank you for your repeated visits and for all the fun reunions back home. **Verena** and **Katja**, thank you for keeping in touch over the years, I always enjoy seeing you and updating each other about our lives on my visits to Nuremberg. **Lena**, thank you for visiting me in the very beginning and for the lovely conversations on the phone and during long walks on my visits home. **Yannick**, I have cherished your company since our high school days. Despite the inevitable changes we have all undergone, it is comforting to see the constancy in our relationship. **Jens**, thank you for initiating me into life in Amsterdam, offering me accommodation during my solicitation, your regular visits, and the delightful holidays and parties we have enjoyed together. **Dominik**, although you have been building a new life in Zürich, our reunions always feel as though nothing has changed. Your steadfast friendship, your kind spirit, and the effort you make to maintain our connection are deeply valued. **Tim**, your discipline in the things you do is admirable, and even more so your loyalty as a good friend. From our traumatic trip to Ameland, to countless enjoyable events shared side by side, I am glad that our friendship has cemented over time. **Philipp**, I appreciate your effort to sustain our friendship over the years despite the distance. Memories of summers by the Rednitz, spinning the "Scheibe", and our deep, reflective conversations are treasures I hold dear, with the hope and confidence that there are many more to come.

Last but certainly not least, I must extend my heartfelt gratitude to family members who have been instrumental in my journey. A special thanks to **Ate** and **Erik**,

and all the kind-hearted members of your family. Your warm welcome into your family provided genuine solace that made me feel at home, and your inclusion of me in various festivities and the lessons on life and customs in the Netherlands have been deeply appreciated. **Maarten**, your witty comments and humorous remarks never fail to bring a smile to my face. Thank you for the delightful nights out and engaging discussions on science and technology. Turning to my immediate family, the Barczyks, I owe a depth of gratitude. To my parents **Grażyna** and **Bogdan**, thank you for your unwavering support and guidance that have been my constant. You have not only helped shape who I am but have also stood by me through every high and low of my life and encouraged me at every step it took to reach this goal. There is more gratitude to you than I can express in these few lines. To my cherished younger sister, **Jessica**, I am proud seeing you carve out your path with determination, and elated that **Michael** is by your side, providing support as you navigate through life. It brings me joy to see that the family's social flair has passed onto you – thank you for shouldering this delightful "burden". Finally, to my beloved partner and paranymph, **Marente**. Meeting you marked a bright chapter of my life abroad, filled with treasured memories. Your presence has brought immense joy and light into my life. With a kind heart, you have provided grounding and support when I needed it most. For all of this and more, 大好きだ.

About the author

René Barczyk was born in 1995 in Nuremberg, Germany. He obtained his undergraduate degree in physics at the Friedrich-Alexander University Erlangen-Nuremberg (Erlangen, DE). He conducted his Bachelor's thesis at the Chair for Laser Physics of Peter Hommelhoff on the optical properties of graphene under femtosecond laser pulse illumination. For this work, he received the Ohm-Award for an excellent Bachelor's thesis in the area of physics from the university. He went on to conduct his Master's thesis on the optical response of chiral nanostructures in the group of Peter Banzer at the Max Planck Institute for the Science of Light, where he was also involved in several other collaborative projects in the field of nanophotonics.

Over the course of his studies, René was employed as a working research student for several projects at Siemens AG in Erlangen. Working in the commissioning department, he served as both a front- and back-end developer, creating software for the automatic readout of control device configuration data and the streamlining of documentation processes.

After obtaining his Master's degree in 2019, René joined the Photonic Forces group at AMOLF to conduct research in the field of topological photonics, including multiple collaborations with the group of Kobus Kuipers at TU Delft. The findings of this research are described in this thesis. René's work has been presented at several national and international conferences and published in refereed journals.

René enjoys time with friends, travelling, music festivals, and good food.